

Endogenous Regulators of Gamma-Secretase and Amyloid-Beta Production, and Engineering of Alzheimer's Disease Therapeutic Tools

THÈSE N° 6897 (2016)

PRÉSENTÉE LE 12 FÉVRIER 2016

À LA FACULTÉ DES SCIENCES DE LA VIE
CHAIRE MERCK SERONO EN NEUROSCIENCE
PROGRAMME DOCTORAL EN NEUROSCIENCES

ÉCOLE POLYTECHNIQUE FÉDÉRALE DE LAUSANNE

POUR L'OBTENTION DU GRADE DE DOCTEUR ÈS SCIENCES

PAR

Sébastien MOSSER

acceptée sur proposition du jury:

Prof. J. Gräff, président du jury
Prof. P. Fraering, directeur de thèse
Dr D. Beher, rapporteur
Prof. U. Konietzko, rapporteur
Prof. D. Schorderet, rapporteur



ÉCOLE POLYTECHNIQUE
FÉDÉRALE DE LAUSANNE

Suisse
2016

TABLE OF CONTENTS

ACKNOWLEDGMENTS	1
ABSTRACT	3
RÉSUMÉ	5
ABBREVIATIONS	7
CHAPTER I : GENERAL INTRODUCTION.....	8
I.1) THE PATHOLOGICAL HALLMARKS OF ALZHEIMER’S DISEASE	9
I.2) CURRENT TREATMENTS AND DETECTION.....	11
I.3) THE AMYLOID CASCADE HYPOTHESIS AND AD GENETICS	13
I.4) APP TRAFFICKING AND A β GENERATION.....	15
I.5) APP CELLULAR FUNCTION	18
I.6) ASSEMBLY AND STRUCTURE OF THE γ -SECRETASE COMPLEX	20
I.7) THERAPEUTIC STRATEGIES IN AD	22
I.8) AIM OF THE THESIS WORK	24
CHAPTER II : MODULATION AND PHYSIOLOGICAL FUNCTIONS OF γ-SECRETASE	26
II.1) INTRODUCTION.....	27
II.1.a) <i>Endogenous modulators of Aβ production</i>	27
II.1.b) <i>Effects of post-translational modifications on the enzymatic activity of γ-secretase</i>	27
II.1.c) <i>The role of γ-secretase in the cytoskeleton dynamics</i>	28
II.2) RESULTS	29
II.2.a) <i>The Adipocyte Differentiation Protein APMAP is an Endogenous Suppressor of Aβ Production in the Brain</i>	29
II.2.b) <i>Identification of New Presenilin-1 Phosphosites: Implication for γ-Secretase Activity and Aβ Production</i>	29
II.2.c) <i>Inactivation of Brain Cofilin-1 by Age, Alzheimer's Disease and γ-Secretase</i>	30

II.3) MANUSCRIPTS	30
II.3.a) <i>The Adipocyte Differentiation Protein APMAP is an Endogenous Suppressor of Aβ Production in the Brain</i>	31
II.3.b) <i>Identification of New Presenilin-1 Phosphosites: Implication for γ-Secretase Activity and Aβ Production</i>	60
II.3.c) <i>Inactivation of Brain Cofilin-1 by Age, Alzheimer's Disease and γ-Secretase</i>	86
CHAPTER III : ENGINEERING NEW TOOLS FOR THE OBSERVATION AND REPAIR OF BRAIN STRUCTURE DAMAGES	116
III.1) INTRODUCTION	117
III.1.a) <i>Monitoring brain structure alterations in AD</i>	117
III.1.b) <i>Rescue brain alteration in neurodegenerative processes</i>	117
III.2) RESULTS	118
III.2.a) <i>Accurate Resistivity Mouse Brain Mapping Using Microelectrode Arrays</i>	118
III.2.b) <i>Detection of Alzheimer's Disease Amyloid-beta Plaque Deposition by Deep Brain Impedance Profiling</i>	118
III.2.c) <i>A Compressible Scaffold for Minimally Invasive Delivery of Large Intact Neuronal Networks</i>	119
III.3) MANUSCRIPTS.....	119
III.3.a) <i>Accurate Resistivity Mouse Brain Mapping Using Microelectrode Arrays</i>	120
III.3.b) <i>Detection of Alzheimer's Disease Amyloid-beta Plaque Deposition by Deep Brain Impedance Profiling</i>	131
III.3.c) <i>A Compressible Scaffold for Minimally Invasive Delivery of Large Intact Neuronal Networks</i>	140
CHAPTER IV : GENERAL DISCUSSION AND PERSPECTIVES.....	177
IV.1) DISCUSSION.....	178
IV.2) PERSPECTIVES	182
BIBLIOGRAPHY	185
CURRICULUM VITAE	212

Acknowledgments

I would like to express my gratitude to my advisor Professor Patrick C. Fraering for accepting me in his lab, and sharing with me his rigor and his passion for science. Thanks for all the constructive remarks and criticisms which taught me to stay objective about my work, and for letting me work on a high diversity of exciting projects.

Also, I want to acknowledge all CMSN lab member for their help all the time of my PhD thesis. I especially thank Dr. Claude Schweizer for sharing with me his knowledge and patience, and trying to convince me not do a PhD. I thank the former lab members Dr. Jemila Houacine, Dr. Isabelle Magold, Dr. Nathalie Bot, Dr. Tristan Bolmont, Prof. Fang Wu and Dr. Jean-René Alattia for their support and interesting discussions. I have to acknowledge our former technicians Lorène Aeschbach and Justine Pascual for their outstanding technical support. Many thanks to our PhD students Dr. Mitko Dimitrov for guiding me along my PhD and for challenging my data, Magda Palczynska for the nice moments and parties. Special thanks to our master students Alexandre Matz for helping me with my work and for the interesting discussion. A warm thanks to current lab members for the great work atmosphere, Dr. Erika Borcel for her kindness and help, Pablo Serrano de Toro for your perseverance and the funny “whaaaat?!?” you say all the time, Hermeto Gerber for breaking the Swiss clichés about strictness and organization, Virginie Braman for her cheerfulness and her sweet French accent, Guillermo Garcia Osuna for his patience during lab meetings, and Chloé Hot for her support help and sincerity. I shall not forget to thank my lab neighbors Anass Chiki, Ossama Khalaf and Bruno Fauvet for teaching me Arabic, and for their cheerful company at any time day and night.

I’m very grateful to all our collaborators from EPFL Dr. Amélie Bédurier, Dr. Pierre Joris, Thibault Francfort and Ren Yufei for the interesting discussions and for making me discover new scientific approaches. I appreciated the help of the SV proteomics facility Dr. Marc Moniatte, his patience and inputs for mass spectrometry experiments. I have to acknowledge the people from the “centre de phénogénomique”, especially Emilie Feignoux and Anouk Berger for their huge support with mice care, as well as Dr. Isabelle Desbaillets for keeping calm and helping me when I had problems with managing animal licenses. Many thanks to my mentor Daniel Schorderet for giving me the opportunity to work with his team, and discover a different working atmosphere.

I address my roommates Stefan, Dr. Florian, Fanny, Pauline, Kevin and Svenja my acknowledgment for their pleasant daily company, and interesting talks we had around a beer. Thank you to my

friends for their help in difficult moment and great time we spent together. Special thanks to Anne-Claire for motivating me to start writing my PhD thesis.

Finally, I would like to thank my parents Colette and Daniel for their precious advices and continuous encouragements through my PhD work and during my life. I also want to acknowledge my brother Thomas and my sister Sandrine for their comprehension, their advices and great discussions we had. To my friend Delphine, thank you for your love, for your precious help and support at the end of my PhD thesis, and for your kindness and comprehension.

Abstract

Alzheimer's disease (AD) is a devastating neurodegenerative disease characterized by strong cognitive impairment and memory loss. These symptoms are caused by neuronal death, induced by two pathological hallmarks: extracellular senile plaques composed of aggregated amyloid-beta ($A\beta$) peptides, and intracellular neurofibrillary tangles generated by the hyperphosphorylation of the actin-binding protein Tau. Genetic and biochemical analysis resulted in the generation of the so-called amyloid cascade hypothesis, which stipulates that $A\beta$ aggregation precedes neurofibrillary tangles and initiate AD pathogenesis. $A\beta$ originates from the proteolytic cleavage of the amyloid precursor protein (APP) by γ -secretase, an intramembrane cleaving protease. Thus, pharmacological modulation of γ -secretase emerged as a promising strategy for the treatment of AD. However, strong side effects, including cognitive function worsening, were reported following clinical inhibition of this enzyme, caused by altered processing of the numerous γ -secretase substrates. Pharmaceutical industries, alongside with academia, oriented their research toward the discovery of compounds selectively affecting the processing of APP, without altering the cleavage of other substrates.

In the first part of this thesis work, we focused our research on endogenous modulation of γ -secretase, and its consequences on actin cytoskeleton dynamics. We performed mass spectrometric analysis of purified γ -secretase, and identified the adipocyte plasma membrane associated protein APMAP as a γ -secretase interacting protein. We showed that APMAP modulates the generation of $A\beta$ peptides without affecting the processing of other γ -secretase substrates, and controls APP degradation by the lysosomal/autophagic pathway. We also investigated the regulation of γ -secretase by post translational modifications, and concluded that its enzymatic activity is not affected by its phosphorylation. We then observed the effects of γ -secretase inhibition on physiological processes, and discovered a γ -secretase-dependent regulation of the binding of Cofilin to actin filaments. These observations showed a direct link between γ -secretase and the actin cytoskeleton required for cell motility and neuronal plasticity.

In the second part of this work, we aimed at finding a new method for monitoring brain structure alteration and provide new tools for the study of neurodegenerative disease progression in animal models. We performed *ex-vivo* electrical impedance measurement from intracerebral electrode in mice brain, and succeeded in the visualization of cortical layers as well as brain nuclei. Moreover, we used this method to visualize structural alteration caused by $A\beta$ plaques in an AD mouse model.

After imaging, we aimed at repairing neuronal loss causing the structural alterations observed in neurodegenerative diseases. We developed a compressible and injectable extracellular-matrix-like cell culture scaffold (cryogel) to promote neuronal growth in brain lesions. Primary cortical neuron culture on our cryogel scaffold showed good axonal sprouting, not affected by cryogel compression.

Keywords:

Alzheimer's Disease, Gamma-Secretase, Amyloid Precursor Protein, Autophagy, Endogenous Modulator, Phosphorylation, Electrical Impedance, Brain Structure, Extracellular Matrix

Résumé

La maladie d'Alzheimer (MA) est une maladie neurodégénérative dévastatrice caractérisée par un important déficit cognitif et la perte de mémoire. Ces symptômes sont causés par la mort de neurones, induite par les deux marqueurs de la MA : les plaques séniles extracellulaires composées de peptides beta-amyloïde (β A) agrégés, et les enchevêtrements neurofibrillaires générés par l'hyperphosphorylation de la protéine Tau. Des analyses génétiques et biochimiques ont permis l'élaboration de l'hypothèse de la cascade amyloïde, qui stipule que l'agrégation des β A précède les enchevêtrements neurofibrillaires et déclenche la pathogénèse de la MA. Les β A proviennent du clivage protéolytique de la protéine précurseur de l'amyloïde (PPA) par la γ -sécrétase, une protéase coupant dans le domaine transmembranaire. C'est pourquoi la modulation pharmacologique de la γ -sécrétase est une stratégie intéressante pour le traitement de la MA. Cependant, d'importants effets secondaires, incluant la détérioration des fonctions cognitives, ont été observés suite à l'inhibition clinique de cette enzyme, causés par l'altération du clivage des nombreux substrats de la γ -sécrétase. En conséquence, les industries pharmaceutiques aux côtés des universités, ont orienté leurs recherches vers la découverte de composés altérant de manière sélective la coupure de la PPA, sans modifier le clivage d'autres substrats.

Dans la première partie de ce travail de thèse, nous focalisons nos recherches sur la modulation endogène de la γ -sécrétase, et les conséquences sur la dynamique du cytosquelette d'actine. Nous avons analysé la γ -sécrétase purifiée par spectrométrie de masse, et avons identifié la protéine membranaire d'adipogénèse APMAP interagissant avec la γ -sécrétase. Nous avons montré que APMAP module la production des β A sans affecter le clivage d'autre substrats de la γ -sécrétase et contrôle la dégradation de la PPA par la voie de signalisation autophagique/lysosomale. Nous avons aussi investigué la régulation de la γ -sécrétase par modifications post-translationnelles, et conclu que la phosphorylation ne modifie pas son activité enzymatique. Puis, nous avons observé les effets de l'inhibition de la γ -sécrétase sur les processus physiologiques, et avons découvert une régulation γ -sécrétase-dépendante de l'interaction entre la Cofilin et les filaments d'actine. Ces observations ont montré un rôle direct de la γ -sécrétase dans l'organisation du cytosquelette d'actine, nécessaire à la mobilité cellulaire et la plasticité neuronale.

Dans la seconde partie de ce travail, nous cherchions une méthode simple pour surveiller l'altération de la structure cérébrale, et permettre l'étude de la progression des maladies neurodégénératives dans les modèles animaux. Nous avons effectué des mesures d'impédance

électrique *ex-vivo* dans le cerveau murin, et avons réussi à visualiser les couches corticales ainsi que des noyaux cérébraux. Cette méthode nous a permis de visionner les altérations structurelles causées par les plaques β A dans un model murin de la MA. Après cette étape de visualisation, nous avons eu pour but de réparer la mort neuronale responsable de changements cérébraux dans les maladies neurodégénératives. Nous avons développé un substrat cellulaire similaire à la matrice extracellulaire (cryogel), compressible et injectable, dans le but de promouvoir l'intégration et la croissance des cellules neuronales dans les lésions cérébrales. La culture de neurones primaires sur nos cryogels a montré un bon développement axonal, non-affecté par la compression du cryogel.

Mots clés:

Maladie d'Alzheimer, Gamma-Sécrétase, Protéine Précurseur de l'Amyloïde, Autophagie, Modulateur endogène, Phosphorylation, Impédance électrique, Structure cérébrale, Matrice Extracellulaire

Abbreviations

A β	Amyloid-beta
ADF	Actin depolymerizing factor
AICD	Amyloid precursor protein intra-cellular domain
Aph1	Anterior pharynx defective 1
APMAP	Adipocyte plasma membrane associated protein
APP	Amyloid precursor protein
C83	83 amino-acid long Amyloid precursor protein C-terminal fragment
C99	99 amino-acid long Amyloid precursor protein C-terminal fragment
CTF	C-terminal fragment
FAD	Familial Alzheimer's disease
FDA	Food and drug administration
iNCT	Immature nicastrin
KO	Knock-out
mAPP	Mature Amyloid precursor protein
MCI	Mild cognitive impairment
mNCT	Mature nicastrin
NCT	Nicastrin
NFT	Neurofibrillary tangles
NMDAR	N-methyl-D-aspartate receptor
NTF	N-terminal fragment
PEN2	Presenilin enhancer 2
PPAR γ	Peroxisome proliferator-activated receptor γ
PS	Presenilin
PTM	Post-translational modification
sAPP	Soluble amyloid precursor protein
SSH1	Slingshot1
WT	Wild type

Chapter I

General introduction

I.1) The pathological hallmarks of Alzheimer's disease

Alzheimer's disease (AD) is the most common dementia affecting the elderly population. Patients suffering of AD display progressive cognitive impairment including memory loss and emotional instability^{1,2}. In the late stages of the disease, metabolism, motor functions and immune system alteration lead to patient's death, often linked to infections by opportunistic diseases (for a review, see ³). By the examination of AD patient's brain, we see that these symptoms are triggered by an important brain shrinkage caused by neuronal death (Fig. 1). At a molecular level, neurodegeneration is triggered by both AD pathological hallmarks, extracellular senile plaques composed of aggregated amyloid-beta peptides ($A\beta$)⁴, and intraneuronal neurofibrillary tangles (NFT) induced by Tau protein hyperphosphorylation⁵ (Fig. 1).

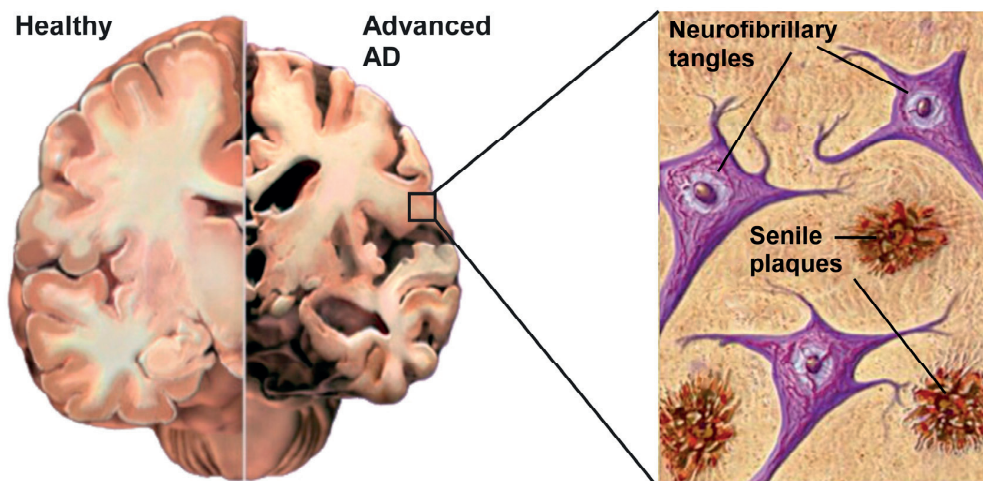


Figure 1: AD pathological hallmarks. Left panel, MRI-based image representing tissue shrinkage in advanced AD versus healthy brain. Right panel, cellular zoom in AD brain where the two AD pathological hallmarks, intraneuronal neurofibrillary tangles and extracellular senile plaques are observed. Adapted from https://www.alz.org/braintour/healthy_vs_alzheimers.asp and <http://www.thealzheimerssolution.com/-category/plaques-tangles/>

Interestingly, both senile plaques and neurofibrillary tangles spread in the human brain according to a well-characterized pattern^{6,7} (Fig. 2). In the early presymptomatic stage of the disease, $A\beta$ aggregation starts in the entorhinal cortex and induces NFT formation. $A\beta$ spread according to a prion-like mechanism⁸, whereas NFT travel through synapses by cell-to-cell transmission^{9,10} and progress to the hippocampus as well as to more distal cortical regions (Fig. 2, stages 1-3). While in AD patients neurodegeneration progresses in the latter brain regions, $A\beta$ reach various pons nuclei

and progressive cognitive impairment is diagnosed (Fig. 2, stage 4). In the last stages of the disease, almost all brain structures are altered by strong neurodegeneration and A β -induced synaptic impairment, leading to dysregulation of a high number of physiological functions (Fig.2, stage 5).

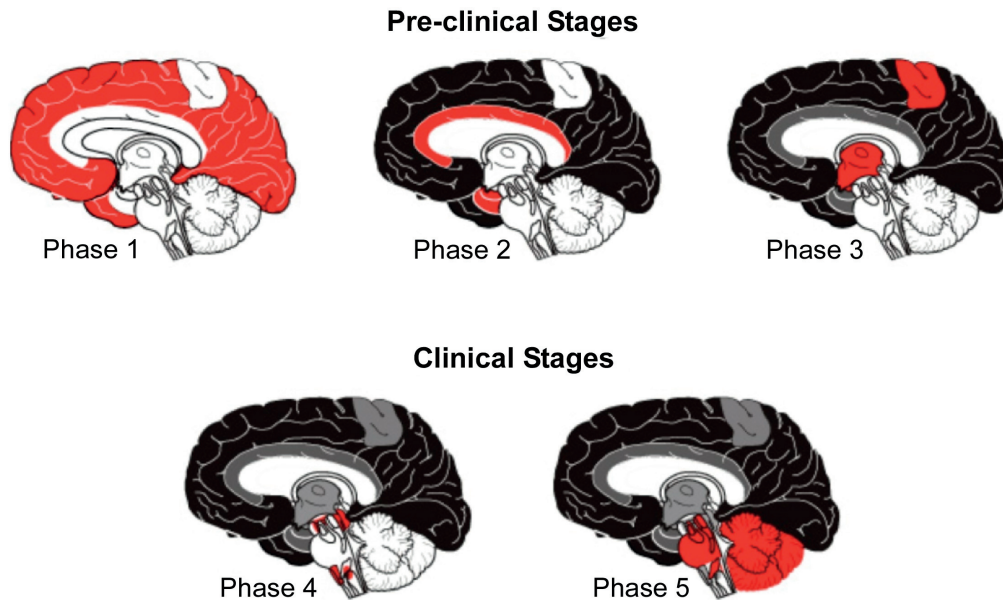


Figure 2 : AD progression pattern. Senile plaques and neurofibrillary tangles generation start in the entorhinal cortex in presymptomatic very early AD, then spread into the hippocampus and extended cortex area and induces neuronal death (black, or grey for lower tissue alteration). Strong alteration in cortical/hippocampal circuitry and affection of pons nuclei lead to important cognitive symptoms. In last phase 5, almost all brain regions are affected. Damaged structures are marked in grey/black, newly altered brain areas are marked in red. Adapted from ¹¹.

Alterations in A β levels precede AD onset and can be detected up to 25 years before the first symptoms appear¹². Patient's death appears on average 8-10 years following AD onset. Progressive loss of cognitive functions and the alteration of AD patients day-to-day life requires long constant care, explaining the high economic burden for this disease (200 billion € / year for 90 million AD patients in Europe in 2015¹³). Moreover, with the progress of medicine and the prolonged human lifespan, a 25% increase in the amount of population suffering from dementia, but also in money expenses are expected in the next 15 years¹³. With this expected economic burden for our society, it becomes urgent to find a solution to slow down or stop the disease's progression.

I.2) Current treatments and detection

1.8 % of total European population suffer from dementia, 60% of them are diagnosed with AD. As people age, AD statistics are striking: the disease affects 10% of individuals over 65 years old, 20% over the age of 80, and more than the third over 90 years old^{14,15}. Because these values are expected to increase, important efforts have been deployed in the discovery of a cure. Despite those efforts, medical expectations have not been met, as of today no treatment has the capacity to alter the progression of AD. The unique AD treatments are solely symptomatic and display important side effects (listed in table 1, for a review see¹⁶).

Drug name	AD stages	Class	Mechanism of action	Side effects
Donepezil®	Mild to severe	Cholinesterase inhibitor	Prevents the breakdown of acetylcholine in the brain	Nausea, vomiting, diarrhea, muscle cramps, fatigue, weight loss
Rivastigmine®	Mild to moderate	Cholinesterase inhibitor	Prevents the breakdown of acetylcholine in the brain	Nausea, vomiting, diarrhea, weight loss, decreased appetite, muscle weakness
Galantamine®	Mild to moderate	Cholinesterase inhibitor	Prevents the breakdown of acetylcholine and stimulates nicotinic receptors to release more acetylcholine in the brain	Nausea, vomiting, diarrhea, weight loss, decreased appetite
Memantine®	Moderate to severe	NMDA receptor antagonist	Blocks the toxic effects associated with excess glutamate and regulates glutamate activation	Dizziness, headache, diarrhea, constipation, confusion

Table 1: Current symptomatic treatments for AD. The four compounds listed are the only FDA-approved drugs and reduce AD symptoms severity. Notice that none of these drugs impact the progression of the disease. Adapted from <https://www.nia.nih.gov/alzheimers/publication/alzheimers-disease-medications-fact-sheet>

Cholinergic neurotransmission is strongly impaired in AD, and its alteration correlates with a strong decrease in individual cognitive functions¹⁷⁻¹⁹. Thus, inhibition of acetylcholine esterase – responsible of acetylcholine neurotransmitter degradation – to stimulate the survival of the cholinergic neurons appeared to be an appealing strategy to compensate network alteration and restore cognitive functions. Indeed, three acetylcholine esterase inhibitors – Donepezil®, Rivastigmine® and Galantamine® – were approved by the US food and drug administration (FDA) 10 years ago, and remain routinely used to treat AD. In addition to its inhibitory effect on

acetylcholine esterase, Galantamine[®] was shown to bind to the allosteric site of the nicotinic acetylcholine receptors and potentiate their activation²⁰. Also, Donepezil[®] inhibits N-methyl-D-aspartate receptor (NMDAR) activation²¹. In addition to cholinergic alteration in AD, overactivation of NMDAR by the main excitatory neurotransmitter, glutamate, has been reported to induce neuronal excitotoxicity and triggers cell death^{22–24}. Treatment with the NMDAR non-competitive partial antagonist Memantine[®] decreased receptor activation, cytotoxicity and improved cognitive functions. In AD's severe stage, synergistic treatment with both Memantine[®] and Donepezil[®] is often recommended²⁵.

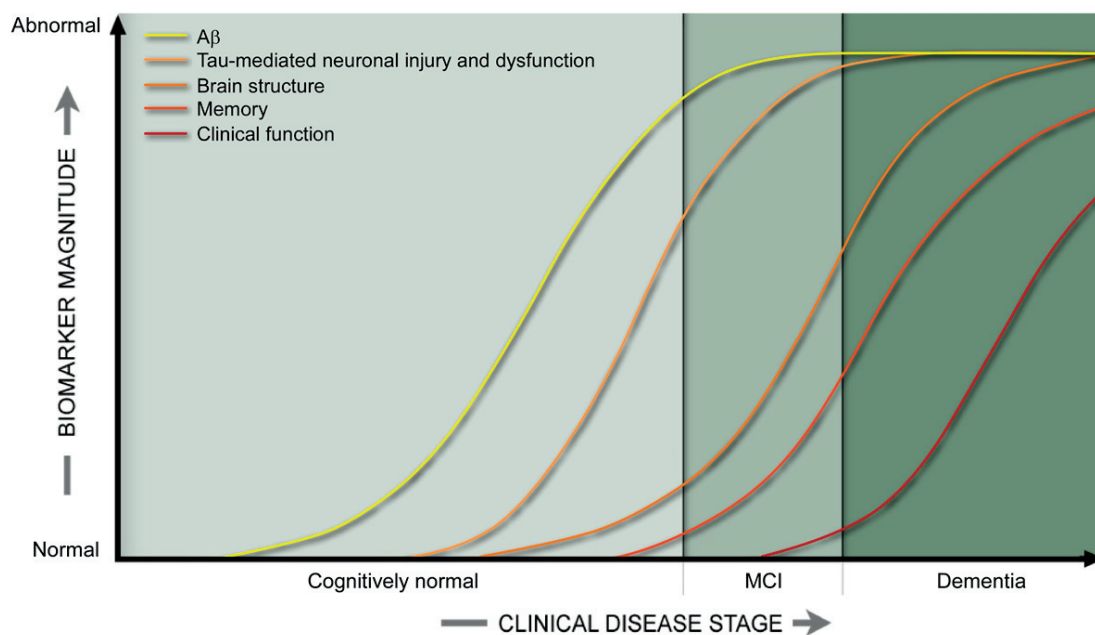


Figure 3: Biomarker dynamics in the pathological cascade of AD. Changes in CSF A β levels and appearance of senile plaques precede Tau-mediated neuronal injury and dysfunction, leading to neuronal death and synaptic impairment. These pathological events trigger brain structure alterations such as white matter changes and volume loss, leading to mild cognitive impairment (MCI). AD progression then affects clinical functions like behavior and social interactions characterized by a dementia stage. Adapted from <http://adni.loni.usc.edu/study-design/background-rationale/>

To initiate potent anti-AD drug research and discovery, the diagnosis has to be performed as early as possible to minimize brain damage and increase chances of complete cognitive function recovery. However, first symptoms characterized by mild cognitive impairment (MCI)²⁶ appear only after the brain reaches high senile plaque load, as well as important neuronal and structural damages. In accordance with the most recent findings, a cascade of neuropathological events occurs in the brain and lead to AD (Fig. 3, reviewed in ^{12,27}): up to 25 years before symptom onset, cerebrospinal fluid

(CSF) biochemical measurements show a decrease in the most pathogenic A β species, A β 42 (see more details in section I.4: APP trafficking and A β generation), linked to its aggregation into senile plaque. The latter can be detected up to 15 years before symptoms appear, by positron-emission topography (PET) of radioactive senile plaque-binding molecules, including the highly used Pittsburgh compound B^{28–30} and more recently synthesized organofluorine compounds³¹.

In parallel, increased Tau is observed in the CSF, highlighted by impaired glucose metabolism measured by F₁₈-fluorodeoxyglucose PET³², and precedes the generation of NFT and NFT-related impairment including neurotoxicity and synaptic dysfunction. These alterations further lead to impaired neuronal network activity^{33,34}, white matter alteration³⁵ and brain shrinkage³⁶ revealed by magnetic resonance imaging. As a consequence, MCI starts and evolves into dementia while progression of the neurotoxic hallmarks and brain volume loss are observed (Fig. 3). Due to treatment unavailability, current AD diagnosis is performed by MCI detection with neuropsychological tests. Because high number of factors may induce MCI including other neurodegenerative diseases, AD diagnostic is confirmed by senile plaques PET scan imaging^{26,37}. The other techniques listed in this section are used for scientific research and clinical trials.

Biomarker analysis (Fig. 3) shows that A β 42 variations in the CSF precedes the AD pathological cascade, and suggest that this short peptide may initiate the pathogenesis of AD.

I.3) The amyloid cascade hypothesis and AD genetics

Since the first diagnosis of AD more than hundred years ago³⁸, tremendous amount of effort has been provided to identify the molecular cause of the disease. While AD onset appears commonly after the age of 65 years old³⁹, several patients exhibited similar symptoms but at a much lower age. Genetic analysis of this group of individuals led to the identification of missense mutations on 3 genes: PSEN1, PSEN2 and APP (reviewed in ⁴⁰). PSEN1 and PSEN2 encode for presenilins (PS), the catalytic subunit of the γ -secretase complex, while APP encodes for the amyloid precursor protein (APP), the cleavage of which produces A β peptides of various length (38 to 43 amino-acid long)⁴¹. Important investigations showed that these mutations either increase the amount of total A β produced, or specifically induce the production of the longest and most pathogenic A β 42 ⁴².

Based on these observations, the amyloid cascade hypothesis (Fig. 4) stipulates that increased A β 42 levels, either caused by mutations in PSEN or APP (early onset familial AD, FAD) or linked to

abnormal A β degradation and risk factors such as the ApoE4 allele (late onset sporadic AD), induces A β oligomerization and initiates the molecular cascade leading to AD pathogenesis⁴³. A β oligomers generate senile plaques, synaptic dysfunctions, induce neuroinflammation and consequently microglia activation^{44,45}. Impaired synaptic activity breaks neuronal ionic homeostasis and deregulates a myriad of physiological processes - including kinases and phosphatases - leading to pathological phosphorylation of Tau, causing the formation of toxic NFT. The latter alters actin cytoskeleton and triggers neuronal death, thus causing dementia (Fig. 4)^{46,47}.

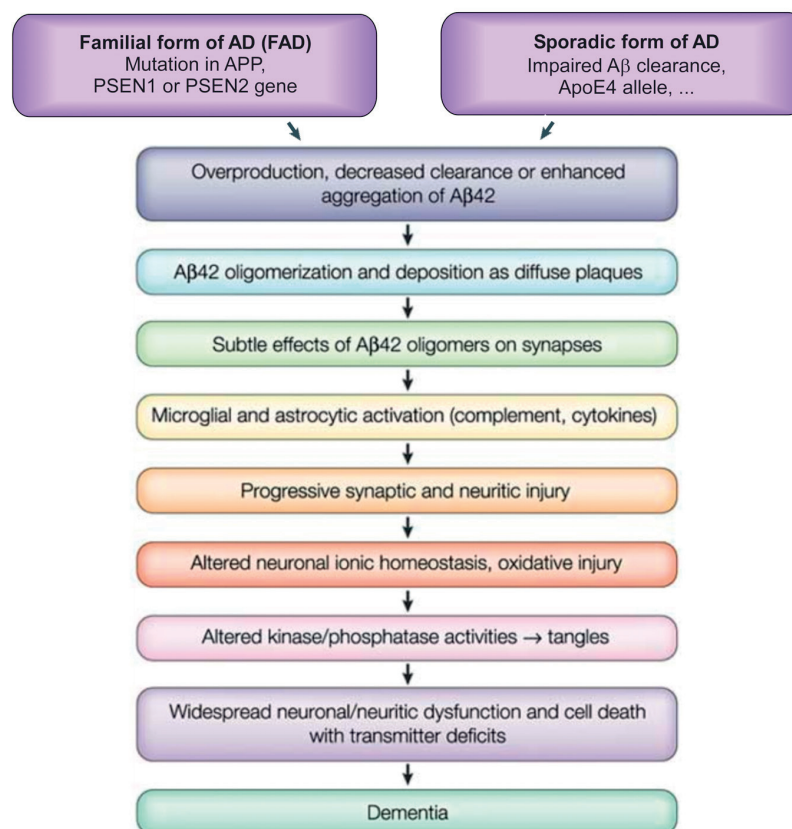


Figure 4: The amyloid cascade hypothesis of AD. The amyloid cascade hypothesis stipulates that increased A β 42 levels, either provoked by genetic mutations in PSEN or APP (familial form of AD) or by a lack of clearance and risk factors including ApoE4 allele, initiate the pathogenesis of AD. Inflammation, altered synaptic function, NFT formation and finally dementia are consequences of A β 42 toxicity. Adapted from ⁴⁸.

This hypothesis is supported by the appearance of the A β phenotype prior to NFT genesis in the brain of AD patients^{12,27}. Indeed, almost all FAD mutations increase brain levels of A β 42, with the exception of APP Dutch mutation (E693Q), which increases A β aggregation without affecting the

processing of APP^{40,49,50}. In addition, triplication of the APP gene-carrier chromosome 21 in Down syndrome increases total A β production, and leads to early AD pathogenesis starting at 12 years old^{51,52}. In contrast, recent investigation highlighted the discovery of a new mutation in APP (A673T) that inhibits its processing by β -secretase and protects against age/AD-related cognitive decline⁵³. These clinical observations provide strong evidence that increased A β 42 levels or aggregation are necessary and sufficient to induce the disease.

I.4) APP trafficking and A β generation

The APP gene is widely expressed and transcribed into 4 major isoforms named according to their length: APP770, APP751, APP714 and APP695, encodes for a type-I transmembrane protein^{54,55}. APP695 is the major central nervous system-specific isoform and consequently the most relevant for AD research^{56,57}. The processing of APP is characterized by two competitive pathways: the non-amyloidogenic and the amyloidogenic pathways, with the latter being toxic and leading to A β production, senile plaque formation and AD (Fig. 5, reviewed in ⁵⁸). In the non-amyloidogenic pathway APP is first processed by α -secretase, releasing its extracellular domain (sAPP α)^{59,60}. Next, the residual membrane embedded C-terminal 83 amino-acid long fragment (C83) is cleaved by γ -secretase, thus liberating the APP intracellular domain (AICD) and the extracellular p3 peptides. In the amyloidogenic pathway, APP is cleaved by β -secretase and generates a 99 amino-acid long (C99) membrane embedded fragment. Its processing by γ -secretase leads to the release of cytosolic AICD and A β in the extracellular space (Fig. 5)⁶¹. Recently, a work of Willem M. and colleagues highlighted the cleavage of APP by η -secretase, leading to the generation of a 192 amino-acid long membrane-embedded C-terminal fragment (CTF). Subsequent processing of this η -CTF by α and β -secretases release soluble toxic A β -like fragments named A η - α and A η - β , as well as C83 and C99, respectively⁶². Importantly, APP and its membrane-embedded fragments can be degraded in a secretase-independent mechanism implicating the lysosomal/autophagy pathway⁶³.

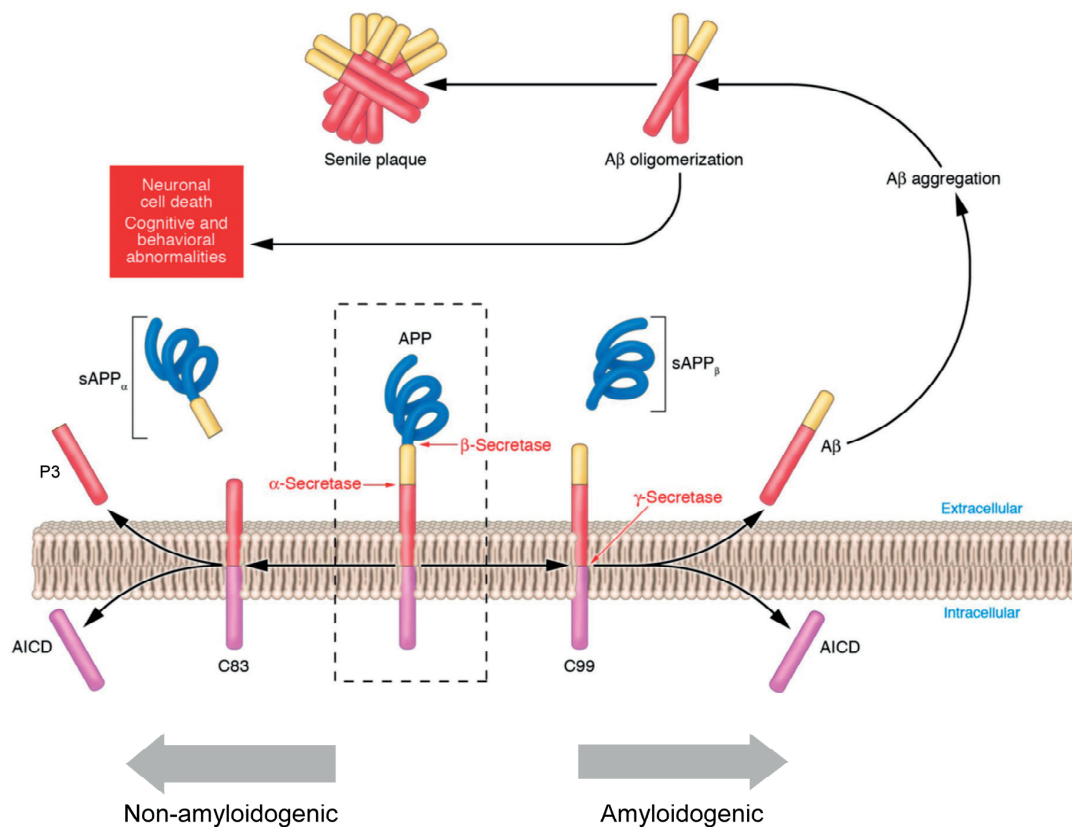


Figure 5: APP processing and A β generation. The transmembrane protein amyloid precursor protein (APP) can be processed in two main pathways. In the non-toxic pathway, APP is first cleaved by α -secretase and releases sAPP α in the extracellular space, generating an 83 amino-acid long C-terminal fragment (C83). Processing of C83 by γ -secretase releases the APP intracellular domain (AICD) into the cytosol and the p3 peptide in the extracellular space. In the toxic or amyloidogenic pathway, APP is first processed by the β -secretase and releases sAPP β in the extracellular space. The residual C-terminal fragment (C99) is finally cleaved by γ -secretase, thus secreting amyloid- β peptides (A β) in the extracellular space and intracellular AICD. A β aggregation into senile plaques is believed to lead to the onset of Alzheimer's disease. Adapted from ⁵⁸.

The release of A β apparently occurs during all stages of human life, suggesting that A β is not toxic if it does not aggregate into oligomers or senile plaques, which are observed in the brain of AD patients⁶⁴⁻⁶⁷. Indeed, C99 can be cleaved in a stepwise process by γ -secretase, liberating 34, 37, 38, 40, 42 or 43 amino-acid long A β peptides, with A β 42 and A β 43 being the most hydrophobic as well as the main aggregating and pathogenic peptides⁶⁸⁻⁷⁰. In addition to these observations, the brain A β 42:A β 40 ratio is equal to 0.1-0.2 in healthy humans and increases up to 2 in AD patients, causing A β plaque formation that initiates the disease^{42,71}.

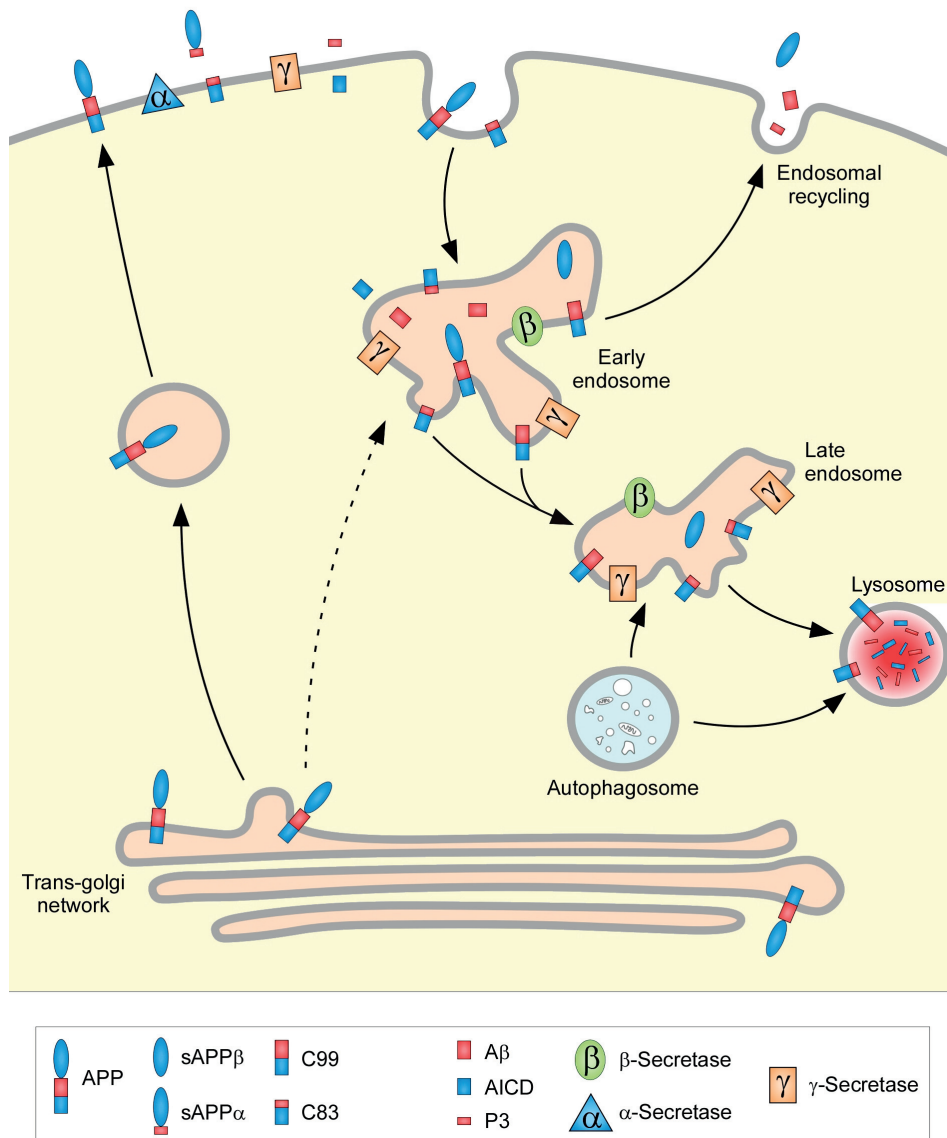


Figure 6: APP trafficking and processing. APP-containing vesicles are transported from the trans-golgi network to the plasma membrane where APP gets cleaved by α -secretase. This step leads to the release of sAPP α in the extracellular space, and the generation of an 83 amino-acid long C-terminal fragment (C83). C83 can either be processed by γ -secretase at the plasma membrane, or be endocytosed with uncleaved APP. Then, APP is processed by β -secretase in the endosome and generate a 99 amino-acid long membrane embedded fragment (C99) and a soluble sAPP β counterpart. Both C83 and C99 are cleaved by γ -secretase and secrete P3 and A β in the lumen, respectively, while cytosolic AICD translocates to the nucleus. Finally, APP fragments are either transported back to the membrane (endosomal recycling) or traffic via late endosome to undergo lysosomal degradation. Also, APP may be directly transported from the golgi directly to the endosome (dashed arrow). Adapted from⁷².

The processing of APP by secretases occurs in distinct cellular organelles (depicted in Fig.6, reviewed in ^{73,74}), thus its trafficking modulates its cleavage and degradation. When traveling through the secretory pathway, the addition of various post-translational modifications (PTM) affects its trafficking and processing. After protein translation in the cytosol, APP is translocated to the endoplasmic reticulum where the phosphorylation of its cytoplasmic domain regulates the later processing of C99/C83 and the translocation of AICD to the nucleus⁷⁵. Its arrival to the golgi apparatus allows immature unglycosylated APP evolution into mature N- and O-glycosylated APP (mAPP), and ensure its proper trafficking and secretion^{76,77}. Additionally, palmitoylation has also been reported on a limited proportion of APP at position Cys¹⁸⁶ and Cys¹⁸⁷: either palmitoylation or disulfide bonds between both cysteins is required for APP to exit the golgi apparatus⁷⁸.

After exiting the trans-golgi network, mAPP is transferred to the plasma membrane of axons and dendrites by vesicular transport. In the vesicles and at the plasma membrane, mAPP is processed by α -secretase, then possibly by γ -secretase (Fig. 6). Then, clathrin-dependent endocytosis brings both α -secretase cleavage product, C83 and intact mAPP to the endosomes, which light acidic pH confers optimal activity to β - and γ -secretase^{79,80}. Cleavage of intact mAPP by β -secretase generates C99 and sAPP β . Then, processing of C83 and C99 by γ -secretase releases p3 and A β in the lumen, respectively, while cytosolic AICD translocates to the nucleus and regulates gene expression⁸¹. Both p3, sAPP β and A β are released in the extracellular space by exocytosis or exosomal transportation. Importantly, C83/C99 and to a lower extent APP can be degraded by the secretase-independent lysosomal/autophagic pathway. Indeed, acidification of late endosomes and fusion with lysosomes leads to APP degradation, likely by cathepsins⁸² (Fig. 6).

I.5) APP cellular function

The evident implication of APP and PSEN genes in AD development led to important findings, to decipher their physiological functions. APP is an evolutionary well conserved protein, showing high sequence homology with the non-amyloidogenic amyloid precursor-like protein 1 and 2 genes (APLP1 and APLP2)⁸³. Genetic depletion of these proteins in mice allowed better understanding of the function of these genes, and revealed important developmental roles for APP (reviewed in ^{84,85}). Constitutive APP deletion (APP-KO) yields in viable and fertile mice displaying several abnormalities, including weight loss as well as a decrease in brain volume and memory ⁸⁶⁻⁸⁸. These phenotypes were explained by the implication of APP in synaptic transmission^{88,89}. Furthermore, increased cholesterol levels in these mice suggest a metabolic role for APP⁹⁰. APLP1-KO mice only

exhibited somatic growth deficit, while no abnormalities have been detected in APLP2-KO mice. In sharp contrast with single knockout models, double KOs exhibited more pronounced phenotypes. Deficiency in APP / APLP2 and APLP1 / APLP2 were lethal whereas APP / APLP1-KO mice displayed no abnormality^{91,92}. Consistent with previous observations, genetic deletion of the 3 APP family members was lethal⁹³. In addition, various studies demonstrated the binding of APP extracellular domain to matrix components, as well as its dimerization, and proposed a cell adhesion function for APP^{94–98}.

The physiological functions of the highly regulated proteolytic processing of APP remains poorly understood, hence it appears that α -secretase-mediated cleavage displays neurotrophic properties, whereas β -secretase processing alters synaptic activity. Indeed, the overexpression in APP-KO mice of sAPP α , but not sAPP β , was shown to rescue the phenotype⁹⁹. Complementarily, several studies highlighted the important role of sAPP α in synaptic plasticity and memory^{100,101}. This observation is of relevance for AD, as reduced levels of sAPP α and α -secretase have been measured in the CSF of AD cases^{102–104}. Striking functional differences between sAPP α and sAPP β were explained by a decrease of Cdk5-mediated Tau phosphorylation by the first¹⁰⁵, while the second may bind the death receptor DR6 and initiate cellular degeneration¹⁰⁶.

The next step in APP processing involves γ -secretase and produces equal amounts of intracellular AICD, and luminal p3 or A β . In contrast to the neuroprotective effects of sAPP α , p3 toxicity – although lower than A β ¹⁰⁷ – has been shown both *in vitro* and *in vivo*^{108–110}. Also, same AICD are generated from the processing of both C99 and C83 by γ -secretase¹¹¹. Translocation of AICD to the nucleus is Fe65-dependent and regulates transcription of AD-related genes involved in A β levels^{112,113}, Tau phosphorylation^{114,115}, as well as a high diversity of cellular pathways including phagocytosis and lipid dynamics¹¹⁶, calcium homeostasis¹¹⁷, cytoskeletal dynamics⁸¹, and tumor regulation¹¹⁸. Additionally, the processing of AICD by caspases leads to the generation of a toxic 31 amino-acid long CTF, supposed to play a minor role in AD pathology^{119–121}. In conclusion, if the implication of A β in the pathogenesis of AD is now well accepted, the physiological and pathological importance played by each APP fragment remains unclear.

I.6) Assembly and structure of the γ -secretase complex

γ -Secretase is an intramembrane cleaving aspartyl protease complex composed of 4 subunits: Aph1, Nicastrin (NCT), PS, and Presenilin enhancer 2 (Pen2), mainly located in the trans-golgi network, on the plasma membrane, in the endosomes and in the lysosome¹²²⁻¹²⁴. It cleaves type-I membrane proteins in their transmembrane domain, thus releasing intra- and extracellular cleavage products¹²⁵. This enzyme is implicated in a high number of physiological processes, as it cleaves many substrates (listed in ¹²⁵), including APP, the cell differentiation protein Notch¹²⁶, the synaptic plasticity-related Neurexin¹²⁷ and Ephrin¹²⁸ as well as the cell adhesion protein N-cadherin¹²⁹. The implication of the γ -secretase complex in a myriad of physiological functions explains the strong adverse effects linked to its *in vivo* enzymatic inhibition¹³⁰⁻¹³³.

The assembly of γ - secretase implicates the association of Aph1 and immature NCT (iNCT) in the endoplasmic reticulum, then supplemented by PS holoprotein (Fig. 7). Binding of Pen2 to the Aph1/iNCT/PS-FL trimeric subcomplex elicits (i) PS endoproteolysis into PS N- and C-terminal fragments (PS-NTF & PS-CTF, respectively), (ii) iNCT maturation into mature NCT (mNCT) induced by changes in glycosylation pattern, and (iii) activation of the γ -secretase complex (Fig. 7, reviewed in ¹³⁴). Whereas PS contains the γ -secretase catalytic site, Aph1 and Pen2 are thought to play a structural role in the transmembrane complex¹³⁴⁻¹³⁶, and NCT might be implicated in substrate recognition¹³⁷. In a mechanism independent of the γ -secretase complex, PS holoprotein was shown by Coen K. and colleagues to modulates lysosomal function by regulating the endosomal/lysosomal calcium influx¹³⁸. Finally, atomic structure of the γ -secretase complex was recently elucidated and gives great hope to the design of new modulators¹³⁹.

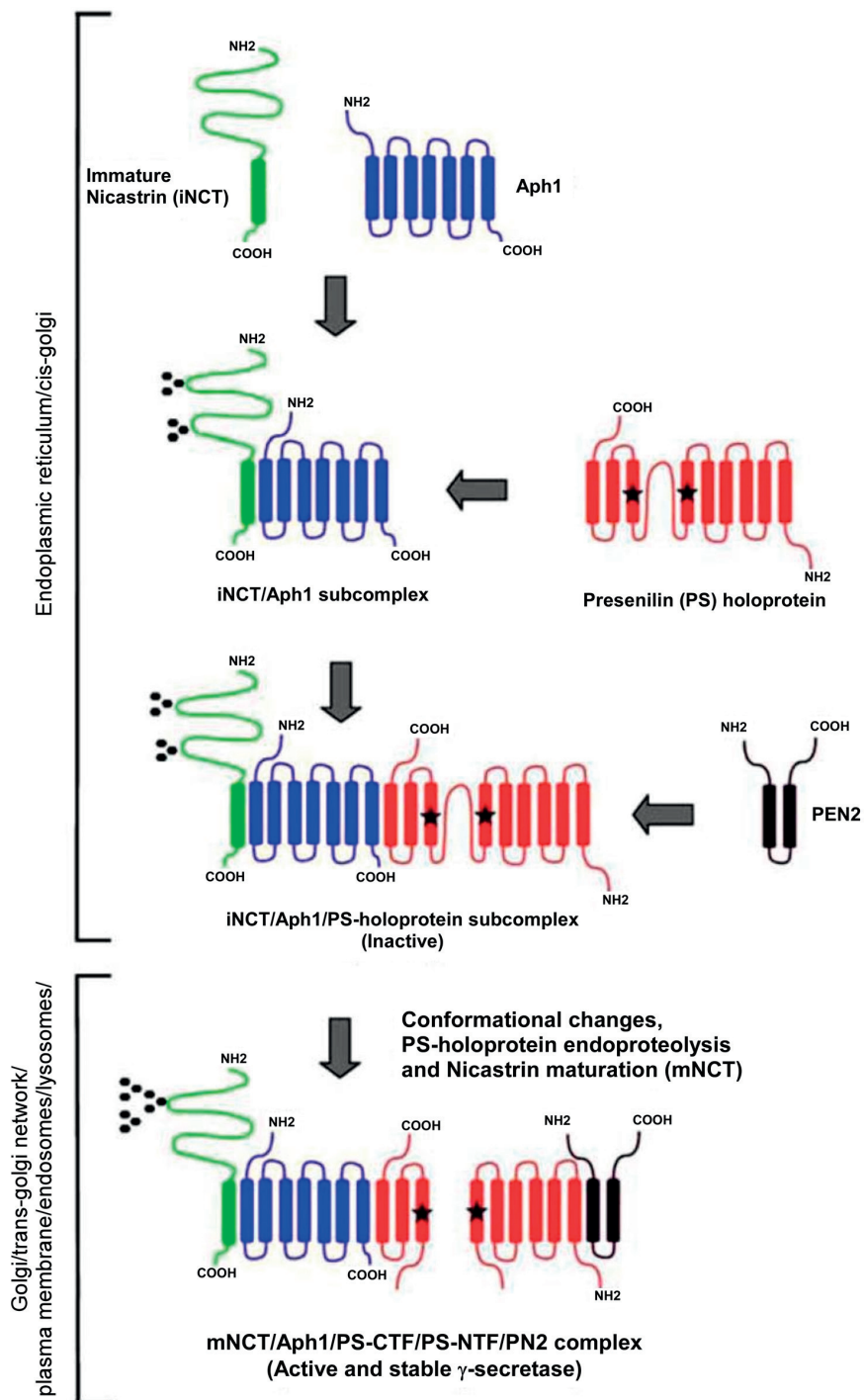


Figure 7: Assembly of the γ -secretase complex. Assembly of γ -secretase starts in the endoplasmic reticulum (ER) / cis-golgi by the formation of a dimeric complex made of partially glycosylated immature NCT (iNCT, green) and Aph1 (blue). Presenilin holoprotein (PS, red) binding generates a trimeric complex, finally supplemented by PEN-2 (black). Addition of the last subunit induces NCT maturation (mNCT) characterized by change in its glycosylation pattern, PS endoproteolysis into N- and C-terminal fragments (PS-NTF and PS-CTF, respectively) leading to the activation of the γ -secretase complex. Black dots on NCT subunit represent complex glycans. Modified from ¹³⁴.

I.7) Therapeutic strategies in AD

Existing AD symptomatic treatments are limited to short term cognitive improvement, hence tremendous efforts have been produced to identify approaches capable to slow down or stop the disease's progression. Depending on their targets, therapeutic strategies can be separated in three main groups (described in Fig. 8, reviewed in ¹⁴⁰): alteration of A β levels and aggregation (in blue), inhibition of its toxic downstream signaling (green), and rescue of disrupted cell homeostasis (purple).

Dysregulation of APP processing and A β aggregation are believed to initiate the first step of AD pathogenesis, thus secretases appeared as a first target to block neurodegeneration. The most direct approach consists of the inhibition of the amyloidogenic β - and γ -secretases. Full depletion of the β -secretase BACE1 in mice abolished A β production while having no major deficits, in contrast to lethal PS removal ^{141,142}. Thus inhibition of β -secretase was supposed safer than γ -secretase. Indeed, phase I clinical trial showed CSF A β reduction following BACE1 inhibitor administration¹⁴³. However poor efficiency linked to weak blood brain barrier penetration and low drug specificity raised additional challenges in the development of such compounds¹⁴⁴.

γ -Secretase is directly implicated in the generation of A β peptides. Thus, inhibiting its enzymatic activity to abolish A β production emerged as a promising opportunity to treat AD, but clinical trials were halted due to strong adverse effects mainly attributed to impaired Notch cleavage^{130–133}. The development of Notch sparing compounds which specifically alters A β production and A β 42:A β 40 ratio is believed to be safer options to treat AD, and are currently tested in clinical trials^{145,146}. Alternatively, activation of the major α -secretase ADAM10¹⁴⁷ competes with A β production and increases production of neuroprotective sAPP α . This protease can be stimulated by upstream M1 muscarinic receptor activation and lower A β ^{148,149}. The development of M1 chemical activators was hampered by the difficulty of generating specific compounds and render this approach risky, especially because α -secretase activation effects remain unknown. To bypass pharmacokinetic challenges faced by the pharmacological inhibition of secretases, other mechanisms were targeted with the aim of lowering A β peptides or senile plaques, including immunotherapies^{150,151}, anti-aggregation compounds^{152,153}, and stimulation of A β degradation/clearance^{154–156} as well as autophagy-mediated APP degradation¹⁵⁷ (fig. 8).

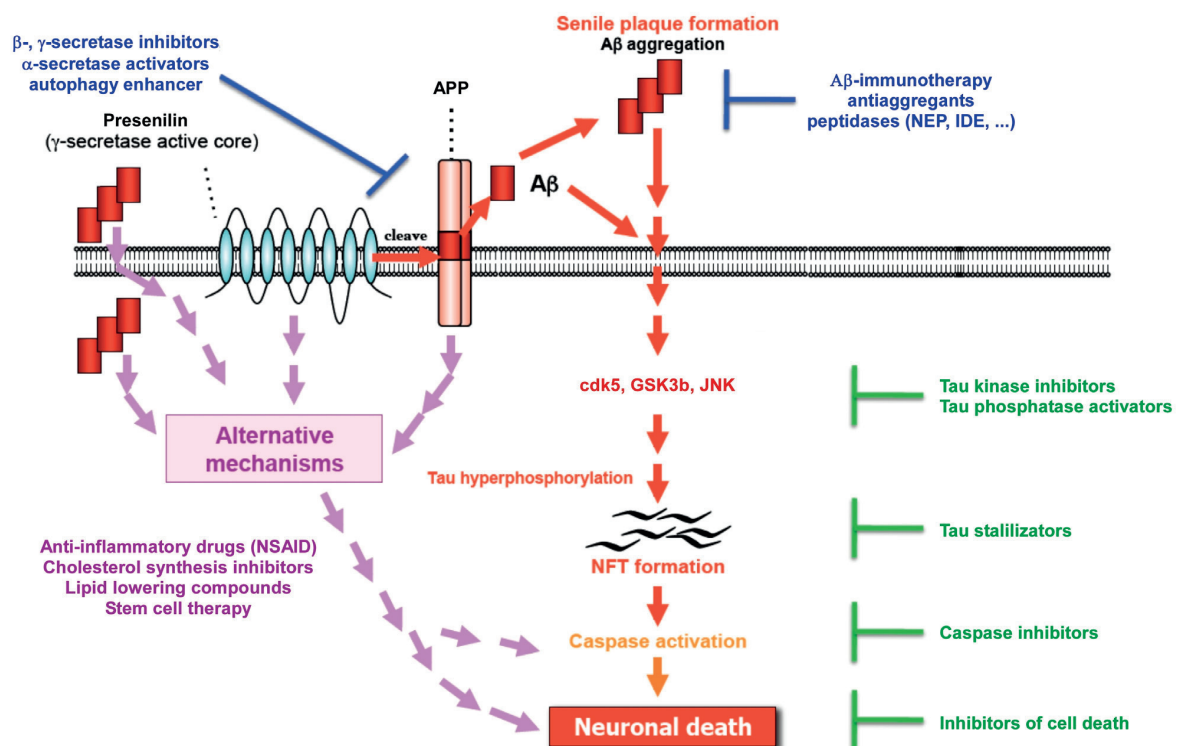


Figure 8: AD therapeutic strategies. Current AD therapeutic strategies can be divided into 3 major groups depending on their targets: alteration of A β levels and aggregation (blue), inhibition of A β – mediated NFT formation and neuronal death (green), and rescue of disrupted cell homeostasis (purple). Modified from ¹⁵⁸.

The second step in AD pathogenesis corresponds to the A β -mediated activation of signaling pathways (reviewed in ¹⁵⁹) affecting the activity of Tau kinases (cdk5, JNK and GSK3 β) and phosphatases (protein phosphatase PP2A, calcineurin) (Fig. 8). This enzymatic dysregulation leads to Tau hyperphosphorylation, NFT formation, and caspase-mediated cell death (Fig. 4). Despite the fact that every single step of this toxic cascade has been pharmacologically targeted, including Tau phosphorylation/aggregation^{160–162} as well as caspase^{163,164} and cell death inhibitors^{165–167}, no significant improvement in the cognitive functions of treated AD patient has been observed so far¹⁵⁹.

A β -induced neuroinflammation and metabolic dysregulation are observed in AD brains, and strongly participate to cognitive impairment and neuronal death (Fig. 8). Their therapeutic potential was confirmed by the identification in genome-wide association studies of inflammatory (eg. Chemokine ligand, interleukin receptor, the triggering receptor expressed on myeloid cells TREM2) as well as metabolic messengers (eg. cholesterol/triglycerides levels, apolipoprotein E) as risk factor

for AD¹⁶⁸⁻¹⁷². Failure of well-known non-steroidal anti-inflammatory drugs to improve cognition in AD patient suggested a preventive use of these compounds rather than a treatment, or can be explained by a lack of efficacy to prevent microglial activation^{173,174}. Interfering with the metabolism appeared less challenging, cholesterol and lipid lowering compound developed for diabetes were “recycled” for AD clinical trials. These trials included cholesterol synthesis inhibitors such as statins or the insulin sensitivity modulator rosiglitazone, but did not show significant benefits in AD patients^{174,175}. A final approach attempted to restore brain integrity by replacing dead neurons by newborn cells, either by promoting endogenous stem cell division, or by transplantation¹⁷⁶. This approach has only been tested on mice models, but its potential may be considered for AD treatment¹⁷⁶.

Although the high amount of therapeutic strategies and drugs tested against AD, no treatment has been proving its efficacy. It should be considered that all these treatments were done on MCI and demented AD patients, where maximum plaque load and strong neurodegeneration are present. Recent refining of selection criteria for clinical tests (early preclinical AD patients, ApoE4 allele, depicted in ¹⁷⁷) supplemented by drug optimization offers great opportunities for next the generation clinical trials.

I.8) Aim of the thesis work

In the first part of this thesis work (Chapter II), we aimed at modulating the enzymatic activity of γ -secretase, and investigate the physiological functions of this enzyme. Endogenous modulation of γ -secretase affects the genesis of A β and is considered as potent therapeutic strategy. For this reason we searched for γ -secretase interacting proteins, and identified 3 new endogenous modulators of A β production. In parallel, we focused on the post translational modifications of γ -secretase, and assessed the effect of PS phosphorylation on the maturation and enzymatic activity of the γ -secretase complex. Modulating γ -secretase may influence the downstream signaling of its numerous substrates. Notably, γ -secretase is implicated in synaptic plasticity, which require the recruitment of the actin cytoskeleton. Hence we investigated the influence of γ -secretase on the regulation of the actin-depolymerizing protein Cofilin.

In the second part of this thesis work (Chapter III), we aimed at monitoring brain structure alterations and repair damage caused by neuronal death in neurodegenerative diseases. We implanted microelectrodes in mice brain and visualized brain nuclei by measuring the electrical

impedance of the tissue. Next, we used this method to detect A β plaques in the brain of a mouse model of AD. In another project, we further developed a neurotrophic extracellular matrix-like polymer to promote neuronal repair in the brains of patients affected by neurodegenerative disorders.

Chapter II

Modulation and physiological functions of γ -secretase

II.1) Introduction

II.1.a) Endogenous modulators of A β production

γ -Secretase processing of C99 is the last step before the release of A β peptides, believed to initiate the pathological cascade of AD. Also, γ -secretase controls the pathophysiological-relevant A β 42:A β 40 ratio, the increase of which is believed to play a central role in the disease^{42,71}. *In vivo* inhibition of γ -secretase induces strong adverse effects mainly attributed to impaired Notch cleavage^{130–133}. Thus clinical research focused on Notch-sparing chemical molecules able to specifically affect APP processing (Notch sparing compounds), and decrease A β 42:A β 40 ratio^{145,146}. In addition to these investigations which focus on chemical compounds, the identification of endogenous γ -secretase interacting protein affecting the generation of A β would also raise great therapeutic potential. Yet, only TMP21¹⁷⁸ and the highly controversial γ -secretase activating protein GSAP^{179,180} have been suggested to be physically associated with the γ -secretase complex and modulate its enzymatic activity.

Other groups focused on APP interacting proteins that affect its trafficking and consequently its cleavage by the secretases. A growing list of proteins fulfill these functions, among them the sorting protein-related receptor sorLA¹⁸¹, X11¹⁸², and the AICD-binding protein Fe65^{183 184}. Autophagy is also known to be altered in AD brain⁶³. Thus, more recent findings focused on regulators of APP degradation and led to the identification of the autophagy regulator Beclin1¹⁸⁵ and the autophagy cargo receptor AP2¹⁸⁶. So far, none of these APP/ γ -secretase interacting proteins have been validated as a therapeutic targets in clinical research.

In the first manuscript described in this PhD thesis (see manuscript page 31), we aimed at identifying new γ -secretase interacting proteins able to specifically modulate the production of A β peptides. In contrast to γ -secretase inhibitors, endogenous γ -secretase modulating proteins do not interfere with the processing of other substrates. Also, we studied the influence of the newly identified γ -secretase modulators on the lysosomal/autophagic pathway.

II.1.b) Effects of post-translational modifications on the enzymatic activity of γ -secretase

Interfering with the activity of an enzyme by controlling the addition of post translational modifications has been widely reviewed^{187,188}, and thus appear to be an elegant possibility for modulating γ -secretase activity. So far, several PTMs including phosphorylation, glycosylation and

palmitoylation have been identified on the γ -secretase subunits NCT, PS and Aph1. NCT complex N-glycosylation is required for the proper subcellular trafficking of active γ -secretase *in vitro*¹⁸⁹, and consequently modulates A β production. In addition, recent purification of active enzyme lacking complex sugar motifs has been achieved recently¹⁹⁰. In accordance with these observations, glycosylation of NCT was proposed to play a role in its trafficking to the plasma membrane, without affecting its enzymatic activity¹⁹¹. In contrast, serine 437 phosphorylation of this subunit by the Akt1 kinase or glucocorticoid-induced protein kinase 1 accelerate its degradation by the lysosomal and proteasomal pathways^{192,193}.

Instead of modulating γ -secretase activity, palmitoylation of Aph1 and NCT appeared to play a role in the subcellular localization and stability of the enzymatic complex¹⁹⁴. PS phosphorylation has been highlighted by several studies demonstrating its involvement in various cellular functions including insulin signaling and cell survival¹⁹⁵⁻¹⁹⁷. Interestingly, PS is phosphorylated by two kinases implicated in Tau phosphorylation in AD, GSK3 β ¹⁹⁸ and (cdk5)¹⁹⁹, and point out a feedback loop for the regulation of γ -secretase activity.

Because the effect of PS phosphorylation on the γ -secretase processing machinery has not been fully characterized, we studied the influence of this PTM on the maturation of the γ -secretase complex and on its enzymatic activity (see manuscript page 60).

II.1.c) The role of γ -secretase in the cytoskeleton dynamics

It is now well assumed that in AD brains, γ -secretase - via A β toxic effects - leads to NFT formation and breaks actin microtubule dynamics⁴³. An emerging idea suggested that the γ -secretase complex may influence the cytoskeleton dynamics under physiological conditions. Indeed, impaired synaptic plasticity has been reported in mice overexpressing PS loss of function FAD mutation, together with variations in actin-binding protein levels²⁰⁰. It was hypothesized that synaptic activity-mediated γ -secretase activation²⁰¹ involves the remodeling of the actin cytoskeleton²⁰⁰, required for synaptic plasticity^{202,203}. Previous studies showed that AICD affected the expression of genes related to cytoskeleton dynamics⁸¹, but the important players of γ -secretase-mediated actin remodeling have yet to be identified.

Among numerous actin binding proteins, the actin depolymerizing factor (ADF)/Cofilin protein family comprises ADF (also known as Destin), the non-muscle type Cofilin1 and the muscle-type Cofilin2. This protein family participates in the depolymerization of actin filaments, and

consequently controls the actin cytoskeleton dynamics^{204,205}. ADF/Cofilin signaling has also been shown to be impaired in AD and may be involved in the disruption of the actin cytoskeleton^{206,207}. The mechanisms linking AD and impaired ADF/Cofilin pathways are not yet clearly understood. This latter observation motivated us to study the implication of γ -secretase in the regulation of the Cofilin1 pathway (see manuscript page 86).

II.2) Results

II.2.a) The Adipocyte Differentiation Protein APMAP is an Endogenous Suppressor of A β Production in the Brain

In this first manuscript (see manuscript page 31), we aimed at identifying new γ -secretase interacting proteins able to modulate the production of A β , without altering the levels and processing of other γ -secretase substrates. We characterized by LC-MS/MS mass spectrometry the proteome of highly purified γ -secretase, and identified the adipogenesis-related protein APMAP (adipocyte plasma membrane associated protein, APMAP), Reticulon4 and Tetraspanin6 as new γ -secretase interacting proteins. We further demonstrated that APMAP is an endogenous suppressor of A β both *in vitro* and *in vivo*, by interacting physically with the γ -secretase complex and its substrate APP. Importantly, APMAP did not affect the cleavage of other γ -secretase substrates. Interestingly, partial depletion of APMAP in cells increased the levels and affected the length of APP-CTFs. Lysosomal inhibition experiments suggested a role for APMAP in the transport/degradation of APP-CTFs through the lysosomal/autophagic pathway.

In this study, I first screened and validated the γ -secretase associated proteins that affect APP processing, by siRNA and overexpression experiments. Then, I performed cell culture and biochemical analyses, APP-CTFs mass spectrometry analysis, cell-free γ -secretase activity assays, mouse primary cortical neurons and immunofluorescence analyses, subcloning and shRNA/siRNA design, as well as *in vivo* stereotaxic injections. I also participated in the experimental design.

II.2.b) Identification of New Presenilin-1 Phosphosites: Implication for γ -Secretase Activity and A β Production

In this study (see manuscript page 60) we questioned the importance of PS phosphorylation for the assembly, maturation and activity of the γ -secretase complex. We performed LC-MS/MS mass

spectrometry analysis on the purified active γ -secretase complex, and identified 15 PS1 phosphorylated peptides corresponding to 12 single and 3 double PS1 phosphosites. Among them, 4 phosphosites have already been investigated by other research groups. Interestingly, no phosphorylation has been detected on the other γ -secretase subunits NCT, Aph1 or PEN2. We focused our study on the 11 newly identified phosphosites including 8 single and 3 double PS1 phosphorylation. Our cell-free γ -secretase activity assays performed with the PS1 phospho-mutants revealed no changes in the maturation or enzymatic activity of γ -secretase.

In this manuscript, I performed cell free γ -secretase activity assay in SH-SY5Y cells, and performed experiments in HEK-N7 cells (supplementary figure 7 and 8, see pages 84 and 85).

II.2.c) Inactivation of Brain Cofilin-1 by Age, Alzheimer's Disease and γ -Secretase

In this study we aimed at understanding the implication of γ -secretase in the regulation of the Cofilin1 pathway (see manuscript page 86) which participates in the depolymerisation of actin filaments. We found an increased phosphorylation/inactivation of Cofilin1 in human AD brains, as well as in the brain of the AD mouse model APPPS1²⁰⁸. Similar observations were made in aged WT mice and in aged mouse primary cortical neurons. In contrast, decreased phosphorylation/inactivation of Cofilin1 was detected following the inhibition of γ -secretase enzymatic activity. Moreover, we showed that these changes in phosphorylation/inactivation state of Cofilin1 were mainly induced by variations in the phosphatase activity of slingshot1 (SSH1). Finally, age-related morphological changes as well as γ -secretase enzymatic activity inhibit SSH1, thus increasing the phosphorylation/inactivation of Cofilin1, and affecting actin cytoskeleton dynamics.

In this study, I prepared mouse primary cortical neurons and performed western blot analyses of supplementary figure 1 and 10 (see pages 98 and 110).

II.3) Manuscripts

The adipocyte differentiation protein APMAP is an endogenous suppressor of A β production in the brain

Sebastien Mosser, Jean-René Alattia, Mitko Dimitrov, Alexandre Matz, Justine Pascual, Bernard L. Schneider and Patrick C. Fraering*

Brain Mind Institute and School of Life Sciences, Ecole Polytechnique Fédérale de Lausanne (EPFL), Lausanne CH1015, Switzerland

Received July 11, 2014; Revised and Accepted August 26, 2014

The deposition of amyloid-beta (A β) aggregates in the brain is a major pathological hallmark of Alzheimer's disease (AD). A β is generated from the cleavage of C-terminal fragments of the amyloid precursor protein (APP-CTFs) by γ -secretase, an intramembrane-cleaving protease with multiple substrates, including the Notch receptors. Endogenous modulation of γ -secretase is pointed to be implicated in the sporadic, age-dependent form of AD. Moreover, specifically modulating A β production has become a priority for the safe treatment of AD because the inhibition of γ -secretase results in adverse effects that are related to impaired Notch cleavage. Here, we report the identification of the adipocyte differentiation protein APMAP as a novel endogenous suppressor of A β generation. We found that APMAP interacts physically with γ -secretase and its substrate APP. In cells, the partial depletion of APMAP drastically increased the levels of APP-CTFs, as well as uniquely affecting their stability, with the consequence being increased secretion of A β . In wild-type and APP/presenilin 1 transgenic mice, partial adeno-associated virus-mediated APMAP knockdown in the hippocampus increased A β production by ~ 20 and $\sim 55\%$, respectively. Together, our data demonstrate that APMAP is a negative regulator of A β production through its interaction with APP and γ -secretase. All observed APMAP phenotypes can be explained by an impaired degradation of APP-CTFs, likely caused by an altered substrate transport capacity to the lysosomal/autophagic system.

INTRODUCTION

In the neurodegenerative amyloid cascade of Alzheimer's disease (AD), quantitative and qualitative changes in the production of amyloid-beta (A β) peptides and their aggregation into senile plaques precede the formation of neurofibrillary tangles and initiate the pathological process causing the disease (1,2). Neurotoxic A β peptides are generated by successive cleavages of the amyloid precursor protein (APP) by β - and γ -secretases. APP is first processed by the β -secretase BACE1, leading to the formation of a 99-amino-acid long APP C-terminal fragment (APP-C99 or APP-CTF β). The cleavage of APP-CTF β by γ -secretase liberates A β peptides that are 38–43 amino acids in length, with A β 42 being a major component of the senile plaques (3). Yet, APP is mainly cleaved within the A β region

by the α -secretases ADAM10/17 to release APP-CTF α , the processing of which by γ -secretase results in N-terminally truncated and non-toxic A β peptides. γ -Secretase is a ubiquitously expressed membrane protease complex that processes a long list of type I transmembrane proteins, including APP, the Notch-1 receptor and several synaptic cell adhesion molecules (4–6). Active γ -secretase is comprised of five protein components: Nicastrin (NCT), Presenilin N- and C-terminal fragments (PS-NTF and PS-CTF), Aph1 and Pen-2 (7). Because they prevent the production of A β peptides, γ -secretase inhibitors (GSI) have been extensively investigated in the clinic for the treatment of AD. However, recent human GSI trials revealed significant side effects linked to impaired Notch cleavage (8). Therefore, specifically modulating γ -secretase and A β production, without interfering with other physiological processes, is

*To whom correspondence should be addressed. Tel: +41 216939651; Fax: +41 216939572; Email: patrick.fraering@epfl.ch

© The Author 2014. Published by Oxford University Press.

This is an Open Access article distributed under the terms of the Creative Commons Attribution Non-Commercial License (<http://creativecommons.org/licenses/by-nc/4.0/>), which permits non-commercial re-use, distribution, and reproduction in any medium, provided the original work is properly cited. For commercial re-use, please contact journals.permissions@oup.com

an attractive strategy to safely treat AD (9). Because endogenous γ -secretase modulating factors are potential therapeutic targets, but also possibly implicated in the sporadic forms of AD, we aimed to identify new γ -secretase-interacting proteins (GSPs) that are capable of modulating A β production.

RESULTS

Identification of GSPs modulating A β production

Highly purified and active γ -secretase prepared from Chinese hamster ovary (CHO) cells overexpressing the four subunits of the protease complex (10) was resolved by blue-native gel electrophoresis (Fig. 1A), and the band corresponding to the complex was excised for protein content analysis by LC-MS/MS mass spectrometry. This approach led to the identification of seven GSPs encoded by the genes *ATP1 α 1*, *RTN4*, *VAMP2*, *VAMP3*, *TSPAN6*, *APMAP* and *HSPA5* (Fig. 1A; peptides identified by LC-MS/MS are listed in Supplementary Material, Fig. S1). As expected from a γ -secretase overexpression system, the silver-stained SDS-PAGE of the protease preparation used for the native gel (Fig. 1A) confirmed the trace amounts of GSPs relative to the predominant γ -secretase subunits (Supplementary Material, Fig. S2). Because *ATP1 α 1*, *VAMP2/3* and *HSPA5* had previously been reported to interact physically with either γ -secretase or APP (11,12), we focused in our study on *RTN4*, *APMAP* and *TSPAN6*. *RTN4* encodes for the myelin-associated multi-pass membrane protein reticulon-4 (Nogo), a neurite outgrowth inhibitor limiting plasticity in the healthy adult brain and neuronal regeneration during brain injury (reviewed in 13). *APMAP* encodes for a 415-amino-acid long single-pass type-II glycosylated membrane protein that is implicated in the regulation of white adipose tissue differentiation (14,15). *TSPAN6* belongs to the tetraspanin superfamily of multi-pass membrane proteins interacting with multiple immune-related molecules, including immune receptors, integrins, signaling molecules and functioning as important immune response modulators (16). The neurobiological functions of *APMAP* and *TSPAN6* remain unknown.

First, the expression of the *RTN4*, *APMAP* and *TSPAN6* genes was reduced by small-interfering RNA (siRNA) in HeLa cells as well as in HEK cells overexpressing APP harboring the Swedish double mutation near the β -secretase cleavage site (mutation resulting in increased total A β levels; HEK-APPSwe). In HeLa and HEK-APPSwe cells, depletion by \sim 60% of *TSPAN6* lowered APP-CTFs levels by 38 and 40%, respectively (Fig. 1B and C). In contrast, depletion of *RTN4* and *APMAP* (both by \sim 75%) caused a strong accumulation of APP-CTFs, respectively, by 181 and 286% in HeLa cells and by 25 and 52% in HEK-APPSwe cells (Fig. 1B and C and Supplementary Material, Fig. S3). This siRNA knockdown of individual genes did not interfere with the maturation or protein levels of α -, β - or γ -secretases, with the exception of increased ADAM10 associated with reduced *RTN4* (Supplementary Material, Fig. S4). Importantly, A β secreted from HEK-APPSwe cells depleted for the expression of *TSPAN6*, *RTN4* and *APMAP* directly reflected the levels of intracellular APP-CTFs (Fig. 1D). Indeed, siRNAs targeting *TSPAN6* reduced the levels of A β 40 by $25 \pm 7.5\%$, while siRNAs targeting *RTN4*, and *APMAP* raised A β 40 levels by 52 ± 1.8 and

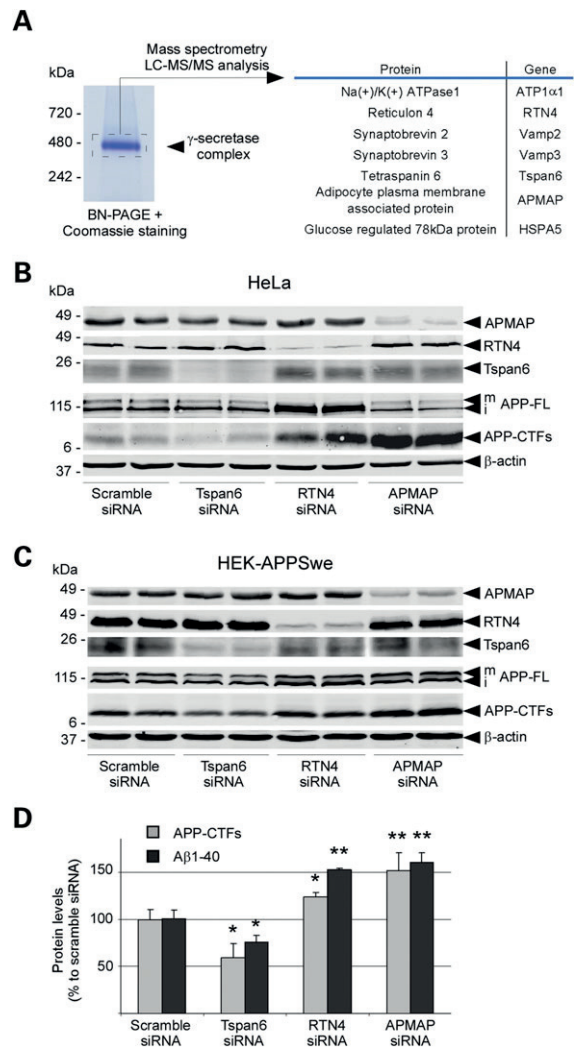


Figure 1. Identification of endogenous modulators of γ -secretase and A β production. (A) Analysis by LC-MS/MS of the protein components of the highly purified γ -secretase complex. (B and C) siRNA knockdown of *TSPAN6*, *RTN4* and *APMAP* affects APP-CTFs in HeLa cells (B) and HEK cells overexpressing APP bearing the Swedish mutation that causes early-onset familial Alzheimer's disease (HEK-APPSwe; C). Biological duplicates are shown for each siRNA condition. (D) Correlation between APP-CTFs levels and A β 40 production in HEK-APPSwe cells with reduced *TSPAN6*, *RTN4* and *APMAP* expression. APP-CTFs levels were estimated by densitometric analysis, while A β 40 levels were quantified by ELISA. Student's *t*-test was applied for statistical analysis; significance is shown as mean \pm SD; **P* < 0.05; ***P* < 0.01; A β 40: *n* = 6/group; APP-CTFs: *n* = 4/Scramble, *TSPAN6* and *APMAP* groups; *n* = 3/*RTN4* group. β -Actin served as a protein loading control. mAPP-FL and iAPP-FL: mature and immature APP full-length.

$60 \pm 10.1\%$, respectively (Fig. 1D). Yet, full-length APP (APP-FL) protein levels remained unchanged in the *APMAP* knockdown experiments (Fig. 1B and C and Supplementary Material, Fig. S3). In contrast, depletion of *RTN4* in both HeLa and HEK-APPSwe cells, respectively, caused \sim 170 and \sim 140% increases in APP-FL levels (Fig. 1B and C).

Genetic inhibition of APMAP increases A β production

We further focused on the adipocyte plasma membrane-associated protein APMAP because (i) its knockdown displayed the biggest variations in APP-CTFs and A β 40 (Fig. 1B–D), (ii) its knockdown was associated with a unique effect on the stability against proteolytic degradation of APP-CTFs (see below and Fig. 3), and (iii) its brain functions remain unknown. First, we confirmed by ELISA and a high-resolution Tris-Tricine urea gel that reduced APMAP expression in HEK-APPSwe cells increased the secretion of full-length total A β (A β 1-x), A β 1-40 and A β 1-42 in a dose-dependent manner (Supplementary Material, Fig. S5), without affecting the levels or the maturation of the secretases (Supplementary Material, Fig. S6). Mass spectrometric analysis of secreted A β revealed no changes in the A β profile (Supplementary Material, Fig. S5), suggesting that APMAP does not affect the sequential and specific processing of APP by γ -secretase. Moreover, APMAP1 purified from *E. coli* or CHO cells did not interfere with the processing of APP-CTF β in our cell-free γ -secretase activity assays, arguing against a direct effect of APMAP on the activity of the mature γ -secretase (Supplementary Material, Figs S7 and S8). Finally, purified APMAP1 did not prove to be a substrate for γ -secretase (Supplementary Material, Figs S7 and S8). The latter observation excludes an APP phenotype (accumulation of APP-CTFs) caused by substrate competition, after siRNA-dependent depletion of APMAP1.

APMAP is expressed in neurons and interacts physically with γ -secretase and APP

Next, the physical interaction between APMAP1 and the γ -secretase complex and APP was confirmed in both HEK-APPSwe and CHO cells overexpressing APMAP1-Flag or an untagged control APMAP1 (Fig. 2 and Supplementary Material, Fig. S9). In these experiments, all subunits of the γ -secretase complex, as well as APP-FL and APP-CTFs, specifically and sequentially co-sedimented and co-precipitated with APMAP1-Flag (Fig. 2A). In sharp contrast, these proteins did not co-precipitate with the untagged control APMAP1 (Fig. 2A). Under our experimental conditions, other APP processing enzymes including BACE1 or ADAM10 did not bind to APMAP (Fig. 2A). Next, by combining immunohistochemistry and confocal imaging, we also found that APMAP1 is highly expressed in mouse primary cortical neurons where it adopts an axonal and somatodendritic distribution (Fig. 2B and Supplementary Material, Fig. S10). Our results further show that APMAP partially co-localizes with Nicastrin, a subunit of the γ -secretase complex, mainly in the neuronal cell body (Fig. 2B and Supplementary Material, Fig. S10). Consistent with the predicted topology of APMAP (type-II transmembrane protein), our data suggest that APMAP1 traffics via the secretory pathway to the plasma membrane and adopts a somatodendritic cellular distribution. We further found that APMAP co-localizes partially with APP-FL/APP-CTFs, both in cytosolic and neuritic cellular compartments (Fig. 2B and Supplementary Material, Fig. S10). Altogether, these data support the existence of neuronal high molecular weight complexes made of APMAP and γ -secretase, APMAP and APP-FL/CTFs, and possibly all three components.

APMAP controls the levels and stability of APP C-terminal fragments

Further supporting an association with APP, we found that partial depletion of APMAP in HeLa cells altered the profile of endogenous APP-CTFs. As observed on a high-resolution Tris-Tricine urea gel, APMAP siRNA combined with low concentrations of the GSI DAPT led to the generation of three distinct forms of APP-CTF α (CTF α 1, α 2 and α 3), with two forms migrating with apparent sizes of \sim 8.5 and 8.0 kDa, instead of 9.0 kDa (Fig. 3A). The mass spectrometric characterization of APP-CTF α 1-3 (APP-C80, C74 and C71; Fig. 3B and C and Supplementary Material, Fig. S11) further suggested that endogenous APP-CTFs undergo either partial degradation by yet unknown proteases or further proteolytic processing [possibly by BACE2 (17)], supporting a possible APP stabilization function for APMAP.

APMAP modulates A β production in WT and Alzheimer's mice

Next, and to determine whether our findings are relevant *in vivo*, we induced the partial knockdown of APMAP in wild-type mice and transgenic APP/ presenilin 1 (PS1) Alzheimer's mice. Five week-old mice (males and females) were bilaterally injected in the dorsal hippocampus with serotype 9 adeno-associated viral vectors (AAV9) encoding shRNAs targeting APMAP (Fig. 4A and C and Supplementary Material, Figs S12 and S13). As recently demonstrated by Aschauer *et al.* (18), AAV9 vectors, when injected in the hippocampus, have a generally broad tropism for many different brain cell types, including oligodendrocytes, microglia, astrocytes and neurons (including inhibitory neurons). In our study, four weeks post-hippocampus injection, the global expression of APMAP was reduced by \sim 50% in male WT mice (Fig. 4B) and by \sim 35% in male APP/PS1 mice (Fig. 4D), whereas A β production was increased by \sim 20% in male WT mice (Fig. 4B) and by \sim 55% in male APP/PS1 mice (Fig. 4D). Interestingly, under our experimental conditions, no significant effect on A β production was found in female mice (Supplementary Material, Fig. S13), which may be linked to the weaker APMAP knockdown observed in these animals (APMAP knockdown by \sim 35% in female WT mice and by \sim 25% in female APP/PS1 mice). Finally, APMAP depletion in the brain of WT and AD mice does not seem to affect APP-CTF levels (Fig. 4B and D), in contrast to HeLa and HEK-APPSwe cells (Fig. 1B and C). This apparent discrepancy may result from the weaker APMAP knockdown in mice (by 35–50%), when compared with that observed in HeLa and HEK-APPSwe cells (by \sim 75%). In support of this explanation, the dose-dependent reduction of APMAP in HEK-APPSwe cells revealed a critical step for APMAP depletion (\sim 50% depletion, 0.2 nM APMAP siRNA), above which small changes in APMAP expression are associated with big changes in APP-CTFs accumulation (Supplementary Material, Fig. S14).

APMAP modulates APP-CTFs through the lysosomal pathway

Finally, we investigated whether the main APMAP phenotype, namely co-increases of both APP-CTFs and A β after APMAP

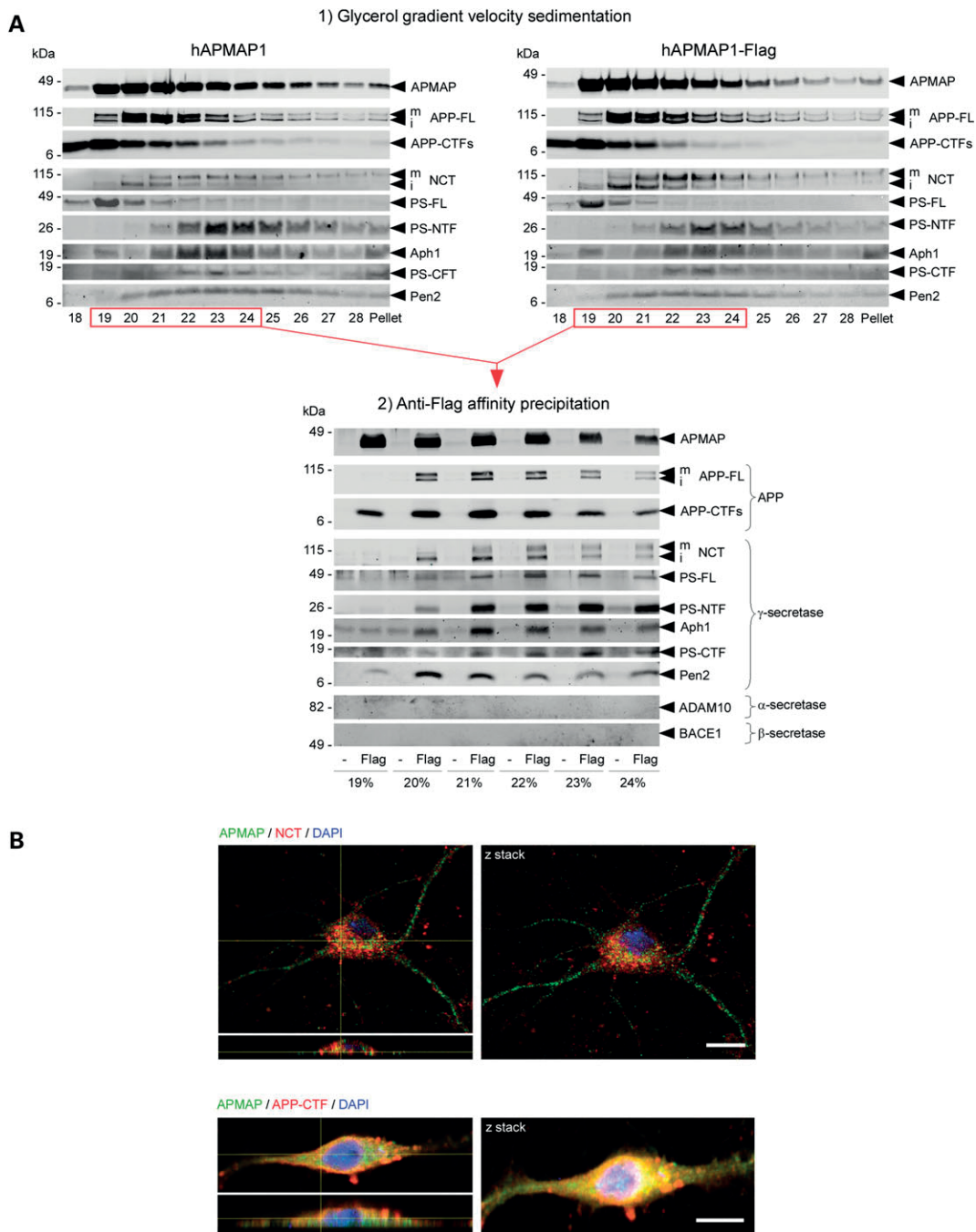


Figure 2. APMAP interacts physically and co-localizes with γ -secretase, APP-FL and APP-CTFs. (A) Velocity co-sedimentation and co-immunoprecipitation of APMAP with the γ -secretase complex, APP-FL and APP-CTFs. Total membrane protein extracts from HEK-APPSwe cells transiently overexpressing hAPMAP1 or hAPMAP1-Flag were sedimented on an 18–28% glycerol gradient containing 0.1% CHAPSO. Each fraction was collected and analyzed by western blot for hAPMAP1, APP-FL, APP-CTFs and mature and immature γ -secretase (top panels). Next, proteins interacting with hAPMAP1-Flag (Flag) were affinity-precipitated in the fractions labeled in red with M2 anti-Flag affinity resin (lower panel). Untagged APMAP (hAPMAP1, also labeled ‘-’ in the figure) served as a control for the specific co-precipitation. (B) Immunohistochemical co-localization of APMAP (green) with the γ -secretase subunit Nicastrin (red, upper panel) or APP (red, lower panel) in 14 days *in vitro* mouse primary cortical neurons. Scale bar: 10 μ m. Both confocal images (left panels) and Z-stack projections (right panels) are shown with a microscope objective magnification of 40 \times . For comparison, un-merged images for APMAP, NCT, APP-CTFs and DAPI are shown in Supplementary Material, Fig. S10. mNCT and iNCT, mature and immature Nicastrin.

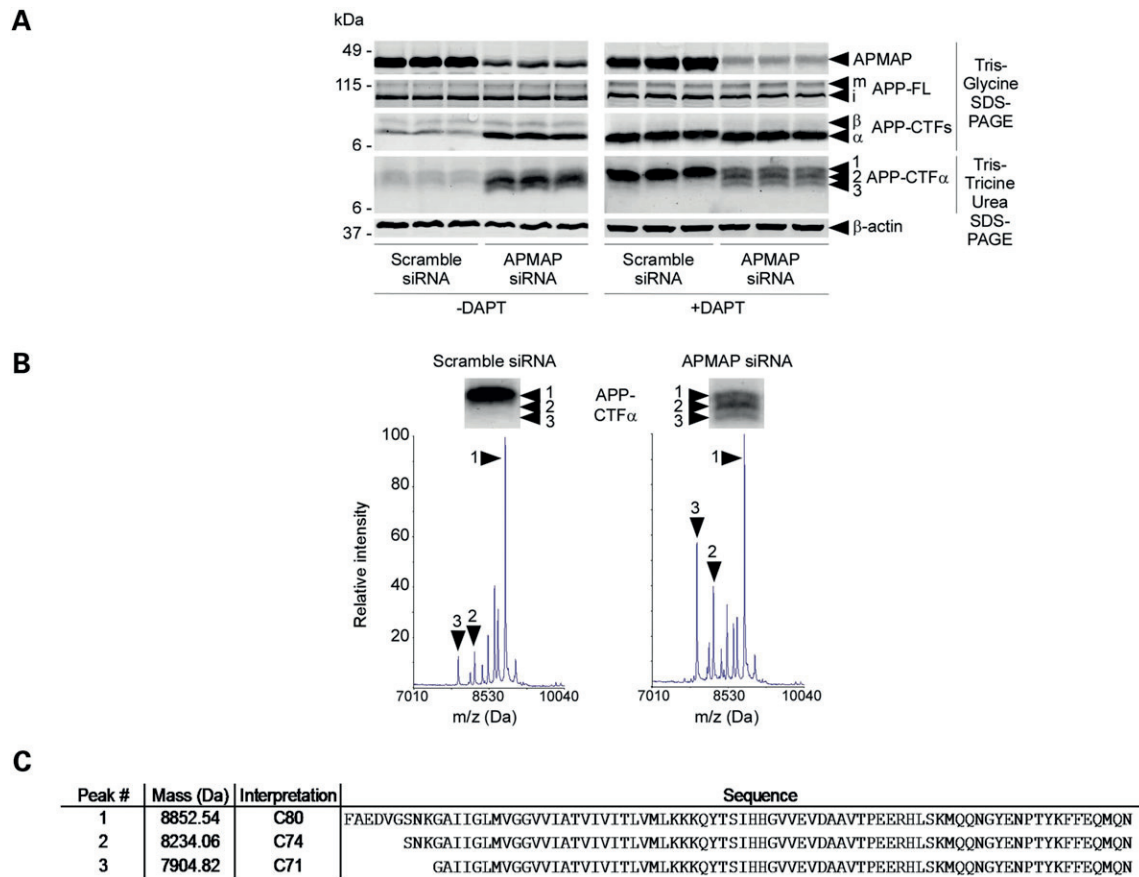


Figure 3. APMAP controls the levels and the stability of APP-CTFs. (A) siRNA knockdown of APMAP in HeLa cells quantitatively and qualitatively impacts APP-CTFs. Reduced APMAP expression correlates with increased APP-CTFs and the formation of 1 μ M GSI DAPT (right panel). Biological triplicates are shown. (B) MALDI-TOF mass spectrometric analysis of APP-CTF α 1, α 2 and α 3 immunoprecipitated from DAPT-treated cells with siRNA-reduced APMAP expression. (C) Peptide sequences of N-terminal truncated APP-CTF α 1 (C80), -CTF α 2 (C74) and -CTF α 3 (C71).

knockdown, could be explained by an impaired degradation of APP-CTFs through the lysosomal–autophagic pathway. To do so, a pharmacological approach was used, by taking advantage of Chloroquine, a well-known inhibitor of the lysosomal–autophagic pathway. Chloroquine is a lysosomotropic agent that impedes the lysosomal pathway by inhibition of lysosomal enzymes and lysosomal protein degradation, and by preventing the fusion of endosomes and lysosomes (19). Chloroquine, because it raises the lysosomal pH, also inhibits autophagy (20). To test whether APMAP can regulate the levels of APP-CTFs through the lysosomal pathway, HEK-APPSwe and HeLa cells were incubated for 12 h with, respectively, 25 and 50 μ M Chloroquine, in the presence of APMAP or after APMAP depletion. As shown in Fig. 5A and B, Chloroquine treatments in the presence of APMAP (scramble siRNA) were associated with a 2.1-fold increase of APP-CTFs in HEK-APPSwe cells and a 3.4-fold increase of the same proteins in HeLa cells, when compared with DMSO-treated controls. This observation clearly supports a lysosomal degradation of the APP-CTFs in these two cell types. Interestingly, APMAP

depletion strongly reinforced the Chloroquine-dependent accumulation of APP-CTFs. The densitometric analysis of the western blots indeed revealed additional 2.2-fold and 1.6-fold increases of APP-CTFs in HEK-APPSwe and HeLa cells co-treated with Chloroquine and the APMAP siRNA, when compared with cells co-treated with Chloroquine and the scramble siRNA. The latter observation is consistent with a Chloroquine- and APMAP-dependent synergistic effect possibly caused by reduced lysosomal degradation and reduced lysosomal transport of APP-CTFs.

Altogether, our data suggest that APMAP modulates the levels of APP-CTFs through the lysosomal–autophagic system.

DISCUSSION

In this study, we analyzed the protein composition of highly purified and active γ -secretase complexes and identified seven proteins that interact physically with the enzymatic complex. Among these proteins, TSPAN6 was found to positively regulate

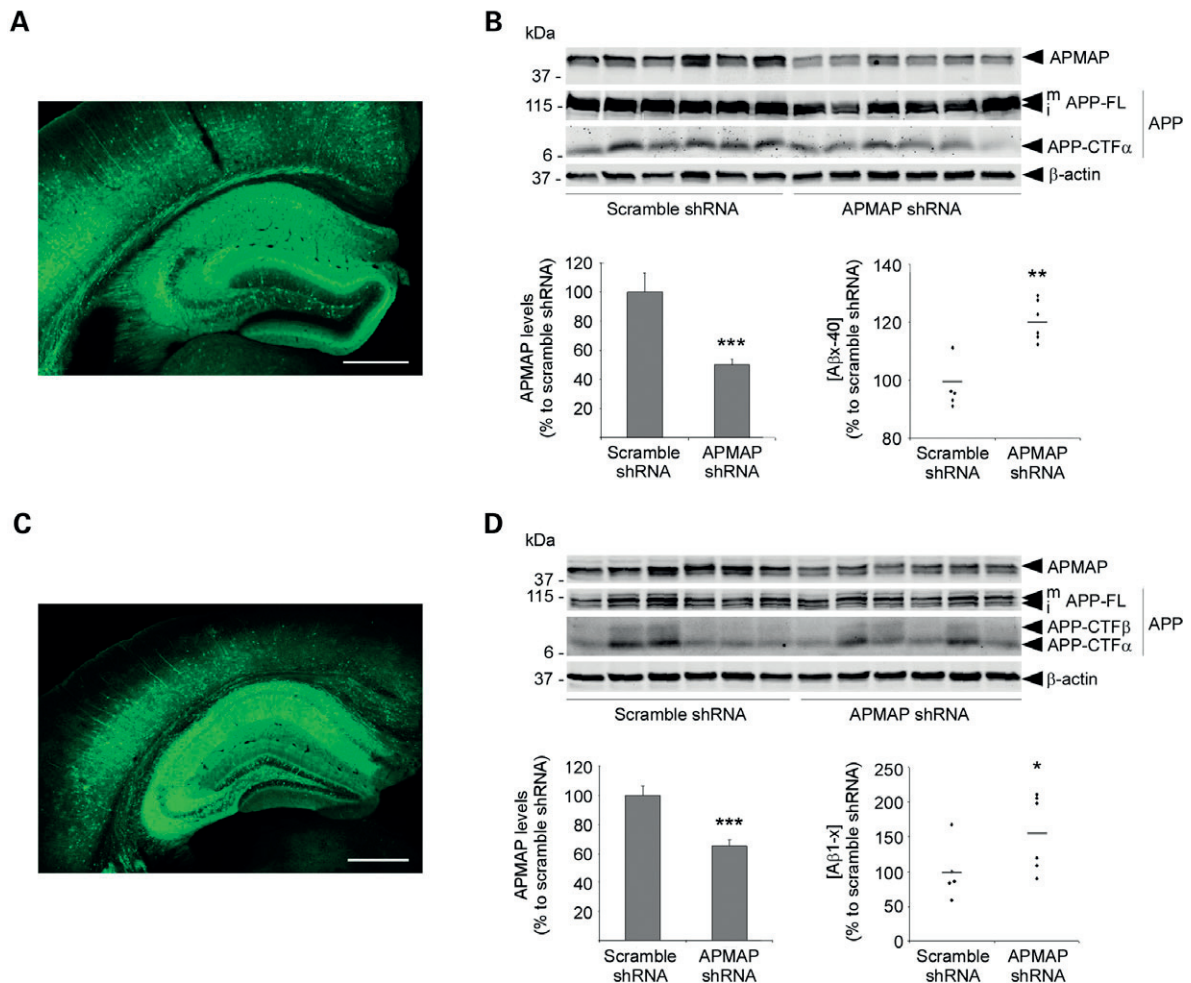


Figure 4. APMAP modulates A β production *in vivo*. Five-week-old wild-type (A and B) or APP/PS1 transgenic (C and D) male mice were injected in the dorsal hippocampus with AAV9 expressing APMAP shRNA or a scrambled control shRNA, together with a GFP reporter. Four weeks post-injection, AAV9 transduction is highly efficient and is mainly restricted to the hippocampus (A and C). Wild-type (B) or APP/PS1 (D) males displayed significant $\sim 50\%$ and $\sim 35\%$ decreases of APMAP expression (mean \pm SD; *** $P < 0.001$; $n = 6$ /group), associated with significant $\sim 20\%$ and $\sim 55\%$ increases in total A β levels in the hippocampus (* $P < 0.05$; ** $P < 0.01$; $n = 6$ /group). Student's *t*-test was applied for the statistical analysis. β -Actin served as a protein loading control. (A and C) Scale bar: 500 μ m.

the processing of APP and the production of A β , consistent with previous work on tetraspanins TSPAN12, TSPAN28 and TSPAN29 (12,21). Another of our proteins identified to be associated with the γ -secretase complex is RTN4, which has been shown previously to negatively regulate A β production by interacting with the β -secretase BACE1 (22). We confirmed this effect, as reduced RTN4 led to increased A β production (Fig. 1D) and suggest for the first time that the A β -suppressing function of RTN4 may also be based on a physical interaction with the γ -secretase complex.

Importantly, we further identified the adipocyte differentiation protein APMAP (15) as an endogenous inhibitor of A β production that binds to both APP and γ -secretase, and controls the levels and the stability of APP-CTFs. Additionally, APMAP does not affect the processing of other γ -secretase substrates,

including the Notch receptor, and the neuronal cell adhesion molecules Neurexin-3 β and Neuroligin-1 (Supplementary Material, Fig. S15). Consistent with the Allen Brain and Human Protein Atlases (Supplementary Material, Fig. S16), we further showed that APMAP is expressed in the brain, and more specifically in neurons where it co-localizes at least partially with APP and γ -secretase (Fig. 2B). In mice, APMAP knockdown in both neuronal and glial cells (18; Fig. 4A and C) increased A β levels in the hippocampus 4 weeks after injection of the AAV9 with shRNAs targeting APMAP (Fig. 4). Yet, a decade of research on which forms and structures of A β impair neuronal functions has concluded that (i) small and diffusible assemblies of misfolded and self-aggregating A β peptides are probably the principal cytotoxic forms, but also that (ii) insoluble amyloid fibrils and the amyloid plaques cause neuritic alterations including a

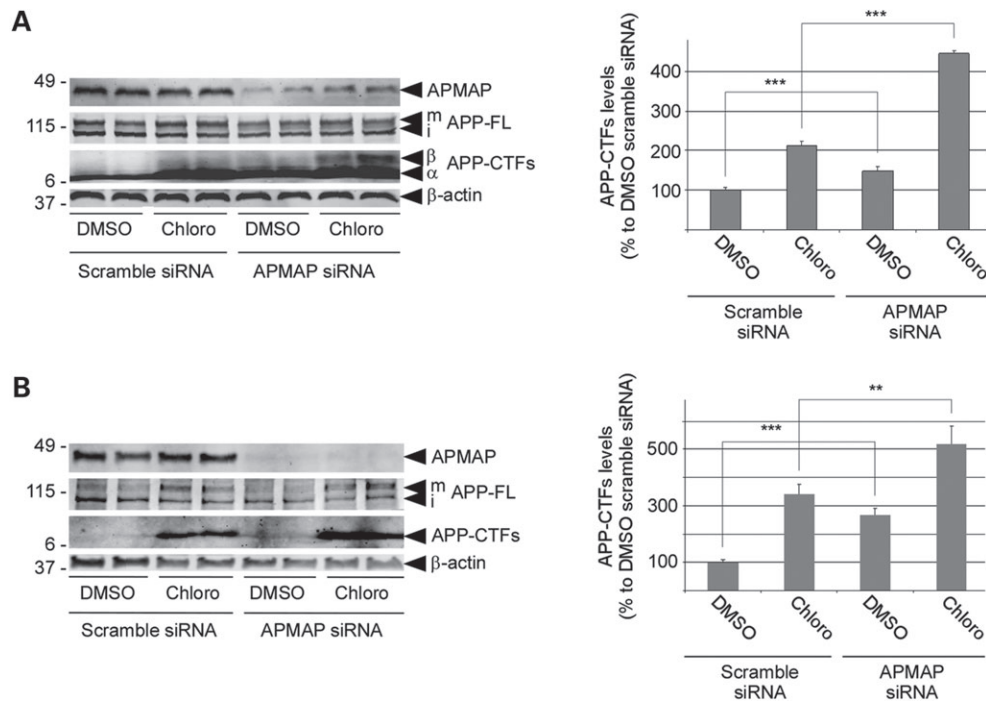


Figure 5. APMAP regulates cellular APP-CTFs levels through the lysosomal–autophagic pathway. HEK-APPSwe (A) and HeLa (B) cells treated either with a scrambled control siRNA or with APMAP siRNA were incubated for 12 h with the lysosomal inhibitor Chloroquine (25 and 50 μ M, respectively). Total membrane protein extracts were prepared and analyzed by western blot for APMAP1, APP-FL and APP-CTFs (left panels). Biological duplicates are shown and β -actin served as a protein loading control. Next, APP-CTFs bands were quantified by densitometry (right panels) and Student's *t*-test was applied for statistical analysis with $n = 4$ /group. ** $P < 0.01$; *** $P < 0.001$.

decreased efficiency of neurotransmission (reviewed in 23). Whether APMAP preferentially affects the production of soluble A β assemblies or the deposition of A β plaques remains unknown and will require specific and long-term investigations in AD transgenic mice.

At the molecular level, APP is cleaved into sAPP- α and CTF- α by α -secretase or cleaved into sAPP- β and CTF- β by β -secretase. Then, γ -secretase cleaves CTF- α into secreted 24–26 residues long P3 peptides and cytoplasmic APP-intracellular domain (AICD), and cleaves CTF- β into 38–43 residues long A β peptides and AICD. Under physiological conditions, APP processing by γ -secretase is associated with increased A β production and reduced CTF β levels. In contrast, if a molecule inhibits γ -secretase, reduced A β production is associated with increased CTF β levels. In our study, depletion of APMAP led to both increases of A β and CTFs (Figs 1 and 3). Moreover, depletion of APMAP did not affect the levels of sAPP- α or sAPP- β (Supplementary Material Figs 4 and 6), or the expression of APP-FL (Figs 1 and 3), suggesting that (i) α - and β -secretases are not targets for APMAP, and (ii) both cleavage and production of APP-FL are not affected by APMAP. All observed phenotypes including the co-increases of APP-CTFs and A β after APMAP knockdown could be explained by an impaired degradation of APP-CTFs (depicted in Fig. 6). This hypothesis is supported by the observation that APMAP depletion caused an increased accumulation of APP-CTFs in cells treated

with Chloroquine, a well-known inhibitor of the lysosomal–autophagic pathway (Fig. 5).

In the molecular hypothesis proposed in Figure 6, APMAP, by interacting physically with APP-CTFs (Fig. 2), would promote the transport of these substrates from the endosomes to the lysosomes, with the consequence being their degradation, thus reducing both APP-CTFs and A β levels. Indeed, it has been previously reported that APP-CTFs can be delivered to the lysosomes by two pathways: the endosomal–lysosomal pathway (heterophagy) and the autophagic pathway, causing the degradation of the A β precursor proteins (24–26). Similar to the phenotypes observed in our study with reduced APMAP, genetic or pharmacological inhibition of the lysosomal–autophagic system led to the significant intracellular accumulation of APP-CTFs and increased A β secretion (27,28). Thus, APMAP depletion would lead to impaired degradation, with the consequence being both increases of APP-CTFs and A β . Moreover, impaired APP-CTFs degradation would make these γ -secretase substrates accessible to yet unidentified proteases and trigger their proteolysis (Fig. 3). Alternatively, and still by interacting physically with APP-CTFs, APMAP could also transport these substrates to the γ -secretase complex, explaining the possible physical interaction between APMAP, APP-CTFs and the enzyme (Fig. 2). Since abnormalities in the neuronal lysosomal–autophagic system have been associated with the pathology of AD (reviewed in 29), understanding the precise

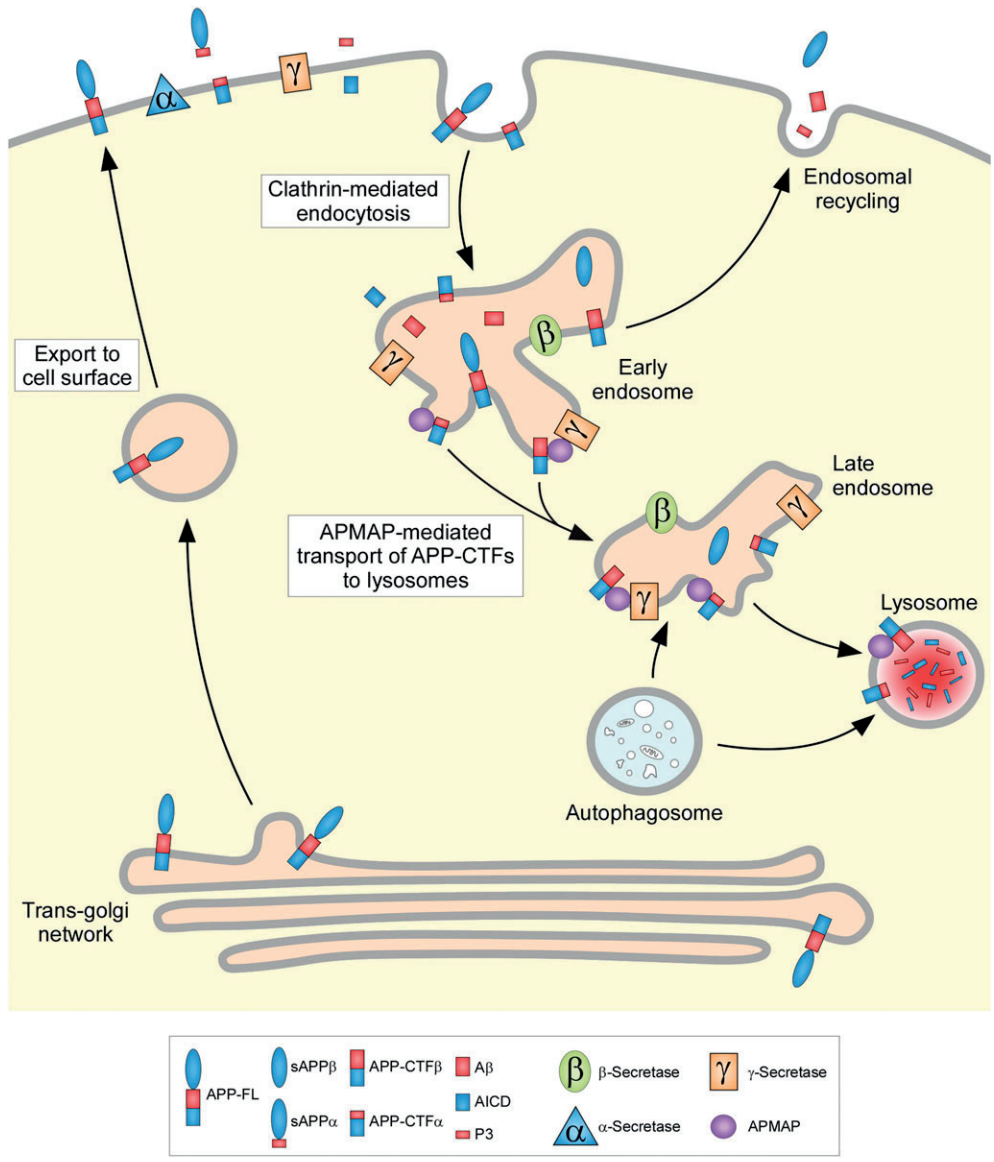


Figure 6. Molecular hypothesis for the regulation of APP-CTFs/A β levels by APMAP. In this hypothesis, APMAP is implicated in the transport of APP-CTFs to the lysosomal–autophagic system, where it undergoes substrate degradation. Consistent with the observed cellular phenotypes (Figs 1 and 3), depletion of APMAP would impair this transport capacity and consequently trigger increased APP-CTFs levels, which in turn cause increased A β production. Impaired degradation would further make APP-CTFs substrates accessible to yet unidentified proteases, explaining the N-terminal truncated species observed in cells with depleted APMAP (Fig. 3).

molecular mechanisms by which APMAP can regulate APP-CTFs degradation deserves further investigation.

Yet, APP-CTFs do not seem to only be degraded through the lysosomal–autophagic system. Indeed, Bustamante *et al.* (30) have recently demonstrated in human H4 neuroglioma cells that APP-C99 is actively degraded in the endoplasmic reticulum in an ubiquitin and proteasome-dependent manner. Whether

APMAP can play an active role in the proteasome-dependent degradation of APP-CTFs (including a crosstalk between the lysosomal and proteasomal systems) also requires further investigation.

APMAP also controls adipogenesis and consequently the adipocytic release of potential γ -secretase modulators, including leptin (31,32) and cholesterol (33–35). Moreover, the

expression of APMAP is regulated by the peroxisome proliferation-activated receptor PPAR γ (14,15), which has also been shown to decrease A β production (36). In return, the processing of Notch by γ -secretase inhibits PPAR γ and adipocyte differentiation (37). Thus, reducing A β production by interfering with the PPAR γ /APMAP/ γ -secretase regulatory loop could potentially represent a therapeutic approach to slow down the pathology of AD. Moreover, APMAP, by participating in the gut/adipose tissue/brain crosstalk and regulating cerebral A β levels, could possibly provide new molecular insight into the statistical link between AD and obesity or diabetes.

MATERIALS AND METHODS

γ -Secretase purification, tryptic digestion and mass spectrometry

The γ -secretase complex was purified as previously described (10) and was run on a NativePAGE Novex[®] Bis-Tris 4–16% gel for BN-PAGE analysis (Invitrogen, Carlsbad, CA, USA). Next, the complex was visualized by Coomassie staining, excised and cut into small pieces. Proteins were reduced, alkylated and subjected to in-gel digestion with trypsin. Briefly, gel pieces were destained, desiccated by incubating twice in 200 μ l of 50 mM ammonium bicarbonate and 50% ethanol for 20 min and dried with a vacuum concentrator. The samples were then incubated overnight at 37°C with trypsin (12.5 ng/ μ l). For liquid chromatography coupled to tandem mass spectrometry (LC-MS/MS) analysis after extraction from gel slices, peptides were resuspended in 2% Acetonitril/0.1% Formic Acid and separated by reverse-phase chromatography on a Dionex Ultimate 3000 RSLC nanoUPLC system connected in-line with an Orbitrap Elite (Thermo Fischer Scientific, Waltham, MA, USA). The instrument was operated in an information-dependent mode where peptide masses were selected for collision-induced dissociation to generate tandem mass spectra. A database search was performed using Mascot 2.3 (Matrix Science, Boston, MA, USA) and SEQUEST in Proteome Discoverer v.1.3 against a human database (UniProt release 2013_01; 87613 sequences) and Mammalian database (UniProt release 2011_07; 91104 sequences). All searches were performed with trypsin cleavage specificity, with up to three missed cleavages allowed, an ion mass tolerance of 10 ppm for the precursor and 0.5 Da for the fragments. Carbamidomethylation was set as a fixed modification, whereas oxidation (M), acetylation (protein N-term) and phosphorylation (STY) were considered variable modifications. Data were further processed and inspected using Scaffold 3 software (Proteome Software).

Cell lines, cell cultures and treatments with siRNA or GSI

Human embryonic kidney cells (HEK 293T), human cervical carcinoma cells (HeLa) and CHO cells were routinely grown in DMEM with 10% fetal bovine serum and penicillin/streptomycin in a humidified 5% CO₂ atmosphere. The CHO cells stably expressing Flag-tagged APMAP and the HEK cells stably expressing APP with the Swedish mutation [HEK-APPSwe (38)] were maintained in DMEM with 10% FBS supplemented with 150 μ g/ml Geneticin G418 (Gibco, Thermo

Fischer Scientific). HEK cells stably expressing the γ -secretase substrate Notch Δ E [HEK-N7 (39)] were cultured in DMEM with 10% FBS supplemented with 250 μ g/ml Zeocin (Gibco). For siRNA knockdown experiments, cells were treated for 3 days with allstar negative control siRNA (Qiagen, Germantown, MD, USA), APMAP (5'-TTCACCGATTCTAGCAGCAA A-3', Qiagen), RTN4 (5'-CAGGGCATATCTGGAATCTGA-3', Qiagen) or Tspan6 (5'-CTCTCGTGCCATAACAAATAA-3', Qiagen) siRNA duplexes complexed with Lipofectamine RNAiMax from Invitrogen. For A β peptides secreted in the conditioned medium of HEK-APPSwe cells, A β 1-X (IBL), A β 1-40 (Invitrogen) and A β 1-42 (Invitrogen) were quantitatively measured by ELISA, according to the protocol provided by the manufacturer. For inhibition of cellular γ -secretase activity, cells were incubated for 4 h with 10 μ M of the γ -secretase-specific inhibitor *N*-[*N*-(3,5-difluorophenacetyl)-*L*-alanyl]-*S*-phenylglycine *t*-butyl ester (DAPT; Sigma-Aldrich, GmbH, Buchs, Switzerland). For inhibition of the lysosomal pathway, HEK-APPSwe and HeLa cells were incubated for 12 h with 25 and 50 μ M of Chloroquine (Sigma-Aldrich), respectively.

Western blotting and antibodies

Whole cell extracts were prepared in 50 mM HEPES buffer containing 1% NP40 and complete protease inhibitor cocktail (Roche Applied Sciences, Basel, Switzerland) and were separated by electrophoresis on homemade 12% acrylamide Tris-glycine SDS-PAGE or NuPAGE Novex[®] 4–12% Bis-Tris gels (Invitrogen) for SDS-PAGE analysis of APMAP purification and γ -secretase activity. High separation of APP-CTFs or A β peptides was resolved using 15% acrylamide and 6 M urea Tris-Tricine SDS-PAGE as described previously (40) or by a Tris-bicine-urea gel (41), respectively. Proteins were transferred onto nitrocellulose membranes and probed with antibodies against APP-FL and APP-CTFs (CT15, Sigma-Aldrich, Saint Louis, MS, USA), as well as sAPP α (6E10; Covance, Berkeley, CA, USA) and total sAPP (22C11; Millipore, Billerica, MA, USA), NCT (N1660 or NCT164, BD Bio-Sciences, Bedford, MA, USA), PS1-NTF (MAB1563, Chemicon International, Temecula, CA, USA), PS1-CTF (MAB5232, Chemicon International), Aph1 (O2C2, Covance), Pen-2 (UD1, a gift from Helena Karlström, KI Stockholm, Sweden), ADAM10 (Prosci, Poway, CA, USA), BACE1 (EE17, Sigma-Aldrich), APMAP (4F6, AbCam, Cambridge, UK), RTN4 (Ab2, Sigma-Aldrich), Tspan6 (AbCam), Notch-ICD (Val1744, Cell Signaling, Boston, MA, USA) or β -actin (Sigma-Aldrich). Anti-mouse, rabbit and rat IgGs conjugated to Alexa 680 were purchased from Invitrogen, and the Odyssey infrared imaging system (LICOR, Lincoln, NE, USA) was used to detect the fluorescent signal.

Glycerol gradient velocity sedimentation and co-immunoprecipitation

Membranes were prepared by osmotic shock from HEK-APPSwe cells transiently expressing either Flag-tagged or untagged human APMAP1, as previously described (4). Next, membrane proteins solubilized in 1% CHAPSO were loaded onto an 18–28% glycerol gradient containing 11 \times 950 μ l fractions prepared in 0.1% CHAPSO. After centrifugation for 15 h at

220 000g, 950 μ l fractions were collected and analyzed by western blotting. For co-immunoprecipitation experiments, all fractions collected after glycerol velocity sedimentation were diluted twice with 0.2% digitonin in Tris-buffered saline (TBS) and incubated with 50 μ l of M2 resin (Sigma-Aldrich) at 4°C overnight. The beads were then washed three times for 15 min in TBS with 0.1% digitonin and collected in 50 μ l of diluted (1:2 in water) Laemmli sample buffer.

Immunostaining

Mouse primary cortical neurons were prepared from embryonic day 17 Of1 fetal mouse brains. Cortices were digested in medium containing papain (20 U/ml, Sigma-Aldrich) and dissociated by mechanical trituration. Cells were plated in the neurobasal medium (Invitrogen) supplemented with B27 (Invitrogen) and 2 mM Glutamax (Life Technologies, Thermo Fischer Scientific) on poly-L-ornithine (Sigma-Aldrich)-coated plates at 37°C in a humidified 5% CO₂ atmosphere. At *in vitro* day 14, neurons were fixed with 4% paraformaldehyde and permeabilized in phosphate buffered saline (PBS) containing 0.1% Triton X-100 for 10 min. The cells were then incubated in citrate buffer (10 mM sodium citrate, 0.05% Tween-20, pH 8.0) for 30 min at 95–100°C. After cooling at room temperature, non-specific antibody binding was prevented by incubation in 0.25% cold water fish gelatin (Sigma-Aldrich) diluted in PBS for 45 min. Following the blocking step, the cells were incubated with antibodies against APMAP (GTX46051, Gentex, Irvine, CA, USA), APP-CTFs (4G8, AbCam Cambridge, UK) or Nicastatin (NCT164, BD Bio-Sciences, Franklin Lakes, NJ, USA). Finally, the fixed cells were incubated with anti-rabbit Alexa 488 and anti-mouse Alexa 568 (Invitrogen) secondary antibodies. Image acquisition was performed with a Zeiss LSM700 UP2 microscope using a 40 \times objective.

Immunoprecipitation-mass spectrometry (IP-MS) analysis of A β and APP-CTFs

A β secreted from HEK-APPSwe cells treated with scrambled or APMAP siRNAs were immunoprecipitated overnight using the monoclonal anti-A β antibody 4G8 (AbCam) and protein G-coupled agarose (Roche Applied Sciences). A β was eluted using a 1:20:20 (vol:vol:vol) mix of 0.1% (vol/vol) trifluoroacetic acid:acetonitrile:H₂O mixed 1:1 (vol:vol) with saturated CHCA (α -cyano-4-hydroxycinnamic acid) and analyzed by MALDI-TOF mass spectrometry in the reflectron mode on an ABI 4800 MALDI-TOF/TOF mass spectrometer (Applied Biosystems, Thermo Fischer Scientific). Intracellular APP-CTFs from whole protein extracts prepared from cells treated with APMAP siRNA and/or DAPT were immunoprecipitated with an antibody targeting the CTF portion of APP (CTF15; Sigma-Aldrich GmbH, Buchs, Switzerland). Next, APP-CTFs were washed two times in 1% NP40-HEPES and two more times in deionized water, and then eluted in 0.1% (vol/vol) trifluoroacetic acid with acetonitrile:H₂O mixed 1:1 (vol:vol), dried with a vacuum pump and finally resolubilized in the same elution buffer saturated with sinapinic acid (3–4-hydroxy-3,5-dimethoxyphenyl prop-2-enoic acid). All spectra were acquired in the linear mode with an ABI 4800 MALDI-TOF/TOF mass spectrometer. Molecular masses were accurately

measured and searched against known amino acid sequences of human APP.

Purification of APMAP in *E. coli* and CHO

For the purification of recombinant human APMAP1-His6 in *E. coli*, a pET21b vector encoding human APMAP1-His6 cDNA was expressed in BL21(DE3) cells and induced with 1 mM isopropyl- β -D-thiogalactopyranoside for 16 h at 24°C at a 600 nm optical density of 0.8. For the purification of human APMAP1-His6, harvested bacteria were lysed with 10 mM Tris pH 7.4, 150 mM NaCl, 1% CHAPSO and complete protease inhibitor cocktail (Roche) and passed three times through a high-pressure homogenizer (Emulsiflex-C5; Avestin, Inc., Mannheim, Germany) at a pressure greater than 1000 psi. The obtained lysate was incubated for 1 h on ice and spun down at 5150g for 20 min at 4°C, and the resulting supernatant was incubated for 30 min with Ni-NTA agarose beads (Invitrogen) at room temperature. Bound proteins were eluted five times in 10 mM Tris pH 7.4, 150 mM NaCl and 1% CHAPSO containing 250 mM imidazole (pH 7.4) and analyzed by Coomassie-stained SDS–PAGE.

For the purification of mammalian APMAP-Flag, a total of 2.64×10^9 CHO cells stably transfected with human APMAP1-Flag were resuspended in MES buffer [50 mM MES pH 6.0, 150 mM NaCl, 5 mM MgCl₂, 5 mM CaCl₂ and protease inhibitor cocktail (Roche)]. The cells were lysed by three passages in a high-pressure homogenizer at a pressure greater than 1000 psi and centrifuged at 3000g for 20 min. The supernatant was further centrifuged at 100 000g for 1 h to pellet microsomes. The pellet was resuspended by pipetting up and down 30 times in bicarbonate buffer (0.1 M NaHCO₃, pH 11.3) and incubated for 20 min at 4°C to remove non-integral proteins. The washed microsomes were pelleted by centrifugation at 100 000g for 1 h. The supernatant was discarded, and the membranes were solubilized in ice-cold 1% CHAPSO-HEPES lysis buffer [50 mM HEPES, 150 mM NaCl, 5 mM MgCl₂, 5 mM CaCl₂, 1% CHAPSO and protease inhibitor cocktail (Roche)] for 1 h at 4°C. The lysate was centrifuged at 16 000g, saved and diluted twice in HEPES buffer [50 mM HEPES, 150 mM NaCl, 5 mM MgCl₂, 5 mM CaCl₂ and protease inhibitor cocktail (Roche)]. The lysate was further diluted six times in 0.1% digitonin-TBS buffer (50 mM Tris–HCl pH 7.4, 150 mM NaCl) and bound to M2 anti-Flag affinity resin (Sigma-Aldrich) overnight. Following three washes in 0.1% digitonin-TBS buffer, the bound proteins were eluted in 1.5 ml of 0.1% digitonin-TBS buffer containing 0.2 mg/ml Flag peptides and used for the *in vitro* γ -secretase assays. In both protocols, the purity of human APMAP1-His6 and APMAP1-Flag was confirmed by SDS–PAGE using Coomassie staining.

γ -Secretase activity assays

γ -Secretase assays using recombinant human APMAP1 and APP-C100-Flag were performed as previously reported (42–44). Briefly, γ -secretase purified from SS20 cells was solubilized in 0.2% (wt/vol) CHAPSO, 50 mM HEPES (pH 7.0), 150 mM NaCl, 5 mM MgCl₂ and 5 mM CaCl₂ and incubated at 37°C for 4 h with 1 μ M substrate, 0.1% (wt/vol) phosphatidylcholine and 0.025% (wt/vol) phosphatidylethanolamine. The resulting products, AICD-Flag and A β , were detected with Flag-specific

M2 antibodies (Sigma-Aldrich) and A β -specific 6E10 (Covance), respectively.

Mice

Male and female WT and APP/PS1 transgenic mice (obtained from Prof. M. Jucker, HIH, Tübingen, Germany) were used. APP/PS1 animals co-express the KM670/671NL Swedish mutation of human APP and the L166P mutation of human PS1 under the control of the Thy-1 promoter and show age-dependent accumulation of parenchymal A β plaques (45). Both WT and APP/PS1 mice were generated on a C57BL/6J background. We conducted all animal experiments in accordance with local and federal directives for the care and use of laboratory animals.

Production and titration of AAV2/9 vectors

The production and titration of AAV vector particles pseudotyped with a serotype 9 capsid has been described previously (46). Briefly, the vectors were obtained by transient co-transfection of 293-AAV cells (Agilent, Santa Clara, CA, USA) with the shuttle plasmid and a pDP9rs.gck helper plasmid, which encodes the *REP* and *CAP* adeno-associated viral genes, as well as genes that are essential to the adenoviral helper function (plasmid kindly provided by Dr J. Kleinschmidt, Deutsches Krebsforschungszentrum, Heidelberg, Germany). Viral vector particles were purified from cell lysates by centrifugation on an iodixanol gradient (OptiPrep, Axis-Shield, Oslo, Norway) followed by anion exchange affinity chromatography on a HiTrap Q-FF column (GE Healthcare Bio-Sciences AB, Uppsala, Sweden). The suspension medium was replaced with Dulbecco's PBS (DPBS, Gibco), and the viral particles were concentrated to a final volume of $\sim 100 \mu\text{l}$ using Centricon Plus-20 filtration devices (regenerated cellulose, 100 000 MWCO, Millipore). Viral titers were determined by measuring the number of viral genomes present in a given volume of the vector suspension using real-time PCR. We used a primer and probe set that anneals to the β -globin intron (fw: 5'-CGTGC CAAGAGTGACGTAAG-3'; rv: 5'-TGGTGCAAAGAGGCA TGATA-3'; TaqMan probe: 5'-FAM-TTGCCCTGAAAGAA AGAGATTAGGGAA-BHQ-1-3'). The reactions were run in a Corbett Rotor-Gene RG-3000 cyclor (Qiagen Inc., Valencia, CA, USA) using the following program: one cycle of 20 min at 95°C for capsid denaturation followed by 40 cycles of 3 s at 95°C and 10 s at 60°C.

Injection of mice and A β measurements

The equivalent of 2.53×10^{10} and 1.10×10^{10} viral particles were injected into 5-week-old WT and APP/PS1 mice, respectively. Bilateral injection was performed at the following stereotaxic coordinates: (in mm, anterior, lateral, ventral to bregma) -2.1, 1.5, 1.7. After 4 weeks, the mice were euthanized, and the right hemisphere was homogenized in a buffer (1 ml buffer/100 mg brain) containing 50 mM NaCl, 0.2% DEA and complete protease inhibitor cocktail (Roche). After centrifugation at 200 000g for 35 min at 4°C, soluble A β peptide analysis in WT and APP/PS1 brain lysates was performed using anti-human/rat A β X-40 (Wako Chemicals, Richmond, VA, USA) and anti-human A β 1-X (IBL International GmbH, Hamburg,

Germany), respectively, according to the manufacturer's instructions. Total proteins were subsequently extracted in 1% NP40 and complete protease inhibitor cocktail (Roche) for western blot analysis.

Statistical analyses

All data are presented as the mean \pm SD. Student's *t*-test (two-tailed) was applied for statistical analysis, and statistical significance is shown as $P < 0.05$ (one asterisks), $P < 0.01$ (two asterisks) or $P < 0.001$ (three asterisks).

SUPPLEMENTARY MATERIAL

Supplementary Material is available at *HMG* online.

AUTHORS' CONTRIBUTIONS

S.M., A.M., J.R.A., M.D. and J.P. performed the experiments; B.L.S. and P.C.F. designed the research; P.C.F. supervised the project; S.M. and P.C.F. wrote the manuscript. All authors edited the manuscript.

ACKNOWLEDGMENTS

The authors also thank M. Moniatte and R. Hamelin (Proteomics Core Facility, School of Life Sciences, Ecole Polytechnique Fédérale de Lausanne, Lausanne, Switzerland) for technical assistance with mass spectrometry. The authors further thank L. Aeschbach and P. Colin for technical help, and V. Padrun and F. Pidoux for technical assistance with AAV production.

Conflict of Interest statement. None declared.

FUNDING

This work was supported by the Swiss National Science Foundation (to P.C.F. and S.M., grant 31003A_152677/1) and the Strauss foundation (to P.C.F. and M.D.). The funders had no role in study design, data collection and analysis, decision to publish or preparation of the manuscript. Funding to pay the Open Access publication charges for this article was provided by EPFL.

REFERENCES

- Hardy, J.A. and Higgins, G.A. (1992) Alzheimer's disease: the amyloid cascade hypothesis. *Science*, **256**, 184–185.
- Kawabata, S., Higgins, G.A. and Gordon, J.W. (1991) Amyloid plaques, neurofibrillary tangles and neuronal loss in brains of transgenic mice overexpressing a C-terminal fragment of human amyloid precursor protein. *Nature*, **354**, 476–478.
- Iwatsubo, T., Odaka, A., Suzuki, N., Mizusawa, H., Nukina, N. and Ihara, Y. (1994) Visualization of A β 42(43) and A β 40 in senile plaques with end-specific A β monoclonals: evidence that an initially deposited species is A β 42(43). *Neuron*, **13**, 45–53.
- Bot, N., Schweizer, C., Ben Halima, S. and Fraering, P.C. (2011) Processing of the synaptic cell adhesion molecule neurexin-3beta by Alzheimer disease alpha- and gamma-secretases. *J. Biol. Chem.*, **286**, 2762–2773.
- De Strooper, B., Annaert, W., Cupers, P., Saftig, P., Craessaerts, K., Mumm, J.S., Schroeter, E.H., Schrijvers, V., Wolfe, M.S., Ray, W.J. *et al.* (1999) A presenilin-1-dependent gamma-secretase-like protease mediates release of Notch intracellular domain. *Nature*, **398**, 518–522.

6. Haapasalo, A. and Kovacs, D.M. (2011) The many substrates of presenilin/ gamma-secretase. *J. Alzheimers Dis.*, **25**, 3–28.
7. Fraering, P.C. (2007) Structural and functional determinants of gamma-secretase, an intramembrane protease implicated in Alzheimer's disease. *Curr. Genomics*, **8**, 531–549.
8. Imbimbo, B.P. (2008) Therapeutic potential of gamma-secretase inhibitors and modulators. *Curr. Top. Med. Chem.*, **8**, 54–61.
9. Dimitrov, M., Alattia, J.R., Lemmin, T., Lehal, R., Fligier, A., Houacine, J., Hussain, I., Radtke, F., Dal Peraro, M., Beher, D. *et al.* (2013) Alzheimer's disease mutations in APP but not gamma-secretase modulators affect epsilon-cleavage-dependent AICD production. *Nat. Commun.*, **4**, 2246.
10. Alattia, J.R., Matasci, M., Dimitrov, M., Aeschbach, L., Balasubramanian, S., Hacker, D.L., Wurm, F.M. and Fraering, P.C. (2013) Highly efficient production of the Alzheimer's gamma-secretase integral membrane protease complex by a multi-gene stable integration approach. *Biotechnol. Bioeng.*, **110**, 1995–2005.
11. Yang, Y., Turner, R.S. and Gaut, J.R. (1998) The chaperone BiP/GRP78 binds to amyloid precursor protein and decreases Abeta40 and Abeta42 secretion. *J. Biol. Chem.*, **273**, 25552–25555.
12. Wakabayashi, T., Craessaerts, K., Bammens, L., Bentahir, M., Borgions, F., Herdewijn, P., Staes, A., Timmerman, E., Vandekerckhove, J., Rubinstein, E. *et al.* (2009) Analysis of the gamma-secretase interactome and validation of its association with tetraspanin-enriched microdomains. *Nat. Cell Biol.*, **11**, 1340–1346.
13. Teng, F.Y. and Tang, B.L. (2008) Cell autonomous function of Nogo and reticulons: the emerging story at the endoplasmic reticulum. *J. Cell Physiol.*, **216**, 303–308.
14. Albrechtsen, T., Richter, H.E., Clausen, J.T. and Fleckner, J. (2001) Identification of a novel integral plasma membrane protein induced during adipocyte differentiation. *Biochem. J.*, **359**, 393–402.
15. Bogner-Strauss, J.G., Prokesch, A., Sanchez-Cabo, F., Rieder, D., Hackl, H., Duszka, K., Krogsdam, A., Di Camillo, B., Walenta, E., Klatzer, A. *et al.* (2010) Reconstruction of gene association network reveals a transmembrane protein required for adipogenesis and targeted by PPARgamma. *Cell Mol. Life Sci.*, **67**, 4049–4064.
16. Hemler, M.E. (2005) Tetraspanin functions and associated microdomains. *Nat. Rev. Mol. Cell Biol.*, **6**, 801–811.
17. Sun, X., He, G. and Song, W. (2006) BACE2, as a novel APP theta-secretase, is not responsible for the pathogenesis of Alzheimer's disease in Down syndrome. *FASEB J.*, **20**, 1369–1376.
18. Aschauer, D.F., Kreuz, S. and Rumpel, S. (2013) Analysis of transduction efficiency, tropism and axonal transport of AAV serotypes 1, 2, 5, 6, 8 and 9 in the mouse brain. *PLoS ONE*, **8**, e76310.
19. Hart, P.D., Young, M.R., Jordan, M.M., Perkins, W.J. and Geisow, M.J. (1983) Chemical inhibitors of phagosome-lysosome fusion in cultured macrophages also inhibit saltatory lysosomal movements. A combined microscopic and computer study. *J. Exp. Med.*, **158**, 477–492.
20. Poole, B. and Ohkuma, S. (1981) Effect of weak bases on the intralysosomal pH in mouse peritoneal macrophages. *J. Cell Biol.*, **90**, 665–669.
21. Xu, D., Sharma, C. and Hemler, M.E. (2009) Tetraspanin12 regulates ADAM10-dependent cleavage of amyloid precursor protein. *FASEB J.*, **23**, 3674–3681.
22. Murayama, K.S., Kametani, F., Saito, S., Kume, H., Akiyama, H. and Araki, W. (2006) Reticulons RTN3 and RTN4-B/C interact with BACE1 and inhibit its ability to produce amyloid beta-protein. *Eur. J. Neurosci.*, **24**, 1237–1244.
23. Mucke, L. and Selkoe, D.J. (2012) Neurotoxicity of amyloid beta-protein: synaptic and network dysfunction. *Cold Spring Harb. Perspect. Med.*, **2**, a006338.
24. Chen, F., Yang, D.S., Petanceska, S., Yang, A., Tandon, A., Yu, G., Rozmahel, R., Ghiso, J., Nishimura, M., Zhang, D.M. *et al.* (2000) Carboxyl-terminal fragments of Alzheimer beta-amyloid precursor protein accumulate in restricted and unpredicted intracellular compartments in presenilin 1-deficient cells. *J. Biol. Chem.*, **275**, 36794–36802.
25. Nixon, R.A. (2007) Autophagy, amyloidogenesis and Alzheimer disease. *J. Cell Sci.*, **120**, 4081–4091.
26. Tian, Y., Chang, J.C., Greengard, P. and Flajolet, M. (2014) The convergence of endosomal and autophagosomal pathways: implications for APP-CTF degradation. *Autophagy*, **10**, 694–696.
27. Tian, Y., Bustos, V., Flajolet, M. and Greengard, P. (2011) A small-molecule enhancer of autophagy decreases levels of Abeta and APP-CTF via Atg5-dependent autophagy pathway. *FASEB J.*, **25**, 1934–1942.
28. Tian, Y., Chang, J.C., Fan, E.Y., Flajolet, M. and Greengard, P. (2013) Adaptor complex AP2/PICALM, through interaction with LC3, targets Alzheimer's APP-CTF for terminal degradation via autophagy. *Proc. Natl Acad. Sci. USA*, **110**, 17071–17076.
29. Salminen, A., Kaamiranta, K., Kauppinen, A., Ojala, J., Haapasalo, A., Soininen, H. and Hiltunen, M. (2013) Impaired autophagy and APP processing in Alzheimer's disease: the potential role of Beclin 1 interactome. *Prog. Neurobiol.*, **106–107**, 33–54.
30. Bustamante, H.A., Rivera-Dictter, A., Cavieres, V.A., Munoz, V.C., Gonzalez, A., Lin, Y., Mardones, G.A. and Burgos, P.V. (2013) Turnover of C99 is controlled by a crosstalk between ERAD and ubiquitin-independent lysosomal degradation in human neuroglioma cells. *PLoS ONE*, **8**, e83096.
31. Tezapsidis, N., Johnston, J.M., Smith, M.A., Ashford, J.W., Casadesus, G., Robakis, N.K., Wolozin, B., Perry, G., Zhu, X., Greco, S.J. *et al.* (2009) Leptin: a novel therapeutic strategy for Alzheimer's disease. *J. Alzheimers Dis.*, **16**, 731–740.
32. Fewlass, D.C., Noboa, K., Pi-Sunyer, F.X., Johnston, J.M., Yan, S.D. and Tezapsidis, N. (2004) Obesity-related leptin regulates Alzheimer's Abeta. *FASEB J.*, **18**, 1870–1878.
33. Yu, B.L., Zhao, S.P. and Hu, J.R. (2010) Cholesterol imbalance in adipocytes: a possible mechanism of adipocytes dysfunction in obesity. *Obes. Rev.*, **11**, 560–567.
34. Thirumangalakudi, L., Prakasam, A., Zhang, R., Bimonte-Nelson, H., Sambamurti, K., Kindy, M.S. and Bhat, N.R. (2008) High cholesterol-induced neuroinflammation and amyloid precursor protein processing correlate with loss of working memory in mice. *J. Neurochem.*, **106**, 475–485.
35. Di Paolo, G. and Kim, T.W. (2011) Linking lipids to Alzheimer's disease: cholesterol and beyond. *Nat. Rev. Neurosci.*, **12**, 284–296.
36. Escribano, L., Simon, A.M., Gimeno, E., Cuadrado-Tejedor, M., Lopez de Maturana, R., Garcia-Osta, A., Ricobaraza, A., Perez-Mediavilla, A., Del Rio, J. and Frechilla, D. (2010) Rosiglitazone rescues memory impairment in Alzheimer's transgenic mice: mechanisms involving a reduced amyloid and tau pathology. *Neuropsychopharmacology*, **35**, 1593–1604.
37. Huang, Y., Yang, X., Wu, Y., Jing, W., Cai, X., Tang, W., Liu, L., Liu, Y., Grottkau, B.E. and Lin, Y. (2010) Gamma-secretase inhibitor induces adipogenesis of adipose-derived stem cells by regulation of Notch and PPAR-gamma. *Cell Prolif.*, **43**, 147–156.
38. Haass, C., Capell, A., Citron, M., Teplow, D.B. and Selkoe, D.J. (1995) The vacuolar H(+)-ATPase inhibitor bafilomycin A1 differentially affects proteolytic processing of mutant and wild-type beta-amyloid precursor protein. *J. Biol. Chem.*, **270**, 6186–6192.
39. Liao, Y.F., Wang, B.J., Cheng, H.T., Kuo, L.H. and Wolfe, M.S. (2004) Tumor necrosis factor-alpha, interleukin-1beta, and interferon-gamma stimulate gamma-secretase-mediated cleavage of amyloid precursor protein through a JNK-dependent MAPK pathway. *J. Biol. Chem.*, **279**, 49523–49532.
40. Schagger, H. (2006) Tricine-SDS-PAGE. *Nat. Protoc.*, **1**, 16–22.
41. Wiltfang, J., Smirnov, A., Schmierstein, B., Kelemen, G., Matthies, U., Klafki, H.W., Staufenbiel, M., Huther, G., Ruther, E. and Kornhuber, J. (1997) Improved electrophoretic separation and immunoblotting of beta-amyloid (A beta) peptides 1–40, 1–42, and 1–43. *Electrophoresis*, **18**, 527–532.
42. Cacquevel, M., Aeschbach, L., Osenkowski, P., Li, D., Ye, W., Wolfe, M.S., Li, H., Selkoe, D.J. and Fraering, P.C. (2008) Rapid purification of active gamma-secretase, an intramembrane protease implicated in Alzheimer's disease. *J. Neurochem.*, **104**, 210–220.
43. Wu, F., Schweizer, C., Rudinskiy, N., Taylor, D.M., Kazantsev, A., Luthi-Carter, R. and Fraering, P.C. (2010) Novel gamma-secretase inhibitors uncover a common nucleotide-binding site in JAK3, SIRT2, and PS1. *FASEB J.*, **24**, 2464–2474.
44. Alattia, J.R., Kuraishi, T., Dimitrov, M., Chang, I., Lemaitre, B. and Fraering, P.C. (2000) Mercury is a direct and potent gamma-secretase inhibitor affecting Notch processing and development in Drosophila. *FASEB J.*, **25**, 2287–2295.
45. Radde, R., Bolmont, T., Kaeser, S.A., Coomaraswamy, J., Lindau, D., Stoltze, L., Calhoun, M.E., Jaggi, F., Wolburg, H., Gengler, S. *et al.* (2006) Abeta42-driven cerebral amyloidosis in transgenic mice reveals early and robust pathology. *EMBO Rep.*, **7**, 940–946.
46. Low, K., Aebischer, P. and Schneider, B.L. (2012) Direct and retrograde transduction of nigral neurons with AAV6, 8, and 9 and intraneuronal persistence of viral particles. *Hum. Gene Ther.*, **24**, 613–629.

Mosser et al., Supplementary Figure 1 (related to Figure 1)

Human RTN4

Uniprot ID: Q9NQC3

Sequence coverage: 5%

MEDLDQSPVLV SSSDSPRRPQ PAFKYQFVRE PEDEEEEEEE EEEDEDEDLE ELEVLERKPA
AGLSAAPVPT APAAGAPLMD FGNDVFPPAP **RGPLPAAPPV** **APER**QPSWDP SPVSSTVPAP
SPLSAAAVSP SKLPEDDEFP ARPPPPPPAS VSPQAEPVWT PPAPAPAAPP STPAAPKRRG
SSGSVDETLF ALPAASEPVI RSSAENMDLK EQPGNTISAG QEDFPSVLL E TAASLPSLSP
LSAASFKEHE YLGNLSTVLP TEGTLQENV S EASKEVSEKA KTL LIDRDLT EFSELEYSEM
GSSFSVSPKA ESAVIVANPR EEIIVKNKDE EEKLVSNNIL HNQQELPTAL TKLVKEDEVV
SSEKAKDSFN EKRVAVEAPM REEYADFKPF ERVWEVKDSK EDSMLAAGG KIESNLESKV
DKKCFADSLE QTNHEKDSSES SNDDTSFSPST PEGIKDRSGA YITCAPFNPA ATESIATNIF
PLLGDPTSEN KTDEKKIEEK KAQIVTEKNT STKTSNPFLV AAQDSETDYV TTDNLTKVTE
EYVANMPEGL TPDLVQEACE SELNEVTGTK IAYETKMDLV QTSEVMQESL YPAAQLCPSF
EESEATPSPV LPDIVMEAPL NSAVPSAGAS VIQPS SSPLE ASSVNYESIK HEPENPPPYE
EAMSVSLKKV SGIKEEIKEP ENINAALQET EAPYISIACD LIKETKLSAE PAPDFSDYSE
MAKVEQVPD HSELVEDSSP DSEPVDFLSD DSIPDVPQKQ DETVMLVKES LTETSFESMI
EYENKEKLSA LPPEGGKPYL ESFKLSLDNT KDTLLPDEV S TLSKKEKIPL QMEELSTAVY
SNDDL F ISKE AQIRETETFS DSSPIEIIIDE FPTLISSKTD SFSKLAREYT DLEVSHKSEI
ANAPDGAGSL PCTELPHDLS LKNIQPKVEE KISFSDDFS K NGSATSKVLL LPPDV SALAT
QAEIESIVKP KVLVKEAEKK LPSDTEKEDR SPSAIFSAEL SKTSVVDLLY WRDIKKTGVV
FGASLFLLLS LTVFSIVSVT AYIALALLSV TISFRIYKGV **IQAIQK**SD EG **HPFR**AYLESE
VAISEELVQK YSNSALGHVN CTIKELRRLF **LVDDLVD**SLK FAVLMWVFTY VGALFNGLTL
LILALISLFS VPVIYER**HQA** **QIDHYL**GLAN **K**NVKDAMAKI QAKIPGLKRK AE

Human HSPA5

Uniprot ID: P11021

Sequence coverage: 58%

MKLSLVAAML LLLSAARA**EE** EDKKEDVGT V VGIDLGTTYS CVGVF**K**NGRV EIIANDQGNR
ITPSYVAFTP EGER**L**IGDAA **KN**QLTSNPEN TVFDA**K**RLIG **RT**WNDPSVQQ **DI**KFLPFKVV
EKKTkPYIQV DIGGG**Q**TKTF APEEISAMVL **T**KMKETA EAY **L**GKkVTHAVV **T**VPAYFNDAQ
RQAT**K**DAGTI AGLNV**M**RIIN EPTAAAIAYG **L**DK**R**EGEKNI LVFDLGGGT F DVSLLTIDNG
VFEVVATNGD **T**HLGGEDFDQ **R**VM EHF**I**KLY KKKTGKDVRK DNRAVQKLRR EVE**K**A**K**RALS
SQH**Q**AR**I**EIE SFYEGEDFSE **T**L**T**R**A**KFEEL **N**MDL**F**R**S**TMK **P**V**Q**K**V**LEDS **L**K**K**S**D**I**D**E**I**V
LVGG**S**T**R**I**P**K **I**Q**Q**L**V**K**E**FFN GKEPSRGINP DEAVAYGAAV QAGVLSGDQD TGDVLVLDVC
PLTLGIETVG GVMTKLIP**R**N TVVPT**K**KSQI **F**STASDNQPT **V**T**L**K**V**YEGER **P**L**T****K**D**N**H**L**L**G**
TFDLTGIPPA **P**R**G**V**P**Q**I**EV**T** **F**E**I**D**V**NG**I**L**R** **V**T**A**ED**K**GT**G**N **K**N**K**I**T**I**T**ND**Q** **N**R**L**T**P**E**E**I**E**R
MVND**A**E**K**FAE ED**K**K**L**K**E**R**I**D **T**R**N**E**L**E**S**Y**A****Y** **S**L**K**N**Q**I**G**D**K**E **K**L**G**G**K**L**S**S**E**D **K**E**T**M**E**K**A**V**E**E
KI**E**W**L**E**S**H**Q**D **A**D**I**E**D**F**K**A**K**K **K**E**L**E**E**I**V**Q**P**I **I**S**K**L**Y**G**S**A**G**P **P**P**T**G**E**E**D**T**A**E **K**D**E**L

Human APMAP1

Uniprot ID: Q9HDC9

Sequence coverage: 16%

MSEADGLRQR RPLRPQVVTD DDQAPEAKD GSSFSGRVFR VTFMLAVSL TVPLL GAMML
LESPIDPQL SFKEPPLLLG VLHPNTKLRQ AERLFENQLV GPESIAHIGD VMFTGTADGR
V**V**K**L**ENGEIE **T**I**A**R**F**GS**G**PC **K**TRDDEPVC G RPLGIRAGPN GTLFVADAYK GLFEVNPWKR
EVKLLSSET PIEGKNMSFV NDLTVTQDGR **K**I**Y**FTD**S**SS**K** WQRDYLLLV MEGTDD**G**R**L**L
EY**D**T**V**T**R**E**V**K **V**L**L**D**Q**L**R**FPN GVQLSPAEDF VLVAETT**M**A**R** **I**R**R****V**Y**V**S**G**L**M** **K**G**G**A**D**L**F**V**E**N
MPGFPDNIRP SSSGGYWVGM STIRPNPGFS MLDFLSERPW IKRMIF**K**L**F**S **Q**E**T**V**M**K**F**V**P**R
YSLVLELSDS GAFRRSLHDP DGLVATYISE VEHHDGHLYL **G**S**F**R**S**P**F**L**C**R LSLQAV

Human ATP1 α 1

Uniprot ID: P05023

Sequence coverage: 29%

MKGKVGGRDKY EPAAVSEQGD KKGKKGKKDR DMDELKKEVS MDDH**KLSLDE** LHR**KY**GTDL**S**
RGLTSARAAE ILARDGNAL TPPPTTPEWI KFCRQLFGGF SMLLWIGAIL CFLAYSIQAA
TEEEPQNDNL YLGVVLSAVV IITGCFSYYQ EAKSSKIMES **FKNMVPQQAL** VIR**NGE**KMSI
NAEEVVVDL VEVKGGDR**IP** ADL**R**IISANG **CKVDNSSLTG** ESE**PQ**TRSPD FTNENPLE**TR**
NIAFFSTNCV EGT**ARGIVVY** TGDR**T**VMGRI ATLASGLEGG QTPIAAEIEH FIIITGVAV
FLGVFFILS LILEYTWLEA VIFLIGIIVA NVPEGLLATV TVCLTLTAKR MARKNCLV**KN**
LEAVETLGST STICSD**K**TGT LTQ**N**RMTVAH MWFDNQIHEA DTENQSGVS FDKTSATWLA
LSRIAGLC**NR** AVFQANQENL PILKRAVAGD ASESALL**K**CI ELCCGSVKEM RERY**A**KIVEI
PFNSTNKYQL SIH**K**NPNTSE PQHLLVMKGA PERILD**R**CSS ILLH**G**KEQPL DEEL**K**DAFQ**N**
AYLELGG**LGE** **R**VLG**F**CHLFL PDEQ**F**PEG**FQ** FDTDDVNFPI DNLCFVGLIS MIDPP**R**AAV**P**
DAVGKCRSAG IKVIMVTGDH PITAKAI**AKG** VGIISEGNET VEDIAARLNI PVSQVNP**R**DA
KACVVHGS**DL** **K**DMTSEQLDD IL**K**YHTEIVF AR**T**SPQ**Q**KLI IVEGC**Q**RQGA IVAVTGDGV**N**
DSPAL**K**KADI GVAMGIAGSD VSKQAADMIL LDDNFASIVT GVEEG**R**LIFD NL**K**KSIAYTL
TSNIPEITPF LIFIIANIPL PLGTVTILCI DLGTMVPAI SLAYEQAESD IMKRQPRNPK
TDKLVNERLI SMAYGQIGMI QALGGFFTYF VILAENGFLP IHLLGLRVDW DDRWINDVED
SYGQOWTYEQ RKIVEFTCHT AFFVSIVVVQ WADLVICKTR RNSVFQQGMK NKILIFGLFE
ETALAAFLSY CPGMGVALRM YPLKPTWWFC AFPYSLIFV YDEVKLIIR **R**RPGGW**VE****K**E
TYY

Human Tspan6

Uniprot ID: O43657

Sequence coverage: 22%

MASPSR**R**LQ**T** KPVITCF**K**SV LLIYTFIFWI TGVILLAVGI **WGK**V**S**LENYF SLLNE**K**ATNV
PFVLIATGTV IILLGTFGCF ATCRASAWML KLYAMFLTLV FLVELVAAIV GFVFRHEIKN
SFKNNYEKAL KQYNSTGDY**R** **SHAVDKIQNT** LHCCGV**T**DY**R** DWTDTNYYSE KGFPKSCCKL
EDCTPQRDAD KVNNEGCFIK VMTIIESEM**G** VVAGISFGVA CFQLIIFLAY CLS**R**AITNN**Q**
YEIV

Human Vamp2

Uniprot ID: P63027

Sequence coverage: 21%

MSATAATAPP AAPAGEGGPP APPPNLTSNR RLQQTQAQVD EVVDIMRVNV DKVLERD**Q****K****L**
SELDDRADAL QAGASQ**F**ETS **AAK**LKRKYWW KNLKMMIILG VICAILIILII IVYFST

Human Vamp3

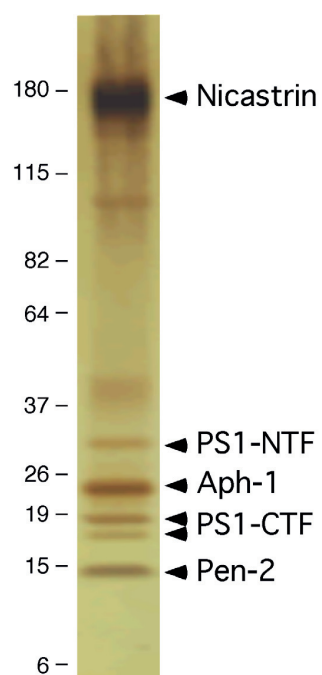
Uniprot ID: Q15836

Sequence coverage: 24%

MSTGPATAATG SNRRLQQTQN QVDEVVDIMR VNVDKVLERD **Q****K**L**S**ELDD**R**A DALQAGAS**Q****F**
ETSAAKLKRK YWWKNCKMWA IGITVLVIFI IIIIVVVSS

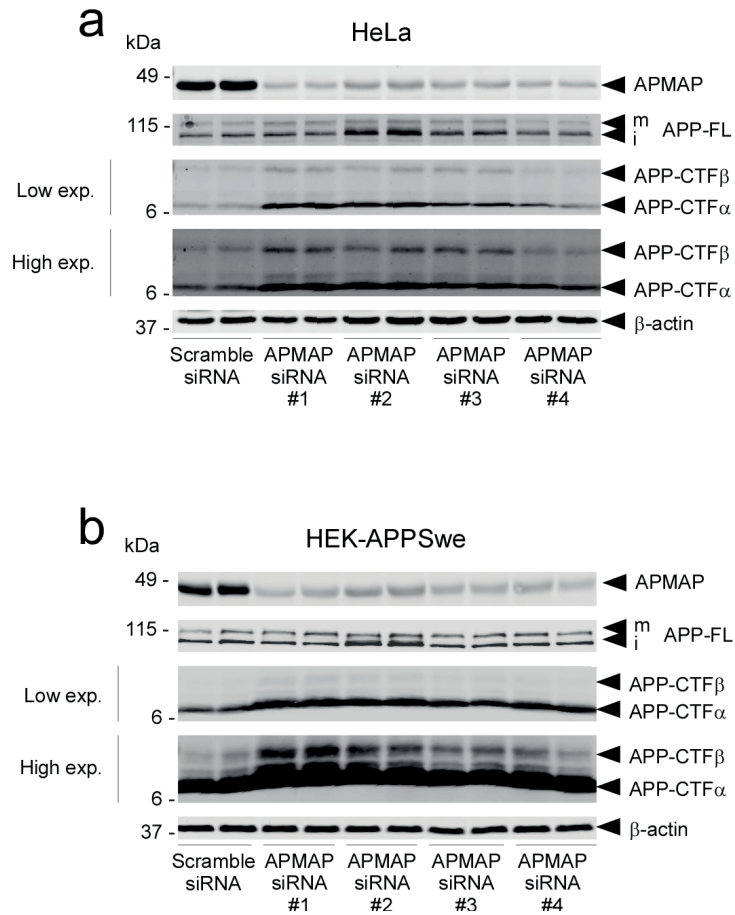
Sup. Fig. 1. Mass spectrometric identification of γ -secretase-interacting proteins. Peptides identified by LC-MS/MS after tryptic digestion of γ -secretase purified from CHO cells are highlighted in yellow in the primary human sequences. Trypsin cleavage sites are indicated in bold.

Mosser et al., Supplementary Figure 2 (related to Figure 1)



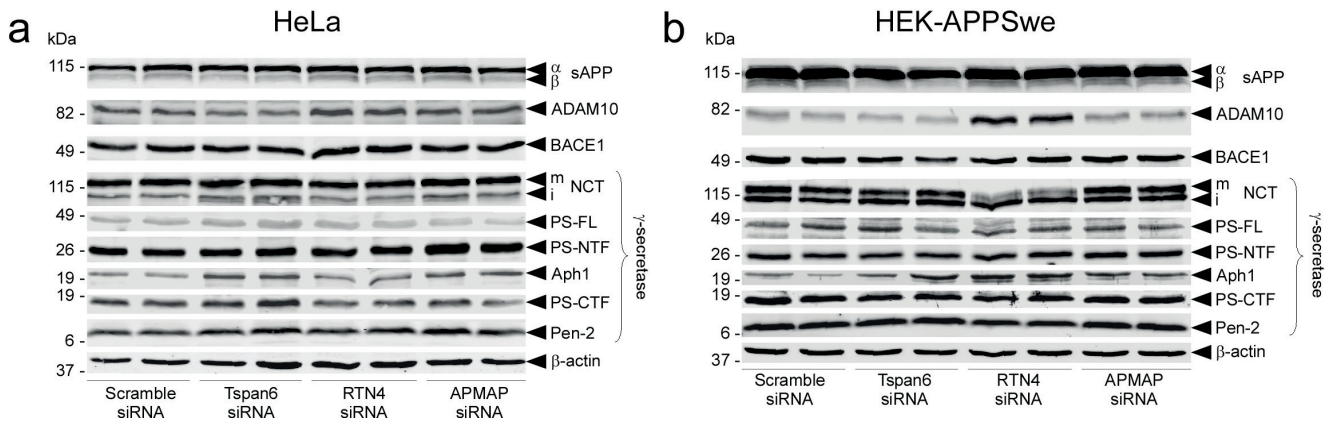
Sup. Fig. 2. Characterization by SDS-PAGE of purified γ -secretase used for the BN-PAGE analysis in Fig. 1a. γ -Secretase purified as described in the Methods section was analyzed by silver-stained SDS-PAGE on a NuPAGE Novex® 4-12% Bis-Tris gel (Life technologies). Western blot and mass spectrometric analyses confirmed that predominant proteins are γ -secretase subunits (labeled bands).

Mosser et al., Supplementary Figure 3 (related to Figure 1)



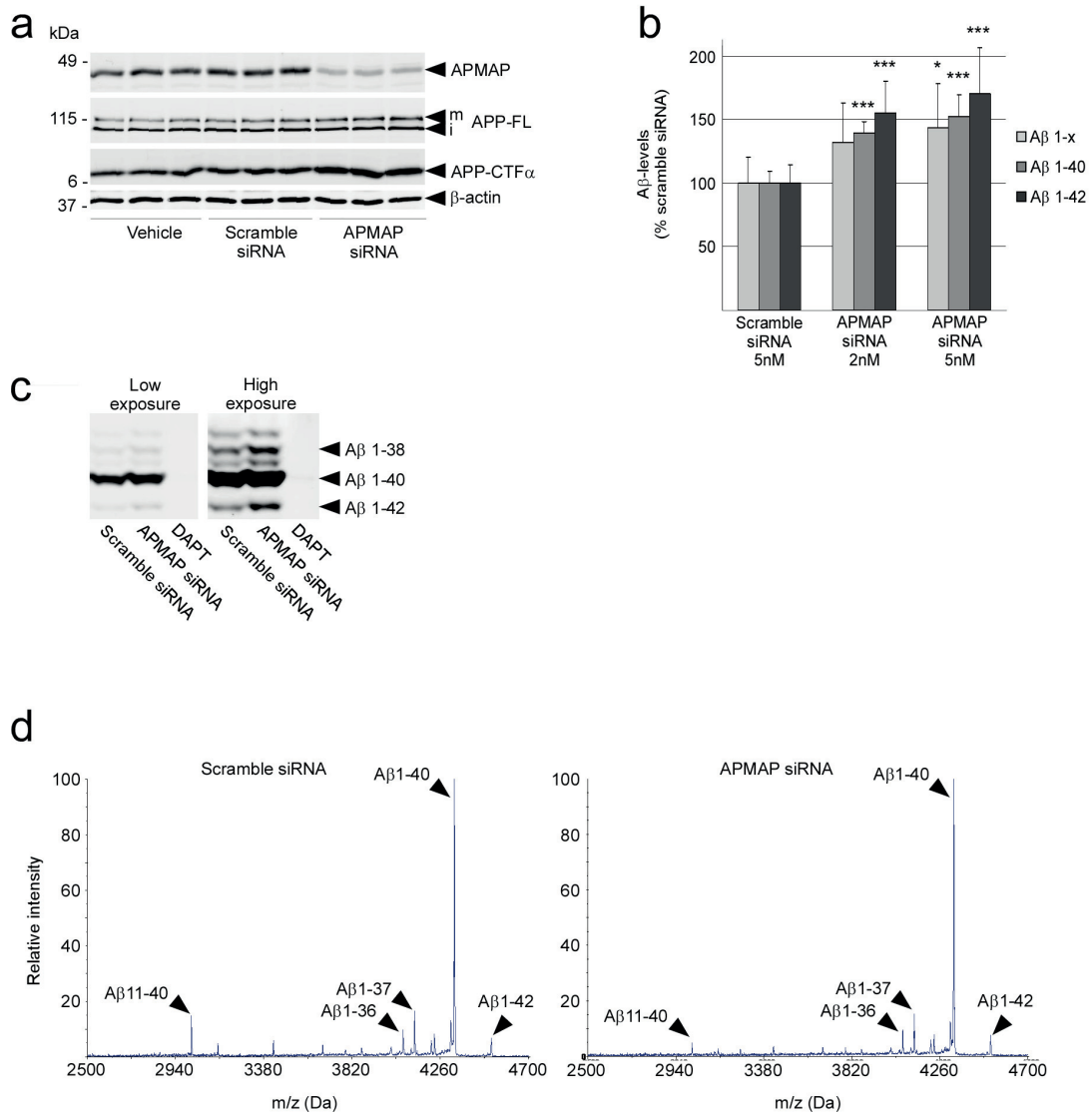
Sup. Fig. 3. Partial depletion of APMAP by different siRNAs raises the levels of APP-CTFs. HeLa cells (a) or HEK-APPSwe cells (b) were treated for 3 days with either negative control scramble siRNA or APMAP siRNA 1 (5'-TTCACCGATTCTAGCAGCAAA-3'), APMAP siRNA 2 (5'-UGAAGUAAAUCCUGGAAA-3'), APMAP siRNA 3 (5'-GCAGAAAGGCUGUUUGAAA-3'), or APMAP siRNA 4 (5'-GGAAGAACAUGUCCUUUGU-3') duplexes. APMAP siRNA 1 was used for experiments described in Figs 1 & 3. β-Actin served as a protein loading control. mAPP-FL and iAPP-FL: mature and immature APP full-length.

Mosser et al., Supplementary Figure 4 (related to Figure 1)



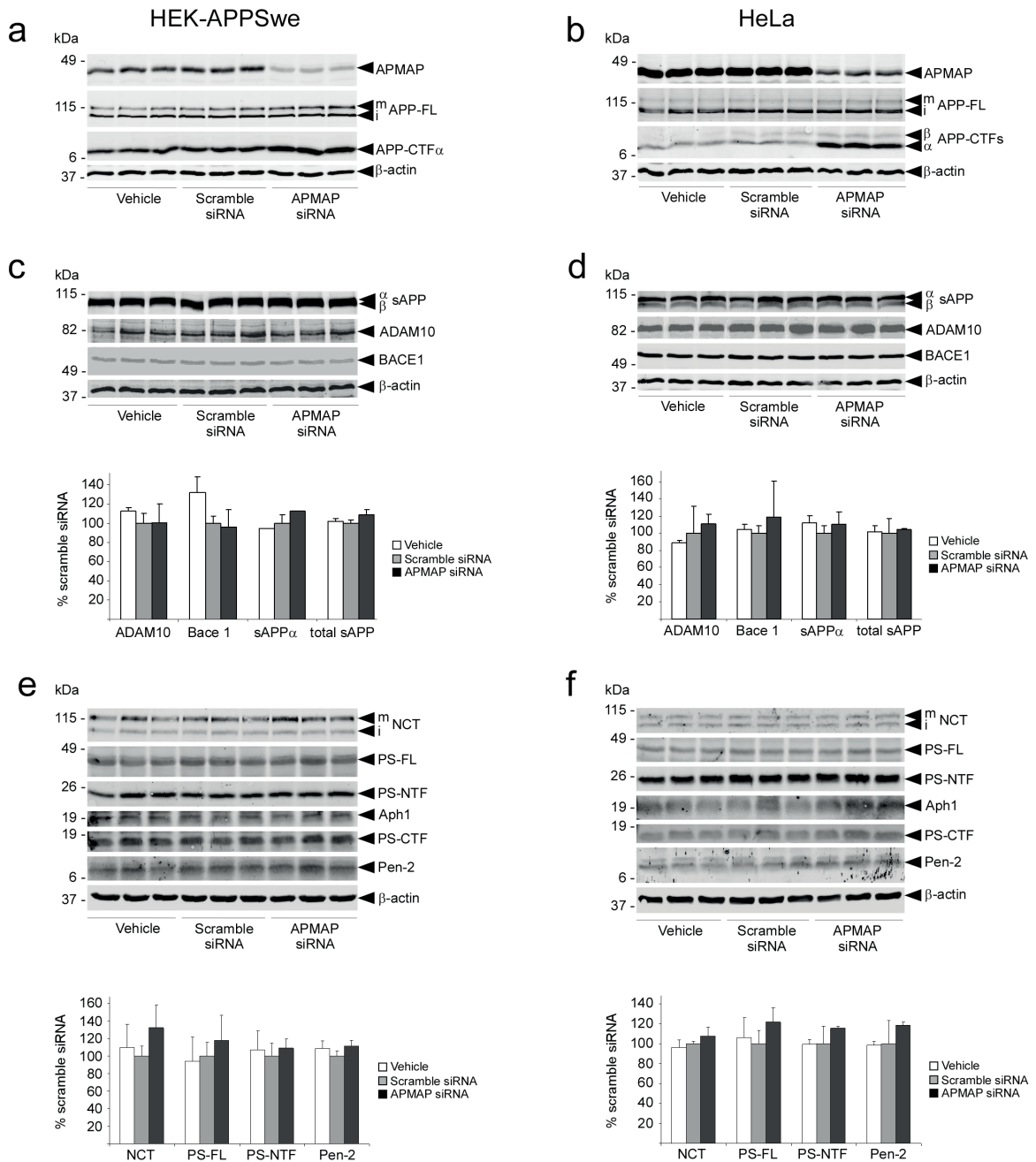
Sup. Fig. 4. Partial depletion of Tspan6, RTN4, and APMAP does not affect the maturation or protein levels of α -, β -, and γ -secretases. The exception to this result was RTN4, in which reduced levels are associated with increased ADAM10 levels. a) HeLa cells; b) HEK-APPSwe cells. β -Actin served as a protein loading control. mNCT and iNCT: mature and immature Nicastrin.

Mosser et al., Supplementary Figure 5 (related to Figure 1)



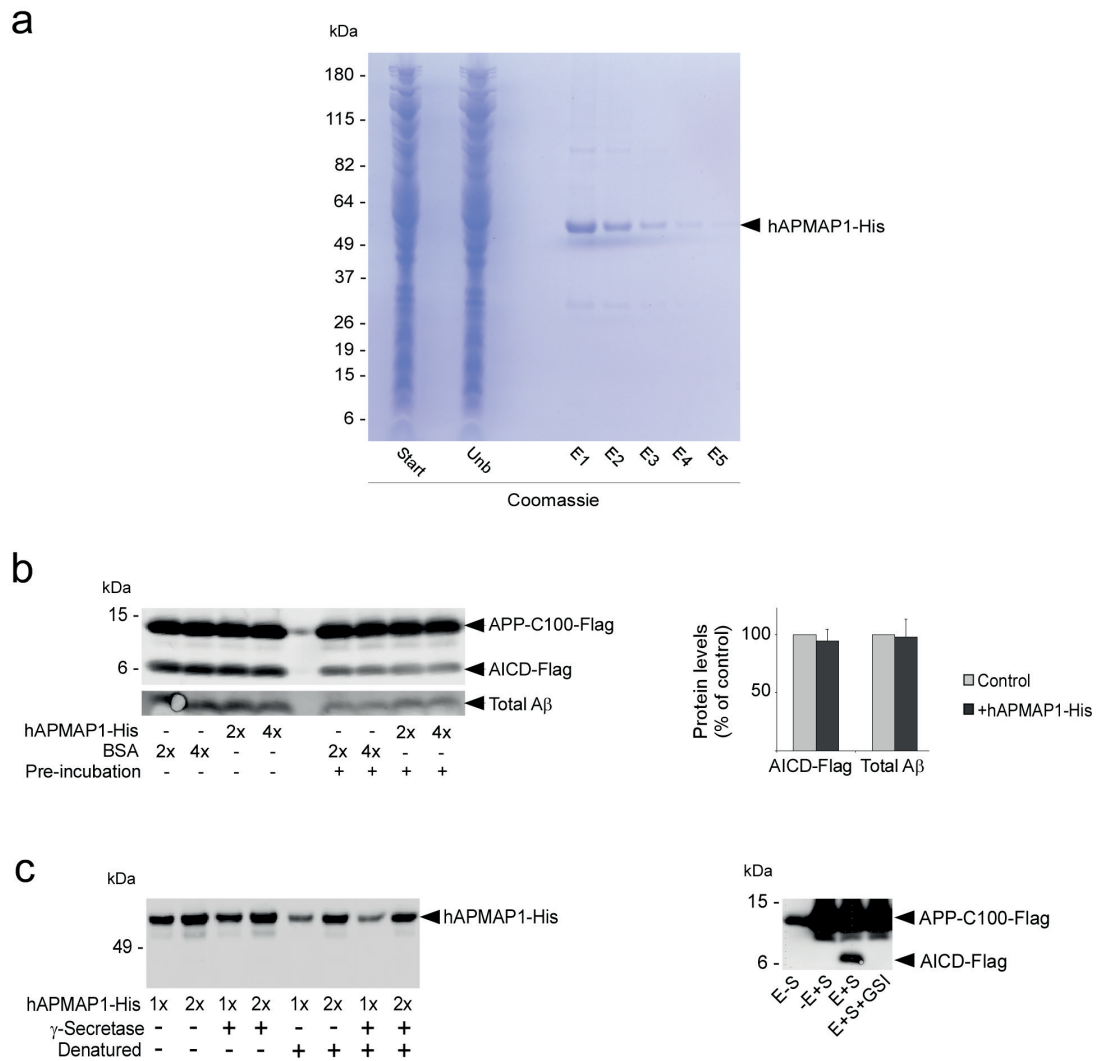
Sup. Fig. 5. APMAP is a negative regulator of A β production. In HEK-APPSwe cells treated with APMAP siRNA, increased levels of APP-CTFs (a) are associated with increased secretion of total A β (A β 1-x), A β 1-40, and A β 1-42, as determined by either ELISA (b) or Western blot on a urea gel (c). The mass spectrometric analysis of secreted A β revealed no changes in the profiles of these peptides (d). (a) Biological triplicates are shown. (b): Student's *t*-test was applied for statistical analyses; mean \pm SD; **P*<0.05; ****P*<0.001; n=4/group. β -Actin served as a protein loading control.

Mosser et al., Supplementary Figure 6 (related to Figure 1)



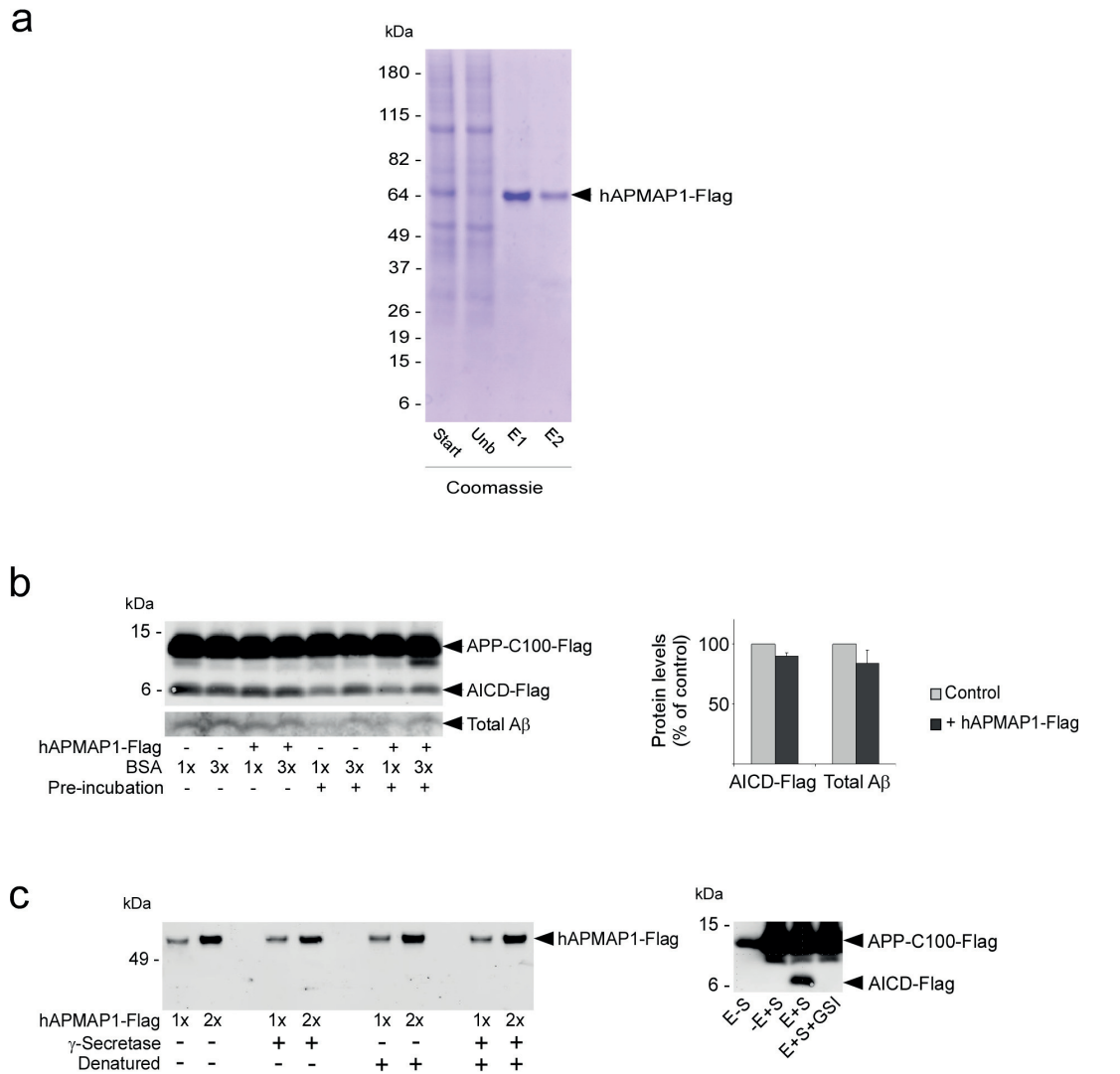
Sup. Fig. 6. The depletion of APMAP in HEK-APPSwe and HeLa cells does not affect the maturation or protein levels of α -, β -, and γ -secretases. Levels of ADAM10, BACE1, and γ -secretase components are shown in HEK-APPSwe cells (a, c, e) or HeLa cells (b, d, f) treated with either negative control scramble siRNA or APMAP siRNA. Biological triplicates are shown. (c-f) Bands revealed by Western blot analysis (upper panels) were quantified by densitometry (lower panels). Student's *t*-test was applied for statistical analyses (mean \pm SD), and revealed no significant differences in ADAM10, BACE1, γ -secretase, and sAPP α/β protein levels.

Mosser et al., Supplementary Figure 7 (related to Figure 1)



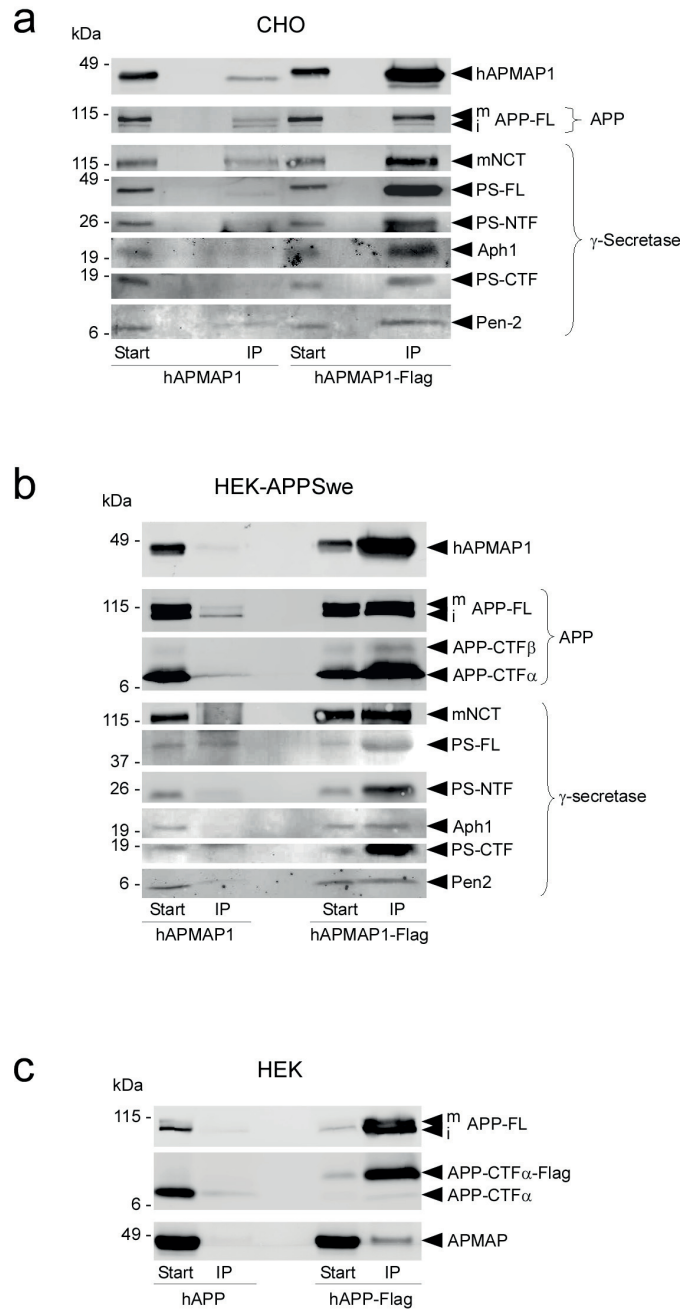
Sup. Fig. 7. APMAP1 purified from *E. coli* is not a substrate for γ -secretase and does not affect the processing of APP-CTF β by purified γ -secretase. a) Affinity purification of human APMAP1-His6 expressed in *E. coli*. The starting material (Start), unbound fraction (Unb), and five elution fractions (E1-5) were resolved by SDS-PAGE on a Tris-glycine gel stained with Coomassie blue. b) Cell-free γ -secretase activity assays with increasing concentrations of purified hAPMAP1-His6 (2x, 4x), pre-incubated (+) or not (-), at 37°C for 60 min before the addition of the substrate APP-C100-Flag. Bands detected by Western blot analysis (left panel) were quantified by densitometry (right panel). Student's *t*-test was applied for statistical analyses (mean \pm SD; n=4/group), and revealed no significant differences in AICD-Flag or total A β levels. c) Purified hAPMAP1-His6 is not a substrate for γ -secretase. Left panel: Increasing concentrations of purified hAPMAP1-His6 (1x, 2x), denatured at 65°C in 0.5% SDS (+) or not (-), were incubated for 4 h at 37°C in the presence (+) or absence (-) of purified γ -secretase and phospholipids (PC+PE). Right panel: APP-C100-Flag served as a positive control for γ -secretase activity. E-S: Enzyme in the absence of substrate; -E+S: Substrate in the absence of enzyme; E+S: Enzyme in the presence of substrate; E+S+GSI: Enzyme in the presence of substrate and 10 μ M γ -secretase inhibitor (GSI) DAPT. Cleavage products were detected with an anti-His6 antibody (hAPMAP1-His6) or anti-Flag antibody (APP-C100-Flag).

Mosser et al., Supplementary Figure 8 (related to Figure 1)



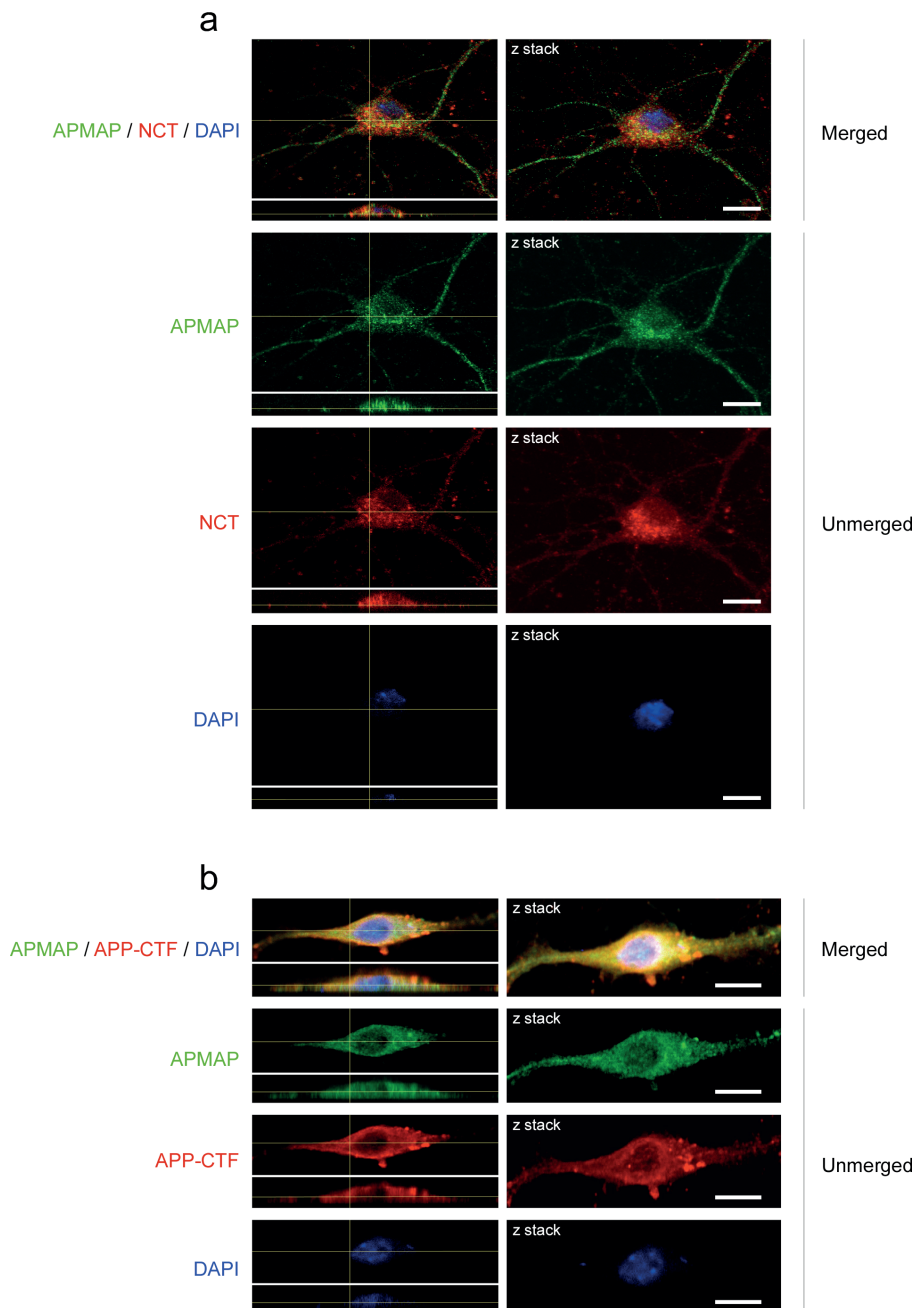
Sup. Fig. 8. APMAP1 purified from CHO cells is not a substrate for γ -secretase and does not affect the processing of APP-CTF β by purified γ -secretase. a) Affinity purification of human APMAP1-Flag stably overexpressed in CHO cells. The starting material (Start), unbound fraction (Unb), and two elution fractions (E1-2) were resolved by SDS-PAGE on a Tris-glycine gel stained with Coomassie blue. b) Cell-free γ -secretase activity assays with increasing concentrations of purified hAPMAP1-Flag (1x, 3x), pre-incubated (+) or not (-) at 37°C for 60 min before addition of the substrate APP-C100-Flag. Bands detected by Western blot analysis (left panel) were quantified by densitometry (right panel). Student's *t*-test was applied for statistical analyses (mean \pm SD; n=4/group), and revealed no significant differences in AICD-Flag or total A β levels. c) Purified hAPMAP1-Flag is not a substrate for γ -secretase. Left panel: Increasing concentrations of purified hAPMAP1-Flag (1x, 2x), denatured at 65°C in 0.5% SDS (+) or not (-), were incubated for 4 h at 37°C in the presence (+) or absence (-) of purified γ -secretase and phospholipids (PC+PE). Right panel: APP-C100-Flag served as a positive control for γ -secretase activity. E-S: Enzyme in the absence of substrate; -E+S: Substrate in the absence of enzyme; E+S: Enzyme in the presence of substrate; E+S+GSI: Enzyme in the presence of substrate and 10 μ M γ -secretase inhibitor (GSI) DAPT. Cleavage products were detected with an anti-Flag antibody.

Mosser et al., Supplementary Figure 9 (related to Figure 2)

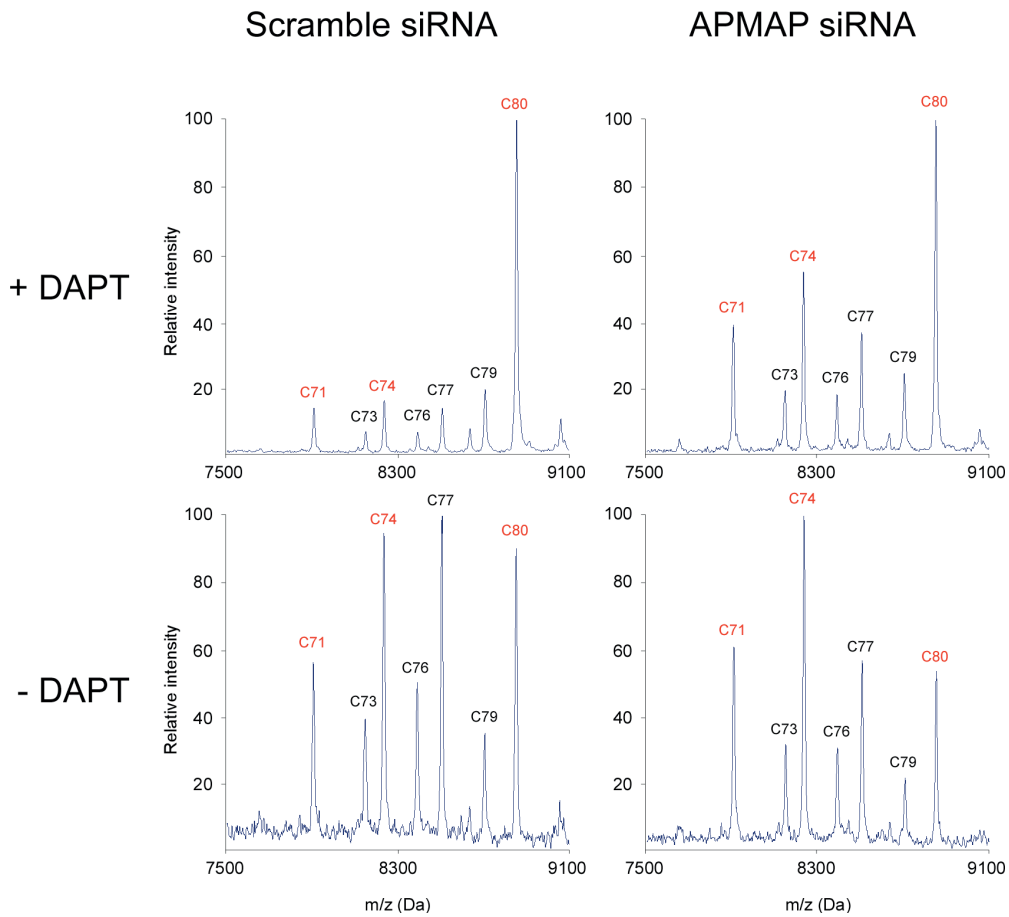


Sup. Fig. 9. APMAP interacts physically with γ -secretase, APP-FL, and APP-CTFs. Co-immunoprecipitation with anti-Flag beads of all γ -secretase components, APP-FL, and APP-CTFs with a Flag-tagged version of hAPMAP1 (hAPMAP1-Flag) overexpressed in CHO cells (a) or HEK-APPSwe cells (b). Untagged APMAP (hAPMAP1) served as a control for the specific co-precipitation. (c) Co-immunoprecipitation of endogenous APMAP with a Flag-tagged version of hAPP (hAPP-Flag) overexpressed in HEK cells. Untagged APP (hAPP) served as a control for the specific co-precipitation.

Mosser et al., Supplementary Figure 10 (related to Figure 2)

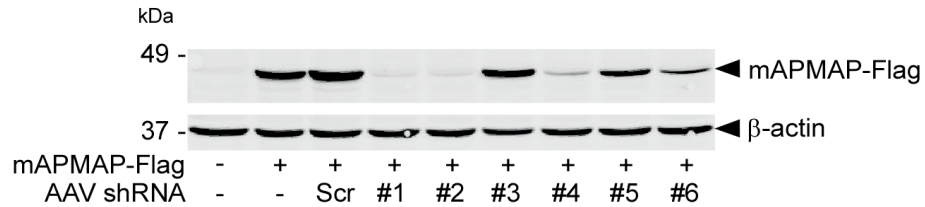


Sup. Fig. 10. Immunohistochemical co-localization of APMAP (green) with the γ -secretase subunit Nicastrin (red, panel a) or APP (red, panel b) in 14 days *in vitro* mouse primary cortical neurons. Scale bar: 10 μ m. Both confocal images (left panels) and Z-stack projections (right panels) are shown with a microscopy objective magnification of 40X. Un-merged images for APMAP, NCT, APP-CTFs, and DAPI are also shown for comparison.



Sup. Fig. 11. APMAP controls the stability of APP-CTFs. MALDI-TOF mass spectrometric analysis of endogenous APP-CTFs immunoprecipitated from HeLa cells treated with scramble or APMAP siRNAs, in the presence (+ DAPT) or absence (- DAPT) of 1 μ M of the γ -secretase inhibitor DAPT. Main changes (increased APP-C71:APP-C80 and APP-C74:APP-C80 ratios) are highlighted in red.

a

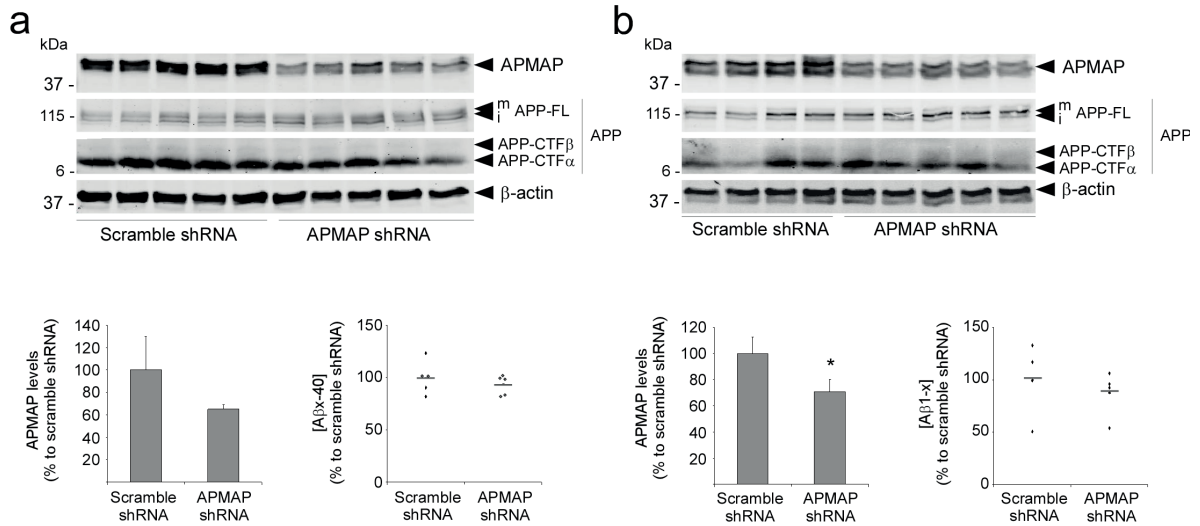


b

shRNA #	shRNA sequence (sense-loop-antisense)
Scamble	5' -CAACAAGATGAAGAGCACCAA-GTGTGCTGTCC-TTGGTGCTCTTCATCTTGTG-3'
1*	5' -TGGACCAGAATCCATAGTAAA-GTGTGCTGTCC-TTACTATGGATTCTGGTCCA-3'
2*	5' -TGAAGTTTGTGCCACGATATA-GTGTGCTGTCC-TATATCGTGCCACAAACTTCA-3'
3	5' -ACCAACTTAGTGGACCAGA-GTGTGCTGTCC-TCTGGTCCACTAAGTTGGT-3'
4	5' -ACGAAGTTGCGGCAAGCAG-GTGTGCTGTCC-CTGCTTGCCGCAACTTCGT-3'
5	5' -TCGAAGTAAATCCTCAGAA-GTGTGCTGTCC-TTCTGAGGATTTACTTCGA-3'
6	5' -GAAAGCCATTTCTCTTTAA-GTGTGCTGTCC-TTAAAGAGAAATGGCTTTC-3'

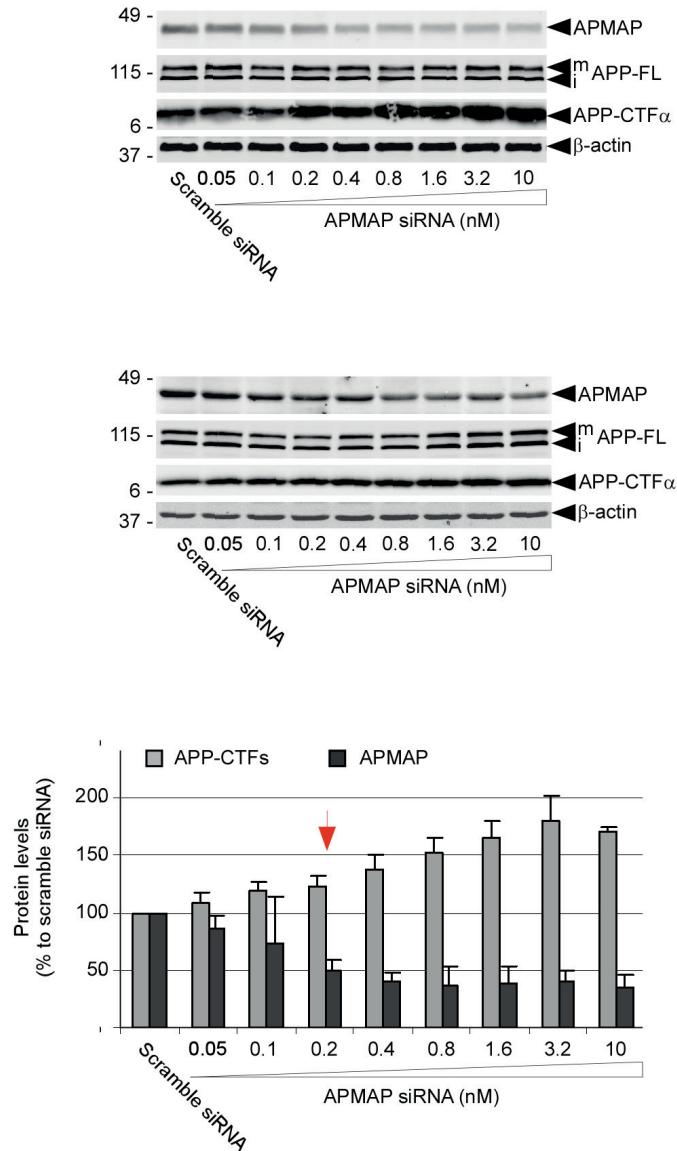
Sup. Fig. 12. Validation of shRNAs targeting mouse APMAP in HEK cells. (a) In this validation experiment, mouse APMAP-Flag was co-expressed in HEK cells (+) with a scramble shRNA (Scr) or with an AAV9-specific vector encoding six different shRNAs targeting mAPMAP (#1-6). After 48 h of culture, cells were collected, and the levels of mAPMAP-Flag were estimated by Western blot analysis with an anti-Flag antibody. (b) Sequences for all shRNAs targeting mAPMAP, tested in HEK cells. The shRNAs # 1 and 2 (labelled with an asterisk) were used for the *in vivo* experiments in WT and APP/PS1 mice, respectively (Fig.4).

Mosser et al., Supplementary Figure 13 (related to Figure 4)



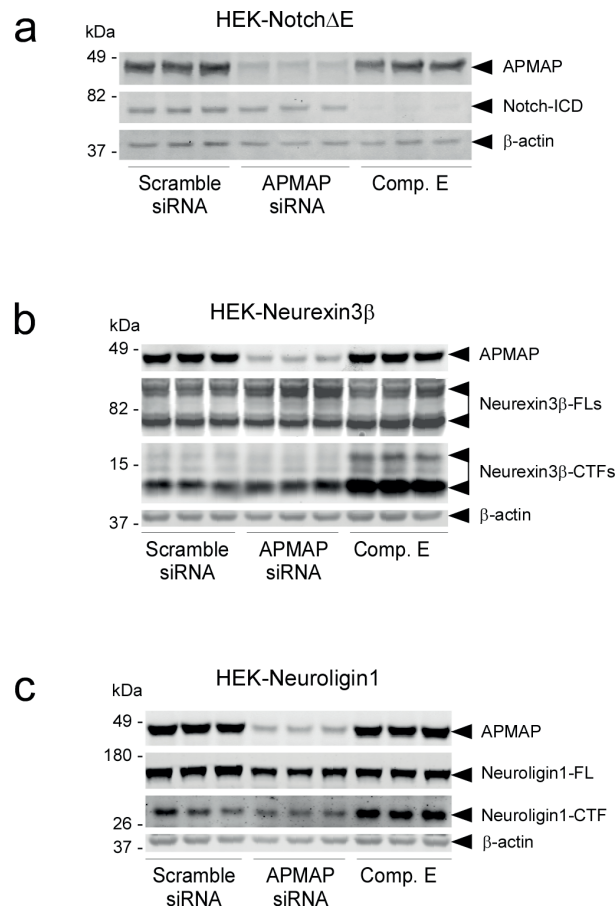
Sup. Fig. 13. APMAP does not affect A β production in wild-type (a) or APP/PS1 transgenic (b) female mice. Five-week-old animals were injected bilaterally in the dorsal hippocampus with AAV9 expressing APMAP shRNA or a scrambled shRNA, together with a GFP reporter. Four weeks post-injection, wild-type (a) or APP/PS1 (b) females displayed a reduction in APMAP expression (mean \pm SD; * P <0.05; n =4-5/group), associated with unchanged A β levels. Student's t -test was applied for statistical analyses. β -Actin served as a protein loading control.

Mosser et al., Supplementary Figure 14 (related to Figure 4)



Sup. Fig. 14. Dose-dependent depletion of APMAP1 and accumulation of APP-CTFs. HEK-APPSwe cells were treated for 3 days with either negative control scramble siRNA or increased concentrations of APMAP siRNA. The two upper panels show Western blots from two independent experiments. The densitometric analysis of APMAP and APP-CTF Western blot bands (lower panel) revealed a critical step for APMAP depletion at ~50% depletion (red arrow), above which small changes in APMAP expression are associated with big changes in APP-CTFs accumulation. β -Actin served as a protein loading control.

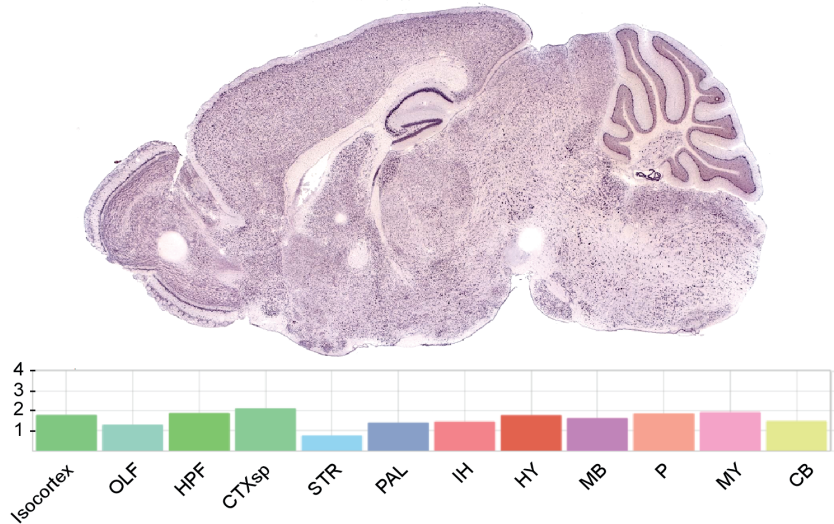
Mosser et al., Supplementary Figure 15 (related to the discussion)



Sup. Fig. 15. APMAP does not affect the processing of the Notch-1 receptor or the synaptic cell adhesion proteins Neurexin3β and Neuroigin1. In contrast to the γ -secretase inhibitor Compound E (Comp. E), APMAP knockdown did not interfere (a) with the processing of the γ -secretase substrate NotchΔE and Notch-intracellular domain (Notch-ICD) production in HEK-N7 stable cells, or (b, c) with the processing of the γ -secretase substrates Neurexin3β and Neuroigin1 transiently expressed in HEK cells. β -Actin served as a protein loading control.

a

Mouse APMAP RNA levels



b

Human APMAP1/2 protein levels

Central nervous system (Brain)			
●	Cerebral cortex	Neuronal cells	High
●	Cerebral cortex	Endothelial cells	Medium
●	Cerebral cortex	Glial cells	Medium
●	Cerebral cortex	Neuropil	Medium
●	Hippocampus	Neuronal cells	High
●	Hippocampus	Glial cells	High
●	Lateral ventricle	Neuronal cells	Medium
●	Lateral ventricle	Glial cells	Medium
●	Cerebellum	Purkinje cells	Medium
●	Cerebellum	Cells in granular layer	High
●	Cerebellum	Cells in molecular layer	High

Level of antibody staining/expression

- High
- Medium
- Low
- Not detected

Sup. Fig. 16. APMAP gene and protein expression patterns in mouse and human brains. (a) APMAP gene expression maps in the mouse brain, according to the Allen Brain Atlas (www.brain-map.org). (b) APMAP protein expression maps in the human brain, according to the Human Protein Atlas (www.proteinatlas.org).

ORIGINAL
ARTICLEIdentification of new Presenilin-1 phosphosites:
implication for γ -secretase activity and A β
production

Alexandre Matz,* Blanka Halamoda-Kenzaoui,* Romain Hamelin,†
Sebastien Mosser,* Jean-René Alattia,* Mitko Dimitrov,* Marc Moniatte†
and Patrick C. Fraering*

*Brain Mind Institute and School of Life Sciences, Ecole Polytechnique Fédérale de Lausanne (EPFL),
Lausanne, Switzerland

†Proteomics Core Facility and School of Life Sciences, Ecole Polytechnique Fédérale de Lausanne
(EPFL), Lausanne, Switzerland

Abstract

An important pathological hallmark of Alzheimer's disease (AD) is the deposition of amyloid-beta (A β) peptides in the brain parenchyma, leading to neuronal death and impaired learning and memory. The protease γ -secretase is responsible for the intramembrane proteolysis of the amyloid- β precursor protein (APP), which leads to the production of the toxic A β peptides. Thus, an attractive therapeutic strategy to treat AD is the modulation of the γ -secretase activity, to reduce A β 42 production. Because phosphorylation of proteins is a post-translational modification known to modulate the activity of many different enzymes, we used electrospray (LC-MS/MS) mass spectrometry to identify new phosphosites on highly purified human γ -secretase. We identified 11

new single or double phosphosites in two well-defined domains of Presenilin-1 (PS1), the catalytic subunit of the γ -secretase complex. Next, mutagenesis and biochemical approaches were used to investigate the role of each phosphosite in the maturation and activity of γ -secretase. Together, our results suggest that the newly identified phosphorylation sites in PS1 do not modulate γ -secretase activity and the production of the Alzheimer's A β peptides. Individual PS1 phosphosites shall probably not be considered therapeutic targets for reducing cerebral A β plaque formation in AD.

Keywords: Alzheimer's disease, amyloid-beta peptides, phosphorylation, phosphosites, Presenilin, γ -secretase.
J. Neurochem. (2015) **133**, 409–421.

Alzheimer's disease (AD) is characterized by two major pathological hallmarks: the extracellular accumulation of amyloid-beta (A β) senile plaques and the intracellular accumulation of Tau proteins leading to the formation of the neurofibrillary tangles. By initiating the toxic amyloid cascade, A β peptides either adopting oligomeric structures or aggregated into senile plaques could be at the origin of the formation of neurofibrillary tangles (Hardy and Allsop 1991). Production of A β is the result of the successive enzymatic processing of the amyloid- β precursor protein (APP) by β - and γ -secretases (Selkoe 1994). However, a deep understanding of the molecular mechanisms regulating the enzymatic activities of these two secretases should allow us to better understand the pathogenesis of AD.

γ -Secretase is a large protease complex composed of four components: Presenilin (PS1 or PS2), Nicastrin (NCT),

Anterior pharynx-defective 1 (Aph-1), and Presenilin enhancer 2 (Pen-2) (De Strooper 2003). The proteolytic activity of this secretase is critical for the processing of many

Received August 29, 2014; revised manuscript received November 2, 2014; accepted November 10, 2014.

Address correspondence and reprint requests to Patrick C. Fraering, Brain Mind Institute and School of Life Sciences, Ecole Polytechnique Fédérale de Lausanne (EPFL), CH1015 Lausanne, Switzerland. E-mail: patrick.fraering@epfl.ch

Abbreviations used: AD, Alzheimer's disease; AICD, APP intracellular domain; Aph-1, Anterior pharynx-defective 1; APP, amyloid- β precursor protein; A β , amyloid-beta peptides; CTF, carboxyl-terminal fragment; FL, full length; GSK3 β , glycogen synthase kinase 3 β ; HL, hydrophilic loop; i, immature; m, mature; MS, mass spectrometry; NCT, Nicastrin; NFT, neurofibrillary tangles; NICD, Notch intracellular domain; NTF, amino-terminal fragment; Pen-2, Presenilin enhancer 2; PS, Presenilin; TMD, transmembrane domain; WT, wild type.

type-I integral membrane proteins including APP and the Notch receptor (Steiner *et al.* 1999; Kimberly *et al.* 2000). Importantly, early-onset familial Alzheimer's disease (FAD) has been largely attributed to mutations in both PS1 (Rogaev *et al.* 1997) or PS2 (Rogaev *et al.* 1995). The vast majority of FAD mutations in Presenilins have been identified in PS1, with around 200 different missense mutations in PS1, but only 30 in PS2 (<http://www.alzforum.org/mutations>). Also, PS1 mutations account for about half of all FAD cases (Schellenberg 1995). Most of these mutations increase the production throughout life of A β 42, the hydrophobic and main component of A β senile plaques (Iwatsubo *et al.* 1994). Several of these mutations also increase the A β 42 to A β 40 ratio (from 0.1 to 0.2 in healthy subjects up to 1 in AD patients), either by increasing A β 42 or by decreasing A β 40 production, or a combination of both (Bentahir *et al.* 2006; Cacquevel *et al.* 2012).

PS1 is an integral membrane protein with nine transmembrane domains (TMD) (Laudon *et al.* 2005); it forms the catalytic subunit of γ -secretase, in which two aspartate residues (Asp²⁵⁷ and Asp³⁸⁵ in human PS1) located in TMD6 and TMD7 are crucial for the catalytic activity of the enzyme (Wolfe *et al.* 1999). In the secretory pathway, PS1 undergoes endoproteolysis, generating stable N-terminal and C-terminal fragments (PS1-NTF and PS1-CTF, respectively). The three other components (NCT, Aph-1, and Pen-2) act as scaffold proteins for the assembly and activation of the γ -secretase protease complex (LaVoie *et al.* 2003; Takasugi *et al.* 2003; Fraering 2007). γ -Secretase is present in multiple cell compartments including the Golgi (Baulac *et al.* 2003), endosomes (Vetrivel *et al.* 2004), lysosomes (Pasternak *et al.* 2003) and plasma membranes (Ray *et al.* 1999).

Interestingly, PS1 is a protein that can be phosphorylated at different sites, by different protein kinases. These include glycogen synthase kinase 3 β (GSK3 β), which phosphorylates PS1 on Ser³⁵³ and Ser³⁵⁷ (Kirschenbaum *et al.* 2001), cyclin-dependent kinase 5/p35 (cdk5/p35) on Thr³⁵⁴ (Lau *et al.* 2002), protein kinase C on Ser³⁴⁶ (Fluhrer *et al.* 2004), and c-Jun N-terminal kinase on the Ser³¹⁹Thr³²⁰ motif (Kuo *et al.* 2008). Many different post-translational modifications of proteins, including phosphorylation and palmitoylation, have been reported to modulate the biological activity of enzymes (Patterson 2002). However, the correlation between PS1 phosphorylation and A β production was examined only by very few groups. Some results have shown that the substitution of Ser³⁵³ and Ser³⁵⁷ residues greatly reduces the ability of PS1 to associate with β -catenin (an intracellular signal

transducer in the Wnt signaling pathway) without having an effect on A β production (Kirschenbaum *et al.* 2001). In contrast, results from another group indicated an increase in the A β 42 : A β 40 ratio in cells treated with LiCl, an inhibitor of GSK3 β , which phosphorylates PS1 on Ser³⁵³ and Ser³⁵⁷ (Maesako *et al.* 2011). Finally, the deletion of amino acid residues 304–371 in the PS1 hydrophilic loop, which is located between TMD6 and TMD7 of PS1 and which harbors the above-described PS1 phosphorylation sites, did not impact the endoproteolysis of PS1 or A β production (Saura *et al.* 2000).

With these opposite statements, we decided to take advantage of our highly purified γ -secretase preparation to identify new phosphorylation sites in PS1, and to analyze their impact on γ -secretase assembly and A β production. Using electrospray (LC-MS/MS) mass spectrometry, we have identified a total of 15 PS1 phosphorylated peptides, including 11 new single or double phosphosites. These new phosphosites were mainly located in the PS1 hydrophilic loop between TMD6 and TMD7, with the others being found in the hydrophilic N-terminal domain located at the N-terminus of the TMD1. Because the new PS1 phosphosites can potentially be associated with late or early-onset non-familial AD, or with other diseases implicating receptor processing by γ -secretase (De Strooper *et al.* 1999; Uemura *et al.* 2006; Bot *et al.* 2011), we have analyzed their effects on γ -secretase maturation and activity, and A β production.

Methods

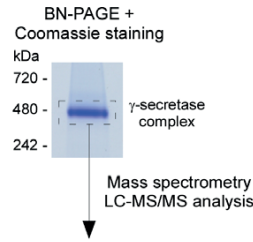
γ -Secretase purification and mass spectrometry analysis

The γ -secretase complex purified as previously described (Alattia *et al.* 2013) was first run on a NativePAGE™ Novex® 4-16% Bis-Tris gel for blue native-PAGE analysis (Invitrogen, Carlsbad, CA, USA). Next, gel band corresponding to the complex (containing PS1) was visualized by Coomassie staining and cut into small pieces. Proteins were reduced, alkylated, and subjected to in-gel digestion with either Glu-C or Trypsin. Briefly, gel pieces were destained, desiccated by incubating them twice in 200 μ L of ammonium bicarbonate 50 mM, 50% ethanol during 20 min and dried with vacuum concentrator. Samples were then incubated overnight at 37°C with either Glu-C or Trypsin (12.5 ng/ μ L). After peptide extraction from gel slices, phosphopeptide enrichments were performed on homemade titania tips (Thingholm and Larsen 2009). Titania tips were first equilibrated with 0.75% trifluoroacetic acid (TFA), 60% acetonitrile (ACN), lactic acid (300 mg/mL) (solution A) prior to loading peptide samples resuspended in 20 μ L of the very same solution A. Titania tips were then successively washed

Fig. 1 Identification of new human Presenilin-1/ γ -secretase phosphosites. (a) The high molecular weight human γ -secretase complex resolved by blue native polyacrylamide gel electrophoresis (BN-PAGE) and stained with Coomassie Brilliant Blue (upper panel) was excised and used for the analysis by electrospray (LC-MS/MS) mass spectrometry and the identification of Presenilin-1 phosphorylated peptides (PS1, lower panel). Phosphosites are highlighted in red. (b)

Representative tandem MS spectrum confirming the identification of the new phosphorylation site at position Ser³⁶⁶ in the sequence of human PS1. All spectra of newly identified phosphosites are in Figure S1. (c) List (left panel) and schematic positioning (right panel) of the PS1 phosphosites identified in this study. The newly identified phosphosites are highlighted in red, while previously reported phosphosites are in blue.

(a)

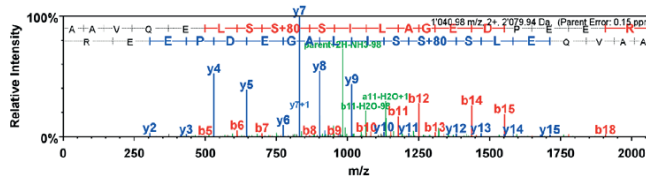


PS1-Sequences	SEQUEST XCorr	Mascot Ion score	Modifications	Observed	Charge	Delta AMU	Delta PPM	Start	Stop	Modified residues
DNHLSNTVRSQNDNRE	1.18	25.24	Phospho (+80)	989.9224	2	0.0013	0.6542	19	34	S28
QVVEQDEEDELTLK	4.63	40.84	Phospho (+80)	671.6238	3	-0.0019	-0.9404	61	76	T74
AQRVRVSKNSKYNAE	2.37	-	Phospho (+80), Phospho (+80)	604.2719	3	0.0014	0.7674	305	318	S310,S313
VSKNSKYNAESTER	3.45	28.68	Phospho (+80)	846.8834	2	0.0007	0.3955	309	322	S313
YNAESTER	2.56	29.07	Phospho (+80)	525.2003	2	-0.0001	-0.1137	315	322	S319
YNAESTERESQDTVAENDDGGFSEEWEAQR	6.59	55.66	Phospho (+80)	1177.1367	3	0.0019	0.5456	315	344	S324
ESQDTVAENDDGGFSEEWEAQR	4.45	42.03	Phospho (+80)	1289.9954	2	-0.0009	-0.3612	323	344	S337
SHLGPVRSKTPESRAAVQE	2.31	-	Phospho (+80)	680.3198	3	-0.0006	-0.2737	346	363	S353
SHLGPVRSKTPESRAAVQE	2.98	-	Phospho (+80)	649.2881	2	0.0003	0.2449	346	356	T354
DSHLGPHRSTPESR	-	18.08	Phospho (+80)	828.3690	2	0.0021	1.258	345	358	S357
AAVQELSSSILAGEDPEER	5.48	65.39	Phospho (+80)	1040.9778	2	0.0047	2.264	359	377	S365
AAVQELSSSILAGEDPEER	4.34	51.95	Phospho (+80)	1040.9756	2	0.0003	0.1527	359	377	S366
AAVQELSSSILAGEDPEER	4.77	60.15	Phospho (+80)	1040.9760	2	0.0011	0.5047	359	377	S367
AAVQELSSSILAGEDPEER	5.63	35.64	Phospho (+80), Phospho (+80)	1080.9595	2	0.0018	0.8143	359	377	S365,S367
AAVQELSSSILAGEDPEER	5.16	33.67	Phospho (+80), Phospho (+80)	720.9745	3	-0.0010	-0.4629	359	377	S366,S367

(b)

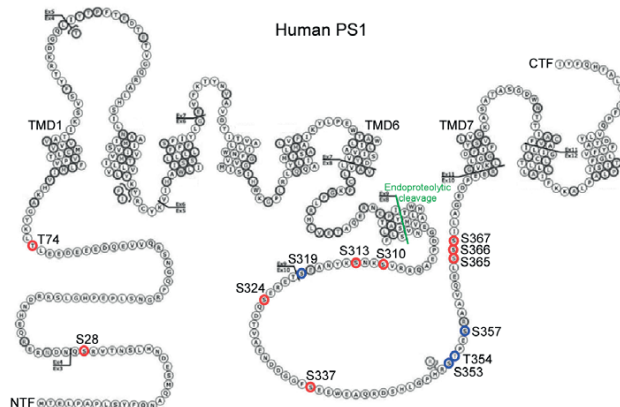
Serine 366

B	B Ions	B+2H	B+NH3	B-H2O	AA	Y Ions	Y+2H	Y+NH3	Y-H2O	Y
1	72.0				A	2'080.9	1'041.0	2'063.9	2'062.9	19
2	143.1				A	2'069.9	1'005.5	1'992.9	1'991.9	18
3	242.1				V	1'938.9	969.0	1'921.8	1'920.9	17
4	370.2		353.2		Q	1'839.8	920.4	1'822.8	1'821.8	16
5	499.3		482.2	481.2	E	1'711.7	856.4	1'694.7	1'693.7	15
6	612.3	306.7	595.3	584.3	L	1'582.7	791.9	1'565.7	1'564.7	14
7	699.4	350.2	682.3	681.4	S	1'469.6	735.3	1'452.6	1'451.6	13
8	866.4	433.7	849.3	848.4	S+80	1'382.6	691.8	1'365.6	1'364.6	12
9	953.4	477.2	936.4	935.4	S	1'215.6	608.3	1'198.6	1'197.6	11
10	1'066.5	533.7	1'049.5	1'048.5	I	1'128.6	564.8	1'111.5	1'110.5	10
11	1'179.6	590.3	1'162.5	1'161.6	L	1'015.5	508.2	998.4	997.4	9
12	1'250.6	625.8	1'233.6	1'232.6	A	902.4	451.7	885.4	884.4	8
13	1'307.6	654.3	1'290.6	1'289.6	G	831.3	416.2	814.3	813.3	7
14	1'436.7	718.8	1'419.6	1'418.7	E	774.3	387.7	757.3	756.3	6
15	1'551.7	776.4	1'534.7	1'533.7	D	645.3		628.3	627.3	5
16	1'648.7	824.9	1'631.7	1'630.7	P	530.3		513.2	512.2	4
17	1'777.8	889.4	1'760.8	1'759.8	E	433.2		416.2	415.2	3
18	1'906.8	953.9	1'889.8	1'888.8	E	384.2		287.1	286.2	2
19	2'080.9	1'041.0	2'063.9	2'062.9	R	175.1		158.1		1



(c)

Residues	Reference
S28	this study
T74	this study
S310,S313	this study
S313	this study
S319	Kuo et al. (2008)
S324	this study
S337	this study
S353	Kirschenbaum et al. (2001)
T354	Lau et al. (2002)
S357	Kirschenbaum et al. (2001)
S365	this study
S366	this study
S367	this study
S365,S367	this study
S366,S367	this study



with solution A and a 0.1% TFA, 80% ACN solution. A two-step elution was performed once with 0.5% ammonium hydroxide followed by once with 5% piperidine. Eluted fractions were immediately acidified with formic acid (FA) and dried under a vacuum concentrator. For LC-MS/MS analysis, peptides were resuspended in 2% ACN, 0.1% FA and separated by reversed-phase chromatography on a Dionex Ultimate 3000 RSLC nano-UPLC system connected in-line with an Orbitrap Elite (Thermo Fischer Scientific, Waltham, MA, USA). The instrument was operated in an information-dependent mode where peptide masses were selected for collision-induced dissociation to generate tandem mass spectra. Database search was performed using Mascot 2.3 (Matrix Science, Boston, MA, USA) and SEQUEST in Proteome Discoverer v.1.3 against a human database (UniProt release 2013_01; 87613 sequences). All searches were performed with Trypsin or Glu-C cleavage specificity, up to two missed cleavages allowed and ion mass tolerance of 10 ppm for the precursor and 0.5 Da for the fragments. Carbamidomethylation was set as a fixed modification, whereas oxidation (M), acetylation (Protein N-term), phosphorylation (STY) were considered as variable modifications. Data were further processed and inspected in the Scaffold 3 software (Proteome Software, Portland, OR, USA). Peptide-spectrum matches with Mascot score > 18 and/or SEQUEST score > 2 were considered as correctly assigned. Phosphorylation site localization was confirmed by manual inspection of the spectra. Tandem MS spectra of phosphorylated peptides identified in the γ -secretase catalytic subunit PS1 are shown in Figure S1.

Plasmid constructs

Human cDNA of wild-type (WT) PS1 was a gift from D. Selkoe. WT PS1 cDNA with a Flag-tag at the N-terminus was subcloned into the mammalian expression vector pcDNA3 (Invitrogen) and the PCR quick-change site-directed mutagenesis kit (Stratagene, La Jolla, CA, USA) was used to generate all PS1 Serine or Threonine to Alanine point mutations tested in this study (see Figure S2).

Cell culture and transfection

Human embryonic kidney 293T (HEK293T) and HeLa cells were cultured as previously described (Bot *et al.* 2011) and transfected with 10 μ g of DNA (plasmids with PS1 WT or mutants) using the calcium phosphate precipitation method and Lipofectamine 2000 (Invitrogen), respectively.

γ -Secretase immunoprecipitation and activity assays

HEK and HeLa cells transfected with PS1 phosphosite mutants were lysed in 1% 3-[(3-Cholamidopropyl)dimethylammonio]-2-hydroxy-1-propanesulfonate (CHAPSO)/HEPES buffer containing protease inhibitors (Roche Applied Sciences, Basel, Switzerland). M2 anti-Flag beads pre-equilibrated with 1% CHAPSO/HEPES buffer were added to the crude protein extract, incubated overnight at 4°C on a wheel, washed multiple times, and resuspended in 47.5 μ L of 0.2% CHAPSO/HEPES buffer containing lipids (5 μ L of phosphatidylcholine [0.01 mg/ μ L] and 2.5 μ L of phosphatidylethanolamine [0.005 mg/ μ L]) and substrate (1 μ M of APP-C100F or Notch-N100F) for on-beads activity tests. The mix was incubated 4 h at 37°C and recovered for A β analysis by ELISA, or for western blot analysis of the cleavage products A β , APP intracellular domain (AICD), and Notch intracellular domain (NICD).

SDS-PAGE and western blot analysis

Cell lysates were resolved on a NuPAGE[®] Novex[®] 4–12% Bis-Tris gel (Invitrogen) or 12% Tris-Glycine sodium dodecyl sulfate-polyacrylamide gel electrophoresis and, respectively, transferred onto a polyvinylidene difluoride membrane or a nitrocellulose membrane. Membranes were incubated with blocking buffer (Invitrogen) and probed with the following primary antibodies: anti-PS1-NTF (Ab10281; Abcam, Cambridge, UK or MAB1563, Chemicon, Temecula, CA, USA), anti-PS1-CTF (MAB5232; Chemicon), anti-NCT (N1660; Sigma-Aldrich, St Louis, MO, USA or NCT164; BD Biosciences, Mississauga, ON, USA), anti-Pen-2 (UD-1, a gift from H. Karlstrom), anti-Aph-1 (O2C2, Covance, Berkeley, CA, USA), anti-APP (CT15; Sigma-Aldrich), anti-A β (6E10; Covance), and anti-Flag (M2; Sigma-Aldrich) for detection of PS1-NTF + PS1-FL, PS1-CTF, NCT, Pen-2, Aph-1, APP-FL + APP-CTF, A β , or Flag-tagged proteins, respectively. Membranes were incubated with the secondary antibodies (anti-mouse, rabbit, or rat IgGs) conjugated to Alexa 680 (Invitrogen) and visualized with the Odyssey infrared imaging system (LICOR, Lincoln, NE, USA).

γ -Secretase limited trypsin digestion

Highly purified γ -secretase (Dimitrov *et al.* 2013) was incubated overnight on ice with trypsin (Thermo Fischer Scientific), with a γ -secretase to trypsin molecular ratio of 1 : 5.

A β analysis

ELISA

Samples from γ -secretase activity assays were assayed using ELISA kits for human A β 1-40 and A β 1-42 (Invitrogen), as previously described (Dimitrov *et al.* 2013).

Immunoprecipitation – mass spectrometry

A β peptides from γ -secretase activity assays were immunoprecipitated overnight using the monoclonal anti-A β antibody 4G8 and protein G-coupled agarose (Roche Applied Sciences) and analyzed by matrix-assisted laser desorption/ionization-time-of-flight (MALDI-TOF) mass spectrometry as previously described (Dimitrov *et al.* 2013).

Statistical analyses

All values are presented as the mean \pm SE. Statistical analyses were performed using an unpaired Student's *t*-test. **p* < 0.05; ***p* < 0.01. *n* = X indicates X-independent experiments.

Results

Identification of PS1 phosphosites by mass spectrometry

To identify human γ -secretase phosphosites, active protease complex purified from Chinese hamster ovary (CHO) cells over-expressing the four subunits of the protease complex (Alattia *et al.* 2013) was resolved by blue-native gel electrophoresis (Fig. 1a, upper panel), and the γ -secretase complex band was excised for protein content analysis by electrospray LC-MS/MS mass spectrometry.

This approach led us to the identification of 15 PS1 phosphorylated peptides, corresponding to 12 single and three

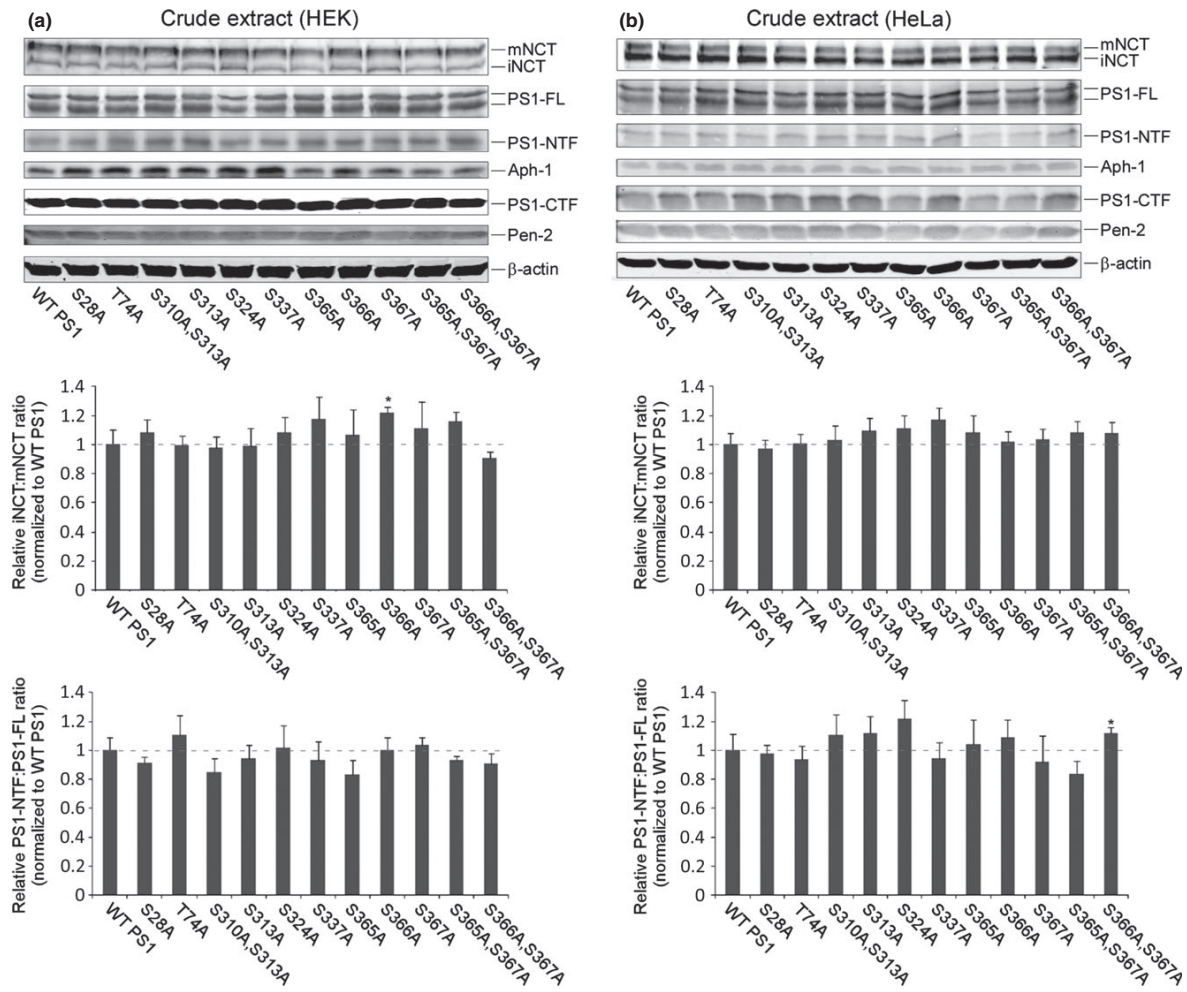


Fig. 2 Maturation in HEK and HeLa cells of γ -secretase complexes with mutated PS1 phosphosites. HEK (a and c) or HeLa (b and d) cells were transiently transfected with Flag-tagged individual PS1 phosphosite mutants. 48 h post-transfection, whole cell protein lysates were prepared for western blot analysis and detection of mature (m) and immature (i) γ -secretase subunits (a and b, upper panels). In parallel, γ -secretase complexes containing Flag-tagged mutated PS1 individual

phosphosites were immunoprecipitated (IP) with an anti-Flag affinity resin, and γ -secretase subunits were revealed by western blot analysis (c and d, upper panels). Densitometric analysis was performed on western blots generated from four different experiments to estimate the iNCT : mNCT ratio (a–d, middle panels) and the PS1-NTF : PS1-FL ratio (a–d, lower panels). Data are means \pm SE with $n = 4$, and normalized to wild-type (WT) PS1. * $p < 0.05$, ** $p < 0.01$.

double phosphosites in PS1 (summarized in Fig. 1a, lower panel). No phosphorylated peptides have been identified in NCT, Aph-1, or Pen-2. Representative tandem MS spectra confirming the localization of all phosphorylation sites are shown in Fig. 1(b) and Figure S1. Among the 15 PS1 phosphosites identified, 11 (eight single and three double) are new (Fig. 1c, red), whereas four have previously been reported (Fig. 1c, blue). Interestingly, almost all phosphosites (13 of 15) are present in the biggest hydrophilic loop of PS1, located between TMD6 and TMD7 (Fig. 1c). This loop (residues 263–374) contains the site of PS1 endoproteolysis,

which is necessary for the formation of PS1-NTF and PS1-CTF, and consequently for the full maturation and activation of γ -secretase. The two additional phosphosites are found in the N-terminal hydrophilic domain, located at the N-terminus of the TMD1.

PS1 phosphosite mutants do not affect the maturation of γ -secretase

To investigate whether absence of phosphorylation of the newly identified phosphosites in PS1 can affect the assembly and maturation of γ -secretase, all newly identified PS1

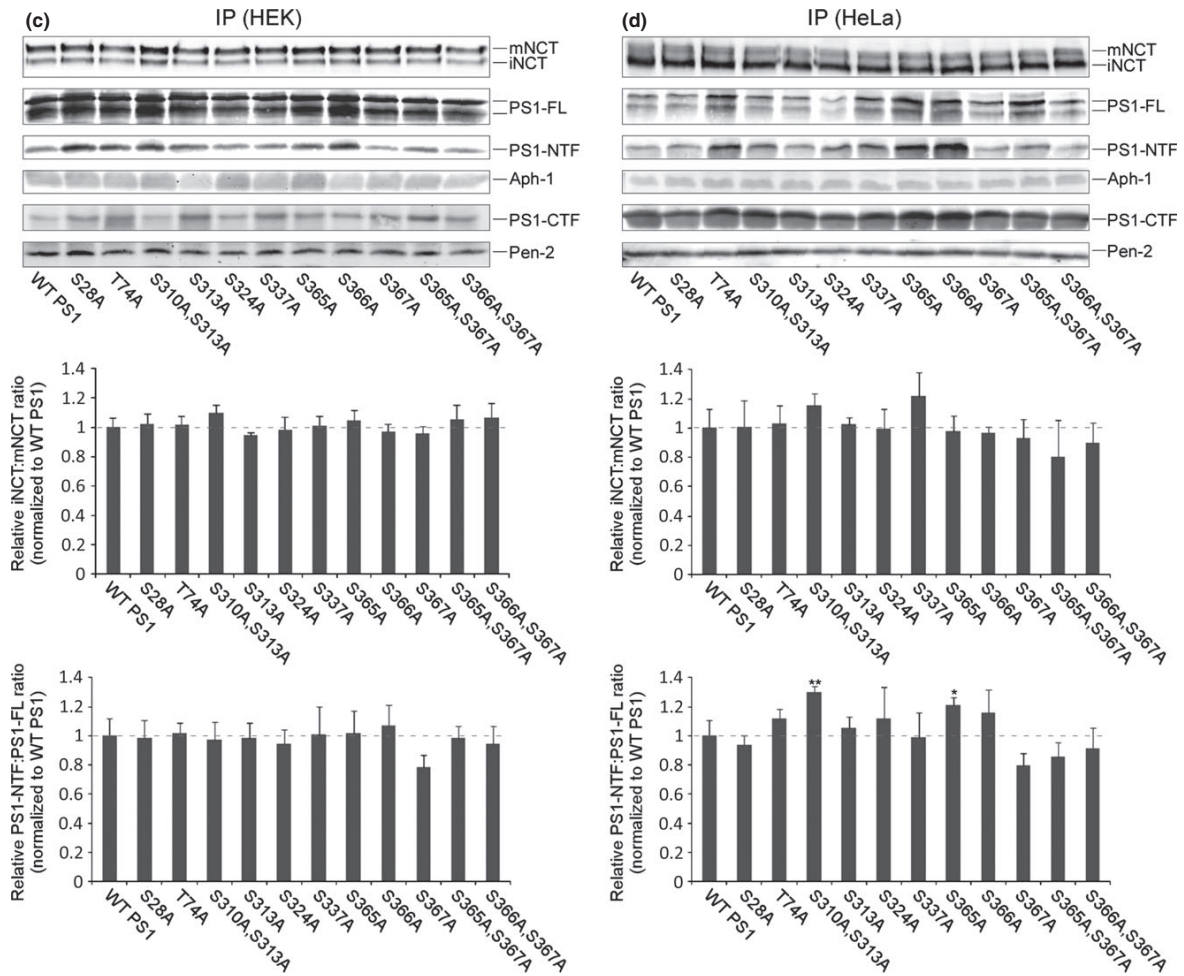


Fig. 2 Continued.

phosphosites were mutated by substituting serine or threonine residues with an alanine (Figure S2). Next, HEK and HeLa cells were transiently transfected for 2 days with plasmids encoding for Flag-tagged WT PS1 or Flag-tagged PS1 phosphosite mutants, and total protein extracts were analyzed for their content in γ -secretase subunits (Fig. 2a and b, upper panels). As shown in Fig. 2, a densitometric approach was next used to estimate the ratio between PS1-NTF and the full-length non-endoproteolyzed PS1 (PS1-FL), and the ratio between immature and mature NCT (iNCT and mNCT, respectively). These ratios are indeed relevant indicators for the maturation of the complex as the highly regulated endoproteolytic processing of PS1 (to generate PS1-NTF and PS1-CTF fragments) is associated with the biological activity of γ -secretase (reviewed in Fraering 2007). Also, NCT is a type-I membrane protein that is associated with active γ -secretase, in the early endosomes and the plasma membrane, in a 'mature' fully N-linked

glycosylated form (Kimberly *et al.* 2002). In contrast, the immature partially glycosylated form of NCT, a post-translational modification that occurs after entering the endoplasmic reticulum and the Golgi apparatus, is associated with inactive γ -secretase. As summarized in Fig. 2(a) and (b), the analysis by western blot of both HEK and HeLa whole cell extracts revealed only minor, non-significant variations in the maturation of γ -secretase. It has to be noted that the few results statistically significant in one specific cell line are not reproducible in the two cell lines tested.

Next, γ -secretase complexes with exogenous PS1 phosphosite mutants were isolated by immunoprecipitation of Flag-tagged mutated PS1, with M2 anti-Flag agarose beads. This procedure allowed us to distinguish between γ -secretase complexes containing endogenous PS1 and those made of exogenous PS1 with different mutated phosphosites (Fig. 2c, d and Figure S3). Similar to the results observed with the whole cell extracts (Fig. 2a and b), the analysis of γ -secretase

immunoprecipitated from HEK (Fig. 2c and Figure S4a) and HeLa (Fig. 2d and Figure S4b) cells revealed only minor but non-significant variations in the PS1-NTF : PS1-FL and the iNCT : mNCT ratios. Again, the very few results significant in one specific cell line are not reproducible in the two cell lines tested.

Altogether, our results indicate that the absence of individual phosphorylation of the newly identified phosphosites does not affect the maturation of γ -secretase, when compared to WT PS1. It further suggests that phosphorylation of the individual phosphosites is not required for the assembly and maturation of the γ -secretase complex. The maturation of the complex being not disturbed, we next decided to investigate whether the activity of γ -secretase can be modified by mutagenesis of the newly identified phosphosites.

PS1 phosphosite mutants do not modulate the activity of γ -secretase

Because our results have shown that PS1 phosphosite mutants have a maturation pattern similar to that observed for the WT PS1 (Fig. 2), we next verified if these mutants can affect the enzymatic activity of the protease complex. To do so, HEK and HeLa cells were first transiently transfected for 2 days with plasmids encoding for Flag-tagged WT PS1 or Flag-tagged PS1 phosphosite mutants. Then, γ -secretase complexes with mutated PS1 phosphosites were immunoprecipitated with anti-Flag M2 beads, and used to perform on-beads γ -secretase activity assays with the APP-based C100F substrate (APP-C100F) or the Notch-based N100F substrate (N100F), and lipids (phosphatidylcholine and phosphatidylethanolamine). The cleavage products AICD-Flag, A β peptides, and NICD-Flag were analyzed by western blot (Fig. 3a and b) and the ratios AICD : PS1-NTF, A β : PS1-NTF, and NICD : PS1-NTF were estimated by densitometry for each individual phosphosite mutant because it reflects directly total activity of γ -secretase (increased PS1-NTF/mature γ -secretase is associated with increased AICD/NICD production). Control experiments with HEK cells treated with the γ -secretase inhibitor Compound-E (Seiffert *et al.* 2000), the γ -secretase modulator GSM-1 (Qin *et al.* 2011; Chavez-Gutierrez *et al.* 2012), or HEK cells over-expressing Pen-2 were performed to show that the above-described assay can detect both inhibition or enhancement of γ -secretase activity (Figure S5). The specific activity of γ -secretase and the specificity of APP-C99 processing at the γ -cleavage site within the TMD of APP were verified by estimating the A β 42 : A β 40 ratio, using A β 1-40- and A β 1-42-specific ELISAs (Fig. 3c and d).

As shown in Fig. 3(a–d), only minor but non-significant variations in the AICD : PS1-NTF, A β : PS1-NTF, NICD : PS1-NTF, and A β 42 : A β 40 ratios were observed, suggesting an activity for γ -secretase complexes with individual mutated phosphosites similar to that observed for γ -secretase

with WT PS1. Further supporting the latter, endogenous levels of both APP-FL and APP-CTF remained unchanged in both HEK and HeLa cells transfected with the PS1 phosphosite mutants (Figure S6), and Notch-ICD production remained unchanged in a HEK cell line stably expressing Notch1 Δ E and transiently transfected with the PS1 phosphosite mutants (Figure S7).

To better recapitulate the neuronal genetic repertoire, the effect of PS1 phosphosite mutants on γ -secretase activity was further tested in SH-SY5Y neuroblastoma cells. As shown in Figure S8, we found that individual mutations of the newly identified phosphosites do not affect APP processing.

Altogether, our data indicate that none of the PS1 phosphosite mutants, when tested individually, affect the activity of γ -secretase when compared to WT PS1. It further suggests that phosphorylation of the individual phosphosites is not a prerequisite for generating γ -secretase activity.

The γ -secretase substrate cleavage specificity is not affected by mutated PS1 phosphosites

Total γ -secretase activity can be associated with changes in the specificity of substrate cleavage. For example, last generation γ -secretase modulators (in opposition to γ -secretase inhibitors) do not affect the production of total AICDs and A β peptides (as estimated by western blot analysis and ELISA), but alter the A β profile, by reducing A β 42 production and increasing A β 38 production (Dimitrov *et al.* 2013). Because of that observation, we investigated whether our newly identified PS1 phosphosites can affect the specificity of APP-C99 cleavage. To do so, MALDI-TOF mass spectrometry was used to analyze the A β cleavage products generated in our cell-free activity assays performed with semi-purified γ -secretase complexes bound to the M2 anti-Flag affinity resin, and containing WT PS1 or individually mutated PS1 phosphosites. As shown in Fig. 4(a), none of the phosphosites analyzed individually did affect the γ -secretase cleavage specificity, when compared to that observed for γ -secretase with WT PS1. In contrast, the known γ -secretase inhibitor Compound-E (Seiffert *et al.* 2000) led to the complete inhibition of total A β production, whereas reduced A β 42 production was associated with increased A β 38 production in the presence of the potent γ -secretase modulator GSM-1 (Qin *et al.* 2011; Chavez-Gutierrez *et al.* 2012) (Fig. 4b).

Proteolytic removal of the PS1 phosphorylated domains does not affect γ -secretase activity and A β production

To support our findings that the phosphorylation status of PS1 at the identified sites does not affect the activity of γ -secretase, we subjected the native purified γ -secretase complex to limited trypsin digestion, to proteolytically remove the two phosphorylation domains in PS1. As shown in Fig. 5(a), limited trypsin digestion of γ -secretase removed both the hydrophilic loop of PS1 located between

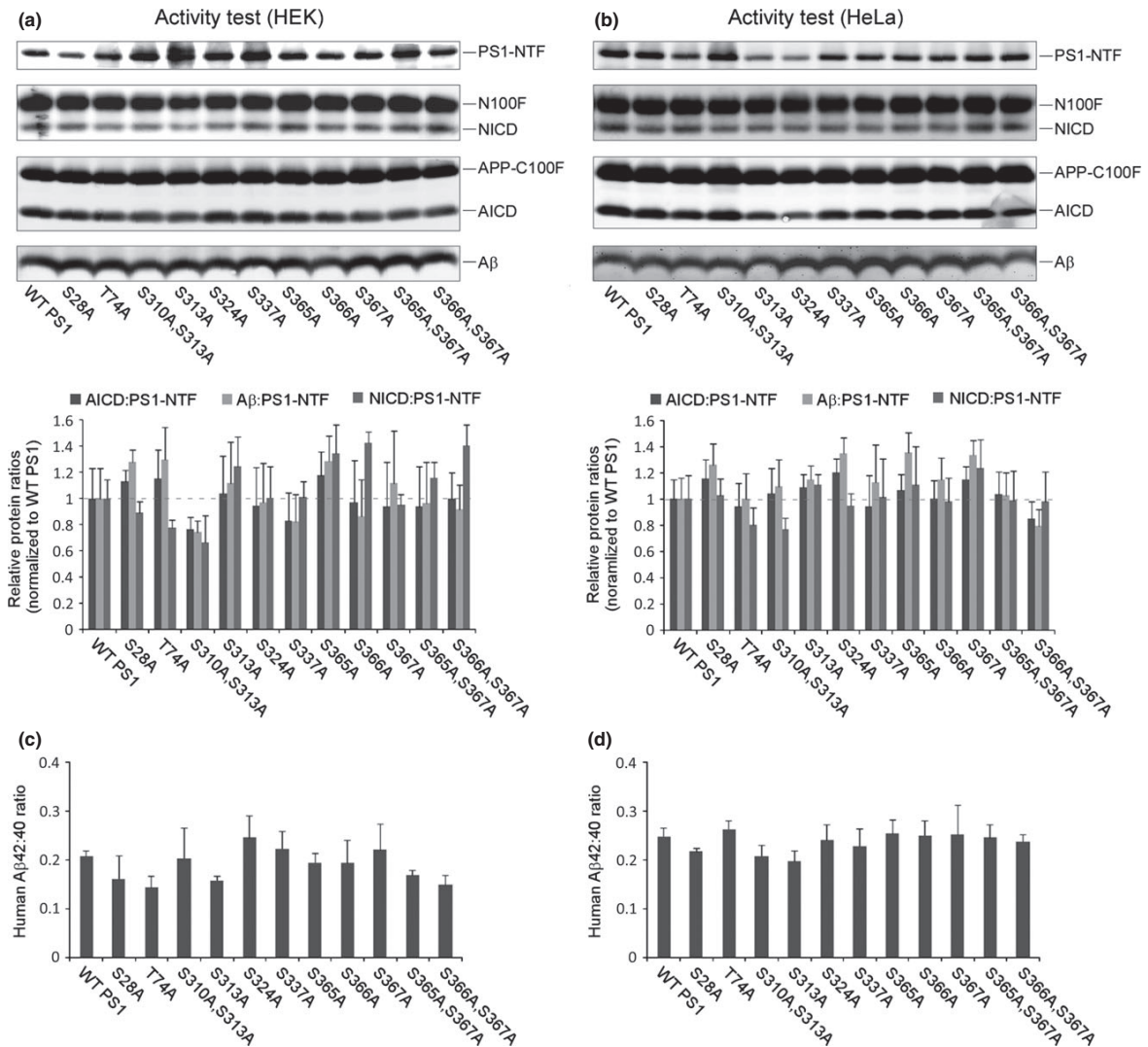


Fig. 3 Activity of semi-purified γ -secretase complexes with mutated PS1 phosphosites. HEK (a and c) or HeLa (b and d) cells were transiently transfected with PS1 individual phosphosite mutants. 48 h post-transfection, cell lysates were prepared and γ -secretase complexes with mutated PS1 phosphosites were immunoprecipitated with an anti-Flag affinity resin. Next, activity assays were performed with γ -secretase bound to the resin and purified amyloid- β precursor protein (APP)-based substrate (APP-C100F) or Notch-based substrate (N100F). Cleavage products APP intracellular domain (AICD)-Flag, Notch intracellular domain (NICD)-Flag and A β were

detected by western blot analysis (a and b, upper panels). AICD, NICD and A β production for all individual phosphosite mutants were estimated by densitometric analysis of western blots from three independent experiments (a and b, lower panels). AICD, NICD and A β productions were normalized to mature PS1-NTF and thus expressed as AICD : PS1-NTF, NICD : PS1-NTF and A β : PS1-NTF ratios. A β 1-40 and A β 1-42 specific ELISAs were used to estimate the A β 42 : A β 40 ratio (c and d). Data are means \pm SE with $n = 3$, and normalized to wild-type (WT) PS1 (except for c and d).

TMD6 and TMD7 (residues 263–374) and the N-terminal hydrophilic domain located at the N-terminus of the TMD1 (residues 1–80). The removal of these domains was confirmed by western blot analysis using antibodies targeting specifically the N-terminal hydrophilic loops of PS1-NTF and PS1-CTF, respectively, MAB1563 targeting the

residues 21–80 and MAB5232 targeting the residues 263–378 (Fig. 5b, middle panel). Next, equal amounts of γ -secretase complexes with or without the phosphorylation domains were probed for specific activity. Western blot analysis of APP cleavage products revealed no changes in AICD and A β production (Fig. 5c), and mass spectrometric

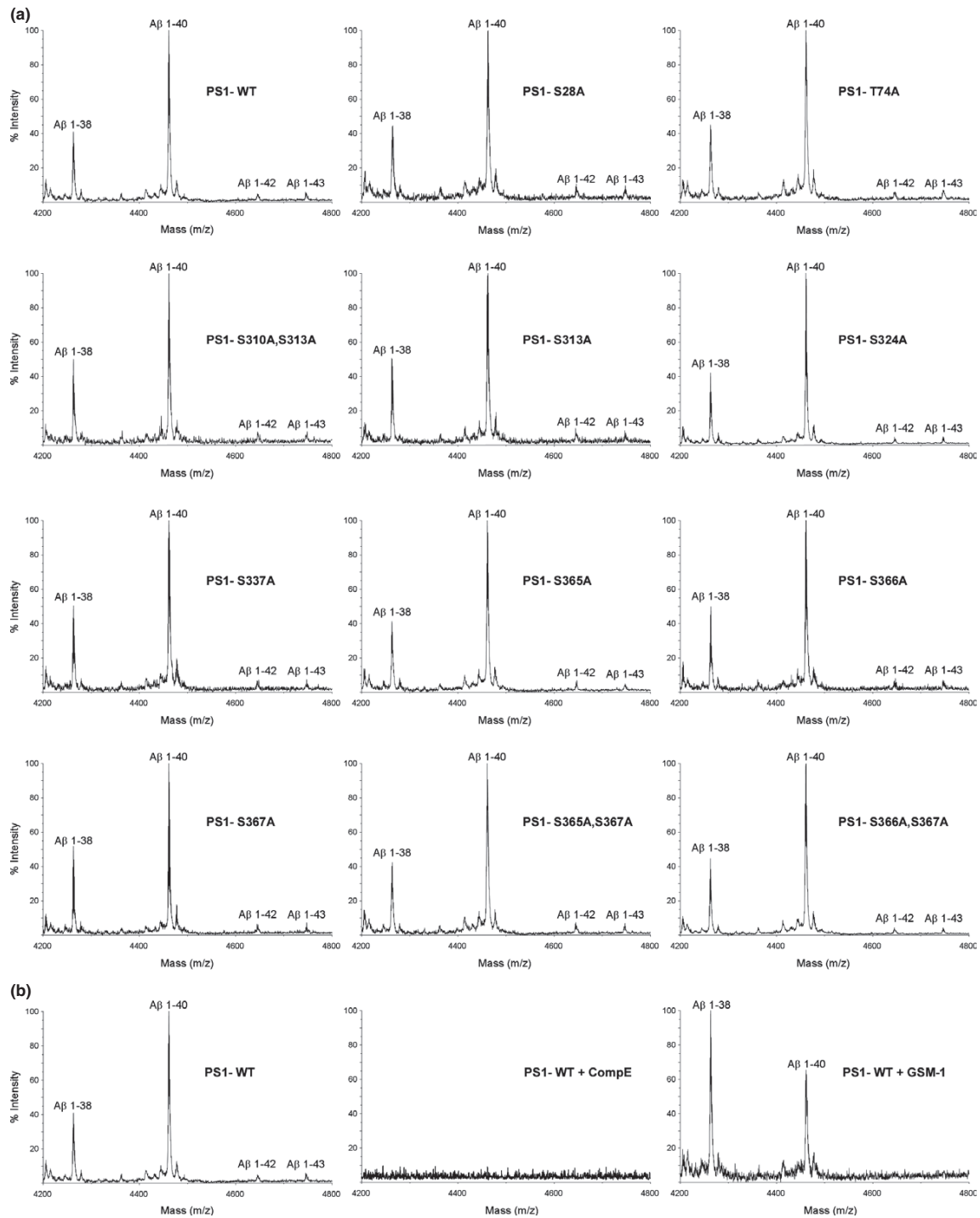


Fig. 4 Mass spectrometric profiles of A β peptides generated from human γ -secretase complexes with mutated PS1 phosphosites. (a) MALDI-TOF mass spectrometric analysis of total A β peptides produced in cell-free activity assays performed with semi-purified γ -secretase complexes harboring the indicated mutated PS1 phosphosites and bound to

an anti-Flag affinity resin. Molecular masses were accurately measured and searched against known amino acid sequences of human amyloid- β precursor protein (APP) for profiling the A β species. (b) The well-known γ -secretase inhibitor Compound-E (CompE) and γ -secretase modulator GSM-1 were used as controls for the specificity of APP processing.

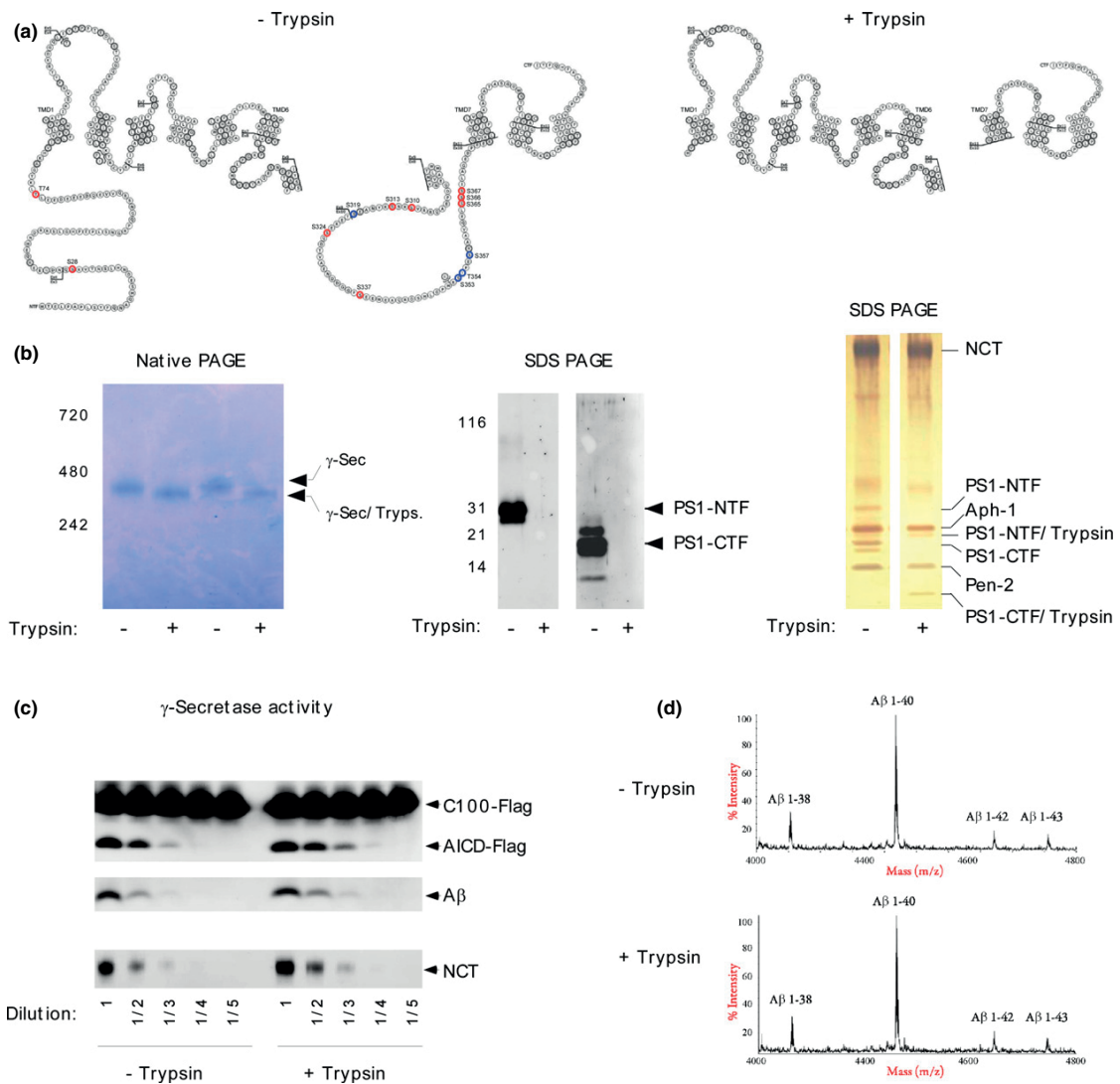


Fig. 5 Removal by trypsin digestion of the phosphorylated domains in PS1 does not affect γ -secretase activity and A β production. (a) Topologies of PS1 before (- Trypsin) and after (+ Trypsin) limited digestion of the native γ -secretase complex with the serine protease trypsin. Red: newly identified phosphosites; blue: previously reported phosphosites. (b) Analysis of the trypsin digested native γ -secretase complex by blue native polyacrylamide gel electrophoresis (BN-PAGE; left), western blot (middle) and denaturing sodium dodecyl sulfate-polyacrylamide gel electrophoresis (SDS-PAGE) followed by silver stain (right). Antibodies used for the detection of the N-terminal hydrophilic loops of PS1-NTF and PS1-CTF were MAB1563 (targeting

residues 21–80 of human PS1) and MAB5232 (targeting residues 263–378 of human PS1), respectively. (c) Dose-dependent activity assays performed with purified γ -secretase before (-Trypsin) and after (+Trypsin) trypsin digestion. Dilutions of the γ -secretase complex are indicated. Amyloid- β precursor protein (APP) cleavage products APP intracellular domain (AICD)-Flag and A β were detected by western blot with M2 anti-Flag and 6E10 anti-A β antibodies, respectively. γ -Secretase protein normalization was confirmed by western blot analysis of Nicastrin (NCT). (d) MALDI-TOF mass spectrometric analysis of total A β peptides produced in activity assays performed with purified γ -secretase before (- Trypsin) and after (+ Trypsin) trypsin digestion.

analysis of A β revealed no changes in A β profile (Fig. 5d). Together, these data suggest that the absence of the two phosphorylated domains of PS1-NTF and PS1-CTF does not affect the sequential and specific processing of APP by γ -secretase.

Discussion

In this study, we used a mass spectrometric approach and highly purified γ -secretase to identify a total of 11 new PS1 phosphorylation sites which, to the best of our knowledge,

have never been reported in the literature. Then we generated individual PS1 phosphosite mutants for all newly identified phosphorylation sites, and completed detailed cell-based and cell-free analyses of their effects on (i) the assembly and maturation of the γ -secretase complex, (ii) the activity of the complex, and (iii) the specificity of APP processing by γ -secretase. Overall, we demonstrate here that none of the newly identified phosphosite mutants affects the maturation or the total and specific activities of γ -secretase.

During the assembly and maturation in the secretory pathway of the γ -secretase complex, PS1 binds to the iNCT/Aph-1 subcomplex and allows the trafficking of the newly formed trimeric intermediate subcomplex to the Golgi apparatus (Fraering 2007). Next, the binding of Pen-2 to PS1 triggers conformational changes in PS1 that initiate the endoproteolytic cleavage to produce PS1-NTF and PS1-CTF, and activate the whole complex in the late Golgi and early endosomes (Fraering 2007). Thus, one could expect that post-translational modifications caused, e.g., by individual or multiple phosphorylation of amino acid residues could modify the conformation of the PS1 protein and/or the global structure of the γ -secretase complex, and modify this complex order of assembly and activation of γ -secretase. Based on our findings, mutagenesis of individual phosphosites does not affect the assembly and the maturation of the complex, raising the question whether phosphorylation of these sites appear during or after the maturation process. Interestingly, we found that the vast majority of the newly identified PS1 phosphosites are located in the loop between TMD6 and TMD7, which contains the endoproteolysis site (Wolfe *et al.* 1999). One could thus hypothesize that phosphorylation, or absence of phosphorylation at the newly identified sites, could modulate the endoproteolysis of PS1. We found that this is not the case, raising again the question whether phosphorylation of these sites occurs before PS1 endoproteolysis 'by default' in the non-processed loop simply because it is the most accessible domain in the γ -secretase complex, or after endoproteolysis in the remaining N- and C-terminal domains exposed to the cytosol.

We further found that individual mutations in the newly identified phosphosites do not interfere with (i) the production of total A β , (ii) the A β 42 : A β 40 ratio, and (iii) the profile of A β species generated by γ -secretase complexes purified from both HEK and HeLa cells. Taken together, it suggests that the absence of phosphorylation at individual sites does not alter the catalytic site of γ -secretase. This is consistent with the predicted topology and biophysical properties of matured PS1 within the γ -secretase complex. Indeed, the positioning of the two catalytic aspartates in the TMD6 and TMD7 contrasts with the positioning of the two phosphorylated regions in PS1, namely the cytosolic N-terminus of PS1-NTF (hydrophilic amino acid residues 1–81), and the cytosolic N-terminus of PS1-CTF (hydrophilic amino acid residues 291–374; see Fig. 1c). Our results are also

consistent with the work by Kirschenbaum *et al.* (2001), showing that transient expression in HEK-APP_{Sw} cells of the PS1 phosphomutants S353A and S357A (a similar approach was used in our study) did not affect A β 1–40 and A β 1–42 production, or the A β 42 : A β 40 ratio. In contrast, Maesako *et al.* (2011) found a decreased A β 42 : A β 40 ratio associated to PS1 phosphorylation, by using the GSK3 β inhibitor LiCl to change the phosphorylation status of PS1 in CHO-APP_{Sw} cells. However, it remains possible that this non-specific chemical-based strategy initiated off-target effects, besides modifying the phosphorylation status of Ser³⁵³ and Ser³⁵⁷ which would explain the observed apparent contradictory results.

Next, about 200 point mutations in PS1 have been reported to cause early-onset FAD, by changing the activity of γ -secretase. While some of these mutations cause a drastic increase in total A β production, most of them are associated with a toxic gain of function by increasing the A β 42 : A β 40 ratio (De Strooper *et al.* 1998). Moreover, several of the FAD mutations in PS1 are characterized by a loss of function causing drastic reductions in AICD production (Bentahir *et al.* 2006; Cacquevel *et al.* 2012). Very interestingly, residues Thr³⁵⁴ and Ser³⁶⁵, both of which are among our newly identified PS1 phosphosites, have also been reported to be part of the FAD-causing double mutations Thr354Ile/Ala431Glu (Lee *et al.* 2006) and Met146Val/Ser365Tyr (Rogaeva *et al.* 2001). However, single mutations at positions 431 and 146 (Ala431Glu and Met146Val, respectively) are also known to cause FAD (Rogaeva *et al.* 2001; Lee *et al.* 2006), raising the question about the significance of the second mutations (Thr354Ile and Ser365Tyr, respectively). Based on our mutagenesis data (Fig. 3), single mutations in Thr³⁵⁴ or Ser³⁶⁵ are not expected to cause AD pathogenesis.

Finally, in this study, only one phosphosite was mutated at the time. Although it remains very possible that multiple phosphosite mutations are required to detect an effect on the maturation and/or activity of γ -secretase, this hypothesis has already been partially challenged by Saura *et al.*, who demonstrated that the deletion of the PS1 hydrophilic loop (HL-residues 304–371) does not affect A β production (Saura *et al.* 2000). Based on this observation, one can anticipate that mutagenesis of multiple phosphosites in this HL domain will give the same results. We indirectly challenged the hypothesis that mutagenesis of multiple phosphosites does not affect the activity of γ -secretase by removing proteolitically the two N-terminal hydrophilic loops of PS1-NTF and PS1-CTF, which contain all identified phosphorylation sites. Consistent with, but going further than the Saura study, we found that the absence of the two phosphorylated domains (residues 1–80 and 263–374) does not affect the specific processing of APP by γ -secretase (Fig. 5).

In conclusion, our results suggest that the γ -secretase complex can be phosphorylated at two well-defined domains within PS1, and that absence of phosphorylation at individual

phosphosites does not modulate APP or Notch processing and A β production. From the latter observation, one can speculate that individual phosphosites do not modulate cerebral A β plaque formation, and consequently will not prove to be therapeutic targets for AD.

Acknowledgments and conflict of interest disclosure

This work was supported by the Swiss National Science Foundation (to P.C.F., grant 31003A_152677/1) and the Strauss foundation (to P.C.F.). The funders had no role in study design, data collection and analysis, decision to publish, or preparation of the manuscript. The authors also thank D. Selkoe for human WT PS1 cDNA, and H. Karlstrom for the UD-1 anti-Pen-2 antibody. Authors declare having no competing financial interests.

All experiments were conducted in compliance with the ARRIVE guidelines.

Author contributions

A.M., B.H.K., S.M., J.R.A. and M.D. performed the experiments. R.H. performed the LC-MS/MS analyses. M.M. and P.C.F. designed the research; P.C.F. supervised the project; A.M. and P.C.F. wrote the manuscript.

Supporting information

Additional supporting information may be found in the online version of this article at the publisher's web-site:

Figure S1. Tandem MS spectra of phosphorylated peptides identified in the γ -secretase catalytic subunit PS1.

Figure S2. DNA sequences used to generate Ser or Thr to Ala phosphosite mutations in PS1, the catalytic subunit of the γ -secretase complex.

Figure S3. Endogenous and exogenous PS1 levels in HEK and HeLa cells of γ -secretase complexes with mutated PS1 phosphosites.

Figure S4. Quantification of γ -secretase subunits in HEK and HeLa cells expressing PS1 phosphosite mutants.

Figure S5. Controls for inhibition or enhancement of γ -secretase activity.

Figure S6. Endogenous APP levels in HEK and HeLa cells of γ -secretase complexes with mutated PS1 phosphosites.

Figure S7. γ -Secretase complexes with mutated PS1 phosphosites do not affect cellular Notch processing.

Figure S8. Activity of γ -secretase complexes with mutated PS1 phosphosites purified from SH-SY5Y neuroblastoma cells.

References

- Alattia J. R., Matasci M., Dimitrov M., Aeschbach L., Balasubramanian S., Hacker D. L., Wurm F. M. and Fraering P. C. (2013) Highly efficient production of the Alzheimer's gamma-secretase integral membrane protease complex by a multi-gene stable integration approach. *Biotechnol. Bioeng.* **110**, 1995–2005.
- Baulac S., LaVoie M. J., Kimberly W. T., Strahle J., Wolfe M. S., Selkoe D. J. and Xia W. (2003) Functional gamma-secretase complex assembly in Golgi/trans-Golgi network: interactions among presenilin, nicastrin, Aph1, Pen-2, and gamma-secretase substrates. *Neurobiol. Dis.* **14**, 194–204.
- Bentahir M., Nyabi O., Verhamme J., Tolia A., Horre K., Wiltfang J., Esselmann H. and De Strooper B. (2006) Presenilin clinical mutations can affect gamma-secretase activity by different mechanisms. *J. Neurochem.* **96**, 732–742.
- Bot N., Schweizer C., Ben Halima S. and Fraering P. C. (2011) Processing of the synaptic cell adhesion molecule neurexin-3beta by Alzheimer disease alpha- and gamma-secretases. *J. Biol. Chem.* **286**, 2762–2773.
- Cacquevel M., Aeschbach L., Houacine J. and Fraering P. C. (2012) Alzheimer's disease-linked mutations in presenilin-1 result in a drastic loss of activity in purified gamma-secretase complexes. *PLoS ONE* **7**, e35133.
- Chavez-Gutierrez L., Bammens L., Benilova I. *et al.* (2012) The mechanism of gamma-secretase dysfunction in familial Alzheimer disease. *EMBO J.* **31**, 2261–2274.
- De Strooper B. (2003) Aph-1, Pen-2, and Nicastrin with Presenilin generate an active gamma-secretase complex. *Neuron* **38**, 9–12.
- De Strooper B., Saftig P., Craessaerts K., Vanderstichele H., Guhde G., Annaert W., Von Figura K. and Van Leuven F. (1998) Deficiency of presenilin-1 inhibits the normal cleavage of amyloid precursor protein. *Nature* **391**, 387–390.
- De Strooper B., Annaert W., Cupers P. *et al.* (1999) A presenilin-1-dependent gamma-secretase-like protease mediates release of Notch intracellular domain. *Nature* **398**, 518–522.
- Dimitrov M., Alattia J. R., Lemmin T. *et al.* (2013) Alzheimer's disease mutations in APP but not gamma-secretase modulators affect epsilon-cleavage-dependent AICD production. *Nat. Commun.* **4**, 2246.
- Fluhrer R., Friedlein A., Haass C. and Walter J. (2004) Phosphorylation of presenilin 1 at the caspase recognition site regulates its proteolytic processing and the progression of apoptosis. *J. Biol. Chem.* **279**, 1585–1593.
- Fraering P. C. (2007) Structural and functional determinants of gamma-secretase, an intramembrane protease implicated in Alzheimer's disease. *Curr. Genomics* **8**, 531–549.
- Hardy J. and Allsop D. (1991) Amyloid deposition as the central event in the aetiology of Alzheimer's disease. *Trends Pharmacol. Sci.* **12**, 383–388.
- Iwatsubo T., Odaka A., Suzuki N., Mizusawa H., Nukina N. and Ihara Y. (1994) Visualization of A beta 42(43) and A beta 40 in senile plaques with end-specific A beta monoclonals: evidence that an initially deposited species is A beta 42(43). *Neuron* **13**, 45–53.
- Kimberly W. T., Xia W., Rahmati T., Wolfe M. S. and Selkoe D. J. (2000) The transmembrane aspartates in presenilin 1 and 2 are obligatory for gamma-secretase activity and amyloid beta-protein generation. *J. Biol. Chem.* **275**, 3173–3178.
- Kimberly W. T., LaVoie M. J., Ostaszewski B. L., Ye W., Wolfe M. S. and Selkoe D. J. (2002) Complex N-linked glycosylated nicastrin associates with active gamma-secretase and undergoes tight cellular regulation. *J. Biol. Chem.* **277**, 35113–35117.
- Kirschenbaum F., Hsu S. C., Cordell B. and McCarthy J. V. (2001) Substitution of a glycogen synthase kinase-3beta phosphorylation site in presenilin 1 separates presenilin function from beta-catenin signaling. *J. Biol. Chem.* **276**, 7366–7375.
- Kuo L. H., Hu M. K., Hsu W. M., Tung Y. T., Wang B. J., Tsai W. W., Yen C. T. and Liao Y. F. (2008) Tumor necrosis factor-alpha-elicited stimulation of gamma-secretase is mediated by c-Jun N-terminal kinase-dependent phosphorylation of presenilin and nicastrin. *Mol. Biol. Cell* **19**, 4201–4212.

- Lau K. F., Howlett D. R., Kesavapany S., Standen C. L., Dingwall C., McLoughlin D. M. and Miller C. C. (2002) Cyclin-dependent kinase-5/p35 phosphorylates Presenilin 1 to regulate carboxy-terminal fragment stability. *Mol. Cell Neurosci.* **20**, 13–20.
- Laudon H., Hansson E. M., Melen K., Bergman A., Farmery M. R., Winblad B., Lendahl U., von Heijne G. and Naslund J. (2005) A nine-transmembrane domain topology for presenilin 1. *J. Biol. Chem.* **280**, 35352–35360.
- LaVoie M. J., Fraering P. C., Ostaszewski B. L., Ye W., Kimberly W. T., Wolfe M. S. and Selkoe D. J. (2003) Assembly of the gamma-secretase complex involves early formation of an intermediate subcomplex of Aph-1 and nicastrin. *J. Biol. Chem.* **278**, 37213–37222.
- Lee P., Medina L. and Ringman J. M. (2006) The Thr354Ile substitution in PSEN1: disease-causing mutation or polymorphism? *Neurology* **66**, 1955–1956.
- Maesako M., Uemura K., Kubota M. *et al.* (2011) Effect of glycogen synthase kinase 3 beta-mediated presenilin 1 phosphorylation on amyloid beta production is negatively regulated by insulin receptor cleavage. *Neuroscience* **177**, 298–307.
- Pasternak S. H., Bagshaw R. D., Guiral M., Zhang S., Ackerley C. A., Pak B. J., Callahan J. W. and Mahuran D. J. (2003) Presenilin-1, nicastrin, amyloid precursor protein, and gamma-secretase activity are co-localized in the lysosomal membrane. *J. Biol. Chem.* **278**, 26687–26694.
- Patterson S. I. (2002) Posttranslational protein S-palmitoylation and the compartmentalization of signaling molecules in neurons. *Biol. Res.* **35**, 139–150.
- Qin J., Zhou W., Huang X. *et al.* (2011) Discovery of a potent pyrazolopyridine series of gamma-secretase modulators. *ACS Med. Chem. Lett.* **2**, 471–476.
- Ray W. J., Yao M., Mumm J., Schroeter E. H., Saftig P., Wolfe M., Selkoe D. J., Kopan R. and Goate A. M. (1999) Cell surface presenilin-1 participates in the gamma-secretase-like proteolysis of Notch. *J. Biol. Chem.* **274**, 36801–36807.
- Rogaev E. I., Sherrington R., Rogaeva E. A. *et al.* (1995) Familial Alzheimer's disease in kindreds with missense mutations in a gene on chromosome 1 related to the Alzheimer's disease type 3 gene. *Nature* **376**, 775–778.
- Rogaev E. I., Sherrington R., Wu C. *et al.* (1997) Analysis of the 5' sequence, genomic structure, and alternative splicing of the presenilin-1 gene (PSEN1) associated with early onset Alzheimer disease. *Genomics* **40**, 415–424.
- Rogaeva E. A., Fafel K. C., Song Y. Q. *et al.* (2001) Screening for PS1 mutations in a referral-based series of AD cases: 21 novel mutations. *Neurology* **57**, 621–625.
- Saura C. A., Tomita T., Soriano S., Takahashi M., Leem J. Y., Honda T., Koo E. H., Iwatsubo T. and Thinakaran G. (2000) The nonconserved hydrophilic loop domain of presenilin (PS) is not required for PS endoproteolysis or enhanced abeta 42 production mediated by familial early onset Alzheimer's disease-linked PS variants. *J. Biol. Chem.* **275**, 17136–17142.
- Schellenberg G. D. (1995) Genetic dissection of Alzheimer disease, a heterogeneous disorder. *Proc. Natl Acad. Sci. USA* **92**, 8552–8559.
- Seiffert D., Bradley J. D., Rominger C. M. *et al.* (2000) Presenilin-1 and -2 are molecular targets for gamma-secretase inhibitors. *J. Biol. Chem.* **275**, 34086–34091.
- Selkoe D. J. (1994) Cell biology of the amyloid beta-protein precursor and the mechanism of Alzheimer's disease. *Annu. Rev. Cell Biol.* **10**, 373–403.
- Steiner H., Duff K., Capell A. *et al.* (1999) A loss of function mutation of presenilin-2 interferes with amyloid beta-peptide production and notch signaling. *J. Biol. Chem.* **274**, 28669–28673.
- Takasugi N., Tomita T., Hayashi I., Tsuruoka M., Niimura M., Takahashi Y., Thinakaran G. and Iwatsubo T. (2003) The role of presenilin cofactors in the gamma-secretase complex. *Nature* **422**, 438–441.
- Thingholm T. E. and Larsen M. R. (2009) The use of titanium dioxide micro-columns to selectively isolate phosphopeptides from proteolytic digests. *Methods Mol. Biol.* **527**, 57–66, xi.
- Uemura K., Kihara T., Kuzuya A., Okawa K., Nishimoto T., Ninomiya H., Sugimoto H., Kinoshita A. and Shimohama S. (2006) Characterization of sequential N-cadherin cleavage by ADAM10 and PS1. *Neurosci. Lett.* **402**, 278–283.
- Vetrivel K. S., Cheng H., Lin W., Sakurai T., Li T., Nukina N., Wong P. C., Xu H. and Thinakaran G. (2004) Association of gamma-secretase with lipid rafts in post-Golgi and endosome membranes. *J. Biol. Chem.* **279**, 44945–44954.
- Wolfe M. S., Xia W., Ostaszewski B. L., Diehl T. S., Kimberly W. T. and Selkoe D. J. (1999) Two transmembrane aspartates in presenilin-1 required for presenilin endoproteolysis and gamma-secretase activity. *Nature* **398**, 513–517.

Identification of new Presenilin-1 phosphosites: implication for γ -secretase activity and A β production

Alexandre Matz^a, Blanka Halamoda-Kenzaoui^a, Romain Hamelin^b, Sebastien Mosser^a, Jean-René Alattia^a, Mitko Dimitrov^a, Marc Moniatte^b, and Patrick C. Fraering^{a,1}

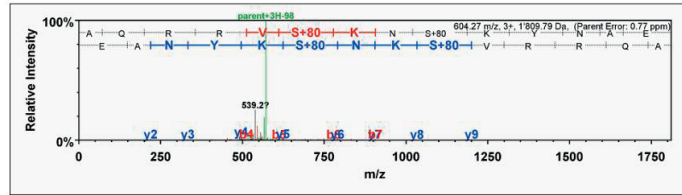
^a Brain Mind Institute and School of Life Sciences, Ecole Polytechnique Fédérale de Lausanne (EPFL), CH1015 Lausanne, Switzerland

^b Proteomics Core Facility and School of Life Sciences, Ecole Polytechnique Fédérale de Lausanne (EPFL), CH1015 Lausanne, Switzerland

¹ Correspondence should be addressed to Patrick C. Fraering, Brain Mind Institute and School of Life Sciences, Ecole Polytechnique Fédérale de Lausanne (EPFL), CH1015 Lausanne, Switzerland.
E-mail: patrick.fraering@epfl.ch

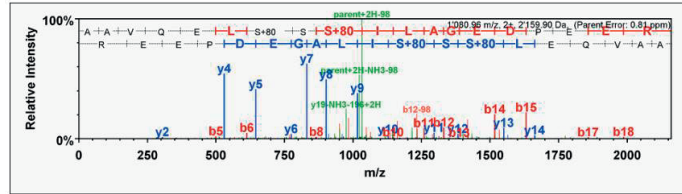
S310, S313

B	B Ions	B+2H	B-NH3	B-H2O	AA	Y Ions	Y+2H	Y-NH3	Y-H2O	Y
1	72.0	36.5			A	1*810.8	905.9	1*793.8	1*792.8	14
2	200.1	100.6	183.1		Q	1*739.8	870.4	1*722.7	1*721.8	13
3	356.2	178.6	339.2		R	1*611.7	806.4	1*594.7	1*593.7	12
4	512.3	256.7	495.3		R	1*455.6	728.3	1*438.6	1*437.6	11
5	611.4	306.2	594.3		V	1*299.5	650.3	1*282.5	1*281.5	10
6	776.4	389.7	761.3	760.4	S+80	1*209.4	600.7	1*183.4	1*182.4	9
7	906.5	453.7	869.4	868.5	K	1*033.4	547.2	1*016.4	1*015.4	8
8	1*020.5	510.8	1*003.5	1*002.5	N	905.3	453.2	889.3	887.3	7
9	1*167.5	584.3	1*170.5	1*169.5	S+80	794.3	396.2	774.3	773.3	6
10	1*315.6	658.3	1*298.6	1*297.6	K	624.3	312.7	607.3	606.3	5
11	1*478.7	739.8	1*461.6	1*460.7	Y	496.2	248.6	479.2	478.2	4
12	1*592.7	798.9	1*575.7	1*574.7	N	333.1	167.1	316.1	315.1	3
13	1*663.7	832.4	1*646.7	1*645.7	A	219.1	110.1		201.1	2
14	1*810.8	905.9	1*793.8	1*792.8	E	148.1	74.5		130.0	1



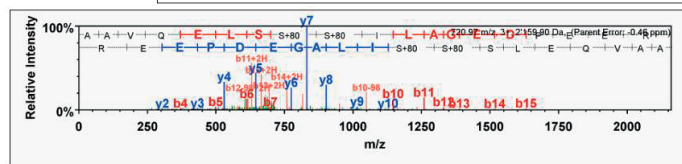
S365, S367

B	B Ions	B+2H	B-NH3	B-H2O	AA	Y Ions	Y+2H	Y-NH3	Y-H2O	Y
1	72.0				A	2*160.9	1*081.0	2*143.9	2*142.9	19
2	143.1				A	2*089.9	1*045.4	2*072.8	2*071.9	18
3	242.1				V	2*018.8	1*009.9	2*001.8	2*000.8	17
4	370.2		353.2		Q	1*919.8	960.4	1*902.7	1*901.8	16
5	499.3		482.2	481.2	E	1*791.7	896.4	1*774.7	1*773.7	15
6	612.3	306.7	595.3	594.3	L	1*662.7	831.8	1*645.6	1*644.7	14
7	776.4	390.2	761.3	761.3	S+80	1*549.6	775.3	1*532.6	1*531.6	13
8	866.4	433.7	849.3	848.4	S	1*382.6	661.8	1*365.6	1*364.6	12
9	1*033.4	517.2	1*016.3	1*015.4	S+80	1*295.6	648.3	1*278.5	1*277.5	11
10	1*146.4	573.7	1*129.4	1*128.4	I	1*128.6	564.8	1*111.5	1*110.5	10
11	1*259.5	630.3	1*242.5	1*241.5	L	1*015.5	508.2	998.4	997.5	9
12	1*330.6	665.8	1*313.5	1*312.6	A	902.4	451.7	885.4	884.4	8
13	1*387.6	684.3	1*370.6	1*369.6	G	831.3	416.2	814.3	813.3	7
14	1*516.6	758.8	1*499.6	1*498.6	E	774.3	387.7	757.3	756.3	6
15	1*631.7	816.3	1*614.6	1*613.6	D	645.3	323.1	628.3	627.3	5
16	1*728.7	864.9	1*711.7	1*710.7	P	530.3	265.6	513.2	512.2	4
17	1*857.8	929.4	1*840.7	1*839.7	E	433.2	217.1	416.2	415.2	3
18	1*986.8	983.9	1*969.8	1*968.8	E	304.2	152.6	287.1	286.2	2
19	2*160.9	1*081.0	2*143.9	2*142.9	R	175.1	88.1	158.1		1



S366, S367

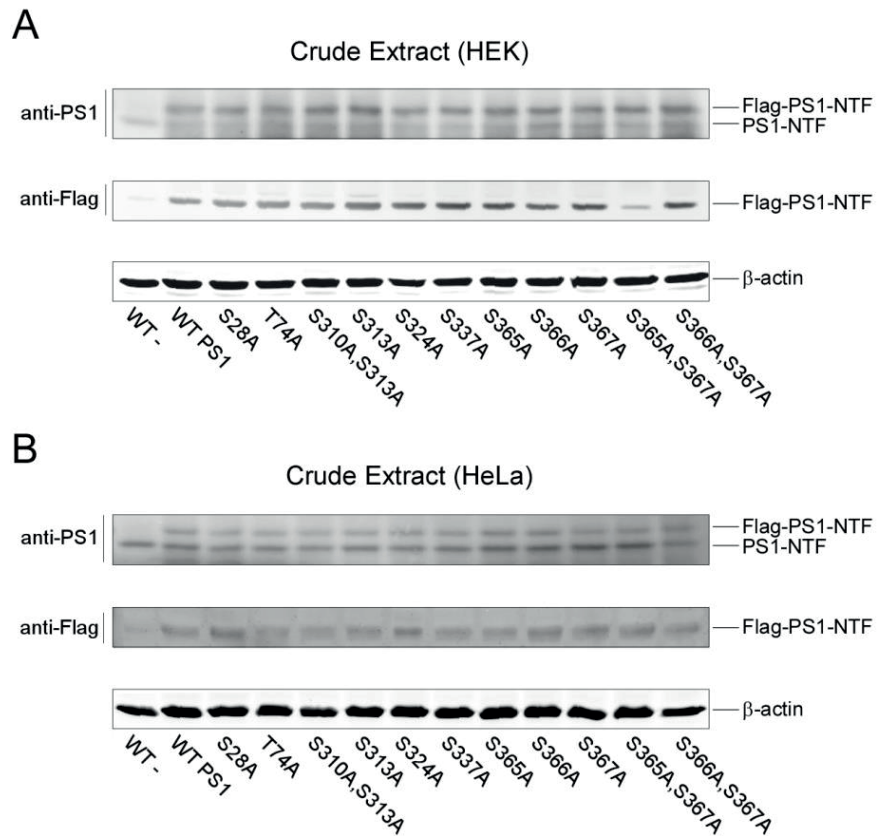
B	B Ions	B+2H	B-NH3	B-H2O	AA	Y Ions	Y+2H	Y-NH3	Y-H2O	Y
1	72.0	36.5			A	2*160.9	1*081.0	2*143.9	2*142.9	19
2	143.1	72.0			A	2*089.9	1*045.4	2*072.8	2*071.9	18
3	242.1	121.6			V	2*018.8	1*009.9	2*001.8	2*000.8	17
4	370.2	185.6	353.2		Q	1*919.8	960.4	1*902.7	1*901.8	16
5	499.3	250.1	482.2	481.2	E	1*791.7	896.4	1*774.7	1*773.7	15
6	612.3	306.7	595.3	594.3	L	1*662.7	831.8	1*645.6	1*644.7	14
7	699.4	350.2	682.3	681.4	S	1*549.6	775.3	1*532.6	1*531.6	13
8	866.4	433.7	849.3	848.4	S+80	1*462.5	731.8	1*445.5	1*444.5	12
9	1*033.4	517.2	1*016.3	1*015.4	S+80	1*295.6	648.3	1*278.5	1*277.5	11
10	1*146.4	573.7	1*129.4	1*128.4	I	1*128.6	564.8	1*111.5	1*110.5	10
11	1*259.5	630.3	1*242.5	1*241.5	L	1*015.5	508.2	998.4	997.5	9
12	1*330.6	665.8	1*313.5	1*312.6	A	902.4	451.7	885.4	884.4	8
13	1*387.6	684.3	1*370.6	1*369.6	G	831.3	416.2	814.3	813.3	7
14	1*516.6	758.8	1*499.6	1*498.6	E	774.3	387.7	757.3	756.3	6
15	1*631.7	816.3	1*614.6	1*613.6	D	645.3	323.1	628.3	627.3	5
16	1*728.7	864.9	1*711.7	1*710.7	P	530.3	265.6	513.2	512.2	4
17	1*857.8	929.4	1*840.7	1*839.7	E	433.2	217.1	416.2	415.2	3
18	1*986.8	983.9	1*969.8	1*968.8	E	304.2	152.6	287.1	286.2	2
19	2*160.9	1*081.0	2*143.9	2*142.9	R	175.1	88.1	158.1		1



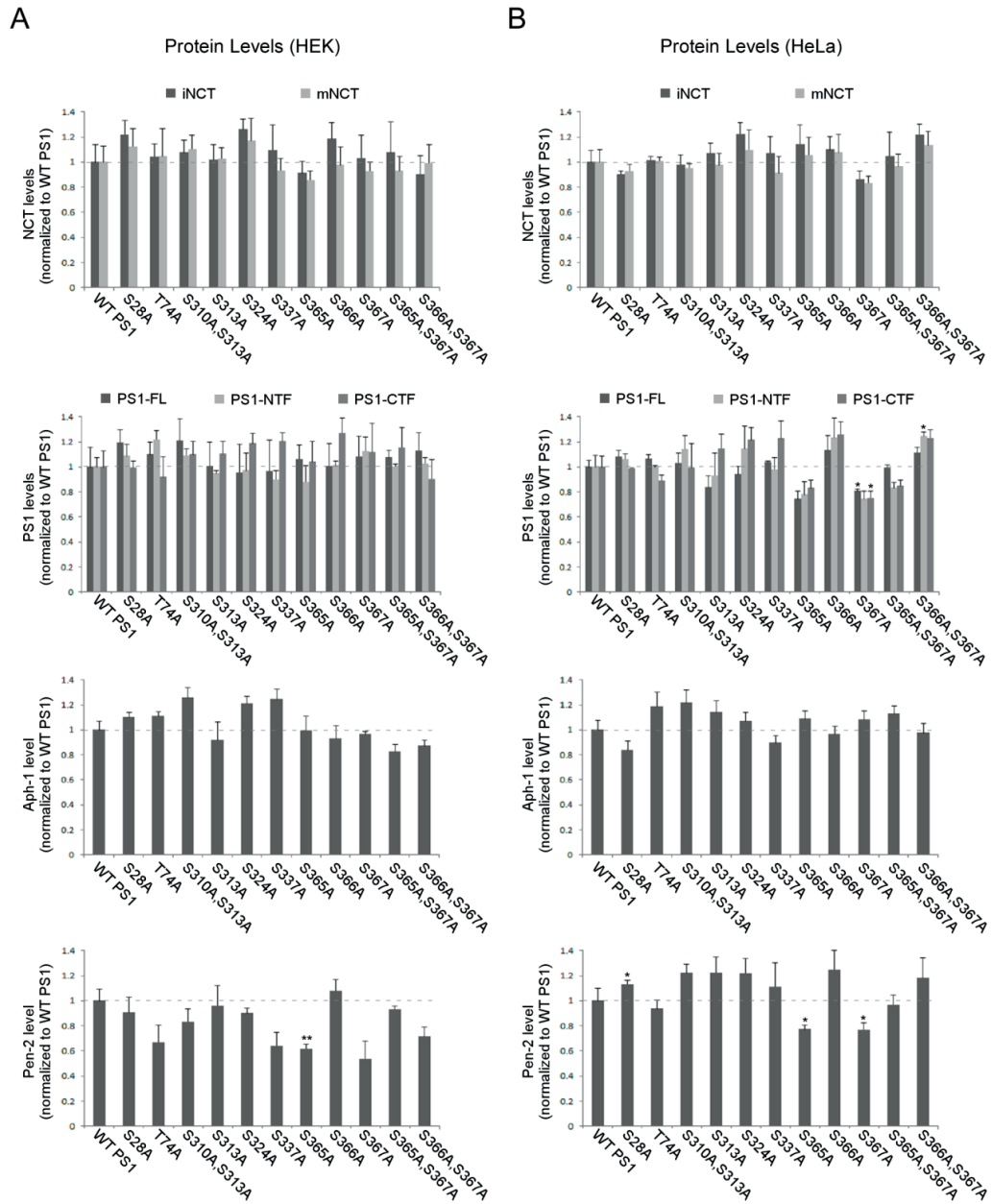
SUPPLEMENTARY FIGURE 1. Tandem MS spectra of phosphorylated peptides identified in the γ -secretase catalytic subunit PS1. The high molecular weight human γ -secretase complex resolved by BN-PAGE and stained with Coomassie Brilliant Blue (Fig. 1) was excised and used for the identification by electrospray LC-MS/MS mass spectrometry of new phosphorylation sites in Presenilin-1. Tandem MS spectra of PS1 phosphorylated peptides are shown, confirming the identification of a total of 15 PS1 phosphorylated peptides, corresponding to twelve single and three double phosphosites in PS1, at the indicated amino-acid residues. Among these, eleven (8 single and 3 double) are newly identified PS1 phosphosites (also summarized in Fig. 1C).

Oligonucleotide	Sequence
FS28A	AGC-AAT-ACT-GTA-CGT-GCC-CAG-AAT-GAC-AAT-AGA
RS28A	TCT-ATT-GTC-ATT-CTG-GGC-ACG-TAC-AGT-ATT-GCT
FT74A	GAA-GAT-GAG-GAG-CTG-GCA-TTG-AAA-TAT-GGC-GCC
RT74A	GGC-GCC-ATA-TTT-CAA-TGC-CAG-CTC-CTC-ATC-TTC
FS310A,S313A	GCT-CAA-AGG-AGA-GTA-GCC-AAA-AAT-GCC-AAG-TAT
RS310A,S313A	ATA-CTT-GGC-ATT-TTT-GGC-TAC-TCT-CCT-TTG-AGC
FS313A	AGA-GTA-TCC-AAA-AAT-GCC-AAG-TAT-AAT-GCA-GAA
RS313A	TTC-TGC-ATT-ATA-CTT-GGC-ATT-TTT-GGA-TAC-TCT
FS324A	AGC-ACA-GAA-AGG-GAG-GCA-CAA-GAC-ACT-GTT-GCA
RS324A	TGC-AAC-AGT-GTC-TTG-TGC-CTC-CCT-TTC-TGT-GCT
FS337A	GAT-GAT-GGC-GGG-TTC-GCT-GAG-GAA-TGG-GAA-GCC
RS337A	GGC-TTC-CCA-TTC-CTC-AGC-GAA-CCC-GCC-ATC-ATC
FS365A	GCT-GTC-CAG-GAA-CTT-GCC-AGC-AGT-ATC-CTC-GCT
RS365A	AGC-GAG-GAT-ACT-GCT-GGC-AAG-TTC-CTG-GAC-AGC
FS366A	GTC-CAG-GAA-CTT-TCC-GCC-AGT-ATC-CTC-GCT-GGT
RS366A	ACC-AGC-GAG-GAT-ACT-GGC-GGA-AAG-TTC-TGG-AC
FS367A	CAG-GAA-CTT-TCC-AGC-GCT-ATC-CTC-GCT-GGT-GAA
RS367A	TTC-ACC-AGC-GAG-GAT-AGC-GCT-GGA-AAG-TTC-CTG
FS365A,S367A	GCT-GTC-CAG-GAA-CTT-GCC-AGC-GCT-ATC-CTC-GCT
RS365A,S367A	AGC-GAG-GAT-AGC-GCT-GGC-AAG-TTC-CTG-GAC-AGC
FS366A,S367A	GTC-CAG-GAA-CTT-TCC-GCC-GCT-ATC-CTC-GCT-GGT
RS366A,S367A	ACC-AGC-GAG-GAT-AGC-GGC-GGA-AAG-TTC-CTG-GAC

SUPPLEMENTARY FIGURE 2. DNA sequences used to generate Ser or Thr to Ala phosphosite mutations in PS1, the catalytic subunit of the γ -secretase complex. Oligonucleotide primers listed above and containing desired Serine or Threonine to Alanine mutations were purchased at Eurogentec (Liège, Belgium) and annealed to the template PS1 vector. Mutagenic primers were extended during temperature cycling of DNA polymerase, resulting in mutated plasmids containing nicked circular strands. Then vectors were treated with the endonuclease *Dpn* I, specific for methylated DNA. The endonuclease allowed the digestion of the non-mutated DNA template and thus selecting vectors with expected mutations. Finally, nicked DNAs were transformed into XL1-Blue supercompetent cells (*E. coli*), to repair nicks in the mutated plasmids. The production of 11 different PS1 phosphosite mutants was completed and all mutants were verified by sequencing (Microsynth AG, Balgach, Switzerland).

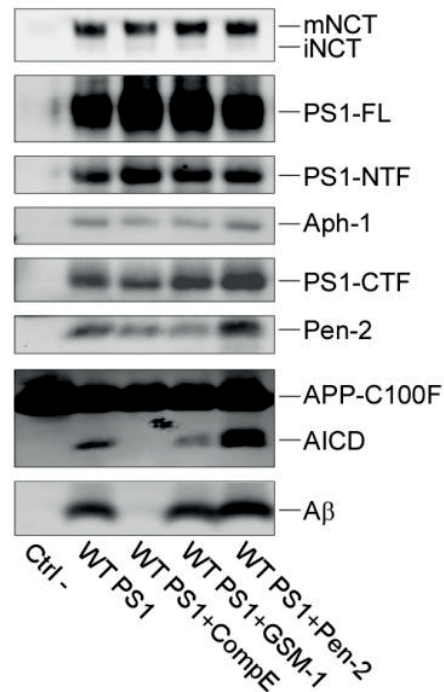


SUPPLEMENTARY FIGURE 3. Endogenous and exogenous PS1 levels in HEK and HeLa cells of γ -secretase complexes with mutated PS1 phosphosites. HEK (A) or HeLa (B) cells transiently transfected with Flag-tagged individual PS1 phosphosite mutants were collected 48 hours post-transfection, and whole cell protein extracts were prepared for Western blot analysis to detect both endogenous (PS1-NTF) and exogenous (Flag-PS1-NTF) PS1 with the MAB1563 anti-PS1 antibody (upper panels), or with the M2 anti-Flag antibody (middle panels). Untransfected cells are labeled WT-. β -actin served as a loading control.



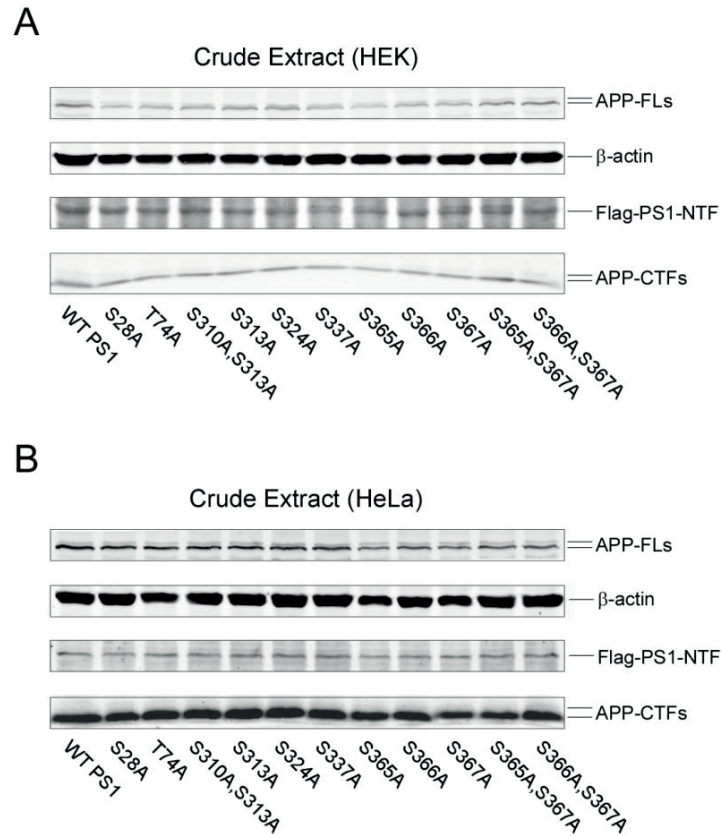
SUPPLEMENTARY FIGURE 4. Quantification of γ -secretase subunits in HEK and HeLa cells expressing PS1 phosphosite mutants. HEK (A) or HeLa (B) cells were transiently transfected with Flag-tagged individual PS1 phosphosite mutants. 48 hours post-transfection, cell lysates were prepared

and γ -secretase complexes with mutated PS1 phosphosites were immunoprecipitated with an anti-Flag affinity resin for Western blot analysis (see Figs. 2C and 2D, upper panels). Densitometric analyses to estimate iNCT, mNCT, PS1-NTF, PS1-CTF, PS1-FL, Aph-1 and Pen-2 protein levels were performed on Western blots from three independent experiments. Data are means \pm S.E. with n = 3, and normalized to WT PS1. *, p<0.05; **, p<0.01.

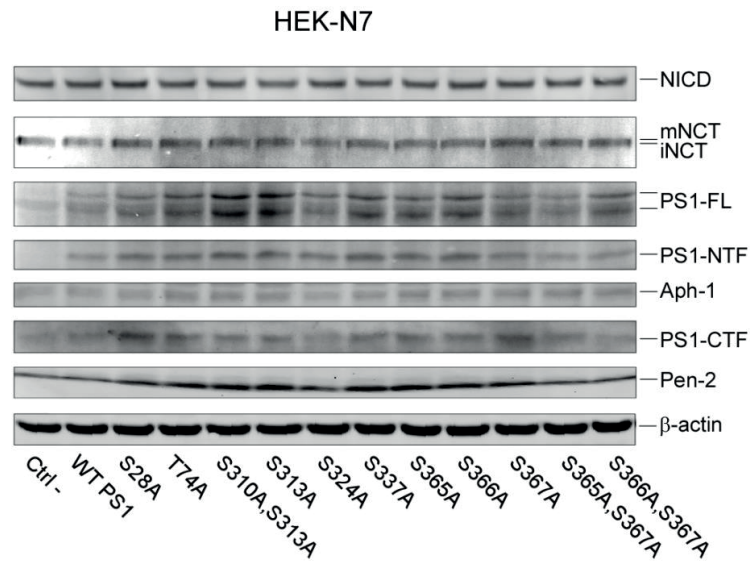


SUPPLEMENTARY FIGURE 5. Controls for inhibition or enhancement of γ -secretase activity.

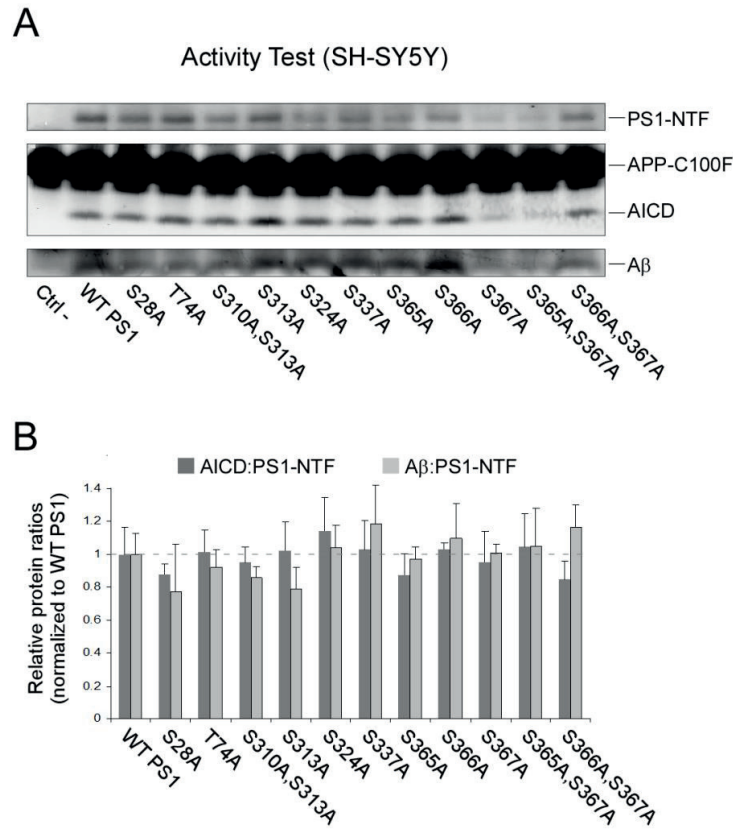
Untransfected HEK cells (Ctrl-), HEK cells transiently transfected with Flag-tagged WT PS1, or HEK cells transiently co-transfected with WT PS1 and Pen-2 (control for enhanced γ -secretase activity) were first incubated for 48 hours. Next, cell lysates were prepared and γ -secretase complexes with Flag-tagged WT PS1 were immunoprecipitated with an anti-Flag affinity resin. Then, activity assays were performed with γ -secretase bound to the resin and purified APP-based substrate (APP-C100F), in the presence or absence of the well-known γ -secretase inhibitor Compound-E (CompE; control for inhibited γ -secretase activity) or the γ -secretase modulator GSM-1. Cleavage products AICD-Flag and A β were detected by Western blot analysis together with γ -secretase subunits. CompE and Pen-2 overexpression caused respectively γ -secretase inhibition and enhancement.



SUPPLEMENTARY FIGURE 6. Endogenous APP levels in HEK and HeLa cells of γ -secretase complexes with mutated PS1 phosphosites. HEK (A) or HeLa (B) cells transiently transfected with Flag-tagged individual PS1 phosphosite mutants were collected 48 hours post-transfection, and whole cell protein extracts were prepared for Western blot analysis to detect both APP-FLs and APP-CTFs with the CT-15 anti-APP antibody, and Flag-tagged PS1-NTF with the M2 anti-Flag antibody. β -actin served as a loading control.



SUPPLEMENTARY FIGURE 7. γ -Secretase complexes with mutated PS1 phosphosites do not affect cellular Notch processing. HEK-N7 cells stably overexpressing the γ -secretase substrate Notch1 Δ E (residues 1704-2184 of human Notch1) were transiently transfected for 48 hours with PS1 phosphosite mutants. Next, protein extracts were prepared and probed by Western blot for γ -secretase subunits and Notch intracellular domain (NICD). Untransfected cells (Ctrl-) and cells transfected with WT PS1 served as controls for NICD production, while β -actin served as a protein loading control. When compared to the control cells expressing WT PS1, PS1 phosphosite mutants do not significantly alter NICD production.



SUPPLEMENTARY FIGURE 8. Activity of γ -secretase complexes with mutated PS1 phosphosites purified from SH-SY5Y neuroblastoma cells. SH-SY5Y cells were transiently transfected with PS1 individual phosphosite mutants. Cell lysates were prepared and γ -secretase complexes with mutated PS1 phosphosites were immunoprecipitated with an anti-Flag affinity resin. Next, activity assays were performed with γ -secretase bound to the resin by using purified APP-based substrate (APP-C100F). (A) Cleavage products AICD-Flag and A β were detected by Western blot analysis. (B) AICD and A β production for all individual phosphosite mutants were estimated by densitometric analysis of Western blots from three independent experiments. AICD and A β productions were normalized to mature PS1-NTF and thus expressed as AICD:PS1-NTF and A β :PS1-NTF ratios. Data are means \pm S.E. with $n = 3$, and normalized to WT PS1.



Inactivation of brain Cofilin-1 by age, Alzheimer's disease and γ -secretase



Eugenio Barone, Sebastien Mosser, Patrick C. Fraering*

Brain Mind Institute and School of Life Sciences, Ecole Polytechnique Fédérale de Lausanne (EPFL), CH1015 Lausanne, Switzerland

ARTICLE INFO

Article history:

Received 26 June 2014

Received in revised form 21 September 2014

Accepted 6 October 2014

Available online 12 October 2014

Keywords:

Alzheimer's disease

Aging

Cofilin1

γ -Secretase

ABSTRACT

Rapid remodeling of the actin cytoskeleton in the pre- and/or post-synaptic compartments is responsible for the regulation of neuronal plasticity, which is an important process for learning and memory. Cofilin 1 plays an essential role in these processes and a dysregulation of its activity was associated with the cognitive decline observed during normal aging and Alzheimer's disease (AD). To understand the mechanism(s) regulating Cofilin1 activity we evaluated changes occurring with regard to Cofilin 1 and its up-stream regulators Lim kinase-1 (LIMK1) and Slingshot phosphatase-1 (SSH1) in (i) human AD brain, (ii) 1-, 4-, and 10-months old APP/PS1 mice, (iii) wild type 3-, 8-, 12-, 18- and 26-months old mice, as well as in cellular models including (iv) mouse primary cortical neurons (PCNs, cultured for 5, 10, 15 and 20 days *in vitro*) and (v) mouse embryonic fibroblasts (MEF). Interestingly, we found an increased Cofilin1 phosphorylation/inactivation with age and AD pathology, both *in vivo* and *in vitro*. These changes were associated with a major inactivation of SSH1. Interestingly, inhibition of γ -secretase activity with Compound-E (10 μ M) prevented Cofilin1 phosphorylation/inactivation through an increase of SSH1 activity in PCNs. Similarly, MEF cells double knock-out for γ -secretase catalytic subunits presenilin-1 and -2 (MEF_{DKO}) showed a strong decrease of both Cofilin1 and SSH1 phosphorylation, which were rescued by the over-expression of human γ -secretase. Together, these results shed new light in understanding the molecular mechanisms promoting Cofilin1 dysregulation, both during aging and AD. They further have the potential to impact the development of therapies to safely treat AD.

© 2014 Elsevier B.V. All rights reserved.

1. Introduction

Alzheimer's disease (AD) is the most common form of dementia among the elderly. Amyloid- β peptides (A β) form senile plaques, which, together with hyperphosphorylated tau-based neurofibrillary tangles (NFT), are the hallmarks of AD neuropathology [1]. From a clinical point of view, a decline in episodic memory is observed, often mistaken with normal aging-related cognitive deficiencies [1]. These similarities raised questions about the role of aging in AD onset and progression, thus demanding major efforts to clarify the molecular mechanisms underlying these processes [2].

A β is strongly suspected to play a major role in the development of dementia. Elevated A β levels produce abnormalities in learning and synaptic functions in amyloid precursor protein (APP) transgenic mice

[3,4]. Furthermore, studies in human [5,6] and 3 \times Tg-AD mice (triple transgenic model of AD) [7] highlighted the importance of soluble endocytosed intraneuronal A β as the initial mediator of Tau pathology and cognitive decline. Indeed, although senile plaque-formation has been widely proposed to be responsible of the A β toxic effects, meticulous analyses of AD patients suggest that the soluble pool of A β_{42} correlates better with cognitive decline than A β plaques [5,6,8]. Oligomers of A β_{42} significantly (i) diminish long-term potentiation (LTP), which is needed for learning and memory [9], (ii) promote an increase of oxidative stress [10–12], (iii) impair synaptic functions [9,12]. Whether these effects are mainly due to the extracellular or to the endocytosed A β remain to be clarified, although disturbances in the metabolism of A β might regionally increase A β_{42} levels that negatively modulate neuronal activity and potentially lead to a decline in cognitive performance [13].

A β peptides are derived from APP, a type I membrane protein that undergoes a first cleavage by β -secretase leading to the production of a 99 amino-acid long APP-C99 (APP-C-terminal fragment). The latter is further processed within the membrane bilayer by the intramembrane aspartyl-protease γ -secretase to generate an APP intracellular domain (AICD) released into the cytoplasm, and A β secreted in the extracellular compartment [14]. Despite the prominent role of γ -secretase in driving A β production, its involvement in the cellular pathways regulating cognitive processes is controversial because both the increase and the lack of γ -secretase activity were reported to impair synaptic function and neuronal survival [15–18]. APP is not the unique substrate for γ -

Abbreviations: AD, Alzheimer's disease; APP, amyloid precursor protein; APP/PS1, APP^{KM670/671NL}/PS1^{L166P} transgenic mice; APP_{KO}, amyloid precursor protein knockout mice; A β , Amyloid- β peptides; Cofilin1, Cofilin isoform 1; CpDE, Compound E; DIV, days *in vitro*; DMSO, dimethyl sulfoxide; LIMK1, LIM kinase isoform 1; MEFs, mouse embryonic fibroblasts; MEF_{DKO}, MEFs lacking both catalytic subunits of γ -secretase, presenilin-1 and -2; MEF_{DKO} + γ -secretase, MEF_{DKO} Cell line stably overexpressing the human γ -secretase complex; NFT, neurofibrillary tangles; PCNs, primary cortical neurons; pCofilin1, phosphorylated Cofilin isoform 1; pLIMK1, phosphorylated LIM kinase isoform 1; PS1, presenilin 1; pSSH1, phosphorylated Slingshot phosphatase isoform 1; SSH1, Slingshot phosphatase isoform 1; WT, wild type

* Corresponding author.

E-mail address: patrick.fraering@epfl.ch (P.C. Fraering).

<http://dx.doi.org/10.1016/j.bbadis.2014.10.004>

0925-4439/© 2014 Elsevier B.V. All rights reserved.

secretase, which is responsible for the cleavage of a broad range of protein receptors playing a role in neuronal trafficking and synaptic plasticity [reviewed in [19]].

Recently, modifications of γ -secretase by nitrosative stress were found to be responsible for an age-dependent increase of the $A\beta_{42}/A\beta_{40}$ ratio in rat hippocampal neurons, thus offering a new possible mechanism linking aging and AD [20]. Indeed, the accumulation of $A\beta_{42}$ would trigger a pathological mechanism leading to an aberrant neuritic morphology, sprouting and breakdown [21], which affect the structure of synapses and lead to (i) altered neuronal electrophysiology [22], (ii) inhibition of long-term potentiation [23] and (iii) transient memory deficits [24].

These phenomena strictly involve the actin cytoskeleton, which actively participates in the maturation and in the maintenance of the synapses by regulating spine morphology [25], receptor anchoring/trafficking and synaptic plasticity [26,27]. Among numerous actin-binding proteins, the actin-depolymerizing factor (ADF)/cofilin family proteins, comprising in mammals Cofilin1 (a non-muscle type), Cofilin2 (a muscle-type) and ADF (also known as destrin), critically control actin filament dynamics and reorganization by severing and depolymerizing actin filaments [28]. A growing body of evidence lends support to a link between neurite transport defects or impaired synaptic plasticity observed with age or in neurodegenerative diseases, and alterations in the organization and dynamics of the actin cytoskeleton initiated by Cofilin1 [27,29–31]. Regulation of Cofilin1 activity is quite complex and involves cross-talking pathways [30]. In particular, Cofilin1 is inactivated by LIM kinase isoform 1 (LIMK1)-mediated phosphorylation at Serine 3 (Ser3), and is reactivated by Slingshot phosphatase isoform 1 (SSH1)-mediated dephosphorylation [28]. Although other kinases and phosphatases can affect Cofilin1 activity, LIMK1 and SSH1 show the highest substrate specificity [30]. Remarkably, phosphorylation of Threonine 508 activates LIMK1 whereas phosphorylation at Serine 937 and 978 inactivates SSH1 [28]. In addition, not only Cofilin1 but also LIMK1 is a substrate for SSH1 activity, which in this way can control Cofilin1 activation either directly or indirectly through an upstream regulation of LIMK1 [32].

In this study, we show that a dysregulation of SSH1/LIMK1/Cofilin1 (hereafter, Cofilin1 pathway) occurs in the brain as an effect of both age and AD pathological features. We further demonstrate that γ -secretase activity is involved in the regulation of both Cofilin1 protein levels and phosphorylation/inactivation, providing potential new insights into the molecular mechanisms that link aging to AD.

2. Materials and methods

2.1. Human tissues

Post-mortem tissues from frontal cortex were obtained from the Joseph and Kathleen Bryan Alzheimer's Disease Research Center, Duke University Medical Center [33]. Controls were compared to patients with moderate to severe Alzheimer's disease. The age of death, gender and postmortem interval were comparable in both groups. Demographic and diagnostic features available for patients used in this study are showed in the Supplementary Table 1.

2.2. Animals

All animal procedures were performed in accordance to Swiss authority guidelines. Animals were sacrificed at the selected age, brains were extracted, weighed, flash-frozen, and stored at -80°C until total protein extraction from one hemisphere and further analyses. Frozen brain specimens were obtained from 3-, 8-, 12-, 18- and 26-months old wild type (WT) (C57Bl/6 J) mice and 1-, 4- and 10-months old $\text{App}^{\text{KM670}/671\text{NL}}/\text{PS1}^{\text{L166P}}$ transgenic mice (APP/PS1) mice [34] or APP knock-out (APP_{KO}) mice [35], and their littermate controls. APP/PS1 mice were studied at 1, 4 and 10 months of age, because this

is the time frame during which these mice develop all pathological AD features [34]. Indeed, cerebral amyloidosis starts at 6–8 weeks, and the ratio of human amyloid $A\beta_{42}/A\beta_{40}$ is respectively 1.5 and 5 in pre-depositing (1 month-old) and amyloid-depositing mice (4 and 10 months-old). Consistent with this ratio, extensive congophilic parenchymal amyloid but minimal amyloid angiopathy is observed [34]. Amyloid-associated pathologies include dystrophic synaptic boutons, hyperphosphorylated tau-positive neuritic structures and robust gliosis, with neocortical microglia number increasing threefold from 1 to 8 months of age. Global neocortical neuron loss is not apparent up to 8 months of age, but local neuron loss in the dentate gyrus is observed. In addition, diffuse $A\beta$ plaques are strongly increased at 8 month and defects in cognition were observed only at 8 month [34]. Because the age process in WT mice is much longer than that observed in APP/PS1 mice, we have decided not to limit the analysis of the Cofilin1 pathway in WT mice to the time points selected for APP/PS1 mice. Indeed, according to the American Federation of Aging Research criteria (<http://www.afar.org/research/funding/animal-use/>), 2–3 months-old mice can be considered young and they represent the biological equivalent of teen-agers and college freshmen, whereas 26 months-old mice can be considered old, taking also into consideration that a median survival is of about 24 months. Finally APP_{KO} mice [35] were studied at the same time points selected for APP/PS1 mice to test whether the changes observed in a model characterized by an accelerated APP cleavage (APP/PS1) were different in the absence of APP protein.

2.3. Cell culture and treatments

Mouse primary cortical neurons (PCNs) were prepared from embryonic day 17 Ofl mouse fetal brains. Cortices were digested in a media containing papain (20 U/ml, Sigma-Aldrich GmbH, Buchs, Switzerland) and dissociated by mechanical trituration. Cells were plated in neurobasal medium (Invitrogen, LuBioScience GmbH, Lucerne, Switzerland) supplemented with B27 (Invitrogen, LuBioScience GmbH, Lucerne, Switzerland) and 2 mM L-glutamine on poly-L-ornithine coated plates at 1×10^5 cells/cm² at 37 °C in a humidified 5% CO₂ atmosphere. At day 5, 10, 15 and 20, neurons were washed twice with PBS and proteins were extracted as described below. The criteria to univocally establish at what age *in vitro* PCNs reflect aging neurons *in vivo* do not appear very clear due to divergent interpretations. Indeed, from one side, it was reported that during the first week, *in vitro* mouse PCNs establish morphological and functional axons and dendrites; during the second week they establish synaptic activity and from the third week on (14 DIV) they begin to show canonical signs of aging, including (i) accumulation of ROS, (ii) lipofuscin granules, (iii) heterochromatic foci, (iv) activation of the c-Jun N-terminal protein kinase (JNK) and (v) the DNA repair p53/p21 pathways as well as (vii) cholesterol loss and (viii) increased cholesterol-24-hydroxylase [36–38]. In addition, *in vitro* hippocampal neurons cultured for 3 weeks (21 DIV) undergo a time-associated increase in tubulin acetylation similar to that observed *in vivo*, and a time-associated increase in the phosphorylation of the microtubule-associated protein Tau [38] similar to those reported either in aged human brains [39] or in mouse models of senescence [40]. On the other side, it has been shown that starting at 28 DIV, mouse PCNs present a time-dependent and significant increase in known features of the aging brain, including protein oxidation, creatine kinase expression and calcium channel density [41,42]. In addition, based on phase contrast microscopy and the evaluation of the neuronal nuclear protein NeuN levels in mouse PCNs cultured from 5 to 60 DIV, it seems that (i) 20–25 DIV cultured neurons show typical signs of neuronal maturation, while (ii) only a subset of the neuronal population survives through DIV60 [43]. Thus, this spontaneous age-related loss of neurons supports an important distinction between DIV 20–25 neurons (“matured neurons”) and DIV60 neurons (“aged neurons”). Based on the above-cited information, 20 DIV neurons used in this study may better reflect mature-to-old neurons *in vivo*, and not exclusively aging neurons in the brain. To test γ -secretase activity-dependent changes of

Cofilin1 pathway, the day before the selected time points, neurons were treated overnight with DMSO (0.25%) or γ -secretase inhibitor Compound E (CpdE) (10 μ M, Merck Millipore, Darmstadt, Germany) and then subjected to Western Blot analysis as described below. Mouse Embryonic Fibroblasts: (i) wild-type (MEF), (ii) double knock-out for presenilin-1 (PS1) and -2 (PS2) [MEF_{DKO}, [44,45]] and (iii) double knock-out overexpressing the human γ -secretase complex [MEF_{DKO} + h γ -secretase, [46]] were grown in 10 cm dishes in DMEM, supplemented with 10% fetal bovine serum (FBS) and penicillin/streptomycin (P/S) (Invitrogen, LuBioScience GmbH, Lucerne, Switzerland).

2.4. Western Blot

Total protein extracts were prepared in 1% NP40-HEPES buffer (50 mM HEPES, pH 7.0, 150 mM NaCl, 5 mM MgCl₂, 5 mM CaCl₂), supplemented with protease inhibitor cocktail (Roche, Rotkreuz, Switzerland), and were clarified by centrifugation for 1 h at 16,000 \times g, 4 °C. Protein concentrations were determined using standard BCA assay (Pierce, Rockford, IL, USA). Ten micrograms of protein were resolved on 4–12% Bis-Tris PAGE gels (Invitrogen, LuBioScience GmbH, Lucerne, Switzerland), or on standard 12% acrylamide/bisacrylamide Tris Glycine gels for SDS-PAGE analysis. For immunoblot analysis, gels were transferred onto nitrocellulose membranes (Whatman, Dassel, Germany), and incubated overnight at 4 °C with the following antibodies: anti-Cofilin1 612144 (1:1000, Bd Transduction Laboratories, Allschwil, Switzerland) anti-phospho(Ser3)-Cofilin1 3311 s (1:500, Cell Signaling, Bioconcept, Allschwil, Switzerland), anti-phospho(Ser3)-Cofilin1 ab12866 (1:1000, abcam, Cambridge, United Kingdom), anti-LIMK1 ab87971 (1:1000, abcam, Cambridge, United Kingdom), anti-phospho(Thr508)-LIMK1 ab38508 (1:500, abcam, Cambridge, United Kingdom), anti-SSH1 ab107799 (1:1000, abcam, Cambridge, United Kingdom), anti-phospho(Ser978)-SSH1 SP3901 (1:500, ECM Biosciences, Versailles, KY, USA), anti-PS1 ab10281 (1:1000, abcam, Cambridge, United Kingdom), anti-APP-C terminal fragments (CTFs) A87717 (1:10,000, Sigma-Aldrich, GmbH, Buchs, Switzerland), anti-Chronophin 4686 (1:500, Cell Signaling, Bioconcept, Allschwil, Switzerland) and anti- β -actin A2066 (1:5000, Sigma-Aldrich GmbH, Buchs, Switzerland). Membranes were developed by using anti-mouse/rabbit/rat IgG conjugated to Alexa 680 or 800 purchased from Invitrogen (LuBioScience GmbH, Lucerne, Switzerland). The Odyssey infrared imaging system (LICOR, Bad Homburg, Germany) was used to detect the fluorescent signal. For each antibody used in this study, a dose–response analysis was performed by loading 15–40 μ g total proteins from 3 months-old WT mouse brain whole homogenate – this is to correlate changes observed in signal strength with changes observed at the protein levels (Supplementary Fig. 1). As shown in Supplementary Fig. 1, all signals exhibit linearity at the protein levels tested and the protein amount (30 μ g) we used for sample analysis all over the manuscript falls into this linear range.

2.5. A β quantification

Cultures media from 5, 10, 15 and 20 days *in vitro* (DIV) neurons were collected, protease inhibitor cocktail (Roche, Rotkreuz, Switzerland) added, and A β peptides were quantified using mouse A β ₄₀ and A β ₄₂ ELISA kits (KHB3481, KHB3441; Invitrogen, LuBioScience GmbH, Lucerne, Switzerland).

2.6. Statistical analysis

All experiments were performed at least twice with comparable results, and all data are presented as means \pm SEM of n independent samples per group. Student's *t* test was applied for statistical analysis. *P* < 0.05 was considered significantly different from the reference value.

3. Results

3.1. The Cofilin1 activation state is altered in AD human brains

Hyperactive cofilin forming rod-shaped cofilin-saturated actin filament bundles (rods) were previously reported over A β plaques in the hippocampus of AD subjects, suggesting abnormal Cofilin1 aggregation in response to neurodegenerative stimuli [47,48]. Because of the pivotal role of γ -secretase in driving AD pathology and based on a significant increase of its activity in the brain of sporadic AD subjects [49], we analyzed the Cofilin1 pathway in the frontal cortex of seven sporadic AD subjects (average age 87.8 \pm 1.6 years) and their age-matched controls (average age 82.6 \pm 2.7 years) [33]. As shown in Fig. 1, a significant \sim 1.6 fold-increase of the pCofilin1/Cofilin1 ratio (Fig. 1-c) is observed in the frontal cortex of AD subjects with respect to controls, suggesting that Cofilin1 gets inactivated in diseased brains. To extend our knowledge about the mechanisms responsible for Cofilin1 inactivation in AD, we further demonstrated defects in SSH1 activity. As shown in Fig. 1-g, a \sim 45% significant reduction of total SSH1 protein levels associated with

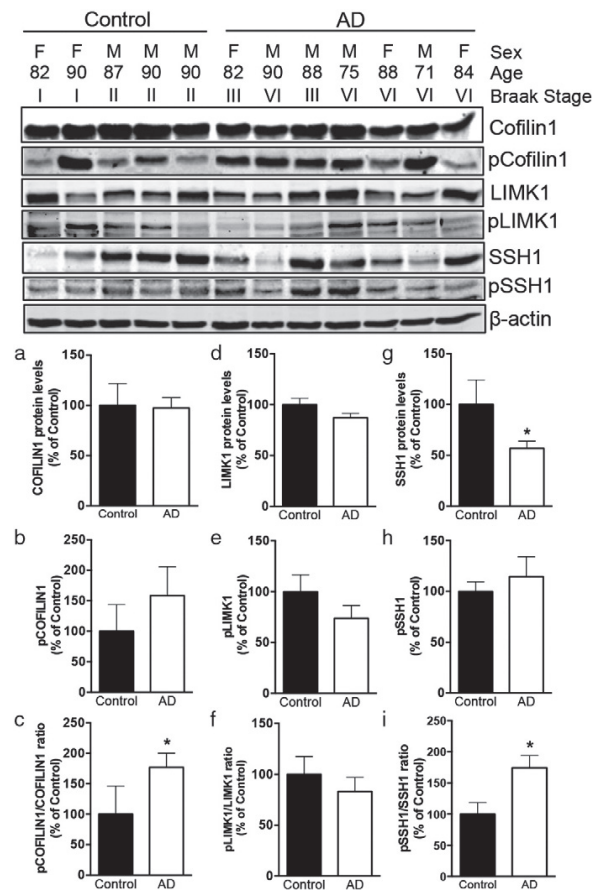


Fig. 1. Cofilin1 inactivation in the frontal cortex of sporadic human Alzheimer's disease. Changes observed with regard to the Cofilin1 pathway in the frontal cortex of sporadic Alzheimer's disease subjects (*n* = 7), relative to their age-matched controls (*n* = 5). *Top panels:* Western blot analyses of total protein extracts. *Bottom panels:* densitometric analyses of Western blot protein bands: (a) Total Cofilin1 protein levels; (b) pCofilin1 levels; (c) pCofilin1/Cofilin1 ratio; (d) Total LIMK1 protein levels; (e) pLIMK1 levels; (f) pLIMK1/LIMK1 ratio; (g) Total SSH1 protein levels; (h) pSSH1 levels; (i) pSSH1/SSH1 ratio. Protein levels were normalized to the loading control β -actin. Densitometric values shown in the histograms are given as percentage of Control samples set as 100%. Means \pm SEM, **P* < 0.05 vs Control.

unchanged pSSH1 levels led to the significant increase of the pSSH1/SSH1 ratio (Fig. 1-i). The latter suggests an inactivation of SSH1 in AD brains. No significant changes were observed for LIMK1 protein levels and phosphorylation (Fig. 1-d–f). Altogether, these observations suggest that the increased Cofilin1 inactivation observed in our AD samples could be mediated, at least in part by the loss of SSH1 activity.

3.2. AD pathology-associated inactivation of Cofilin1 in the brain of APP/PS1 mice

To better understand the altered pattern of expression/activation of Cofilin1 in AD, we analyzed changes of the Cofilin1 pathway in 1-, 4-, and 10-months old APP/PS1 mice [34], a well-known model of AD characterized by age-associated increase of pathological features including A β senile plaques and cognitive deficits [34]. As shown in Fig. 2A-a, Cofilin1 protein levels are significantly reduced by ~65% and ~50% at 4- and 10-months of age, with respect to 1-month-old mice. The analysis of pCofilin1 further revealed a significant ~70% decrease at 4 months of age, whereas an increase of about 70% was observed at 10 months (Fig. 2A-b). Interestingly, 10-months old APP/PS1 mice showed a 7-fold increase in the pCofilin1/Cofilin1 ratio, with respect to the young, 1-month old mice (Fig. 2A-c). In order to assess whether alteration of Cofilin1 phosphorylation can be explained by modifications of its upstream regulators, we next evaluated changes occurring for LIMK1 and SSH1. As shown in Fig. 2A-d, total LIMK1 did not show any significant changes at 1-, 4- and 10-months. Conversely, pLIMK1 levels were drastically increased (by ~200%) at 10-months of age, with respect to the 1-month-old mice (Fig. 2A-e). Consequently, the pLIMK1/LIMK1 ratio showed a 3.5-fold increase at 10-months (Fig. 2A-f), suggesting an overactivation of LIMK1 in aged mice. With regard to SSH1 phosphatase the most drastic effect was observed for the inactive pSSH1 at 10-months of age, with an increase of ~200% with respect to 1-month-old mice (Fig. 2A-h). As a consequence, a 3.9-fold increase of the pSSH1/SSH1 ratio was observed (Fig. 2A-i), suggesting an inactivation of SSH1 in aged mice.

Finally, in order to evaluate whether the increased phosphorylation/inactivation of Cofilin1 in 10-months-old APP/PS1 mice was the result of AD-related pathology, the Cofilin pathway was examined in APP/PS1 mice and their littermate WT controls. As shown in Fig. 2B, Cofilin1 and pCofilin1 protein levels were respectively reduced by ~45% (Fig. 2B-a) and increased by ~80% (Fig. 2B-b) in AD mice, with respect to the littermate matched WT controls. As a consequence of these changes, the pCofilin1/Cofilin1 ratio showed a significant 6-fold increase (Fig. 2B-c), suggesting again an inactivation of Cofilin1 in AD mice. These lines of evidence parallel with changes observed with regard to LIMK1 and SSH1. Indeed, in APP/PS1 mice both LIMK1 and SSH1 protein levels were reduced by ~40% (Supplementary Fig. 2-a and b), while pLIMK1 and pSSH1 levels were significantly increased by ~40% and ~140%, respectively (Supplementary Fig. 2-b and e). The drastic increases of both pLIMK1/LIMK1 (~2.5-fold, Supplementary Fig. 2-c) and pSSH1/SSH1 (~5-fold, Supplementary Fig. 2-f) ratios suggest again an activation of LIMK1 and an inactivation of SSH1 in the brain of 10-months old AD mice.

3.3. Age-dependent Cofilin1 inactivation in the brain of WT mice

We next investigated whether aging, in the absence of AD, plays a role in the Cofilin pathway alterations observed in AD human/mice

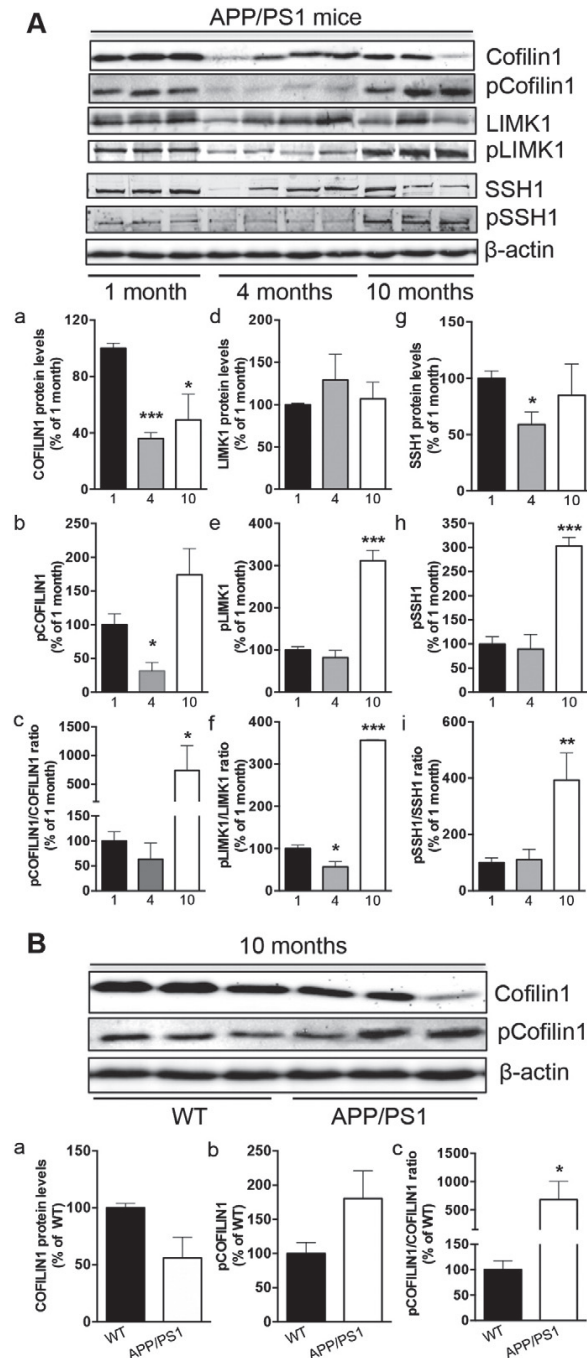


Fig. 2. Alzheimer's disease pathology-associated changes of the Cofilin1 pathway proteins in the brain of APP/PS1 mice. (A) Age-dependent changes observed with regard to proteins controlling the Cofilin1 pathway, in the brain of 1- (n = 3), 4- (n = 4) and 10-months old (n = 3) APP/PS1 mice. Top panels: Western blot analyses of total protein extracts. Bottom panels: densitometric analyses of Western blot protein bands: (a) Total Cofilin1 protein levels; (b) pCofilin1 levels; (c) pCofilin1/Cofilin1 ratio; (d) Total LIMK1 protein levels; (e) pLIMK1 levels; (f) pLIMK1/LIMK1 ratio; (g) Total SSH1 protein levels; (h) pSSH1 levels; (i) pSSH1/SSH1 ratio. (B) Decreased total Cofilin1 protein levels and increased pCofilin1 levels in 10-months old APP/PS1 mice (n = 3), with respect to their littermate WT controls (n = 3). Top panels: Western blot analyses of total protein extracts. Bottom panels: densitometric analyses of Western blot protein bands: (a) Total Cofilin1 protein levels; (b) pCofilin1 levels; (c) pCofilin1/Cofilin1 ratio. Protein levels were normalized to the loading control β -actin. Densitometric values shown in the histograms are given as percentage of 1-month-old mice (A) or WT mice (B) set as 100%. Means \pm SEM, *P < 0.05, **P < 0.01 and ***P < 0.001 vs Control (A) or WT (B).

samples. To do so, we evaluated changes in the Cofilin pathway occurring in the brains of 3-, 8-, 12-, 18- and 26-month old WT mice. When compared to 3-month old mice, Cofilin1 protein levels were significantly reduced by ~25% both at 8 and 26 months (Fig. 3-a). Yet, the major change was observed for pCofilin1, which was increased by ~76% in the oldest 26 months-old mice (Fig. 3-b), leading to a ~2.3-fold increase of the pCofilin1/Cofilin1 ratio (Fig. 3-c). No significant differences were observed for LIMK1 total and phosphorylated protein levels (Fig. 3-d-e). In contrast, an interesting trend was observed for pSSH1. After a significant reduction at both 8 and 12 months (by ~45% and ~35%, respectively), pSSH1 levels significantly raised (by ~27%) at 26 months (Fig. 3-h). Together, and despite the drastic increase of both pCofilin1 levels and pCofilin1/Cofilin1 ratio, no significant changes were found for both pLIMK1/LIMK1 and pSSH1/SSH1 ratios in 26 months-old mice (Fig. 3-f and i). At a first glance, the latter observation does not explain changes observed with regard to Cofilin1. However, an in-depth analysis of the results suggests that 8 months possibly represents a turning point in the aging process occurring in our mice. Indeed, from 8 to 26 months, a clear increase of pCofilin1 occurs (Fig. 3-b), possibly caused by an age-dependent inactivation of SSH1 revealed by the rise of the pSSH1 levels (Fig. 3-h) and the pSSH1/SSH1 ratio (Fig. 3-i) in the same time frame.

3.4. Inactivation of Cofilin1 during neuronal maturation in vitro

We next assessed whether changes in the Cofilin1 pathway could be observed during neuronal maturation, in mouse PCNs cultured for 5, 10, 15 and 20 days. These time points were selected because (i) an increase of synaptic density [50], (ii) a linear increase of A β production [51] and (iii) a shift with regard to γ -secretase activity towards more amyloidogenic pathways [20] occur within this time frame. Also, primary neuronal cultures undergo a whole series of morphological and functional maturation processes that reflect at least partially those of their counterparts *in vivo* [20,36,37,41,42,52]. As shown in Fig. 4-a and b, Cofilin1 and pCofilin1 protein levels were respectively reduced and increased in an age-dependent manner from 5 to 20 DIV (Fig. 4-a). These changes led to age-dependent increases in the pCofilin1/Cofilin1 ratio, starting at 10 DIV (~2.6 fold), increasing at 15 DIV (~3.3 fold) and reaching the maximum at 20 DIV (~4.5 fold), with respect to 5 DIV (Fig. 4-c). Similarly, changes of total LIMK1 (Fig. 4-d) and pLIMK1 (Fig. 4-e) protein levels lead to an age-dependent increase in the pLIMK1/LIMK1 ratio, reaching about 75% at 20 DIV (Fig. 4-f). Interestingly, significant and age-associated increases in SSH1 and pSSH1 protein levels were also observed (Fig. 4-g and h), causing a marked increase in the pSSH1/SSH1 ratio both at 15 DIV (~1.9-fold)

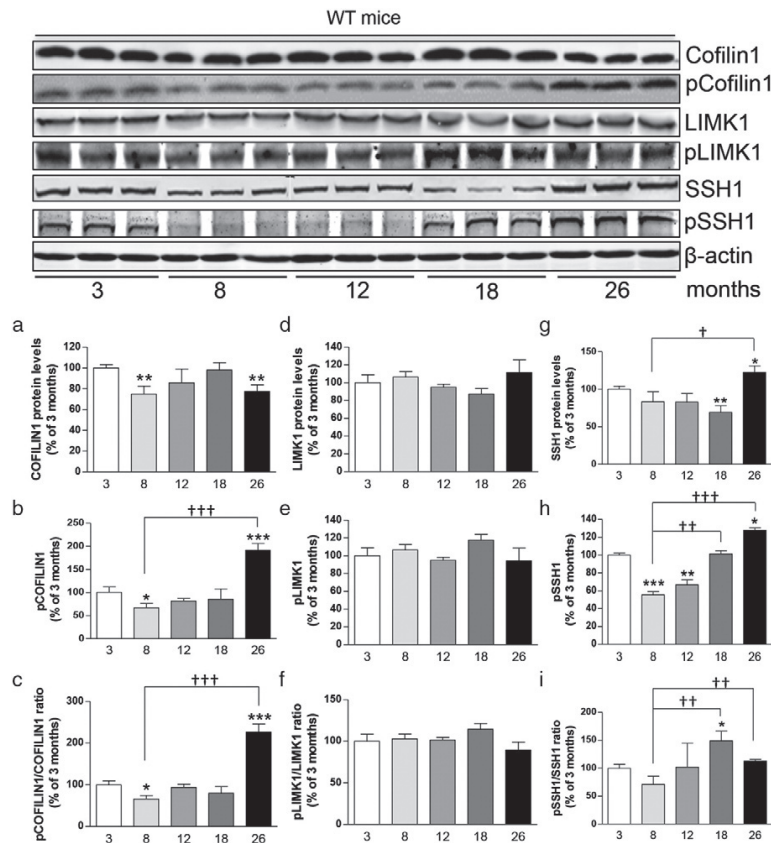


Fig. 3. Age-associated changes of the Cofilin1 pathway in the brain of WT mice. Age-associated changes observed with regard to proteins implicated in the Cofilin1 pathway, in the brain of 3- (n = 5), 8- (n = 4), 12- (n = 5), 18- (n = 5) and 26-months old (n = 4) WT mice. Representative gels obtained with 3 blind selected samples per group are shown. *Top panels:* Western blot analyses of total protein extracts. *Bottom panels:* densitometric analyses of Western blot protein bands: (a) Total Cofilin1 protein levels; (b) pCofilin1 levels; (c) pCofilin1/Cofilin1 ratio; (d) Total LIMK1 protein levels; (e) pLIMK1 levels; (f) pLIMK1/LIMK1 ratio; (g) Total SSH1 protein levels; (h) pSSH1 levels; (i) pSSH1/SSH1 ratio. Protein levels were normalized to the loading control β -actin. Densitometric values shown in the histograms are given as percentage of 3 months-old mice set as 100%. Means \pm SEM, *P < 0.05, **P < 0.01 and ***P < 0.001 vs 3-months old mice; †P < 0.05, ††P < 0.01 and †††P < 0.001 vs 8-months old mice.

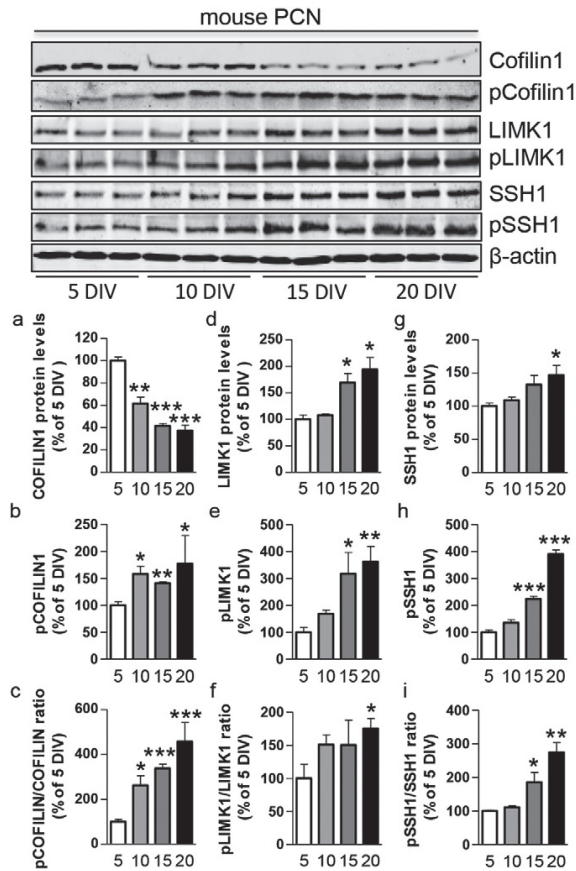


Fig. 4. Cofilin1 pathway changes during mouse primary cortical neurons (PCNs) maturation *in vitro*. Age-associated changes of proteins from the Cofilin1 pathway in mouse PCNs at 5, 10, 15, and 20 days *in vitro* (DIV) ($n = 3$ independent cultures/group). *Top panels:* Western blot analyses of total protein extracts. *Bottom panels:* densitometric analyses of Western blot protein bands: (a) Total Cofilin1 protein levels; (b) pCofilin1 levels; (c) pCofilin1/Cofilin1 ratio; (d) Total LIMK1 protein levels; (e) pLIMK1 levels; (f) pLIMK1/LIMK1 ratio; (g) Total SSH1 protein levels; (h) pSSH1 levels; (i) pSSH1/SSH1 ratio. Protein levels were normalized to the loading control β -actin. Densitometric values shown in the histograms are given as percentage of 5 DIV PCNs set as 100%. Means \pm SEM, * $P < 0.05$, ** $P < 0.01$ and *** $P < 0.001$ vs 5 DIV.

and at 20 DIV (~2.7-fold), in comparison to the younger 5 DIV neurons (Fig. 4-i). Altogether, both LIMK1 activation (Fig. 4-f) and SSH1 inactivation (Fig. 4-i) with age are very consistent with the observed Cofilin1 inactivation (Fig. 4-c).

3.5. γ -Secretase is a negative regulator of Cofilin1 activation

In agreement with previous results [20], we observed in our PCNs cultures that increased secreted $A\beta_{42}$ and $A\beta_{40}$ levels (Supplementary Fig. 3A) are associated with changes of the $A\beta_{42}/A\beta_{40}$ ratio, from 5 to 20 DIV (Supplementary Fig. 3B). These changes include a switch towards the production of the more amyloidogenic $A\beta_{42}$ peptides, possibly suggesting age-dependent modifications of the γ -secretase specific activity. Because of that observation, we further hypothesized that γ -secretase activity can affect the Cofilin1 pathway, possibly in an age-dependent manner. To challenge this hypothesis, 5, 10, 15 and 20 DIV mouse PCNs were treated for 24 h with 10 μ M of CpdE, a potent γ -secretase inhibitor. First, we found that DMSO alone did not affect

Cofilin-1 protein levels and phosphorylation changes observed in untreated neurons with age (Fig. 5A-a-c). Conversely, inhibition of γ -secretase activity promotes a significant decrease (by about 35%) of total Cofilin1 levels, only at 20 DIV with respect to DMSO-treated PCNs (Fig. 5A-a). Importantly, pCofilin1 levels were reduced at 10, 15 and 20 DIV (by ~40%, ~50% and ~50, respectively) in CpdE-treated neurons, reaching statistical significance at 15 DIV and 20 DIV (Fig. 5A-b). Together, a significant decrease of the pCofilin1/Cofilin1 ratio was observed in CpdE-treated neurons at 10 DIV (~1.5 fold), 15 DIV (~1.4 fold) and 20 DIV (~1.3 fold) (Fig. 5A-c). Since we observed a γ -secretase dependent reduction of both total Cofilin1 and pCofilin1 protein levels only in 20 DIV neurons, and since older PCNs showed a significant increase in the $A\beta_{42}/A\beta_{40}$ ratio (Supplementary Fig. 3B), we decided to further evaluate the effect of γ -secretase activity on LIMK1 and SSH1 in 20 DIV PCNs. As shown in Figs. 5B-d-e, inhibition of γ -secretase did not affect LIMK1 protein levels or phosphorylation. Conversely, we observed a drastic ~50% decrease of pSSH1 levels in CpdE-treated neurons, with respect to DMSO-treated cells (Fig. 5B-h). The consistent reduction of pSSH1 levels together with no changes of SSH1 levels resulted in a strong ~1.6-fold reduction of the pSSH1/SSH1 ratio (Fig. 5B-i). Altogether, these results suggest that γ -secretase activity could induce Cofilin1 phosphorylation through the inhibition of SSH1. To exclude any off-target phenotype caused by the use of a chemical γ -secretase inhibitor, we next analyzed the Cofilin pathway in MEF_{DKO} cells characterized by a complete genetic inhibition of γ -secretase activity, caused by the knock-out of both PS1 and PS2 catalytic subunits [44,45]. In this cell line, and with respect to MEFs WT, we found decreased total Cofilin1 (~50%, Fig. 5C-a) and pCofilin-1 (~70%, Fig. 5C-b) levels, as well as a reduced pCofilin1/Cofilin1 ratio (~1.4-fold, Fig. 5C-c). A significant decrease was also observed for SSH1 protein levels (~30%, Fig. 5C-d) and phosphorylation (~45%, Fig. 5C-e), as well as for pLIMK1 (~35%, Supplementary Fig. 4B-b). To confirm that changes observed in MEF_{DKO} cells were indeed dependent on γ -secretase activity, we took advantage of the MEF_{DKO} + h γ -secretase stable cell line previously generated in our laboratory [46], and that is characterized by a rescued γ -secretase activity via the overexpression of human γ -secretase. When compared to MEF_{DKO} cells, restored γ -secretase activity triggers a significant increase of pCofilin1 (~80%, Fig. 5C-b), to levels comparable to those of the control MEFs WT cell line. Furthermore, both SSH1 total protein levels and phosphorylation were rescued in MEF_{DKO} + h γ -secretase (Fig. 5C-d and C-e) and a net increase of the pSSH1/SSH1 ratio with respect to MEF_{DKO} cells was observed (Fig. 5C-f). These results are in good agreement with those obtained in mouse PCNs treated with CpdE and suggest a role for γ -secretase in SSH1-mediated regulation of Cofilin1 phosphorylation/inactivation.

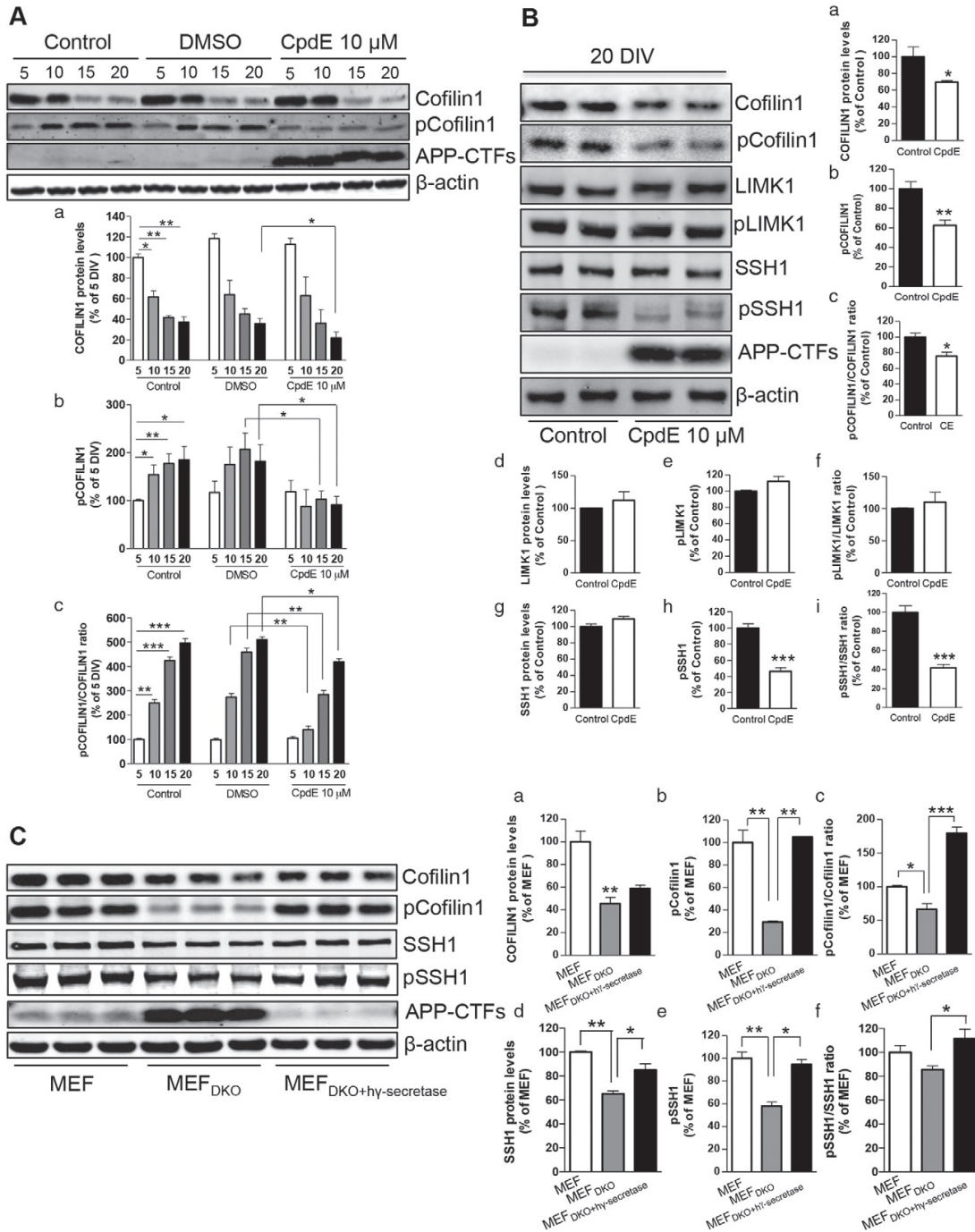
4. Discussion

The mechanisms by which Cofilin1 regulates cognitive processes remain quite controversial, as either an excessive activation [47,48,53–56] or inactivation [27,31,57–61] have been reported to contribute to the actin-dependent impairment of synaptic plasticity, and thus learning.

Here we provide new data about changes in the Cofilin1 pathway with age and AD. The significant increase of the pCofilin1/Cofilin1 ratio (Figs. 1, 2A-c and B-c) suggest that Cofilin1 gets inactivated in the brain of AD patients and APP/PS1 mice as a consequence of AD pathology. Furthermore, the age-associated changes observed in WT mice (Fig. 3) and mouse PCNs (Fig. 4), indicate that Cofilin1 inactivation could also be an age-dependent event. To unravel if Cofilin1 inactivation is a cause or a consequence of AD pathology needs further investigation. So far, based on our data, the significant increase of pCofilin1/Cofilin1 ratio in the brain of 10-months old APP/PS1 mice compared to the littermate WT controls (Fig. 2B-c), suggests that AD pathology could accelerate the aging process via Cofilin1 phosphorylation.

Yet, Kim et al. recently reported a decrease of the pCofilin1/Coilin1 ratio in the frontal cortex of sporadic AD patients [56]. Interestingly, and possibly explaining this apparent discrepancy, an in-depth analysis of the latter study revealed a major difference with regard to our work, concerning the age of the subjects analyzed. Indeed, brain samples analyzed in the Kim study came from younger patients (average age;

Controls: 59.6 ± 4.4 ; AD: 62.5 ± 0.6), when compared to the cortical samples characterized in our study, and collected from older patients (Controls: 87.8 ± 1.6 years; AD: 82.6 ± 2.7 years). Because the same antibodies were used in both studies for the analysis by Western blot of Cofilin1 levels, the apparent discrepancy cannot be attributed to the use of different technical approaches (Supplementary Fig. 5), thus



reinforcing our findings supporting a role of both age and AD pathology in the Cofilin1 pathway regulation.

Interestingly, increased pCofilin1 was also observed in maturing mouse PCNs (Fig. 4-b,c), consistent (i) with the role of Cofilin1 in dendritic spine maturation [25,27,28,62] and (ii) the observed increase of synapses density from 5 to 21 DIV [50,63]. Because either loss or inactivation of Cofilin1 is associated with spine morphology alteration and impaired associative learning and extinction memory [27,29,59,63,64] as well as inhibition of long-term depression (LTD) of the N-methyl-D-aspartate (NMDA) receptors [58], it is conceivable that an aberrant inactivation of Cofilin1 observed in human AD brain and both aged WT and APP/PS1 mice (Figs. 1–3) could be responsible for the negative effects on synaptic plasticity and cognition [27,29,59,60,64–67]. This would represent an intriguing link between age and AD pathology (Fig. 6).

The mechanisms driving Cofilin1 activation or phosphorylation/inactivation may be different and dependent, at least in part, on A β levels and aggregation state [53–57]. Most importantly, soluble and fibrillary A β may differentially affect Cofilin1 by promoting either its activation [53] or its inactivation [57]. Whether these events could happen simultaneously or sequentially still remains unclear. Based on our results in APP/PS1 mice, it seems that – with the progression of AD pathology an activation of Cofilin1 occurs at 4 months of age (Fig. 2A-b and Supplementary Fig. 6B-b) followed by a strong inactivation at 10 months (Fig. 2A-b,c and B-c), probably associated with the different pattern of A β deposition in the brain of these mice [34]. From a molecular point of view, A β peptides can differentially impact LIMK1 [30,68] whose activity was found dysregulated in AD and other neurodegenerative disorders [57,69,70]. The novelty of our work is to show for the first time the inactivation of SSH1 in AD brain (Figs. 1-i, 2A-h,i and B-c), thus strengthening the hypothesis that the equilibrium between LIMK1 and SSH1 activities is disrupted in AD. Within that frame, the significant correlations found between pCofilin1 or pCofilin1/Cofilin1 ratio and (i) SSH1 inactivation or (ii) LIMK1 activation in APP/PS1 (Supplementary Fig. 7A-a–g) and WT mice (Supplementary Fig. 8-a–d), as well as in mouse PCNs (Supplementary Figs. 9-a–c and 4A-a–d) likely account for a main role of these two upstream effectors in mediating Cofilin1 dysregulation.

To better understand the molecular mechanisms underlying the observed increase of Cofilin1 phosphorylation both *in vivo* and *in vitro*, we assessed the involvement of γ -secretase (one of the main proteins responsible of A β production) in these processes. A striking finding was that both chemical and genetic inhibition of γ -secretase activity promoted a significant decrease of pCofilin1 and pCofilin1/Cofilin1 ratio, and that this effect was associated with a reduction of SSH1 inhibition (Fig. 5A, B and C). This finding was further supported by the observation that overexpression of human γ -secretase in MEF_{DKO} rescued the observed phenotype (Fig. 5C-b,c and C-e,f), suggesting that γ -secretase activity might promote Cofilin1 phosphorylation through SSH1 inactivation. These changes could result from the reduced processing of one or more γ -secretase substrates whose cleavage products, in turn, regulate cell fate decision [19]. In this regard, APP represents a good candidate substrate. Indeed, the significant decrease of both pCofilin1 and relative pCofilin1/Cofilin1 ratio observed in APP_{KO} mice versus WT mice (Supplementary Fig. 10A-a and B-a) resemble the results obtained following chemical inhibition of γ -secretase activity in mouse PCNs (Fig. 5A and B), or genetic

inhibition γ -secretase in MEF_{DKO} cells (Fig. 5C). Similarly, the increase of both Cofilin1 and SSH1 phosphorylation/inactivation following APP overexpression in MEF cells (Supplementary Fig. 11) recall what we observed in AD brain (Figs. 1 and 2). To unravel whether these changes are directly linked to the loss (APP_{KO} mice) or to an increase (MEF overexpressing APP) of the γ -secretase-dependent cleavage of APP needs further investigations, especially because no significant changes were observed with regard to LIMK1 (Supplementary Fig. 10A-b and B-b), SSH1 (Supplementary Fig. 10A-c and B-c) or Chronophin phosphatase (Supplementary Fig. 10A-d and B-d) in APP_{KO} mice.

Finally, early-onset familial Alzheimer's disease (FAD)-linked PS1 mutants have been reported to cause a drastic loss of γ -secretase activity in cell-free [46], cell-based [71] and *in vivo* [15] experiments. As previously observed *in vivo* [72,73], this loss-of-function is asymmetrical as all FAD-linked PS1 mutants seem to generate higher A β ₄₂/A β ₄₀ ratio compared to PS1-WT. It consequently causes an increased production of the longer and more hydrophobic A β species, namely A β , that accumulates and aggregates early in the course of the disease. Thus, one could anticipate that FAD-linked PS1 mutants would promote Cofilin1 phosphorylation, in line with (i) the observation that fibrillary A β promotes Cofilin1 phosphorylation [57], and (ii) our preliminary results showing that PS1-L166P promotes Cofilin1 phosphorylation (see Supplementary Fig. 12).

5. Conclusions

In conclusion, our work demonstrates an age-dependent increase of Cofilin1 phosphorylation, both in maturing PCNs and in WT mice, which resembles the Cofilin1 phenotype observed in sporadic human AD brain. γ -Secretase seems to play a fundamental role in the proposed mechanism by enhancing Cofilin1 phosphorylation via SSH1 inhibition (Fig. 6). The implication of these results on understanding the molecular mechanisms leading to impaired synaptic plasticity both during aging and AD are profound, and offer a molecular bridge connecting age, AD and the activity of γ -secretase. They further have the possibility to impact the development of therapies to treat AD.

Disclosure statement

The authors all state that there are no conflicts of interests associated with the research presented in this paper.

Acknowledgements

The authors thank M. Staufenbiel for the APP_{KO} mice (a kind gift from Novartis, Basel, Switzerland), M. Jucker for the APP/PS1 mice, B. De Strooper for the MEF_{DKO} cell line, and the Kathleen Bryan Alzheimer's Disease Research Center, Duke University Medical Center funded by NIA grant P30AG028377 for Alzheimer's disease brain tissue samples [33]. The funders had no role in study design, data collection and analysis, decision to publish, or preparation of the manuscript. This work was supported by the Swiss National Science Foundation (to P.C.F., grant 31003A_134938/1), and the Strauss foundation (to P.C.F. and E.B.).

Fig. 5. Chemical and genetic inhibition of γ -secretase activity is associated with Cofilin1 activation. (A) Inhibition of γ -secretase activity with 10 μ M Compound E (CpdE) promotes Cofilin1 activation in mouse PCN at 10, 15 and 20 DIV ($n = 3$ independent cultures/group). A representative WB is shown. *Top panels:* Western blot analyses of total protein extracts. *Bottom panels:* densitometric analyses of Western blot protein bands: (a) Total Cofilin1 protein levels; (b) pCofilin1 levels; (c) pCofilin1/Cofilin1 ratio. (B) Cofilin1 protein levels and phosphorylation are decreased following γ -secretase activity inhibition with 10 μ M Compound E (CpdE) in mouse PCN at 20 DIV ($n = 4$ independent cultures/group). Activation of Cofilin1 parallels with a decrease of SSH1 phosphorylation. A representative WB is shown. *Top left panels:* Western blot analyses of total protein extracts. *Bottom and right panels:* densitometric analyses of Western blot protein bands: (a) Total Cofilin1 protein levels; (b) pCofilin1 levels; (c) pCofilin1/Cofilin1 ratio; (d) Total LIMK1 protein levels; (e) pLIMK1 levels; (f) pLIMK1/LIMK1 ratio; (g) Total SSH1 protein levels; (h) pSSH1 levels; (i) pSSH1/SSH1 ratio. (C) Cofilin1 protein levels and phosphorylation are decreased in mouse embryonic fibroblast (MEF) cells lacking presenilin-1 and -2, the catalytic subunits of the γ -secretase complex (MEF_{DKO}). These changes parallel with a decrease of SSH1 protein levels and phosphorylation. Overexpression of the human γ -secretase complex in MEF_{DKO} cells (MEF_{DKO} + γ -secretase) rescues Cofilin1 phosphorylation (pCofilin1) through the increase of SSH1 inactivation (pSSH1) ($n = 3$ independent cultures/group). *Left panels:* Western blot analyses of total protein extracts. *Right panels:* densitometric analyses of Western blot protein bands: (a) Total Cofilin1 protein levels; (b) pCofilin1 levels; (c) pCofilin1/Cofilin1 ratio; (d) Total SSH1 protein levels; (e) pSSH1 levels; (f) pSSH1/SSH1 ratio. Protein levels were normalized to the loading control β -actin. Densitometric values shown in the histograms are given as percentage of 5 DIV PCNs (Aa–Ac), untreated Control PCNs (Ba–Bi) and uninfected WT MEF (Ca–Cf) set as 100%. Means \pm SEM, * $P < 0.05$, ** $P < 0.01$ and *** $P < 0.001$.

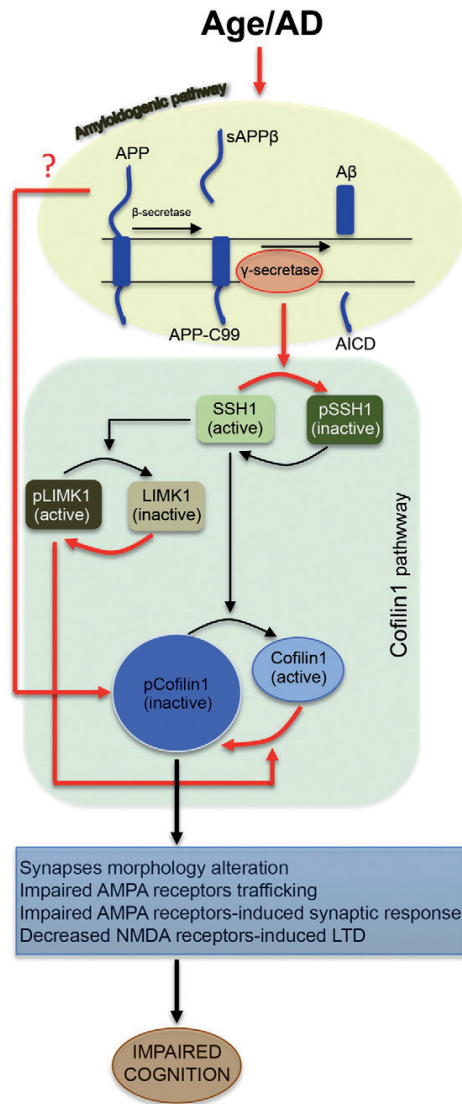


Fig. 6. Model for Age, Alzheimer's disease and γ -secretase-dependent Cofilin 1 inactivation. In this model, we propose that γ -secretase activity, which controls the production of A β peptides, is also regulating the phosphorylation/inactivation of the protein phosphatase Slingshot1 (pSSH1). Reduced SSH1 phosphatase activity promotes an increase of Cofilin1 phosphorylation/inactivation (pCofilin1). Similarly, inactive pSSH1 is no longer able to promote the dephosphorylation/inactivation of the LIMK1 protein kinase (LIMK1), thus contributing both directly and indirectly to maintaining elevated inactive pCofilin1 levels. Finally, the decreased pCofilin1 levels observed in mice lacking APP suggests that APP could promote Cofilin1 phosphorylation/inactivation. Whether the decrease of pCofilin1 observed in APP_{KO} mice is directly linked to the loss of the γ -secretase-dependent cleavage of APP needs further investigation (?). Altogether, increased pCofilin1 could be responsible for (i) synapse morphology alteration; (ii) impaired AMPA receptors trafficking and AMPA receptors-mediated responses; and (iii) decreased NMDA receptors-induced long term depression (LTD), which all together negatively affect cognitive processes. Arrow: stimulation; Red arrow: pathways found altered in our study.

Appendix A. Supplementary data

Supplementary data to this article can be found online at <http://dx.doi.org/10.1016/j.bbadis.2014.10.004>.

References

- [1] H.W. Querfurth, F.M. LaFerla, Alzheimer's disease, *N. Engl. J. Med.* 362 (2010) 329–344.
- [2] A. Kern, C. Behl, The unsolved relationship of brain aging and late-onset Alzheimer disease, *Biochim. Biophys. Acta* 1790 (2009) 1124–1132.
- [3] A.Y. Hsia, E. Masliah, L. McConlogue, G.Q. Yu, G. Tatsuno, K. Hu, D. Kholodenko, R.C. Malenka, R.A. Nicoll, L. Mucke, Plaque-independent disruption of neural circuits in Alzheimer's disease mouse models, *Proc. Natl. Acad. Sci. U. S. A.* 96 (1999) 3228–3233.
- [4] K. Hsiao, P. Chapman, S. Nilsen, C. Eckman, Y. Harigaya, S. Younkin, F. Yang, G. Cole, Correlative memory deficits, Abeta elevation, and amyloid plaques in transgenic mice, *Science* 274 (1996) 99–102.
- [5] L.F. Lue, Y.M. Kuo, A.E. Roher, L. Brachova, Y. Shen, L. Sue, T. Beach, J.H. Kurth, R.E. Rydel, J. Rogers, Soluble amyloid beta peptide concentration as a predictor of synaptic change in Alzheimer's disease, *Am. J. Pathol.* 155 (1999) 853–862.
- [6] C.A. McLean, R.A. Cherny, F.W. Fraser, S.J. Fuller, M.J. Smith, K. Beyreuther, A.I. Bush, C.L. Masters, Soluble pool of Abeta amyloid as a determinant of severity of neurodegeneration in Alzheimer's disease, *Ann. Neurol.* 46 (1999) 860–866.
- [7] R. Medeiros, M.A. Chabrier, F.M. LaFerla, Elucidating the triggers, progression, and effects of Alzheimer's disease, *J. Alzheimers Dis.* 33 (Suppl. 1) (2013) S195–S210.
- [8] J. Hardy, The amyloid hypothesis for Alzheimer's disease: a critical reappraisal, *J. Neurochem.* 110 (2009) 1129–1134.
- [9] D.J. Selkoe, Alzheimer's disease is a synaptic failure, *Science* 298 (2002) 789–791.
- [10] S. Varadarajan, S. Yatin, M. Aksenova, D.A. Butterfield, Review: Alzheimer's amyloid beta-peptide-associated free radical oxidative stress and neurotoxicity, *J. Struct. Biol.* 130 (2000) 184–208.
- [11] D.A. Butterfield, J. Drake, C. Pocernich, A. Castegna, Evidence of oxidative damage in Alzheimer's disease brain: central role for amyloid beta-peptide, *Trends Mol. Med.* 7 (2001) 548–554.
- [12] D.A. Butterfield, The 2013 SFRBM discovery award: Selected discoveries from the butterfly laboratory of oxidative stress and its sequelae in brain in cognitive disorders exemplified by Alzheimer disease and chemotherapy induced cognitive impairment, *Free Radic. Biol. Med.* 74C (2014) 157–174.
- [13] W.L. Klein, Synaptotoxic amyloid-beta oligomers: a molecular basis for the cause, diagnosis, and treatment of Alzheimer's disease? *J. Alzheimers Dis.* 33 (Suppl. 1) (2013) S49–S65.
- [14] C. Haass, A.Y. Hung, M.G. Schlossmacher, T. Oltersdorf, D.B. Teplow, D.J. Selkoe, Normal cellular processing of the beta-amyloid precursor protein results in the secretion of the amyloid beta peptide and related molecules, *Ann. N. Y. Acad. Sci.* 695 (1993) 109–116.
- [15] C.A. Saura, S.Y. Choi, V. Beglopoulos, S. Malkani, D. Zhang, B.S. Shankaranarayana Rao, S. Chattarji, R.J. Kelleher 3rd, E.R. Kandel, K. Duff, A. Kirkwood, J. Shen, Loss of presenilin function causes impairments of memory and synaptic plasticity followed by age-dependent neurodegeneration, *Neuron* 42 (2004) 23–36.
- [16] Y. Mitani, J. Yarimizu, K. Saita, H. Uchino, H. Akashiba, Y. Shitaka, K. Ni, N. Matsuoka, Differential effects between gamma-secretase inhibitors and modulators on cognitive function in amyloid precursor protein-transgenic and nontransgenic mice, *J. Neurosci. Off. J. Soc. Neurosci.* 32 (2012) 2037–2050.
- [17] S.H. Nam, S.J. Seo, J.S. Goo, J.E. Kim, S.I. Choi, H.R. Lee, I.S. Hwang, S.W. Jee, S.H. Lee, C.J. Bae, J.Y. Park, H.S. Kim, S.B. Shim, D.Y. Hwang, Pen-2 overexpression induces Abeta-42 production, memory defect, motor activity enhancement and feeding behavior dysfunction in NSE/Pen-2 transgenic mice, *Int. J. Mol. Med.* 28 (2011) 961–971.
- [18] B.P. Imbimbo, G.A. Giardina, gamma-secretase inhibitors and modulators for the treatment of Alzheimer's disease: disappointments and hopes, *Curr. Top. Med. Chem.* 11 (2011) 1555–1570.
- [19] A. Haapasalo, D.M. Kovacs, The many substrates of presenilin/gamma-secretase, *J. Alzheimers Dis.* 25 (2011) 3–28.
- [20] F.X. Guix, T. Wahle, K. Vennekens, A. Snellinx, L. Chavez-Gutierrez, G. Ill-Raga, E. Ramos-Fernandez, C. Guardia-Laguarta, A. Lleó, M. Arimon, O. Berezovska, F.J. Munoz, C.G. Dotti, B. De Strooper, Modification of gamma-secretase by nitrosative stress links neuronal ageing to sporadic Alzheimer's disease, *EMBO Mol. Med.* 4 (2012) 660–673.
- [21] I. Benilova, E. Karran, B. De Strooper, The toxic Abeta oligomer and Alzheimer's disease: an emperor in need of clothes, *Nat. Neurosci.* 15 (2012) 349–357.
- [22] D.M. Hartley, D.M. Walsh, C.P. Ye, T. Diehl, S. Vasquez, P.M. Vassilev, D.B. Teplow, D.J. Selkoe, Protofibrillar intermediates of amyloid beta-protein induce acute electrophysiological changes and progressive neurotoxicity in cortical neurons, *J. Neurosci. Off. J. Soc. Neurosci.* 19 (1999) 8876–8884.
- [23] D.M. Walsh, I. Klyubin, J.V. Fadeeva, W.K. Cullen, R. Anwyl, M.S. Wolfe, M.J. Rowan, D.J. Selkoe, Naturally secreted oligomers of amyloid beta protein potently inhibit hippocampal long-term potentiation in vivo, *Nature* 416 (2002) 535–539.
- [24] J.P. Cleary, D.M. Walsh, J.J. Hofmeister, G.M. Shankar, M.A. Kuskowski, D.J. Selkoe, K.H. Ashe, Natural oligomers of the amyloid-beta protein specifically disrupt cognitive function, *Nat. Neurosci.* 8 (2005) 79–84.
- [25] K. Okamoto, T. Nagai, A. Miyawaki, Y. Hayashi, Rapid and persistent modulation of actin dynamics regulates postsynaptic reorganization underlying bidirectional plasticity, *Nat. Neurosci.* 7 (2004) 1104–1112.
- [26] Y. Fukazawa, Y. Saitoh, F. Ozawa, Y. Ohta, K. Mizuno, K. Inokuchi, Hippocampal LTP is accompanied by enhanced F-actin content within the dendritic spine that is essential for late LTP maintenance in vivo, *Neuron* 38 (2003) 447–460.
- [27] M.B. Rust, C.B. Gurniak, M. Renner, H. Vara, L. Morando, A. Gorlich, M. Sasseo-Pognetto, M.A. Banchaibouchi, M. Giustetto, A. Triller, D. Choquet, W. Witke, Learning, AMPA receptor mobility and synaptic plasticity depend on n-cofilin-mediated actin dynamics, *EMBO J.* 29 (2010) 1889–1902.

- [28] J.J. Bravo-Cordero, M.A. Magalhaes, R.J. Eddy, L. Hodgson, J. Condeelis, Functions of cofilin in cell locomotion and invasion, *Nat. Rev. Mol. Cell Biol.* 14 (2013) 405–415.
- [29] J. Gu, C.W. Lee, Y. Fan, D. Komlos, X. Tang, C. Sun, K. Yu, H.C. Hartzell, G. Chen, J.R. Bamburg, J.Q. Zheng, ADF/cofilin-mediated actin dynamics regulate AMPA receptor trafficking during synaptic plasticity, *Nat. Neurosci.* 13 (2010) 1208–1215.
- [30] M. Van Troys, L. Huyck, S. Leyman, S. Dhaese, J. Vandekerckhove, C. Ampe, Ins and outs of ADF/cofilin activity and regulation, *Eur. J. Cell Biol.* 87 (2008) 649–667.
- [31] G.C. Belenchi, C.B. Gurniak, E. Perlas, S. Middei, M. Ammassari-Teule, W. Witke, N-cofilin is associated with neuronal migration disorders and cell cycle control in the cerebral cortex, *Genes Dev.* 21 (2007) 2347–2357.
- [32] K. Mizuno, Signaling mechanisms and functional roles of cofilin phosphorylation and dephosphorylation, *Cell. Signal.* 25 (2013) 457–469.
- [33] C.M. Hulette, K.A. Welsh-Bohmer, B. Crain, M.H. Szymanski, N.O. Sinclair, A.D. Roses, Rapid brain autopsy. The Joseph and Kathleen Bryan Alzheimer's Disease Research Center experience, *Arch. Pathol. Lab. Med.* 121 (1997) 615–618.
- [34] R. Radde, T. Bolmont, S.A. Kaeser, J. Coomaraswamy, D. Lindau, L. Stoltze, M.E. Calhoun, F. Jaggi, H. Wolburg, S. Gengler, C. Haass, B. Ghetti, C. Czech, C. Holscher, P.M. Mathews, M. Jucker, Abeta42-driven cerebral amyloidosis in transgenic mice reveals early and robust pathology, *EMBO Rep.* 7 (2006) 940–946.
- [35] M.E. Calhoun, P. Burgermeister, A.L. Phinney, M. Stalder, M. Tolnay, K.H. Wiederhold, D. Abramowski, C. Sturchler-Pierrat, B. Sommer, M. Staufenbiel, M. Jucker, Neuronal overexpression of mutant amyloid precursor protein results in prominent deposition of cerebrovascular amyloid, *Proc. Natl. Acad. Sci. U. S. A.* 96 (1999) 14088–14093.
- [36] M.G. Martin, S. Perga, L. Trovo, A. Rasola, P. Holm, T. Rantamaki, T. Harkany, E. Castren, F. Chiara, C.G. Dotti, Cholesterol loss enhances TrkB signaling in hippocampal neurons aging in vitro, *Mol. Biol. Cell* 19 (2008) 2101–2112.
- [37] A.O. Sodero, L. Trovo, F. Iannilli, P. Van Veldhoven, C.G. Dotti, M.G. Martin, Regulation of tyrosine kinase B activity by the Cyp46/cholesterol loss pathway in mature hippocampal neurons: relevance for neuronal survival under stress and in aging, *J. Neurochem.* 116 (2011) 747–755.
- [38] A.O. Sodero, C. Weissmann, M.D. Ledesma, C.G. Dotti, Cellular stress from excitatory neurotransmission contributes to cholesterol loss in hippocampal neurons aging in vitro, *Neurobiol. Aging* 32 (2011) 1043–1053.
- [39] M. Pikkarainen, T. Kauppinen, I. Alafuzoff, Hyperphosphorylated tau in the occipital cortex in aged nondemented subjects, *J. Neuropathol. Exp. Neurol.* 68 (2009) 653–660.
- [40] K. Tomobe, Y. Nomura, Neurochemistry, neuropathology, and heredity in SAMP8: a mouse model of senescence, *Neurochem. Res.* 34 (2009) 660–669.
- [41] M.V. Aksenova, M.Y. Aksenov, W.R. Markesbery, D.A. Butterfield, Aging in a dish: age-dependent changes of neuronal survival, protein oxidation, and creatine kinase BB expression in long-term hippocampal cell culture, *J. Neurosci. Res.* 58 (1999) 308–317.
- [42] N.M. Porter, O. Thibault, V. Thibault, K.C. Chen, P.W. Landfield, Calcium channel density and hippocampal cell death with age in long-term culture, *J. Neurosci. Off. J. Soc. Neurosci.* 17 (1997) 5629–5639.
- [43] C. Lesuisse, L.J. Martin, Long-term culture of mouse cortical neurons as a model for neuronal development, aging, and death, *J. Neurobiol.* 51 (2002) 9–23.
- [44] A. Herreman, D. Hartmann, W. Annaert, P. Saftig, K. Craessaerts, L. Serneels, L. Umans, V. Schrijvers, F. Checler, H. Vanderstichele, V. Baekelandt, R. Dressel, P. Cupers, D. Huylebroeck, A. Zwijsen, F. Van Leuven, B. De Strooper, Presenilin 2 deficiency causes a mild pulmonary phenotype and no changes in amyloid precursor protein processing but enhances the embryonic lethal phenotype of presenilin 1 deficiency, *Proc. Natl. Acad. Sci. U. S. A.* 96 (1999) 11872–11877.
- [45] A. Herreman, G. Van Gassen, M. Benthair, O. Nyabi, K. Craessaerts, U. Mueller, W. Annaert, B. De Strooper, gamma-Secretase activity requires the presenilin-dependent trafficking of nicastrin through the Golgi apparatus but not its complex glycosylation, *J. Cell Sci.* 116 (2003) 1127–1136.
- [46] M. Cacquevel, L. Aeschbach, J. Houacine, P.C. Fraering, Alzheimer's disease-linked mutations in presenilin-1 result in a drastic loss of activity in purified gamma-secretase complexes, *PLoS One* 7 (2012) e35133.
- [47] L. Zhao, Q.L. Ma, F. Calon, M.E. Harris-White, F. Yang, G.P. Lim, T. Morihara, O.J. Ubeda, S. Ambegaokar, J.E. Hansen, R.H. Weisbart, B. Teter, S.A. Frautschy, G.M. Cole, Role of p21-activated kinase pathway defects in the cognitive deficits of Alzheimer disease, *Nat. Neurosci.* 9 (2006) 234–242.
- [48] L.S. Minamide, A.M. Striegel, J.A. Boyle, P.J. Meberg, J.R. Bamburg, Neurodegenerative stimuli induce persistent ADF/cofilin-actin rods that disrupt distal neurite function, *Nat. Cell Biol.* 2 (2000) 628–636.
- [49] A.R. Gwon, J.S. Park, T.V. Arumugam, Y.K. Kwon, S.L. Chan, S.H. Kim, S.H. Baik, S. Yang, Y.K. Yun, Y. Choi, S. Kim, S.C. Tang, D.H. Hyun, A. Cheng, C.E. Dann 3rd, M. Bernier, J. Lee, W.R. Markesbery, M.P. Mattson, D.G. Jo, Oxidative lipid modification of nicastrin enhances amyloidogenic gamma-secretase activity in Alzheimer's disease, *Aging Cell* 11 (2012) 559–568.
- [50] M.S. Kayser, M.J. Nolt, M.B. Dalva, EphB receptors couple dendritic filopodia motility to synapse formation, *Neuron* 59 (2008) 56–69.
- [51] W.T. Kimberly, J.B. Zheng, T. Town, R.A. Flavell, D.J. Selkoe, Physiological regulation of the beta-amyloid precursor protein signaling domain by c-Jun N-terminal kinase JNK3 during neuronal differentiation, *J. Neurosci. Off. J. Soc. Neurosci.* 25 (2005) 5533–5543.
- [52] M.J. Kim, S.J. Oh, S.H. Park, H.J. Kang, M.H. Won, T.C. Kang, J.B. Park, J.I. Kim, J.Y. Lee, Neuronal loss in primary long-term cortical culture involves neurodegeneration-like cell death via calpain and p35 processing, but not developmental apoptosis or aging, *Exp. Mol. Med.* 39 (2007) 14–26.
- [53] M.T. Maloney, L.S. Minamide, A.W. Kinley, J.A. Boyle, J.R. Bamburg, Beta-secretase-cleaved amyloid precursor protein accumulates at actin inclusions induced in neurons by stress or amyloid beta: a feedforward mechanism for Alzheimer's disease, *J. Neurosci. Off. J. Soc. Neurosci.* 25 (2005) 11313–11321.
- [54] A. Mendoza-Naranjo, E. Contreras-Vallejos, D.R. Henriquez, C. Otth, J.R. Bamburg, R.B. Maccioni, C. Gonzalez-Billault, Fibrillar amyloid-beta1–42 modifies actin organization affecting the cofilin phosphorylation state: a role for Rac1/cdc42 effector proteins and the slingshot phosphatase, *J. Alzheimers Dis.* 29 (2012) 63–77.
- [55] J.A. Woo, A.R. Jung, M.K. Lakshmana, A. Bedrossian, Y. Lim, J.H. Bu, S.A. Park, E.H. Koo, I. Mook-Jung, D.E. Kang, Pivotal role of the RanBP9-cofilin pathway in Abeta-induced apoptosis and neurodegeneration, *Cell Death Differ.* 19 (2012) 1413–1423.
- [56] T. Kim, G.S. Vidal, M. Djurisic, C.M. William, M.E. Birnbaum, K.C. Garcia, B.T. Hyman, C.J. Shatz, Human LirB2 is a beta-amyloid receptor and its murine homolog PirB regulates synaptic plasticity in an Alzheimer's model, *Science* 341 (2013) 1399–1404.
- [57] L. Heredia, P. Helguera, S. de Olmos, G. Kedikian, F. Sola Vigo, F. LaFerla, M. Staufenbiel, J. de Olmos, J. Busciglio, A. Caceres, A. Lorenzo, Phosphorylation of actin-depolymerizing factor/cofilin by LIM-kinase mediates amyloid beta-induced degeneration: a potential mechanism of neuronal dystrophy in Alzheimer's disease, *J. Neurosci. Off. J. Soc. Neurosci.* 26 (2006) 6533–6542.
- [58] W. Morishita, H. Marie, R.C. Malenka, Distinct triggering and expression mechanisms underlie LTD of AMPA and NMDA synaptic responses, *Nat. Neurosci.* 8 (2005) 1043–1050.
- [59] Y. Wang, Q. Dong, X.F. Xu, X. Feng, J. Xin, D.D. Wang, H. Yu, T. Tian, Z.Y. Chen, Phosphorylation of cofilin regulates extinction of conditioned aversive memory via AMPAR trafficking, *J. Neurosci. Off. J. Soc. Neurosci.* 33 (2013) 6423–6433.
- [60] E.Y. Yuen, W. Liu, T. Kafri, H. van Praag, Z. Yan, Regulation of AMPA receptor channels and synaptic plasticity by cofilin phosphatase Slingshot in cortical neurons, *J. Physiol.* 588 (2010) 2361–2371.
- [61] Q.L. Ma, F. Yang, F. Calon, O.J. Ubeda, J.E. Hansen, R.H. Weisbart, W. Beech, S.A. Frautschy, G.M. Cole, p21-activated kinase-aberrant activation and translocation in Alzheimer disease pathogenesis, *J. Biol. Chem.* 283 (2008) 14132–14143.
- [62] B.W. Bernstein, J.R. Bamburg, ADF/cofilin: a functional node in cell biology, *Trends Cell Biol.* 20 (2010) 187–195.
- [63] Y. Shi, C.G. Pontrello, K.A. DeFea, L.F. Reichardt, I.M. Ethell, Focal adhesion kinase acts downstream of EphB receptors to maintain mature dendritic spines by regulating cofilin activity, *J. Neurosci. Off. J. Soc. Neurosci.* 29 (2009) 8129–8142.
- [64] L.Y. Chen, C.S. Rex, M.S. Casale, C.M. Gall, G. Lynch, Changes in synaptic morphology accompany actin signaling during LTP, *J. Neurosci. Off. J. Soc. Neurosci.* 27 (2007) 5363–5372.
- [65] A.C. Paula-Lima, J. Brito-Moreira, S.T. Ferreira, Deregulation of excitatory neurotransmission underlying synapse failure in Alzheimer's disease, *J. Neurochem.* 126 (2013) 191–202.
- [66] N.W. Hu, T. Ondrejcek, M.J. Rowan, Glutamate receptors in preclinical research on Alzheimer's disease: update on recent advances, *Pharmacol. Biochem. Behav.* 100 (2012) 855–862.
- [67] S. Camandola, M.P. Mattson, Aberrant subcellular neuronal calcium regulation in aging and Alzheimer's disease, *Biochim. Biophys. Acta* 1813 (2011) 965–973.
- [68] M.T. Maloney, J.R. Bamburg, Cofilin-mediated neurodegeneration in Alzheimer's disease and other amyloidopathies, *Mol. Neurobiol.* 35 (2007) 21–44.
- [69] Q.L. Ma, F. Yang, S.A. Frautschy, G.M. Cole, PAK in Alzheimer disease, Huntington disease and X-linked mental retardation, *Cell. Logist.* 2 (2012) 117–125.
- [70] S. Bellani, A. Mescola, G. Ronzitti, H. Tsushima, S. Tilve, C. Canale, F. Valtorta, E. Chierregatti, GRP78 clustering at the cell surface of neurons transduces the action of exogenous alpha-synuclein, *Cell Death Differ.* (2014), <http://dx.doi.org/10.1038/cdd.2014.111> (in press).
- [71] M. Benthair, O. Nyabi, J. Verhamme, A. Tolia, K. Horre, J. Wiltfang, H. Esselmann, B. De Strooper, Presenilin clinical mutations can affect gamma-secretase activity by different mechanisms, *J. Neurochem.* 96 (2006) 732–742.
- [72] M. Citron, D. Westaway, W. Xia, G. Carlson, T. Diehl, G. Levesque, K. Johnson-Wood, M. Lee, P. Seubert, A. Davis, D. Kholodenko, R. Motter, R. Sherrington, B. Perry, H. Yao, R. Strome, I. Lieberburg, J. Rommens, S. Kim, D. Schenk, P. Fraser, P. St George-Hyslop, D.J. Selkoe, Mutant presenilins of Alzheimer's disease increase production of 42-residue amyloid beta-protein in both transfected cells and transgenic mice, *Nat. Med.* 3 (1997) 67–72.
- [73] K. Duff, C. Eckman, C. Zehr, X. Yu, C.M. Prada, J. Perez-tur, M. Hutton, L. Buee, Y. Havigaya, D. Yager, D. Morgan, M.N. Gordon, L. Holcomb, L. Refolo, B. Zenk, J. Hardy, S. Younkin, Increased amyloid-beta42(43) in brains of mice expressing mutant presenilin 1, *Nature* 383 (1996) 710–713.

Supplementary Materials for

Inactivation of brain cofilin-1 by age, alzheimer's disease and γ -secretase

Eugenio Barone^a, Sebastien Mosser^a, and Patrick C. Fraering^{a,*}

^aBrain Mind Institute and School of Life Sciences, Ecole Polytechnique Fédérale de Lausanne (EPFL), CH1015 Lausanne, Switzerland

*Correspondence should be addressed to Patrick C. Fraering, Brain Mind Institute and School of Life Sciences, Ecole Polytechnique Fédérale de Lausanne (EPFL), CH1015 Lausanne, Switzerland. E-mail: patrick.fraering@epfl.ch

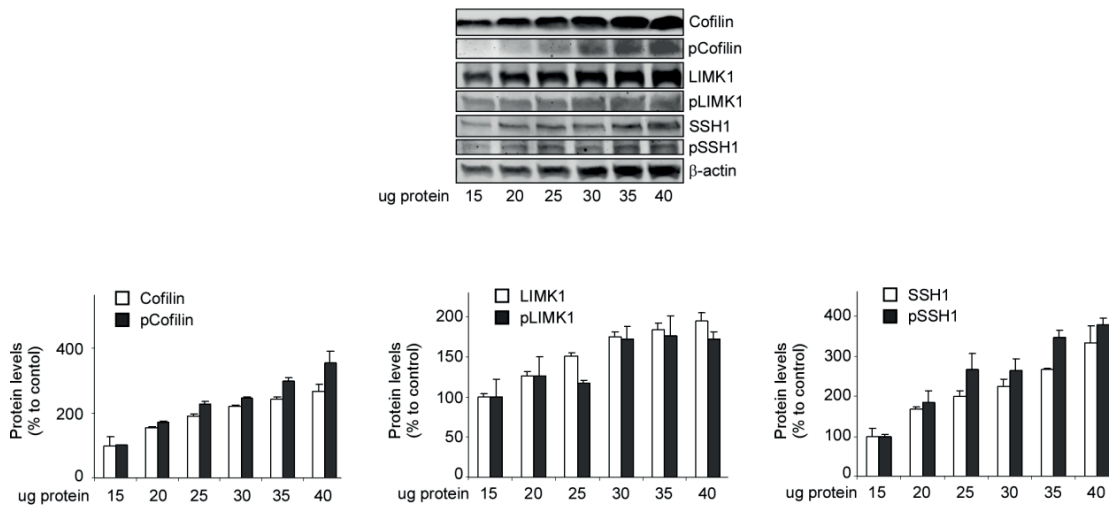
Keywords: Alzheimer's disease, ageing, cofilin1, γ -secretase

Supplementary Table 1. Demographic and diagnostic features of the human brain samples used in this study.

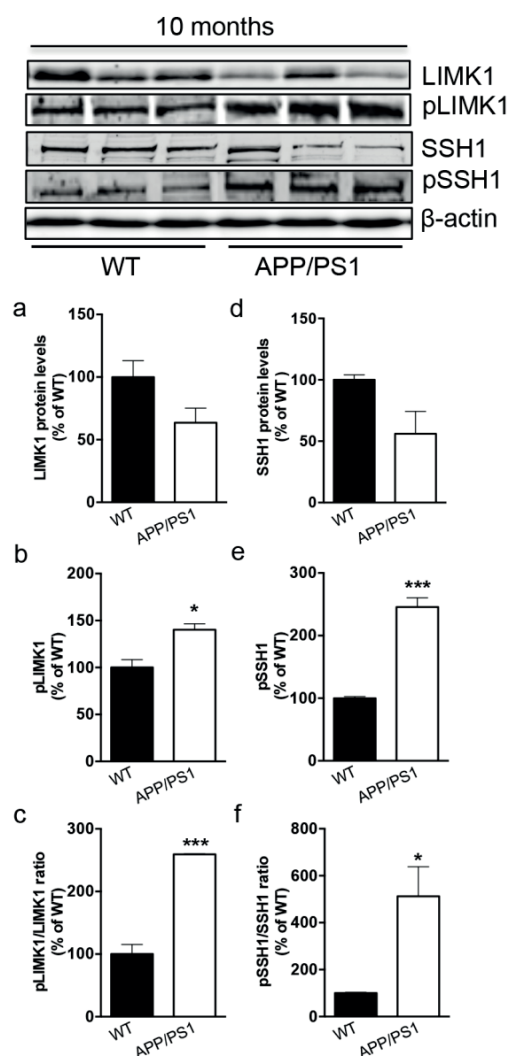
	Age	Gender	Apo E	PMD	Braak
Control (CERAD 1B)	82	F	3/3	15:30	I
Control (CERAD 1B)	90	F	3/3	23:00	I
Control (CERAD 1A)	87	M	3/3	18:30	II
Control (CERAD 1A)	90	M	3/3	7:20	II
Control (CERAD 1B)	90	M	3/3	4:00	II
AD	82	F	4/4	7:30	III
AD	90	M	3/4	17:00	VI
AD	88	M	3/4	NA	III
AD	75	M	3/4	2:30	VI
AD	88	F	3/4	2:00	VI
AD	71	M	3/3	25:09	VI
AD	84	F	3/4	13:25	VI

PMD, post mortem delay

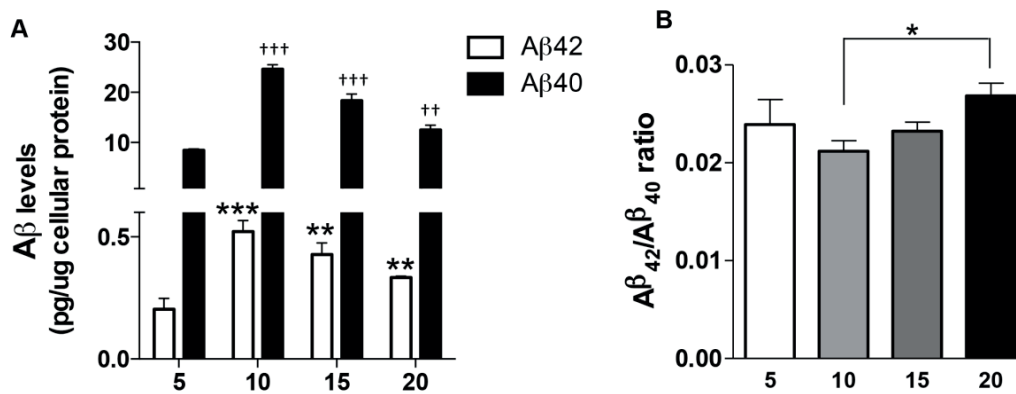
Supplementary Figures



Supplementary Figure 1. Linearity of dose-curve for Western blot analysis of antibodies used in our study. Signals displayed by antibodies targeting Cofilin, phospho-Cofilin, LIMK1, phospho-LIMK1, SSH1 and phospho-SSH1 were estimated on protein levels ranging from 15 to 40 μ g of a wild-type 3-month-old mouse brain total protein extract. As estimated by densitometry, all signals exhibit linearity at the protein levels tested (lower panels), and the protein amount (30 μ g) we used for sample analysis all over the manuscript falls into this linear range. Plots display densitometric estimations from $n=2$ independent Western blots, for each antibody; β -actin is used as a loading control.

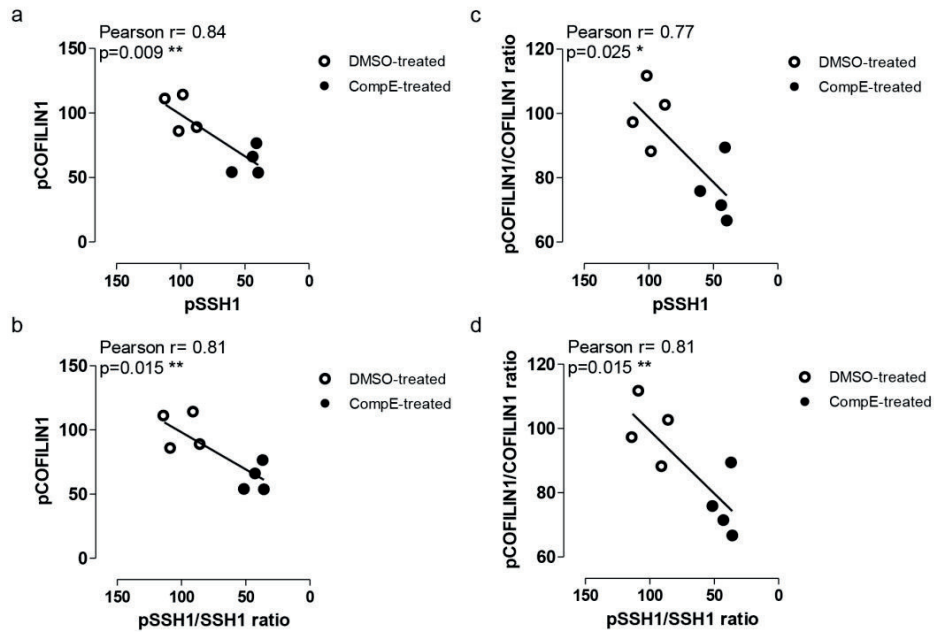


Supplementary Figure 2 (related to Fig. 2). LIMK1 activation and SSH1 inactivation in the brain of 10-months old APP/PS1 mice. Brain samples from 10-months old APP/PS1 mice (n=3) show a significant decrease in LIMK1 (a) and SSH1 (d) protein levels, together with a significant increase of their phosphorylation (b and e) with respect to aged-matched WT controls (n=3). These changes resulted in a significant increase of both pLIMK1/LIMK1 (c) and pSSH1/SSH1 (f) ratios. Top panels: Western blot analyses of total protein extracts. Bottom panels: densitometric analyses of indicated Western blot protein bands. Protein levels were normalized to the loading control β -actin. Densitometric values shown in the histograms are given as percentage of WT mice set as 100%. Means \pm SEM, *P<0.05, **P<0.01 and ***P<0.001 vs WT.

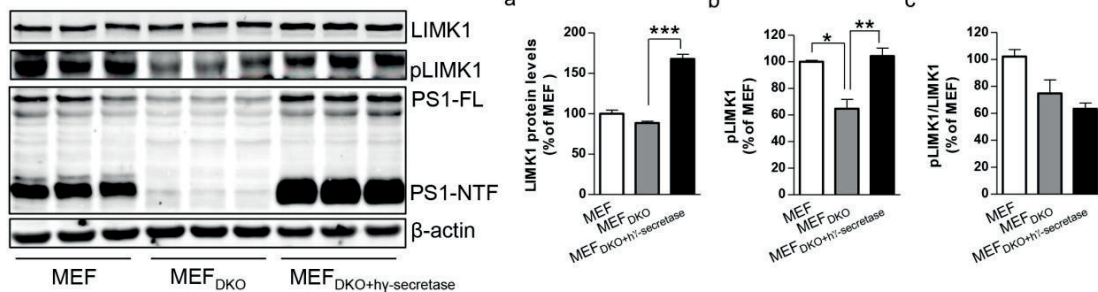


Supplementary Figure 3. The increase of Cofilin1 phosphorylation during neuronal maturation *in vitro* parallels with a more amyloidogenic Aβ production. (A) Changes of Aβ₄₀ and Aβ₄₂ production during neuronal maturation *in vitro*, as estimated by ELISA. (B) Quantitative measurements of the Aβ₄₂/Aβ₄₀ ratio during neuronal maturation *in vitro* show a cellular shift towards the more amyloidogenic pathway, possibly caused by a modified γ-secretase specific activity. Means ± SEM of n=3 independent cultures/group. ** or ††P<0.01 and *** or †††P<0.001 vs 5 DIV (B). *P<0.05 vs 10 DIV (C).

A

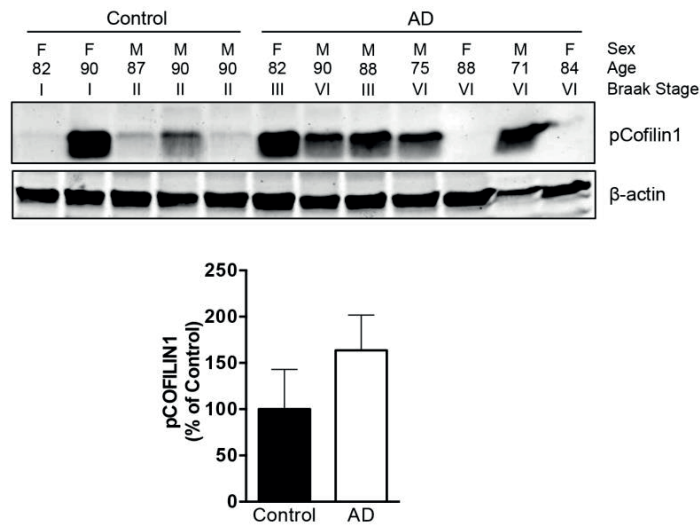


B

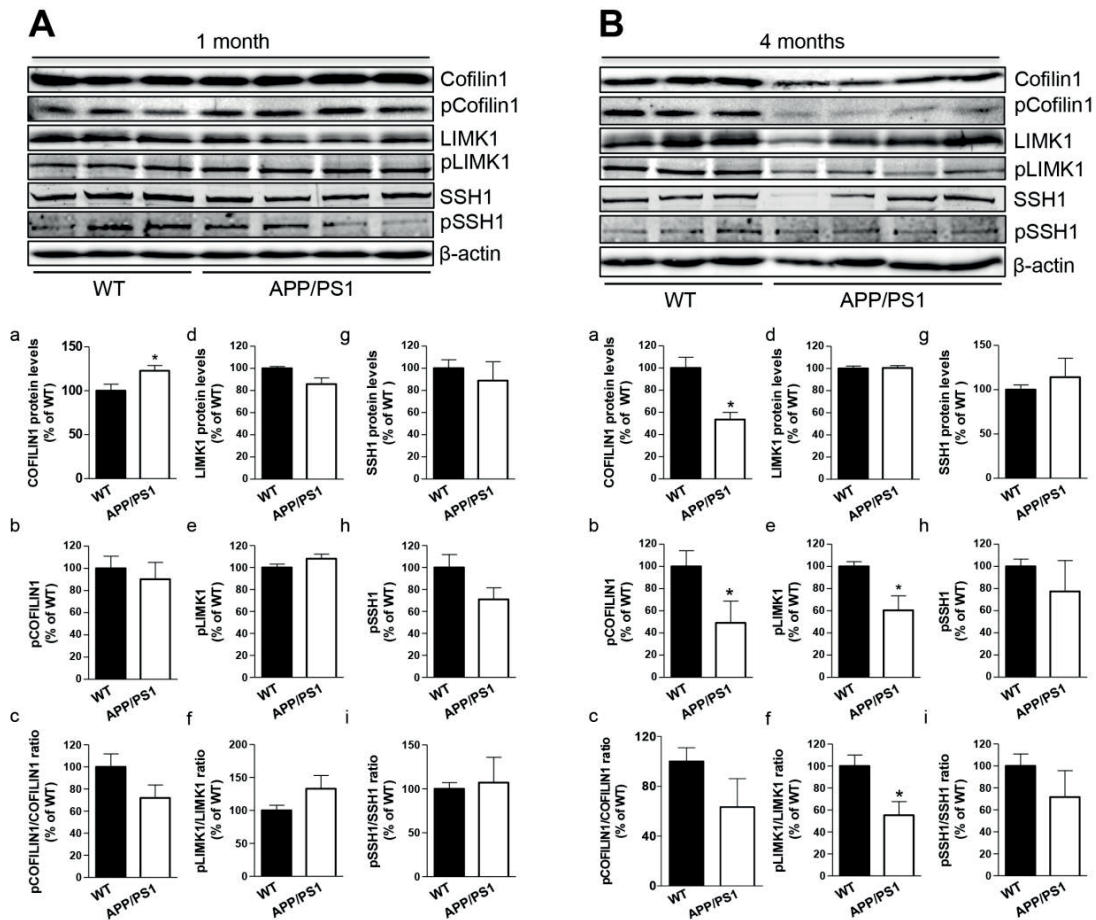


Supplementary Figure 4 (related to Fig. 5). The decrease of Cofilin1 phosphorylation following γ -secretase inhibition is associated with an increased SSH1 activation. (A) In 20 DIV mouse primary cortical neurons (PCNs) treated overnight with DMSO (n=4) or 10 μ M of the γ -secretase inhibitor Compound E (CpdE) (n=4 independent cultures/group), positive and significant correlations were found between pCofilin1 levels or pCofilin1/Cofilin1 ratio and pSSH1 levels (a,c) or between pCofilin1 levels or pCofilin1/Cofilin1 ratio and the pSSH1/SSH1 ratio (b,d). (B) Mouse embryonic fibroblasts (MEF) lacking the catalytic γ -secretase subunits presenilin-1 and -2 (MEF_{DKO}) showed unchanged LIMK1 total protein

levels (a) and a decrease of pLIMK1 (b), resulting in a decrease of the pLIMK1/LIMK1 ratio (c). Overexpression of human γ -secretase in MEF_{DKO} cells (MEF_{DKO+ γ -secretase}) promoted an increase of both LIMK1 (a) and pLIMK1 levels (b) associated with a further decrease of the pLIMK1/LIMK1 ratio (c), with respect to MEF_{DKO} and MEF cell lines. Thus, the increase of pCofilin1 observed in MEF_{DKO+ γ -secretase} cells is likely independent on LIMK1 because a net reduction of its activation (decreased pLIMK1/LIMK1 ratio) was observed. These results suggest that the decrease of pCofilin1 observed following γ -secretase inhibition (Fig. 5C-b,c) can possibly be mediated by the observed activation of SSH1 (Fig.5C-e,f). Top panels: Western blot analyses of total protein extracts. Bottom panels: densitometric analyses of Western blot protein bands. Protein levels were normalized to the loading control β -actin. Densitometric values shown in the histograms are given as percentage of WT MEF set as 100%. Means \pm SEM of n=3 independent cultures/group. *P<0.05, **P<0.01 and ***P<0.001 vs MEF WT or MEF_{DKO}. PS1-FL, presenilin-1 full length; PS1-NTF, presenilin-1 N-terminal fragment.

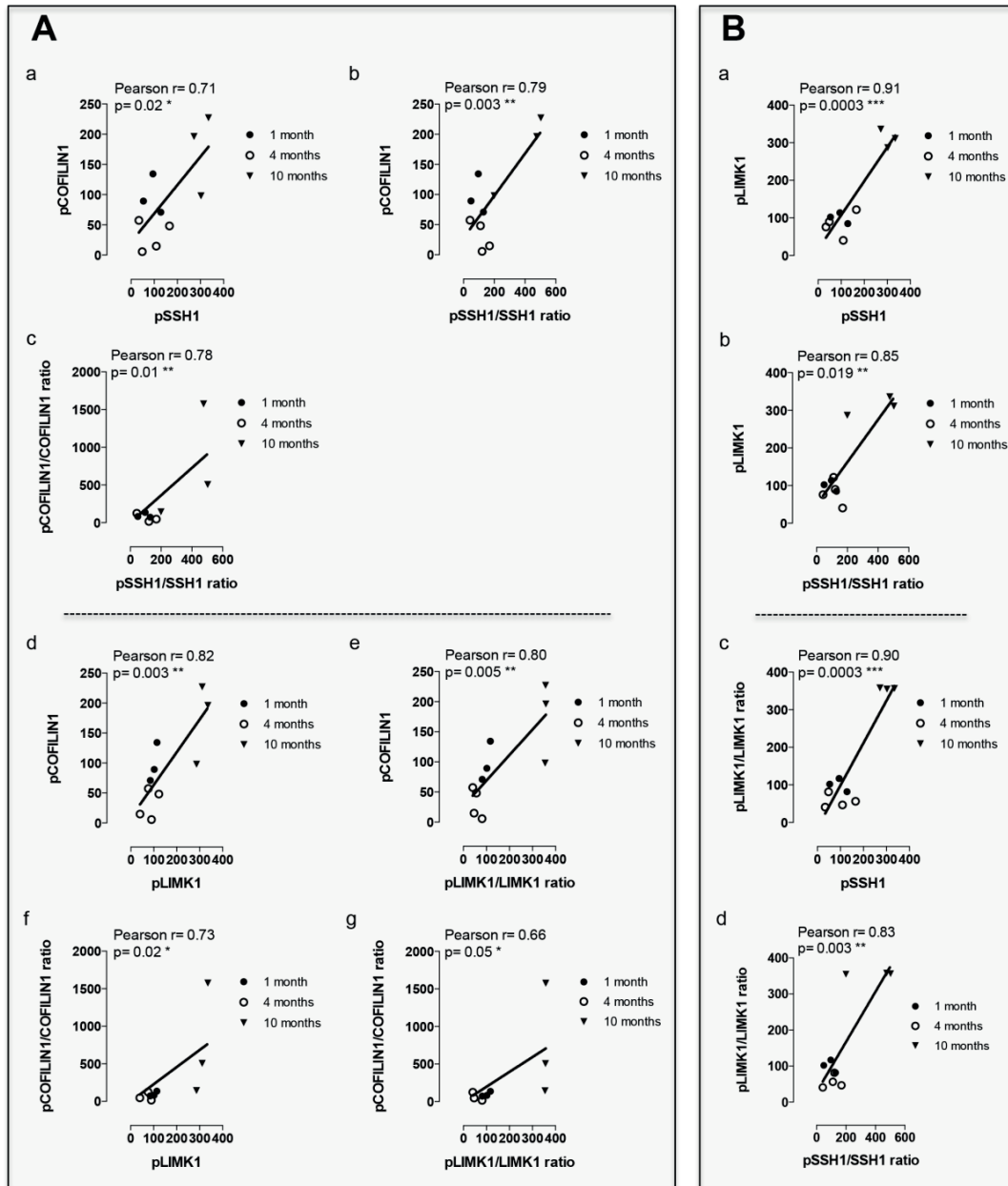


Supplementary Figure 5 (related to Figure 1). Cofilin1 phosphorylation/inactivation in the frontal cortex of human sporadic Alzheimer’s disease patients, evaluated by using the anti-phospho(Ser3)-Cofilin1 (#ab12866, 1:1000, abcam, Cambridge, United Kingdom) antibody as in (Kim, et al., 2013). Top panels: Western blot analyses of total protein extracts, showing increased phospho-Cofilin1 (pCofilin1) in the frontal cortex of sporadic Alzheimer’s disease subjects (n=7), relative to their age-matched controls (n=5). Similar results were found by using the anti-phospho-Cofilin1 antibody #3311s (1:500, Cell Signaling, Bioconcept, Allschwill, Switzerland) (Fig. 1-b). Bottom panels: densitometric analyses of Western blot protein bands. Protein levels were normalized to the loading control β -actin. Densitometric values shown in the histograms are given as percentage of Control samples set as 100%.



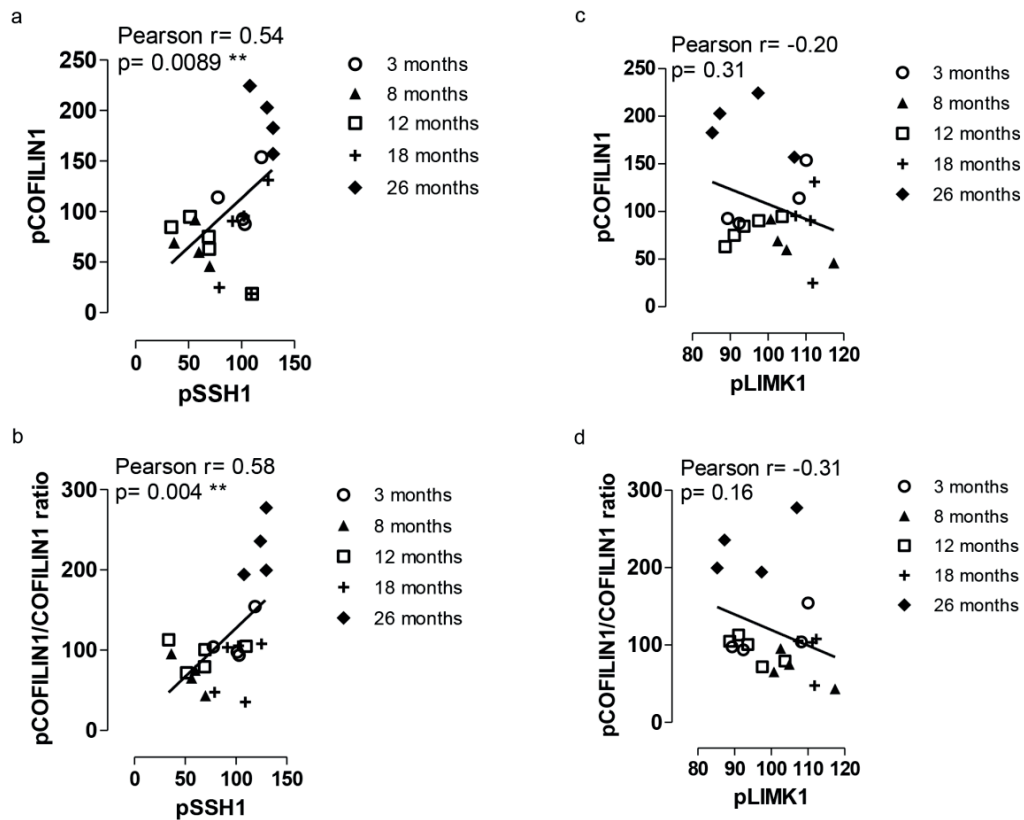
Supplementary Figure 6 (related to Figure 2). Changes in proteins of the Cofilin1 pathway in brains of 1- and 4-months old APP/PS1 mice. (A) Brain total protein extracts from 1-month old APP/PS1 mice (n=4) show a significant increase of total Cofilin1 protein levels with respect to age-matched littermate WT controls (n=3). No significant changes were observed with regard to LIMK1 or SSH1 protein levels and activation state. *Top panels:* Western blot analyses of total protein extracts. *Bottom panels:* densitometric analyses of Western blot protein bands: (a) Total Cofilin1 protein levels; (b) pCofilin1 levels; (c) pCofilin1/Cofilin1 ratio; (d) Total LIMK1 protein levels; (e) pLIMK1 levels; (f) pLIMK1/LIMK1 ratio; (g) Total SSH1 protein levels; (h) pSSH1 levels; (i) pSSH1/SSH1 ratio. **(B)** Brain samples from 4-months old APP/PS1 mice (n=4) show a significant decrease of total Cofilin1 protein levels and phosphorylation (pCofilin1) associated with a significant decrease of LIMK1 phosphorylation (pLIMK1), with respect to age-matched littermate WT controls (n=3). *Top panels:* Western blot analyses of total protein extracts. *Bottom panels:*

densitometric analyses of Western blot protein bands: (a) Total Cofilin1 protein levels; (b) pCofilin1 levels; (c) pCofilin1/Cofilin1 ratio; (d) Total LIMK1 protein levels; (e) pLIMK1 levels; (f) pLIMK1/LIMK1 ratio; (g) Total SSH1 protein levels; (h) pSSH1 levels; (i) pSSH1/SSH1 ratio. Protein levels were normalized per β -actin as loading control. Densitometric values shown in the histograms are given as percentage of 5 DIV set as 100%. Means \pm SEM, *P<0.05 vs WT.

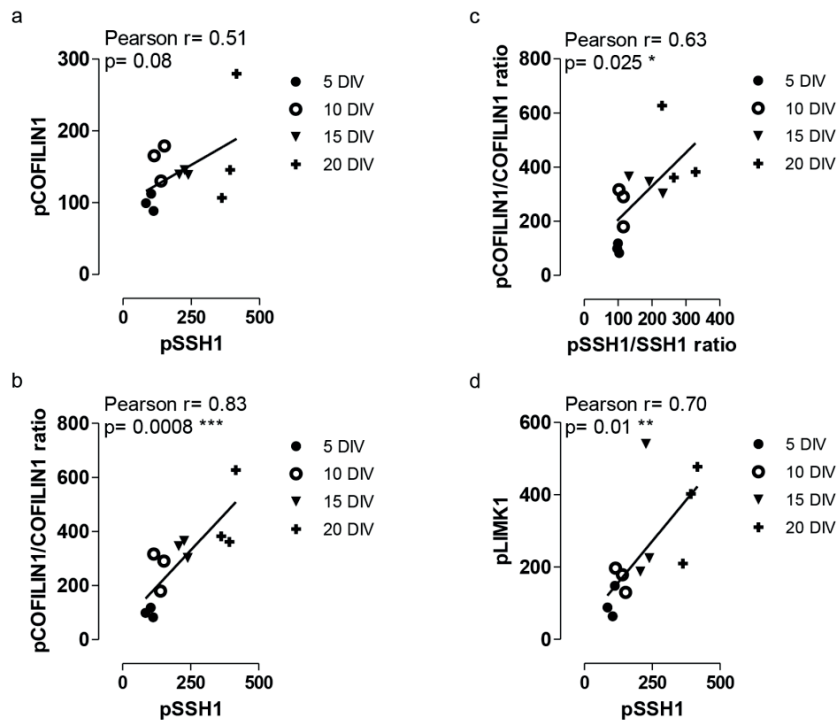


Supplementary Figure 7 (related to Fig. 2). Age-dependent Cofilin1 phosphorylation is associated with LIMK1 activation and SSH1 inactivation in the brain of APP/PS1 mice. In the brain of 1-, 4- and 10-months old APP/PS1 mice, positive and significant correlations were found (A) between pCofilin1 levels or pCofilin1/Cofilin1 ratio and (a-c) pSSH1 levels or pSSH1/SSH1 ratio or (e-g) pLIMK1 levels or pLIMK1/LIMK1 ratio, or (B) between pSSH1 or pSSH1/SSH1 ratio and pLIMK1 or pLIMK1/LIMK1 ratio (a-d). Because SSH1 can dephosphorylate/inactivate LIMK1, the significant correlation found in (B) suggests that

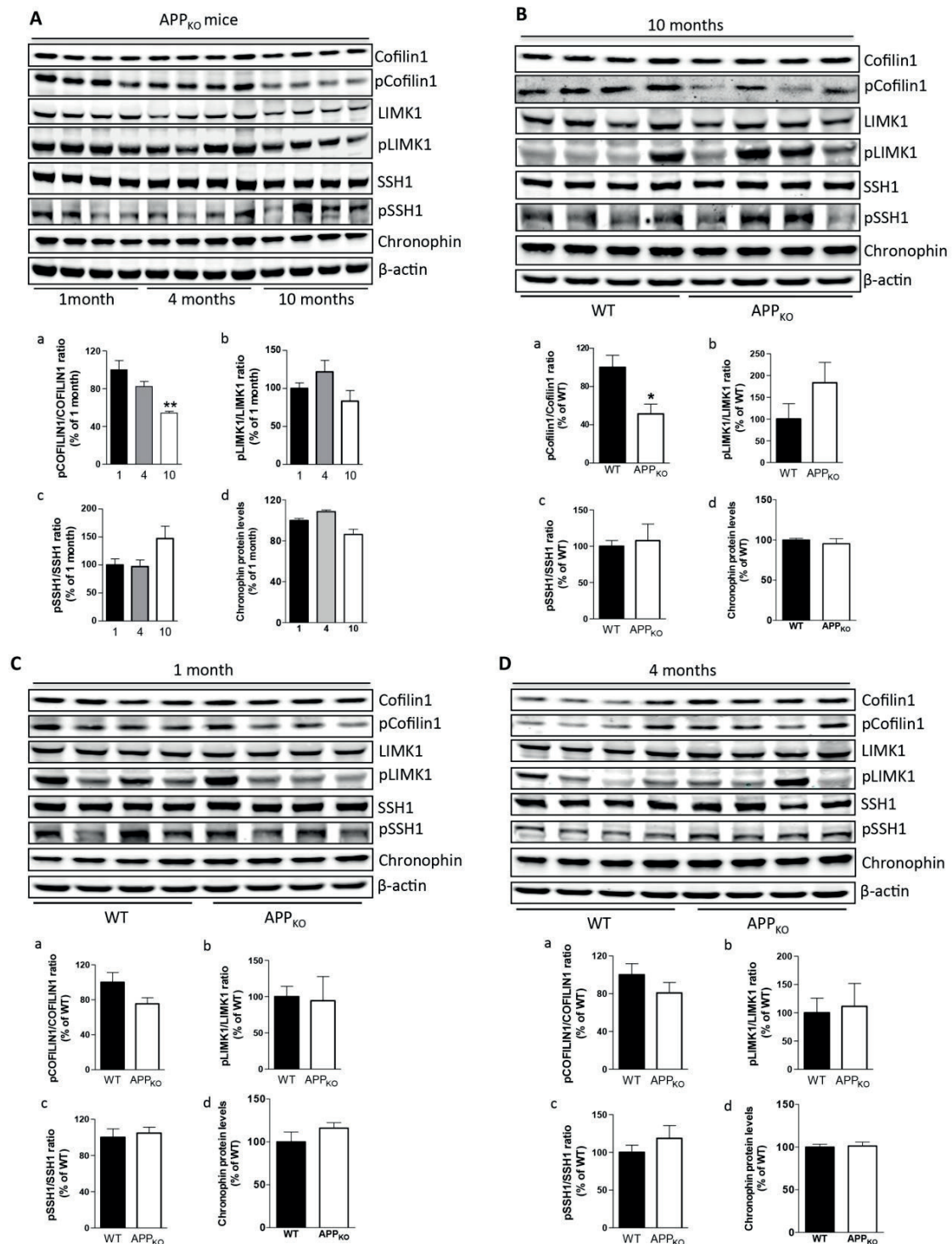
SSH1 inactivation could promote Cofilin1 phosphorylation, both directly and indirectly, through an effect on LIMK1.



Supplementary Figure 8 (related to Fig. 3). The age-dependent increase of Cofilin1 phosphorylation is associated with SSH1 inactivation in the brain of WT mice. In the brain of 3- (n=5), 8- (n=4), 12- (n=5), 18- (n=5) and 26-months old (n=4) WT mice, positive and significant correlations were found between pCofilin1 levels or pCofilin1/Cofilin1 ratio and pSSH1 levels (a and b). The absence of significant correlations between pCofilin1 or pCofilin1/Cofilin1 ratio and pLIMK1 levels (c and d) suggests a major involvement of SSH1 inactivation in promoting Cofilin1 phosphorylation.



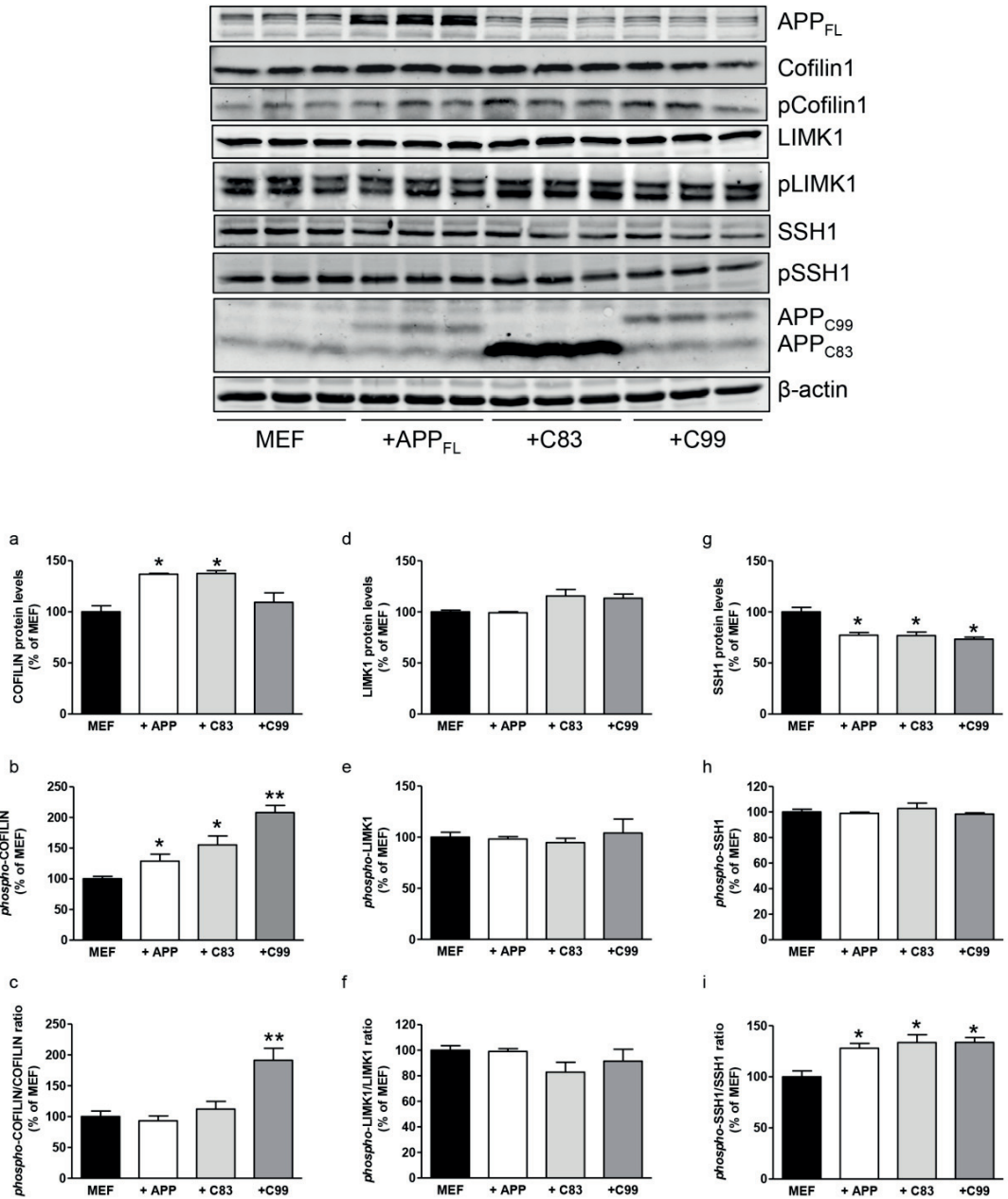
Supplementary Figure 9 (related to Fig. 4). The increase of Cofilin1 phosphorylation during neuronal maturation *in vitro* is associated with SSH1 inactivation. pCofilin1 or pCofilin1/Cofilin1 ratio are positively and significantly associated with pSSH1 (a,b) or pSSH1/SSH1 ratio (c) in mouse PCNs cultured from 5 to 20 DIV. A significant correlation was also found between pSSH1 and pLIMK1 (d), thus suggesting age-associated SSH1 inactivation as an event promoting Cofilin1 phosphorylation during neuronal maturation.



Supplementary Figure 10. Changes in Cofilin1 pathway proteins in the brain of APP_{KO} mice. (A) Age-associated decrease of Cofilin1 phosphorylation in the brain of 1- (n=4), 4- (n=4) and 10-months old (n=4) APP knock-out mice (APP_{KO}). *Top panels*: Western blot

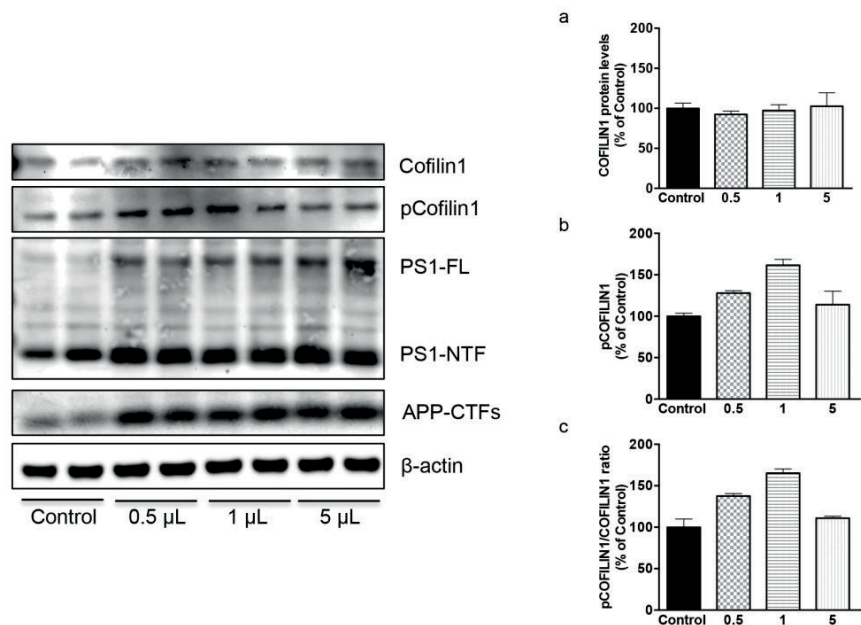
analyses of total protein extracts. *Bottom panels*: densitometric analyses of Western blot protein bands: (a) pCofilin1/Cofilin1 ratio; (b) pLIMK1/LIMK1 ratio; (c) pSSH1/SSH1 ratio; (d) Chronophin protein levels. **(B)** Brain samples from 10-months old APP_{KO} mice (n=4) show a significant decrease of pCofilin1/Cofilin1 ratio with respect to their age-matched littermate WT controls (n=4). No significant changes were observed for both pLIMK1/LIMK1, SSH1/pSSH1 ratio or Chronophin levels. *Top panels*: Western blot analyses of total protein extracts. *Bottom panels*: densitometric analyses of Western blot protein bands: (a) pCofilin1/Cofilin1 ratio; (b) pLIMK1/LIMK1 ratio; (c) pSSH1/SSH1 ratio; (d) Chronophin protein levels. **(C, D)** Analyses of Cofilin1 pathway proteins in brain samples from 1- (n=4) and 4-months old (n=4) APP_{KO} mice showing the absence of significant changes with regard to aged-matched WT controls (n=4). *Top panels*: Western blot analyses of total protein extracts. *Bottom panels*: densitometric analyses of Western blot protein bands: (a) pCofilin1/Cofilin1 ratio; (b) pLIMK1/LIMK1 ratio; (c) pSSH1/SSH1 ratio; (d) Chronophin protein levels. Protein levels were normalized to the loading control β -actin. Densitometric values shown in the histograms are given as percentage of 1 month (A) or WT (B-D) mice set as 100%. Means \pm SEM, *P<0.05, **P<0.01 and ***P<0.001 vs 1 month-old mice (A) or WT mice (B). Interestingly, reduction of Cofilin1 phosphorylation (reduced pCofilin1/Cofilin1 ratio) in the brain of 10-months old APP_{KO} mice (A-a), when compared to their age-matched littermate WT controls (B-a), resemble the reduction of Cofilin1 phosphorylation observed following the inhibition of γ -secretase activity in mouse PCNs (Figs.5A and 5B) and MEF_{DKO} (Fig.5C). The lack of significant effects on LIMK1 and SSH1 activities with respect to WT mice could suggest that at the age of 10 months other mechanism(s) could occur, different than those involving LIMK1 and SSH1. In that frame the Chronophin (or CIN) phosphatase has also been suggested to be able to promote Cofilin desphosphorylation (Gohla A et al, Nat Cell Biol, 2005; Huang TY et al, Curr Opin Cell Biol, 2006). However, it has recently been reported that the knock-down of SSH1 was associated with a consistent and strong increase of Cofilin1 phosphorylation. That was not the case for the knock-down of Chronophin, further highlighting the dominant role for SSH1 as a specific regulator of Cofilin1 desphosphorylation (Yan-Ting Zhang et al, J Cell Biochem, 2013; Posadas Inmaculada et al, J Neurochem, 2012; Klygis K et al. J Biol Chem, 2007). Moreover, the pSSH1/SSH1 ratio remains unaffected in APPKO mice (Ac, Bc). Altogether, it suggests that SSH1 fulfills its dominant effector function, over Chronophin, for which no changes

were observed at the protein levels (Ad, Bd) [anti-Chronophin antibody #4686 (1:500, Cell signalling, Bioconcept, Allschwil, Switzerland)].



Supplementary Figure 11. Overexpression of full-length amyloid precursor protein (APP) or APP-C-terminal fragments (C99 and C83) promotes Cofilin1 phosphorylation in mouse embryonic fibroblast (MEF). Mouse embryonic fibroblasts (MEF) transiently transfected for 48 hours with a mammalian vector carrying the gene encoding for (i) full-length amyloid precursor protein (APP), (ii) α -secretase-dependent APP-cleavage product APP-C83 (C83), or (iii) β -secretase-dependent APP-cleavage product APP-C99 (C99) were characterized by an increase of Cofilin1 and Slingshot-1 phosphorylation (pCofilin1 and

pSSH1, respectively). *Top panels:* Western blot analyses of total protein extracts. *Bottom panels:* densitometric analyses of Western blot protein bands: (a) Total Cofilin1 protein levels; (b) pCofilin1 levels; (c) pCofilin1/Cofilin1 ratio; (d) Total LIMK1 protein levels; (e) pLIMK1 levels; (f) pLIMK1/LIMK1 ratio; (g) Total SSH1 protein levels; (h) pSSH1 levels; (i) pSSH1/SSH1 ratio. Protein levels were normalized per β -actin as loading control. Densitometric values shown in the histograms are given as percentage of MEF set as 100%. Means \pm SEM of n=3 independent cultures/group. *P<0.05 and ** or P<0.01 vs MEF.



Supplementary Figure 12. The γ -secretase Presenilin-1 L166P mutation causing early-onset familial AD is associated with an increase of pCofilin1 in mouse PCNs. Mouse primary cortical neurons (PCNs) (n=2 independent cultures/group) infected from 6 to 20 DIV with increasing concentrations (0.5 – 5 μ L) of the lentiviral vector carrying the gene encoding for the mutated human Presenilin-1 (PS1) L116P were characterized by an increase of pCofilin1 (b) and pCofilin1/Cofilin1 ratio (c). *Left panels:* Western blot analyses of total protein extracts. *Right panels:* densitometric analyses of Western blot protein bands: (a) Total Cofilin1 protein levels; (b) pCofilin1 levels; and (c) pCofilin1/Cofilin1 ratio. Protein levels were normalized to the loading control β -actin. Densitometric values shown in the histograms are given as percentage of Control uninfected PCNs set as 100%.

Chapter III

Engineering new tools for the observation and repair of brain structure damages

III.1) Introduction

III.1.a) Monitoring brain structure alterations in AD

AD spreads in the central nervous system according to a well-defined pattern and leads to important brain shrinkage (see Fig. 2, chapter I), inducing the loss of cognitive functions. In order to understand better the propagation of the disease and to develop therapeutic strategies, transgenic mouse models that reproduce AD patterns including senile plaques, NFT and neurodegeneration have been generated (reviewed in ^{209,210}). However the observation of such patterns require heavy and time-consuming procedures such as PET- / MRI-scans^{29,36}, cranial window imaging²¹¹, CSF collection or sacrifice of the animal for histological analysis.

Both senile plaques and NFT cause neurodegeneration that affects cellular organization and consequently brain structures. Because of these observations, we investigated the potential of electrical impedance measurements for detecting these structural alterations (see manuscripts pages 120 and 131). Electrical impedance represents the electrical resistance of a tissue when an alternating current is applied. In this context, electrical impedance provides information concerning cellular/tissue organization and integrity. Although this method would require neurosurgery for the cerebral implantation of the electrode, electrical impedance recordings may be done at any time without interfering with the animal well-being. Finally this method may be used for visualizing the progression of pathological phenotypes and their repair in a wide range of neuropathologies, as soon as alteration in the tissue structure is observed.

III.1.b) Rescue brain alteration in neurodegenerative processes

The major brain shrinkage observed in neurodegenerative diseases including AD is linked to cell loss. While most therapies focus on pharmacological and immunological blockage of A β -mediated cell death, replacing dead neurons by newborn neurons has been suggested for rescuing cognitive functions¹⁷⁶. Generating these new cells can be achieved by two strategies: 1) stimulating adult neurogenesis, or 2) neurosurgical injection of induced pluripotent stem cells directly at seizure sites. While the first strategy clearly lacks of specific molecules^{212,213}, the second showed very promising results in human patients^{214,215}. Indeed, previous studies showed the integration and propagation of engrafted material into living tissues²¹⁶⁻²¹⁸. However, the empty space left by dead cells – particularly large for stroke lesions – hardly recovers initial cell density²¹⁶⁻²¹⁸. To overcome this limitation and promote cell growth, several groups proposed polymers scaffold mimicking cellular

matrix^{219–221}. These scaffolds shall fulfill numerous conditions to be used in clinics: stable, biocompatible, autoclavable, neurotrophic, injectable, hydrophilic and cheap. In the last study of this PhD thesis, we first optimized the synthesis of a polymer that meets all of these expectations. Next, we developed a procedure to culture primary cortical neurons on this polymer, in order to recreate an as physiological as possible brain tissue matrix (see manuscript page 140).

III.2) Results

III.2.a) Accurate Resistivity Mouse Brain Mapping Using Microelectrode Arrays

In this manuscript, we optimized the detection of brain structures by electrical impedance measurements (see manuscript page 120). We implanted a microelectrode in WT euthanized mice brain (*ex vivo*) at precise stereotaxic coordinates, and recorded electrical impedance in various brain structures. We succeeded with our method in discriminating brain structures such as the cortical layers, ventricles, the corpus callosum and the thalamus. Furthermore, we showed that damaged tissue integrity can be observed with our method.

In this study, I performed mice euthanasia, stereotaxic positioning of the electrodes, and participated in the experimental design.

III.2.b) Detection of Alzheimer's Disease Amyloid-beta Plaque Deposition by Deep Brain Impedance Profiling

As tissue integrity affects electrical impedance (see section III.2.a), we aimed at using this method for detecting A β plaques in AD brain (see manuscript page 131). We thus performed *ex-vivo* electrical impedance recordings in the cortex and the hippocampus of the AD mouse model APPPS1²⁰⁸. We detected a decrease in electrical impedance correlated with A β plaque loads. Analysis of our data suggested that our method does not directly detect A β plaques, but rather structural changes surrounding these plaques linked to cellular disorganization.

In this study, I performed mice euthanasia, stereotaxic positioning of the electrodes, and participated in the experimental design.

III.2.c) A Compressible Scaffold for Minimally Invasive Delivery of Large Intact Neuronal Networks

In the last study of this PhD thesis, we aimed at synthesizing a polymer-based neuronal scaffold, compatible with a therapeutic application (see manuscript page 140). We synthesized an extracellular matrix-like polymer scaffold (cryogel), and characterized its physical properties. We optimized the culture of mouse primary cortical neurons on our cryogel and visualized high axonal sprouting. Moreover, compressing the cryogel for injecting in patient's brain did not disrupt neuronal integrity. In conclusion, we report the synthesis and characterization of a potent cellular scaffold chemically stable, biocompatible, autoclavable, neurotrophic, injectable, hydrophilic and cheap with high therapeutic potential.

In this investigation, I prepared the mouse primary cortical neurons and participated in the optimization of cell culture conditions, as well as in the experimental design.

III.3) Manuscripts



Contents lists available at ScienceDirect

Biosensors and Bioelectronics

journal homepage: www.elsevier.com/locate/bios

Accurate resistivity mouse brain mapping using microelectrode arrays

Amélie Bédurier^{a,*}, Pierre Joris^{a,1}, Sébastien Mosser^b, Vincent Delattre^c,
Patrick C. Fraering^b, Philippe Renaud^a^a Microsystems Laboratory, Ecole Polytechnique Fédérale de Lausanne (EPFL), CH-1015 Lausanne, Switzerland^b Laboratory of Molecular & Cellular Biology of Alzheimer's Disease, Brain Mind Institute and School of Life Sciences,

Ecole Polytechnique Fédérale de Lausanne (EPFL), CH-1015 Lausanne, Switzerland

^c Laboratory of Neural Microcircuitry, Brain Mind Institute, Ecole Polytechnique Fédérale de Lausanne (EPFL), CH-1015 Lausanne, Switzerland

ARTICLE INFO

Article history:

Received 20 January 2014

Received in revised form

11 March 2014

Accepted 21 March 2014

Available online 13 April 2014

Keywords:

Impedance spectroscopy

Neural probe

Microelectrodes array

Mouse brain

Cortical layers

Thermal cauterization

ABSTRACT

Electrical impedance spectroscopy measurements were performed in post-mortem mice brains using a flexible probe with an embedded micrometric electrode array. Combined with a peak resistance frequency method this allowed obtaining intrinsic resistivity values of brain tissues and structures with submillimetric resolution. Reproducible resistivity measurements are reported, which allows the resistivity in the cortex, ventricle, fiber tracts, thalamus and basal ganglia to be differentiated. Measurements of brain slices revealed resistivity profiles correlated with the local density of cell bodies hence allowing to discriminate between the different cortical layers. Finally, impedance measurements were performed on a model of cauterized mouse brain evidencing the possibility to measure the spatial extent and the degree of the tissue denaturation due to the cauterization.

© 2014 Elsevier B.V. All rights reserved.

1. Introduction

Neurosurgery can be considered as a high-tech speciality which is strongly dependent on technological innovations aiming at improving patient treatment and clinical outcome. During the last decades neurosurgery has improved substantially, thanks to the introduction of applied imaging technologies such as computed tomography and magnetic resonance tomography, and new surgical modalities like brain navigation (Kikinis et al., 1994; Mohri et al., 2012). In particular, accuracy of targeting is critical for the success of numerous brain surgery techniques because brain damage has a very negative impact on the patient's quality of life. For example, in Parkinson disease, precise placement of electrodes for deep brain stimulation (DBS) is an essential determinant of outcome: electrodes have to be placed accurately in the hypothalamus in order to stimulate the appropriate neurons and reduce side effects to a minimum. Similarly, proper electrode placement is essential for the correct interpretation of stereoelectroencephalography recordings used to identify the area of the brain where epileptic seizures originate. In operations involving resective surgery such as radio-frequency ablation, thermal ablation or cryoablation for medically refractory epilepsy (Gigante and Goodman, 2012), hypothalamic

hamartoma (Mittal et al., 2013) or metastatic brain tumors (Li et al., 2010), precise localization but also precise information about the extent of the ablated tissue is absolutely essential in order to minimize the damage caused to the brain. Recently, it has been estimated that around 10% of patients who had resective epilepsy surgery have to undergo a second intervention (Surges and Elger, 2013). Causes of failure in the first epilepsy surgery vary but they include incorrect localization and incomplete resection of the seizure focus. Finally, information about the extent and development of local tissues abnormalities such as tumors and lesions are also valuable for the medical diagnosis before and during surgery.

Standard magnetic resonance imaging and X-ray computed tomography are typically used for imaging the brain and taking landmarks for the later surgical operation before opening the skull of the patient. As such, these techniques take into account neither brain release at the moment of skull opening nor possible accidental movements during the surgery. Techniques such as intraoperative magnetic resonance imaging (iMRI) and intraoperative computed tomography (iCT) are used for brain imaging and needle guidance during surgical operations, for example for deep brain stimulation needle placement (Burchiel et al., 2013; Lim et al., 2013) and recently also for tumor ablation with high-intensity focused ultrasounds (Ellis et al., 2013). However these techniques imply complex surgical conditions and organization and also require complex data treatment and expensive equipment. Further, iCT implies irradiation of the patient or use of radioactive contrast agents, putting the patient's health at risk when used too frequently.

* Correspondence to: EPFL STI IMT LMIS4, BM 3.125, Station 17, CH-1015 Lausanne, Switzerland. Tel.: +41 21 693 66 27.

E-mail address: amelie.beduer@epfl.ch (A. Bédurier).

¹ These authors contributed equally to this work.

In addition, image quality in magnetic resonance imaging (MRI) is degraded by the metallic objects such as the implanted electrodes.

In order to overcome these difficulties, the neurosurgical procedure would benefit from new simple instruments or techniques enabling localizing directly and precisely brain structures or distinguishing different types of tissues, such as for example healthy and tumor tissues for proper resection of the latter with minimal damage to the former. Furthermore, an “in situ” and “real time” technique allowing obtaining information on the properties of tissues could open wide possibilities for the research of the direct effects of drug delivery and local stimulation on the long term evolution of diseased tissue.

The imaging of conductivity distributions gives valuable information on physiological and pathological parameters, which are not obtained by anatomical imaging. For example, conductivity measurements can be used to classify different tissue types (Mayer et al., 2006), and to detect edema (Merwa et al., 2004). Electrical impedance tomography (EIT), in which surface potentials are measured during application of currents via surface electrodes, has been applied to obtain conductivity distributions in living bodies (Metherall et al., 1996; Saulnier et al., 2001). However, EIT has relatively low spatial resolution when using a limited number of surface electrodes. Moreover, conductivity distributions of the brain are difficult to obtain with EIT because most of the current does not penetrate the skull due to its low conductivity (Sekino and Ueno, 2002). Recently, Wang et al. (2008) proposed another method to estimate conductivity from diffusion tensor MRI, though the application of this method is limited to white matter tissues. An alternative to EIT is electrical impedance spectroscopy (EIS), which has already been used for detecting both local pathologies such as brain tumors in rats (Jahnke et al., 2013) and global abnormalities such as hypoxic ischemic encephalopathy of neonates (Seoane et al., 2012). It has also been proven useful to monitor temporal changes such as the evolution of the tissue reaction to neuroprostheses (Mercanzini et al., 2009). Recently, impedance-based tissue discrimination for needle guidance has been proposed (Kalvøy et al., 2009; Trebbels et al., 2012). However, impedance measurements with very high resolution enabling discrimination of submillimetric structures are still missing.

In this report, we propose the usage of electrical impedance spectroscopy (EIS) for a fine discrimination in brain tissue structures. By taking advantage of the latest advances in both microelectrode fabrication and EIS analysis, we demonstrate that impedance spectroscopy can be performed in a minimally invasive fashion and that it allows distinguishing fine brain structures such as the cortical layers of a mouse brain. The peak resistance frequency (PRF) analysis method allowed obtaining intrinsic “tissue resistivity” values that depend neither on the electrode size nor on the measurement frequency, as soon as tissue structures of interest are larger than electrode diameter. In this work, the term “resistivity” does not refer to the classical configuration in which homogeneous materials with defined dimensions are investigated but reports values for sub-millimetric volumes of the brain surrounding measurement electrodes. Measurements were performed first on post-mortem mice brains and then on brain slices for a better understanding of the mechanisms at play. We demonstrate the distinction of brain structures such as different cortical layers, fiber tracts, ventricles, thalamus and basal ganglia and evidence the impact of cell density on impedance measurements. In an application perspective, we further demonstrate that our method can be used to discriminate healthy and cauterized tissue in the brain and quantify the graduated cauterization effects. The developed flexible microelectrodes can be easily integrated on existing electrodes already used for DBS or epilepsy issues. The integration of local impedance measurements in real time during probe implantation or tissue stimulation would also raise knowledge on tissue integrity and on the propagation of electrical stimulation, i.e. lead to a better knowledge of the passive electrical properties of the brain tissues.

2. Materials and methods

2.1. Probe microfabrication

Neural probes were fabricated using standard clean room procedures. Fig. 1a and b shows the resulting microfabricated neural probe. The fabrication process has been presented in detail elsewhere (Cheung et al., 2007; Mercanzini et al., 2008; Metz et al., 2004).

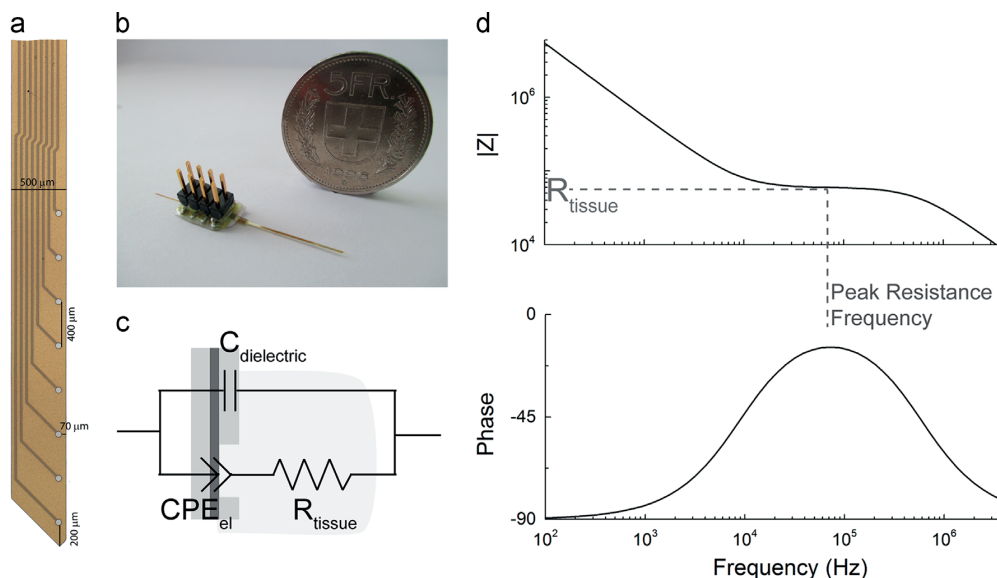


Fig. 1. Impedance measurement device and configuration. a. Microscope image of the polyimide probe used for measurements consisting of an array of eight 50 μm diameter platinum electrodes. b. Photograph image of the probe with glued connector and capillary. c. Electrical circuit model for the electrode/tissue/counter-electrode system. d. Corresponding impedance modulus, phase spectra and peak resistance frequency measurement method.

Briefly, a sacrificial aluminum layer is first deposited on a silicon wafer. A 20 μm thick layer of polyimide (PI2611, HD Microsystems GmbH, Germany) is then spin coated. A Ti/Pt/Ti sandwich is sputter deposited with thicknesses of 50/200/50 nm respectively. The first titanium layer serves as an adhesion layer whereas the second one constitutes a protection layer for the platinum during subsequent process steps and will be finally removed. The platinum layer is photolithographically defined and etched, thus determining the microelectrode array. A 4 μm thick layer of polyimide is then spin coated onto the metallic layer. Finally, both the device structure outline and the openings for the electrodes are defined by dry etching the polyimide through a silicon oxide mask. Polyimide devices are then detached from the silicon wafer by anodic dissolution of the sacrificial aluminum layer. A surface mount connector is glued to the bond pads at the end of the device using conductive silver epoxy (EPO-TEK H20E, Epoxy Technology Inc., USA). Electrical contacts are subsequently isolated with epoxy. In order to facilitate insertion into the brain tissues, the probe shaft is stiffened by gluing a fused silica capillary of an outer diameter of 150 μm on its backside, as shown in Fig. 1b.

2.2. Electrical impedance spectroscopy measurements

Impedance is measured with an impedance analyzer (Agilent 4294A, Agilent Technologies, USA). A sinusoidal voltage of 50 mV is applied between an electrode and a counter-electrode and the current is measured simultaneously, giving the impedance. Fig. 1c and d presents the electrical model of a tissue and the methodology used for impedance measurements. For each measurement the frequency is swept on a logarithmic scale from 100 Hz to 4 MHz. At each frequency, impedance magnitude and phase are recorded. The PRF method is applied to the obtained spectrum. This method has been described in detail elsewhere (Mercanzini et al., 2009). Briefly, the measured system comprises a microelectrode device, counter-electrode (platinum wire) and tissue. The interface between microelectrode and tissue is modeled by a constant phase element (CPE) whereas the counter-electrode contribution is neglected due to its large surface. The tissue is modeled by a resistor placed in series with the microelectrode CPE. Indeed, brain tissues are mostly resistive at the frequencies of interest in this work, with a resistive component being 20–100 times larger than the reactive one (Gabriel et al., 1996). The dielectric capacitance through the polyimide between metal trace and tissue is placed in parallel to these elements (see Fig. 1c). The resulting spectrum, presented in Fig. 1d, shows a decreasing impedance at low frequency due to the microelectrode CPE followed by a plateau corresponding to the tissue resistance. At higher frequencies, the dielectric capacitance becomes predominant. The tissue resistance value is given by the impedance modulus at the frequency at which the phase is closest to 0°. According to the model used here, the impedance at this frequency is a close approximation to R_{tissue} . The resistivity of the tissue surrounding the microelectrode is extracted from the tissue resistance using the relationship

$$R_{\text{tissue}} = \kappa \rho_{\text{tissue}} \quad (1)$$

where ρ_{tissue} is the resistivity of the tissue surrounding the electrode, d is the electrode diameter and κ is a constant factor, called cell constant. For an ideal disc electrode (with a diameter d) the cell constant is equal to $1/2d$ (Newman, 1966). In practice, every microelectrode has a slightly different cell constant, due to possible impurities adsorbed on the electrode surface. However, this factor is easily determined by measuring the impedance spectrum of the microelectrode placed in a saline solution of known resistivity. Before use, neural probes were rinsed with ethanol and plasma, and treated (Femto, Diener Electronic GmbH, Germany) at a pressure of 0.6 mbar and a power of 100 W for 6 s. All experiments were carried out at room temperature (24–25 °C).

2.3. Surgery and setup

2.3.1. *ex vivo* brains preparation

All experimental procedures were carried out according to the Swiss federation rules for animal experiments. Eight 4–6 weeks old mice were euthanatized through carbon dioxide inhalation; brains were extracted and placed into dedicated machined polymer molds in order to avoid any displacement during the experiments. Phosphate buffered saline solution (PBS) was added to avoid brains drying out. Measurements were carried out within 2 h of the death of the animal. The counter-electrode consisting of a platinum wire was immersed in the PBS solution next to the brain. The probe was mounted on a microcontroller and gradually inserted vertically into the brain. The whole electrode array composed of eight microelectrodes was used.

Measurements were also performed on brains remaining inside the skull of the euthanatized animal. In this case, a stereotaxic frame was used. Incisions were made in the skin and the periosteum overlying the skull, after which the periosteum was scraped away from the bone. Several coordinates were investigated based on a mouse brain atlas (Paxinos, 2004). Holes were drilled using a dummy cannula (25G) bilaterally at the following stereotaxic coordinates (anterior to bregma; medio-lateral in mm): $-0.7;1$ and $-0.7;1.5$. The counter-electrode was placed inside the brain approximately 3 mm anterior to bregma. Care was taken to avoid drying of the cortical surface and the skull was covered with PBS. The cortex was never left exposed to air since transient drying can alter the surface impedance. The probe was placed in the tatic clamp of the stereotaxic frame and gradually inserted vertically into the skull and brain. The whole electrode array composed of eight microelectrodes was used.

2.3.2. Acute slices preparation

All experimental procedures were carried out according to the Swiss federation rules for animal experiments. Five 12–16 days old mice were rapidly decapitated and neocortical slices (sagittal; 300 μm thick, lateral between 1.56 mm and 2.28 mm) were cut using a vibratome (Microslicer; DSK) filled with iced extracellular solution (artificial cerebrospinal fluid containing 125 mM NaCl, 25 mM NaHCO₃, 2.5 mM KCl, 1.25 mM NaH₂PO₄, 2 mM CaCl₂, 1 mM MgCl₂, and 25 mM D-glucose). Slices were incubated for 30 min at 34 °C and then at room temperature (24–25 °C).

For impedance measurements, slices were placed in a petri dish containing PBS solution under a 10 \times microscope objective. The counter-electrode consisting of a platinum wire was placed in contact with the brain slice. The tilted probe was inserted vertically into different slice areas by using a manual microcontroller. All measurements were performed with the microelectrode situated at the tip of the probe.

2.4. Cauterization

A short and rigid copper wire was firmly attached to a soldering iron which was used as a constant heat source. The temperature at the tip of the wire was monitored using a thermocouple and the power on the heat source was regulated in order to reach a steady temperature of 70–80 °C. Once this steady temperature was reached, the wire was carefully implanted into the brain for 60 s and then removed.

For slices cauterization, slices were placed in a petri dish and covered by a thin layer of PBS to avoid drying of the slice. Again, once a steady temperature of 70–80 °C was reached, the tip of the wire was put in contact with the slice for 60 s. The color change linked to the denaturation of the tissue following cauterization is directly observed with a binocular.

2.5. Histology and imaging

Standard coronal paraffin sections through the regions of interest were selected for visualizing the localization of the performed measurements (microtome Microm HM325). Small recesses located at the probe implantation site confirmed the measurement sites. Series of 4 μm sections (20 μm interval) were stained with hematoxylin–eosin and analyzed using light microscopy (Leica DM5500).

2.6. Cell density quantification

Fluorescence images were captured using a fluorescent microscope (ZEISS LSM 700 UPRIGHT). Quantification of cell density for each cortical layer was achieved by counting Dapi-stained nuclei. Cells counting data were generated from the observation of five independent fields using a pre-defined template, for each cortical layer.

2.7. Statistics

Statistical analysis was based on at least five independent series of experiments. Standard deviations are indicated on the graphs. By using a paired *t*-test, data were considered to be statistically significant when the two-tailed *p*-values were $p < 0.001$ (***), $p < 0.01$ (**) or $p < 0.05$ (*).

3. Results and discussion

3.1. Probe design

3.1.1. Microelectrodes diameter

Our measurement configuration involves micrometric electrodes and a counter-electrode measuring approximately 2 cm placed at least at 1 cm from the measurement point. This asymmetric geometry leads to a non-linear voltage drop between microelectrode and counter-electrode. In the case of a homogeneous tissue, it has been shown that most of the voltage drop occurs within short distance from the microelectrode. The order of magnitude of this distance is a few times the microelectrode diameter *d*. At a distance *d*, the voltage falls to 50% of its value on the microelectrode and at a distance 2*d* to 20% of it (Newman, 1966). Consequently, the volume contributing mostly to the impedance measurement (i.e. the volume of tissue of which the resistivity is actually measured) is a half sphere of a diameter of a few times *d* surrounding the microelectrode. This implies that microelectrode dimensions have to be carefully determined taking into account the size of the desired measurement volume. In this study, we intended to distinguish structural and cellular organizations of brain tissues having typical sizes of several hundreds of microns and composed of several types of cells, whose cell bodies diameters are in the range of 10 μm . To this end, we need to measure the resistivity of small volumes so as to be able to differentiate structures down to the scale of 100 μm . On the other hand, the measurement volume has to be large enough to constitute a representative sample of the investigated structure, i.e. it has to contain the different constitutive elements such as neurons, glial cells, fibers, myelinated axons and extracellular matrix. For these reasons, we chose a sampling volume on the order of 50–100 μm size and consequently designed and fabricated disc microelectrodes measuring 50 μm in diameter.

3.1.2. Microelectrodes spacing

The probe design resulted from a compromise between a high number of microelectrodes and a minimal invasivity. The total

shaft width is determined by the number of metal traces linking the microelectrodes to the connector. In this work we chose to pattern 8 electrodes on the probe, resulting in a total probe width of 500 μm which was considered a reasonable induced invasivity for future *in vivo* measurements on mice brains (one of the smallest *in vivo* model brains) (Lee et al., 2013; Polikov et al., 2005). The electrodes are placed in a vertical array (Fig. 1a). Inter-electrode spacing has been chosen to measure impedances over a large range of depths inside the brain without moving the device. Considering these different requirements the chosen tradeoff inter-electrode spacing was 400 μm , enabling measuring simultaneously impedance at 8 depths over a total range of 2.8 mm.

3.1.3. Probe stiffness

In order to minimize invasivity and to allow tissues enfolding tightly the probe, it was microfabricated with a thickness of only 20 μm at its tip. It is thus flexible and enables a good conformity with the penetrated tissues.

3.2. Discriminating brain structures with impedance spectroscopy

3.2.1. Brain resistivity profiles

In order to observe the probe penetration into the brain tissues during the measurements, impedance measurements were first performed on an extracted brain placed in a dedicated mold. The probe equipped with a vertical array of aligned microelectrodes was gradually inserted vertically into the brain in the motor area of the cortex (M1) and below for several mm, as shown in Fig. 2a. Fig. 2b shows resistivity values obtained during probe penetration. Since the inter-microelectrode distance is 400 μm , successive measurements were performed each 400 μm . This allowed recording several times the resistivity of the same tissue (micro-region, each time with a successive microelectrode of the vertical array. Fig. 2c presents resistivity measurements performed during the penetration of a probe into the brain at six different depths separated by the inter-electrode distance of 400 μm . For microelectrodes located outside the brain, we measured extremely high resistivities, in the order of several hundreds of ohm meters. In this situation, microelectrodes are in contact only with a small film of PBS attracted by capillary forces due to the hydrophilicity of the plasma treated polyimide probe. When microelectrodes penetrate the tissue, the resistivity drops abruptly to values between 0.5 and 10 Ωm . This abrupt change in resistivity correlates with the “real time” observation of the probe penetration in the brain. The resistivity value of each electrode corresponds to a tiny volume of tissue (a half sphere of 50–100 μm diameter in our case, as explained in Section 3.1) and is specific to the structure in which the electrode is placed. This abrupt decrease of resistivity when the electrode enters into the brain and the subsequent increase of resistivity at higher depths are measured by the different electrodes. Furthermore, we observe comparable values for a same region for successive measurements performed with successive microelectrodes of the array. This shows that the resistivity measurement is electrode-independent and demonstrates that the penetration of the developed neural probe inside the brain tissues is minimally invasive. The progression of the probe inside the brain was monitored the same way as that of its penetration. Fig. 2d–f shows resistivity profiles obtained by progressing deeper in the mouse brain. We observe significant resistivity inhomogeneities inside the brain tissues that we can repeatedly measure by descending the probe by steps of a distance equal to the inter-electrode distance. This is important since it shows that the brain has not been distorted while moving the electrodes, such that the relationship between electrode positions and tissue boundaries remains intact.

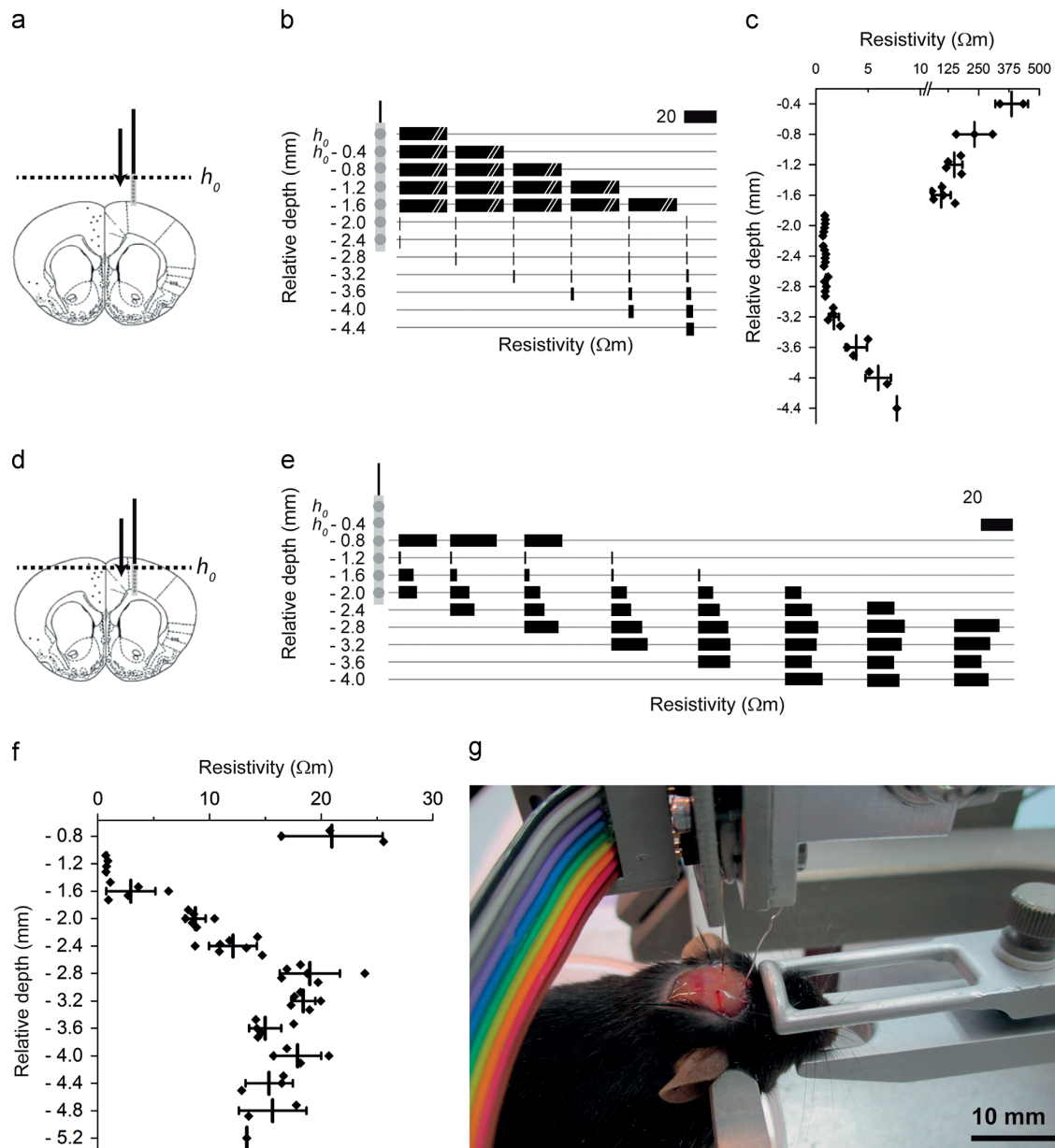


Fig. 2. Monitoring of probe penetration into the brain. a and d. Schematic representation of probe penetration and progression. b and e. Resistivity profiles measured with 8 different microelectrodes on the same probe while penetrating into the brain and while progressing inside the brain. c and f. Measurements grouped as a function of the position of the electrode (mean \pm SD). g. Photograph image of a post-mortem stereotaxic implanted mouse.

These results lead us to investigate systematically the resistivity of brain tissues along the vertical axis over several millimeters. To this end, we determined the probe insertion coordinates by stereotaxy and inserted it gradually thanks to the z-micromanipulator of the stereotaxic frame, as illustrated in Fig. 2g. As before, we cross checked resistivity values obtained at the same brain depth by taking advantage of the specific configuration of the microelectrode array. Fig. 3 displays typical resistivity z-profiles obtained for two different insertion coordinates. To relate the actual electrode position to a particular cytoarchitectonic layer, histological sections were performed after measurement sessions. By combining observations

of these sections and z-depth measurements thanks to the stereotaxic frame, we were able to position very precisely the measurement points on the mouse brain atlas. This allowed linking resistivity values to specific brain structures/areas. Fig. 3a–c shows the resistivity profile obtained at 0.7 mm anterior to bregma, and bilaterally medio-lateral 1.5 mm. In the first millimeters, the probe progresses inside the cortex. We noted low resistivities, namely 1–2 Ω m, until a depth of 250 μ m corresponding to the first cortex layers (layer I and beginning of layer II). Resistivity grows to values of approximately 6 Ω m for the deeper cortex layers. After the cortex, the probe penetrates inside the corpus callosum.

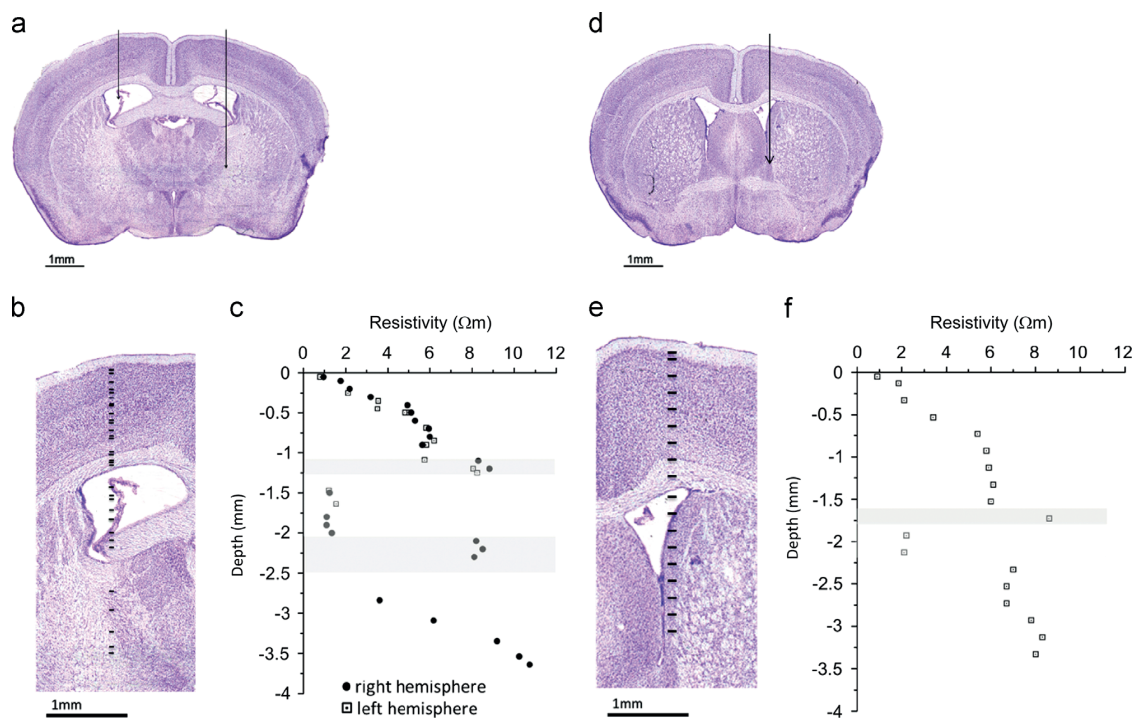


Fig. 3. Post-mortem measurements of vertical resistivity profiles within the mouse brain. a–c. Resistivity profile for same positions in both hemispheres (bregma -0.7 mm, lateral 1.5 mm). d–f. Resistivity profile for bregma 0.26 mm, lateral 1 mm. a and d. Illustration of the probe progression in the brain on a coronal cross section map. b and e. Illustration of each electrode position. Dashes on the map correspond to resistivity measurement positions. c and f. Measured resistivity as a function of the electrode depth. Each measurement point in b and e corresponds to a resistivity value depicted at the corresponding height respectively in c and f.

This structure forming a flat bundle of neural fibers and thus connecting left and right cerebral hemispheres constitutes the largest white matter structure in the brain. This fiber tract exhibits the highest resistivity comprised between 8 and $9 \Omega \text{ m}$. These values are significantly higher than those obtained for the gray matter of the cortex. This trend is in accordance with those reported in the literature where white matter tissues exhibit higher resistivity values compared to the gray matter tissues. For example, [Latikka et al. \(2001a, 2001b\)](#) reported that for gray matter the average resistivity was $5.96 \Omega \text{ m}$ (standard deviation: $1.42 \Omega \text{ m}$) whereas white matter had an average resistivity of $9.02 \Omega \text{ m}$ (standard deviation: $2.61 \Omega \text{ m}$). [Gabriel et al. \(1996\)](#) as well as [Bao et al. \(1997\)](#) reported white matter resistivity being respectively 1.25 and 1.65 times larger than that of the gray matter. It is difficult to compare absolute impedance values with our results because different animal models were used and they also can depend on the type of electrode used. Nevertheless, we observed the same tendency. The brain is not a homogeneous medium. There are important differences in the histological properties of the gray and white matter, and it comes as no surprise that they also differ in electric impedance. The higher impedance of the white matter is often explained by the fact that this area is mostly composed of myelinated fibers exhibiting much higher electrical resistance ([Nicholson, 1965](#)).

Cortical impedance measurements have been discussed with two perspectives: frequency dependence and inhomogeneity/anisotropy. Regarding frequency dependence, in this study, we always used the PRF to determine the tissue resistivity from the impedance measurements done on the electrode–tissue system as described in [Section 3.2.2](#) and demonstrated by [Mercanzini et al. \(2009\)](#). The PRF method is particularly recommended in the case of microelectrodes because the electrode capacitance is small and dominates the impedance values at low frequencies whereas the

parasitic capacitance dominates at high frequencies. The plateau, corresponding to the actual resistivity value of the tissue surrounding the electrode, is consequently located in a short frequency window. The PRF method enables locating precisely this window and obtaining resistivity values close to the tissues intrinsic values. It is more efficient than conventional impedance measurements at 1 kHz because such measurements performed with microelectrodes would lead to values corresponding mostly to the interfacial capacitance between electrode and tissue. This value is strongly electrode dependent, contrarily to the values presented in this work. The PRF is consequently a pertinent method to combine the advantages of micrometric electrodes with impedance measurements and allowed us to obtain intrinsic resistivity values of the tissues with sub-millimetric resolution. For a more detailed explanation of the PRF, see [Mercanzini et al. \(2009\)](#). The frequency window of actual tissue resistivity measurement can vary slightly depending on the local resistivity value. As a consequence, the measurements are not always performed at the exact same frequency. Nevertheless, the frequency dependence of the brain tissue at the frequencies of interest in this work (10 – 500 kHz) is far less pronounced than dependency on the measured structure, i.e. on the electrode localization in our case. Several studies report impedance measurements performed at different frequencies in the brain. [Logothetis et al. \(2007\)](#) concluded from their measurements on the cortex of macaque between 10 Hz and 50 kHz that the impedance is almost purely resistive, and thus almost independent of the frequency. [Nicholson \(1965\)](#) measured the resistivity of fiber tracts of cats between 20 Hz and 20 kHz. He reported a very strong dependency on the direction of measurements but almost no dependency on the frequency. [Gabriel et al. \(1996\)](#) measured impedance of white and gray matter in bovine brains. For frequencies between 10 kHz and

100 kHz they reported a resistivity of white matter changing from 16.5 Ω m to 14 Ω m (a drop of around 15%) whereas the resistivity of gray matter at comparable frequencies is reported to be approximately 8 Ω m (i.e. half of the white matter values). Some studies reported a high anisotropy in the white matter (Güllmar et al., 2010; Ranck and Bement, 1965). In our case we always used the same measurement configuration, thus measuring resistivity always in the same direction.

Inside homogeneous structures like in the corpus callosum, we did not note any variability of impedance, as shown in Fig. 3a–c. Several measurement points are located inside corpus callosum and gave same high values of resistivity ($8.3 \pm 0.37 \Omega$ m). Descending the probe further inside the brain leads to an abrupt resistivity decrease to values around 1 Ω m (mean value is $1.28 \pm 0.12 \Omega$ m). This is explained by the penetration of the probe inside the lateral ventricle, which is filled with cerebrospinal fluid characterized by an impedance of 0.7–0.8 Ω m. Indeed, Baumann et al. (1997) reported values for the human cerebrospinal fluid at room temperature of around 0.7 Ω m at a frequency ranging from 10 Hz to 10 kHz. Latikka et al. (2001) obtained values of approximately 0.8 Ω m in humans at 50 kHz. Here again, we observed same impedance values for all measurements performed inside the ventricle. On the impedance profile presented in Fig. 3a–c, we observe a second abrupt impedance change (from 1 Ω m to 8 Ω m). The probe is again localized in the corpus callosum, which is situated below the ventricle in this brain region. For higher brain depths, namely in the thalamus structure, we noted a high distribution of impedance values. This can be explained by the heterogeneity of this brain structure. Because of the small measured tissue volume, resistivity values can reflect various parts of this

composition explaining the value distribution inside this area. On the impedance profile presented in Fig. 3f, below the lateral ventricle (and corresponding low impedance values), we observe an increase of impedance (around 7 Ω m and 8 Ω m deeper). At these depths, measurements were performed in the basal ganglia. Probe insertion and impedance measurements were performed in both brain hemispheres for the same stereotaxic coordinates. As shown in Fig. 3c, we obtained same resistivity values for the same depths for both hemispheres, demonstrating the reliability and accuracy of the measurement method. Comparable profiles were obtained three times for three different mice.

3.2.2. Cortex layers resistivity

The micrometric dimensions of our electrodes allowing small volume resistivity measurements combined with high precision z-displacements lead us to demonstrate inhomogeneities inside the cortical gray matter (Fig. 2, depths from 0 to –1 mm and 0 to –1.5 mm). One would expect that these differences could be related to the cortex organization in several layers. Although, as mentioned before, numerous studies have shown resistivity differences between gray and white matter, the resistivity differences within the gray matter have been less studied and no clear relation to the histological structure has been shown. In order to investigate the hypothesis that the resistivity profiles in the cortex are related to histological structures, we measured impedance on brain slices instead of a complete brain. Indeed, this new configuration allowed visualizing properly and in real time the measurement localization. Fig. 4a presents the setup used. 300 μ m thick sagittal brain slices are placed in a petri dish filled with phosphate

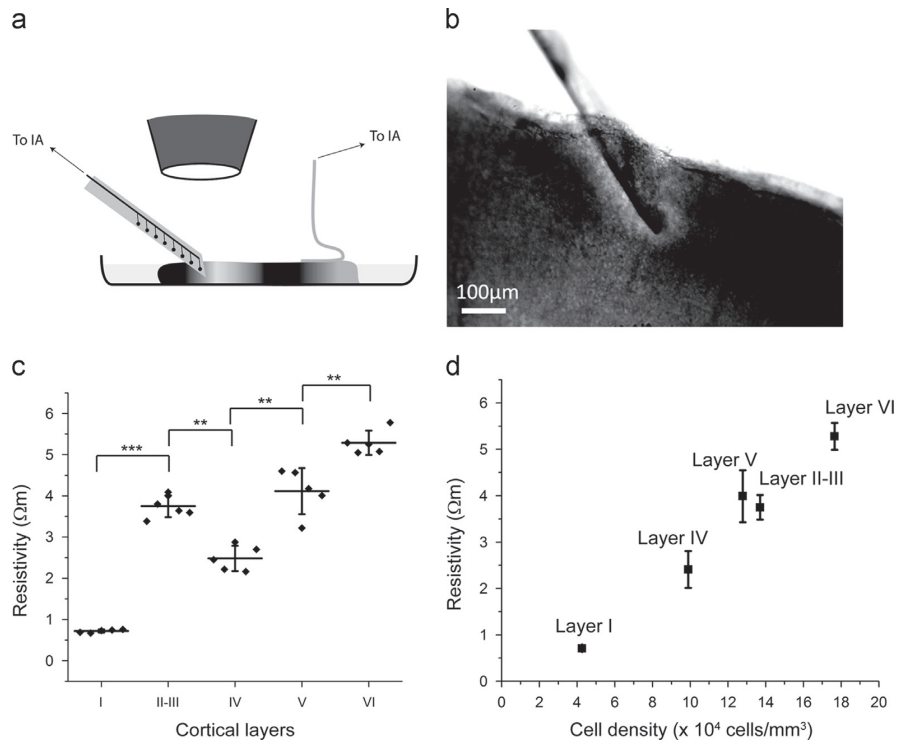


Fig. 4. Resistivity measurements in the different cortical layers on acute brain slices. a. Experimental setup used for measurements on brain slices. b. Microscope image of a slice with inserted probe tip for resistivity measurement. c. Boxplot of the resistivity values obtained for the different cortical layers (mean \pm SD, $n=6$). Paired t -test: $p < 0.001$ (***); $p < 0.01$ (**) or $p < 0.05$ (*). d. Measured resistivity (mean \pm SD) as a function of the cell body density (mean \pm SD). Standard deviations in cell body density are too small to be visible. Note that on the graphs, layers are depicted with equivalent weight whereas layers have different thicknesses in reality.

buffered saline under an optical microscope. Differential interface contrast microscopy allowed distinguishing the different cortical layers. Thanks to a micromanipulator, a probe tip was inserted precisely in each cortex layer at middle height within the slice. Fig. 4b presents a microscope image of the probe tip inserted within a slice. We can distinguish the round electrode appearing black in the picture. The counter-electrode is placed in contact with the slice at a distance of approximately 1 cm from the measured region. The small thickness of the probe and its flexibility enabled an excellent contact between tissue and electrodes which is observed in situ when the probe is inserted and withdrawn from the tissue. This strong contact excludes any impedance alteration due to the presence of a liquid film or gap between electrode and tissue, confirming that our measurements correspond to the actual electrical properties of the tissue region. Combining microscopic observation and data from the mouse brain atlas, measurements were performed in the five layers of the somatosensory cortex and in corresponding layers in the cortex motor area. Due to the thinness of layer II it was impossible to distinguish it from layer III. We thus treated layer II and III as one single region. Measurements were performed several times on the same slice and on different slices, in the primary and somatosensory cortex.

Fig. 4c presents the measured resistivity for layers I–VI. Resistivity values are between $0.72 \pm 0.03 \Omega \text{ m}$ for layer I and $5.28 \pm 0.26 \Omega \text{ m}$ for layer VI. For each layer, we observed characteristic resistivity values. Measurements were repeatable inside a layer for a same slice and for different slices. Layer I exhibits a low resistivity ($0.72 \pm 0.03 \Omega \text{ m}$) and layers II/III and V show a higher resistivity with respective mean values of $3.78 \pm 0.25 \Omega \text{ m}$ and $4.11 \pm 0.15 \Omega \text{ m}$. Layer IV reveals a lower resistivity with a mean value of $2.48 \pm 0.27 \Omega \text{ m}$. At the bottom of the cortex, layer VI exhibits the highest resistivity with a mean value of $5.28 \pm 0.26 \Omega \text{ m}$. Each layer has resistivity values statistically different from its adjacent layer ($p < 0.01$ for each comparison between neighbor layers and $p < 0.001$ in the case of layer I). Indeed, cortical layers are different in function and structure. For instance, layer I contains few neuronal cell bodies and consists mainly of fiber tracts and glial cells. Other layers contain a higher number of neurons of different types and sizes depending on the layer.

For describing rigorously the measured cortical layers, we quantified cell body density for each layer. The graph presented in Fig. 4d shows the resistivity as a function of the cell density for each cortical layer. Layers with low cell body densities (layer I and to a lesser extent layer IV) exhibit low resistivity values. Layers II/III and V have higher and comparable cell body densities and exhibit larger and comparable resistivity values. Layer VI has the largest cell body density ($\sim 180,000 \text{ cells/mm}^3$) and the largest resistivity. We observed that resistivity is linearly correlated with cell density (correlation coefficient is 0.96). Measurements performed using a probe equipped with only one electrode would lead to uncertainty and would not allow discriminating reliably the electrode position in the in vivo situation. Using numerous microelectrodes confirms thus the opportunity of possible cross-checking measurements on different electrodes placed at a determined distance from each other. By comparing the cortex resistivity values we obtained on slices with those obtained in complete brains, we observe the same tendencies. In both configurations, we noted very low resistivity values for the first cortical layer and an impedance increase for layers II/III, V and VI. However, at corresponding localizations in the “complete brain configuration”, layer IV does not exist or has a very low thickness ($< 100 \mu\text{m}$). The corresponding drop of resistivity measured in the “slice configuration” can consequently be hardly measured. Taking this element into account, the results presented here on sagittal slices are in good accordance with the measurements performed in the cortex in the “complete brain configuration”.

A few studies reported impedance differences inside the cortex. Hoeltzell and Dykes reported relative vertical conductivities in the

somatosensory cortex of cats. Their data showed marked and abrupt changes with cortical depth (Hoeltzell and Dykes, 1979). Goto et al. evaluated the conductivity profile in the somatosensory barrel cortex of wistar rats and found impedance anisotropies. However, they did not find any correlation between the conductivity profile and the density of cell bodies, either for neurons and astrocytes, or for oligodendrocytes (Goto et al., 2010). This can be potentially explained by the fact that the authors investigated only the specific frequency of 500 Hz. Besides these measurements on animal cortex, in vitro models have also been developed in order to investigate tissue reaction to inserted microprobes using impedance measurements. Frampton et al. (2010) constructed an in vitro model of rat cortex consisting of a three dimensional architecture of cells encapsulated in alginate with an implanted microprobe, with which impedance measurements were performed. They showed that cell density is the critical factor in determining the resistance of the tissue surrounding the electrodes.

3.3. Measurement of the spatial extent and gradation of brain tissue denaturation induced by cauterization

The results presented so far demonstrate that our impedance measurement setup can be used to perform repeatable measurements in the brain with high spatial accuracy. In the following sections, we aim at demonstrating that impedance spectroscopy performed with microelectrode arrays can help to qualify brain tissues modified during surgical procedures, as for example tissue coagulation following thermal ablation. Thermal ablation is currently used in a wide range of diseases or disorders, like brain tumors, or epilepsy. In each case, a very important focus is to limit the ablation to the desired part. However, surgeons rarely get an immediate feedback of their actions.

In order to imitate a local thermal ablation, we locally cauterized the somatosensory cortex of an ex vivo mouse brain using a copper wire (300 μm in diameter) attached to a heating element. During this operation, the 70–80 °C hot copper wire is placed inside the brain for 60 s. The local heat of the wire dissipates, inducing a temperature gradient from a central hot point in all directions. This heating results usually in a radial wound with a central part composed of necrotic tissue with a loss of cellular integrity and a peripheral part with shrunken neurons and glial cells with condensed nuclei (Miao et al., 2002). Fig. 5a shows a histological section of the cauterized brain stained with hematoxylin–eosin (HE). We observe color changes of the HE-stained slice in the cauterized area. The wound is not clearly demarcated from the healthy tissue, but a penumbra surrounds it, in which the tissue changes progressively from healthy to necrotic with a progressive loss of cellular integrity (Hsu et al., 2000; Miao et al., 2002). In Fig. 5a, the necrotic area and the penumbra are delimited by gray dashed lines. Black dashes represent measurement positions located every 250 μm inside the cauterized brain region, surrounding penumbra and healthy tissue located more deeply in the brain.

Fig. 5b shows the obtained resistivity profile. We observe a low resistivity (values are between 0.5 and 2 $\Omega \text{ m}$) for depths corresponding to the wound region. In the penumbra, resistivity values grow steadily from the wound region to healthy tissues. For depths corresponding to corpus callosum region we note a high impedance increase that was already observed in healthy brains, thus meaning that corpus callosum is not affected by the cauterization in this experiment.

In order to investigate more precisely the cauterization effect and its spatial extent, we repeated the cauterization and resistivity measurements on brain slices (see Fig. 6). This planar configuration allowed observing the slice directly with a microscope and thus determining precisely where to measure the impedance. As before,

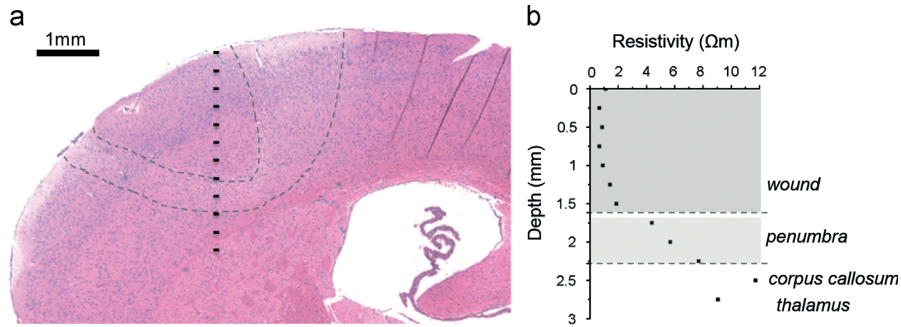


Fig. 5. Resistivity profile of a locally cauterized ex vivo mouse brain. a. Microscope image of a histological section in the cauterized area of the brain. Cauterized portion of the brain and penumbra are delimited by dashed lines. Electrode position for each measurement of the vertical profile is represented by a bold dash. b. Resistivity values as a function of depth. Black dots representing resistivity values in b and corresponding black dashes representing the electrode position are depicted at the same heights.

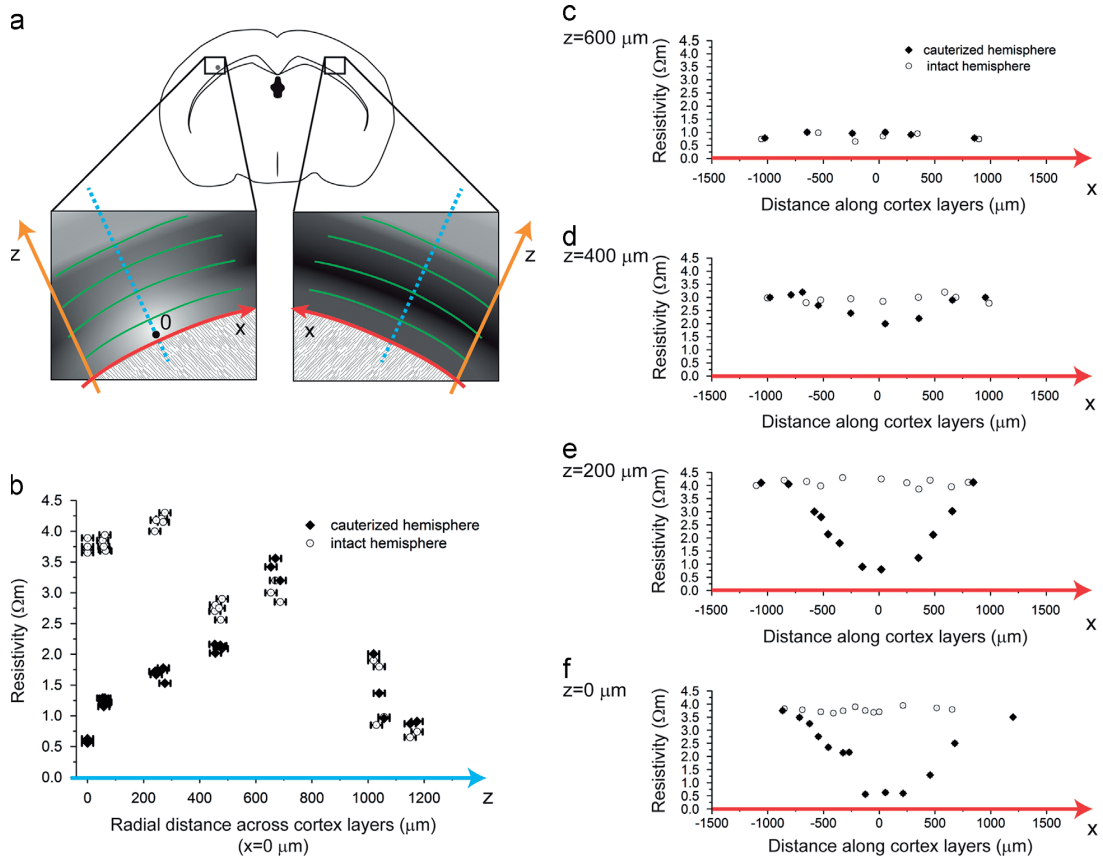


Fig. 6. Resistivity measurement of a locally cauterized coronal brain slice a. Schematic representation of the slice. Cauterization point is represented by the black dot in the left hemisphere. The right hemisphere was kept intact. Resistivity is represented by gray scale in the cortex, dark gray corresponds to high resistivity. b. Resistivity values obtained for various radial distances across the cortical layers (z-axis in a) from the center of the cauterization in the right hemisphere (black dots) and from the corresponding point in the left hemisphere (clear dots). c–f. Resistivity along cortical layers (x-axis in a) for different distances from the center of cauterization (arc lines in a) in the cauterized (black dots) and intact (clear dots) hemisphere. The zero point on the x-axis corresponds to the point at the minimal distance of the center of cauterization (intersection of the arc lines with the dotted line in a).

cauterization was executed by heating a specific point of the slice with a copper wire at a temperature of 70–80 °C for 60 s. Cauterization was performed on the right hemisphere of a 300 μm thick coronal brain slice while the left hemisphere was kept intact. The heat dissipated and propagated within the slice, creating a radial thermal gradient from the heating point in all directions. At the

center of the heated area, the tissue appeared visually clearer than normal, showing strong denaturation. Most of the cell membranes were lysed, leading to local necrosis (Hsu et al., 2000). Microscope observation of the slice showed that damages caused on the tissue decreased gradually with increasing distance from the insertion site of the heat source. For large distances, the tissue appeared intact.

A schematic view of the brain slice summing up these observations is presented in Fig. 6a. In order to determine the impact of the cauterization on the resistivity and characterize its spatial extent, impedance measurements were performed in the direction of the arrows depicted in Fig. 6a, i.e. i) orthogonally to the layers (resulting graph is presented in Fig. 6b) and ii) along the cortical layers at different distances from the heated point (resulting graphs are presented in Fig. 6c–f). In order to obtain control values, impedance measurements were done at the corresponding symmetric points in the intact hemisphere.

Resistivity values measured along an orthogonal line to cortical layers in both hemispheres are presented in Fig. 6b. On the intact hemisphere, we noted variations of the resistivity inherent to the layer organization of the cortex. However, resistivity profile on the cauterized hemisphere differs strongly evidencing the effect of the cauterization on the tissue. From Fig. 6b, we observe a significant decrease of the resistivity in the heated area which does not appear in the intact hemisphere. Values change from 3.5 to 4 Ω m in the intact hemisphere to around 0.5 Ω m for symmetrical coordinates in the cauterized hemisphere. In this region, the tissue is strongly denatured: cell membranes have lost their integrity and the remaining tissue is composed uniquely of lysate comparable to cerebrospinal fluid and with corresponding measured resistivity.

For radial distances from the insertion site of the heat source comprised between 0 and 600 μ m, the resistivity increases steadily on the cauterized side from 0.6 to 3.2 Ω m. On the healthy side, it is clearly layer dependent. For larger distances, both hemispheres show similar, layer dependent values. The resistivity profile obtained for the cauterized side results from two types of contribution: inherent resistivity and cauterization induced by the cauterization. With increasing radial distance, the difference between values for cauterized and intact hemispheres decreases gradually. For radial distances superior to 600 μ m, both hemispheres exhibit comparable resistivity values and cauterization effects are not measurable anymore. Resistivity results presented in Fig. 6b can be consequently considered as an accurate measurement of the radial extent and the gradation of the progressive wound caused by the thermal treatment.

As observed previously (see Fig. 4), resistivity is homogeneous inside each cortex layer and differs between them. In order to overcome the issue of inherent resistivity variability due to the layer organization of the cortex and to measure impedance changes only due to the cauterization, measurements were also performed inside layers at different distances from the heated point (along the arc lines of Fig. 6a). Results are presented in Fig. 6c–f. In the intact hemisphere (clear dots on the graphs), we observe again that resistivity is homogeneous within layers and differs between them. On the contrary, in the cauterized hemisphere, we clearly observe an impedance decrease in the vicinity of the cauterization point source. For layers located in the direct vicinity of the heated point (100–300 μ m distance), the impedance drop is strong and resistivity values are comparable to those of cerebrospinal fluid. Values become comparable to those obtained in the intact hemisphere only at high distances from the heated point (approximately 1 mm along the layer, see Fig. 6c). On the layers placed gradually further from the heated point (300 and 500 μ m), the resistivity drop decreases gradually both in depth and in extent (Fig. 6d and e). No drop has been measured on the farthest layer (Fig. 6f). Here again, the impedance measurements enable qualifying the extent and gradation of the wound and induced penumbra area caused by the cauterization. Thus, these measurements demonstrate the possibility of using impedance measurements performed with an implantable microelectrode array in order to determine the extent of the denaturation caused during surgery. Combined with existing surgical tools for performing thermoablation, this could enable checking in real time the localization and propagation of the induced necrosis.

4. Conclusion

Impedance measurements in the brain using macroscopic needles were reported by many researchers previously. They allowed obtaining resistivity values of big structures, discriminating for example brain gray and white matters. A few studies report the use of micrometric electrodes for impedance measurements with higher spatial resolution. However, these measurements were performed at mostly specific frequencies, leading to resistivity values dependent on both the measurement frequency and electrode design. Here, we reported the use of the PRF method to obtain intrinsic resistivity values of brain tissues that are independent of the microelectrodes size. In this study we could demonstrate that impedance spectroscopy measurements with microelectrodes embedded in a specifically designed neural probe is a suitable method to systematically identify tiny cerebral structures. Thanks to a micrometric electrode array we were able to distinguish and localize cortical layers measuring hundreds of micrometers inside the mouse brain, thus demonstrating high localization and resistivity accuracy. We were further able to show that tissue resistivity inside the cortex is positively correlated with cellular density. To the best of our knowledge, such measurements along with a clear correlation with the underlying histological cortical structures have never been reported elsewhere. In addition, impedance spectroscopy based real-time measurement on a cauterized mouse model revealed impedance spectra characteristics that could be used for the discrimination of healthy tissue from cauterized tissue and also for measuring the spatial extent of the induced wound.

Ultimately such a technique can be used in several clinical applications. For example, it could be potentially used to monitor in real time the extent of a radiofrequency ablation, with the advantage that the electrode array required for the measurement could be placed directly on the radiofrequency ablation device. The flexible microelectrode array could also be easily integrated on existing neural probes used clinically for deep brain stimulation. As such, it could be a simple, precise and real-time localization device used in addition to conventional imaging techniques. For research and more fundamental studies, this method can bring information about the evolution of tissue integrity or structural modifications related to the local administration of a drug or to tissue stimulation for example. In the case of studies of dynamical effects involving animal models, using this real time monitoring could also help to reduce the number of animals euthanized at different time points.

Acknowledgments

Stoicescu Foundation and Brazilian Swiss Joint Research Programme No. BJRP 0112-09 are gratefully acknowledged for their partial financial contribution to this work. We would like to thank Dr. Thomas Braschler and Dr. Maurizio Pezzoli for their helpful discussions and the EPFL histology and biomaging and optics core facilities for their excellent technical assistance.

References

- Baumann, S.B., Wozny, D.R., Kelly, S.K., Meno, F.M., 1997. *IEEE Trans. Biomed. Eng.* 44, 220–223, <http://dx.doi.org/10.1109/10.554770>.
- Burchiel, K.J., McCartney, S., Lee, A., Raslan, A.M., 2013. *J. Neurosurg.* 119, 301–306, <http://dx.doi.org/10.3171/2013.4.JNS12324>.
- Cheung, K.C., Renaud, P., Tanila, H., Djupsund, K., 2007. *Biosens. Bioelectron.* 22, 1783–1790, <http://dx.doi.org/10.1016/j.bios.2006.08.035>.
- Ellis, S., Rieke, V., Kohn, M., Westphalen, A.C., 2013. *J. Med. Imaging Radiat. Oncol.* 57, 391–399, <http://dx.doi.org/10.1111/1754-9485.12085>.
- Frampton, J.P., Hynd, M.R., Shuler, M.L., Shain, W., 2010. *Ann. Biomed. Eng.* 38, 1031–1047.
- Gabriel, S., Lau, R.W., Gabriel, C., 1996. *Phys. Med. Biol.* 41, 2251–2269, <http://dx.doi.org/10.1088/0031-9155/41/11/002>.

- Gigante, P.R., Goodman, R.R., 2012. *Eur. Neurol. Rev.* 7, 140–144.
- Goto, T., Hatanaka, R., Ogawa, T., Sumiyoshi, A., Riera, J., Kawashima, R., 2010. *J. Neurophysiol.* 104, 3388–3412, <http://dx.doi.org/10.1152/jn.00122.2010>.
- Güllmar, D., Hauelsen, J., Reichenbach, J.R., 2010. *NeuroImage* 51, 145–163, <http://dx.doi.org/10.1016/j.neuroimage.2010.02.014>.
- Hoeltzell, P.B., Dykes, R.W., 1979. *Brain Res.* 177, 61–82, [http://dx.doi.org/10.1016/0006-8993\(79\)90918-1](http://dx.doi.org/10.1016/0006-8993(79)90918-1).
- Hsu, T.H., Fidler, M.E., Gill, I.S., 2000. *Urology* 56, 872–875, [http://dx.doi.org/10.1016/S0090-4295\(00\)00737-8](http://dx.doi.org/10.1016/S0090-4295(00)00737-8).
- Jahnke, H.G., Heimann, A., Azendorf, R., Mpoukouvalas, K., Kempfski, O., Robitzki, A.A., Charalampaki, P., 2013. *Biosens. Bioelectron.* 46, 8–14, <http://dx.doi.org/10.1016/j.bios.2013.02.013>.
- Jian-Zhong, Bao, Shin-Tsu, Lu, Hurt, W.D., 1997. *IEEE Trans. Microw. Theory Tech.* 45, 1730–1741, <http://dx.doi.org/10.1109/22.641720>.
- Kalvøy, H., Frich, L., Grimnes, S., Martinsen, Ø.G., Hol, P.K., Stubhaug, A., 2009. *Physiol. Meas.* 30, 129, <http://dx.doi.org/10.1088/0967-3334/30/2/002>.
- Kikinis, R., Gleason, P.L., Lorensen, W.E., Wells III, W.M., Grimson, W.E.L., Lozano-Perez, T., Ettinger, G.J., White, S.F., Jolesz, F.A., 1994. Image guidance techniques for neurosurgery. pp. 537–540. 10.1117/12.185217
- Latikka, J., Kuurte, T., Eskola, H., 2001a. *Phys. Med. Biol.* 46, 1611, <http://dx.doi.org/10.1088/0031-9155/46/6/302>.
- Latikka, J.A., Hyttinen, J.A., Kuurte, T.A., Eskola, H.J., Malmivuo, J.A., 2001b. The conductivity of brain tissues: comparison of results in vivo and in vitro measurements. In: Proceedings of the 23rd Annual International Conference of the IEEE Engineering in Medicine and Biology Society. 2001, vol. 1, pp. 910–912. <http://dx.doi.org/10.1109/IEMBS.2001.1019092>
- Lee, S., Kanno, S., Kino, H., Tanaka, T., 2013. *Jpn. J. Appl. Phys.*, 52, <http://dx.doi.org/10.7567/JJAP.52.04CL04>.
- Li, C., Wu, L., Song, J., Liu, M., Lv, Y., Sequeiros, R.B., 2010. *Eur. Radiol.* 20, 404–409, <http://dx.doi.org/10.1007/s00330-009-1554-8>.
- Lim, T.T., Fernandez, H.H., Cooper, S., Wilson, K.M.K., Machado, A.G., 2013. *Neurosurgery* 73, E184–E187, <http://dx.doi.org/10.1227/01.neu.0000429852.45073.73>.
- Logothetis, N.K., Kayser, C., Oeltermann, A., 2007. *Neuron* 55, 809–823, <http://dx.doi.org/10.1016/j.neuron.2007.07.027>.
- Mayer, M., Brunner, P., Merwa, R., Smolle-Jüttner, F.M., Maier, A., Scharfetter, H., 2006. *Physiol. Meas.* 27, S93, <http://dx.doi.org/10.1088/0967-3334/27/5/S08>.
- Mercanzini, A., Cheung, K., Buhl, D.L., Boers, M., Maillard, A., Colin, P., Bensadoun, J.C., Bertsch, A., Renaud, P., 2008. *Sens. Actuators Phys.* 143, 90–96, <http://dx.doi.org/10.1016/j.sna.2007.07.027>.
- Mercanzini, A., Colin, P., Bensadoun, J.C., Bertsch, A., Renaud, P., 2009. *IEEE Trans. Biomed. Eng.* 56, 1909–1918, <http://dx.doi.org/10.1109/TBME.2009.2018457>.
- Merwa, R., Hollaus, K., Oszkar, B., Scharfetter, H., 2004. *Physiol. Meas.* 25, 347–354.
- Metherall, P., Barber, D.C., Smallwood, R.H., Brown, B.H., 1996. *Nature* 380, 509–512, <http://dx.doi.org/10.1038/380509a0>.
- Metz, S., Bertsch, A., Bertrand, D., Renaud, P., 2004. *Biosens. Bioelectron.* 19, 1309–1318, <http://dx.doi.org/10.1016/j.bios.2003.11.021>.
- Miao, Y., Ni, Y., Yu, J., Zhang, H., Marchal, G., 2002. *J. Neurooncol.* 56, 119–126, <http://dx.doi.org/10.1023/A:1014538011293>.
- Mittal, S., Mittal, M., Montes, J.L., Farmer, J.P., Andermann, F., 2013. *Neurosurg. Focus* 34, E7, <http://dx.doi.org/10.3171/2013.3.FOCUS1356>.
- Mohri, K., Honkura, Y., Panina, L.V., Uchiyama, T., 2012. *J. Nanosci. Nanotechnol.* 12, 7491–7495.
- Newman, J., 1966. *J. Electrochem. Soc.* 113 (501), 502, <http://dx.doi.org/10.1149/1.2424003>.
- Nicholson, P.W., 1965. *Exp. Neurol.* 13, 386–401, [http://dx.doi.org/10.1016/0014-4886\(65\)90126-3](http://dx.doi.org/10.1016/0014-4886(65)90126-3).
- Paxinos, G., 2004. *The Mouse Brain in Stereotaxic Coordinates*. Gulf Professional Publishing.
- Polikov, V.S., Tresco, P.A., Reichert, W.M., 2005. *J. Neurosci. Methods* 148, 1–18, <http://dx.doi.org/10.1016/j.jneumeth.2005.08.015>.
- Ranck Jr, J.B., Bement, S.L., 1965. *Exp. Neurol.* 11, 451–463.
- Saulnier, G.J., Blue, R.S., Newell, J.C., Isaacson, D., Edic, P.M., 2001. *IEEE Signal Process. Mag.* 18, 31–43, <http://dx.doi.org/10.1109/79.962276>.
- Sekino, M., Ueno, S., 2002. *J. Appl. Phys.* 91, 8730–8732, <http://dx.doi.org/10.1063/1.1454987>.
- Seoane, F., Ward, L.C., Lindecrantz, K., Lingwood, B.E., 2012. *Physiol. Meas.* 33, 1363, <http://dx.doi.org/10.1088/0967-3334/33/8/1363>.
- Surges, R., Elger, C.E., 2013. *Seizure J. Br. Epilepsy Assoc.* 22, 493–501, <http://dx.doi.org/10.1016/j.seizure.2013.04.020>.
- Trebbels, D., Fellhauer, F., Jugl, M., Haimerl, G., Min, M., Zengerle, R., 2012. *IEEE Trans. Biomed. Eng.* 59, 494–503, <http://dx.doi.org/10.1109/TBME.2011.2174990>.
- Wang, K., Zhu, S., Mueller, B.A., Lim, K.O., Liu, Z., He, B., 2008. *IEEE Trans. Biomed. Eng.* 55, 2481–2486, <http://dx.doi.org/10.1109/TBME.2008.923159>.

Note

Detection of Alzheimer's disease amyloid-beta plaque deposition by deep brain impedance profiling

Amélie Bédier^{1,3}, Pierre Joris^{1,3}, Sébastien Mosser²,
Patrick C Fraering² and Philippe Renaud¹

¹ Microsystems Laboratory, Ecole Polytechnique Fédérale de Lausanne (EPFL), CH-1015 Lausanne, Switzerland

² Laboratory of Molecular and Cellular Biology of Alzheimer's Disease, Brain Mind Institute and School of Life Sciences, Ecole Polytechnique Fédérale de Lausanne (EPFL), CH-1015 Lausanne, Switzerland

E-mail: amelie.beduer@epfl.ch

Received 14 October 2014, revised 12 December 2014

Accepted for publication 16 January 2015

Published 16 February 2015



CrossMark

Abstract

Objective. Alzheimer disease (AD) is the most common form of neurodegenerative disease in elderly people. Toxic brain amyloid-beta ($A\beta$) aggregates and ensuing cell death are believed to play a central role in the pathogenesis of the disease. In this study, we investigated if we could monitor the presence of these aggregates by performing *in situ* electrical impedance spectroscopy measurements in AD model mice brains. **Approach.** In this study, electrical impedance spectroscopy measurements were performed post-mortem in APPPS1 transgenic mice brains. This transgenic model is commonly used to study amyloidogenesis, a pathological hallmark of AD. We used flexible probes with embedded micrometric electrodes array to demonstrate the feasibility of detecting senile plaques composed of $A\beta$ peptides by localized impedance measurements. **Main results.** We particularly focused on deep brain structures, such as the hippocampus. **Ex vivo** experiments using brains from young and old APPPS1 mice lead us to show that impedance measurements clearly correlate with the percentage of $A\beta$ plaque load in the brain tissues. We could monitor the effects of aging in the AD APPPS1 mice model. **Significance.** We demonstrated that a localized electrical impedance measurement constitutes a valuable technique to monitor the presence of $A\beta$ -plaques, which is complementary with existing imaging techniques. This method does not require prior $A\beta$ staining, precluding the risk of variations in tissue uptake of dyes or tracers, and consequently ensuring reproducible data collection.

Keywords: impedance spectroscopy, neural probe, microelectrodes array, mouse brain, Alzheimer's disease, $A\beta$ plaques, APPPS1 model

(Some figures may appear in colour only in the online journal)

1. Introduction

Alzheimer's disease (AD) is one of the most widespread and cognitively devastating neurodegenerative diseases (Nestor

et al 2004). In this disease, cognitive deficiencies include early clinical hallmarks that consist of difficulties in learning and recent memory storage. AD is also characterized by a number of organic pathological features, in particular extracellular senile plaques composed of 4 kDa beta-amyloid peptides ($A\beta$). These amyloid plaques are believed to play a

³ These authors contributed equally to this work.

central role in the pathogenesis of the disease (Hardy and Higgins 1992), and their preferential localization in the cortex and hippocampus (Ball 1977, Ball *et al* 1985, Hyman *et al* 1990) correlates with the primary cognitive and memory disturbances (Killiany *et al* 2002). $A\beta$ aggregates into toxic plaques up to several years before first clinical symptoms appear, and their detection and monitoring is of primary interest, both for diagnostic purposes, and for fundamental research. The amyloid plaques are formed by the progressive deposition and transformation of soluble $A\beta$ monomers into insoluble and fibrillar aggregates that contain $A\beta$ in a beta-pleated plaque conformation. Soluble $A\beta$ monomers are present in the cortical extracellular space and in the cerebrospinal fluid and can be detected by chemical analysis of the fluid composition (Portelius *et al* 2006).

A number of techniques have been developed for detecting and monitoring the presence of insoluble $A\beta$ -aggregates *in vivo*, although a lack of sensitive, label-free techniques still exists, namely for the detection of senile plaques in deeper structures such as the hippocampus. Indeed, a number of relatively sensitive whole-brain or local imaging techniques exist, such as positron emission tomography (Mosconi *et al* 2010), single photon emission computed tomography or molecular optical imaging (Bloudek *et al* 2011), including multiphoton microscopy (Yan *et al* 2009), but these techniques require the use of contrast agents or dyes directed against specific molecular markers. The delivery of contrast agents in animal models of AD is typically carried out in an invasive fashion in the vicinity of the plaques, due to the need to avoid the blood-brain barrier. This, and direct molecular action of the contrast agents on the actual formation and stability of the plaques, raises concerns about the experimental results obtained with these techniques, outlining the need for label-free approaches. Magnetic resonance imaging (MRI) and computed tomography are such label-free whole brain imaging techniques. These techniques are currently limited by an insufficient spatial resolution for senile plaque detection, although in particular high-field MRI systems are approaching the necessary spatial resolution. Senile plaques in the cortex can be detected via optical coherence tomography (Bolmont *et al* 2012), but short of taking a biopsy, no such option is as yet available for the detection of plaques in deeper structures such as the hippocampus.

Here we present a novel protocol that enables the detection of amyloid plaques in the brain of an APPPS1 transgenic mouse model of AD in deep brain areas, typically inside the hippocampus. In this study, measures were performed post-mortem but the same tools and methods could be applied *in vivo* for research purposes. APPPS1 mice constitute a commonly used model for the study of AD characterized by $A\beta$ accumulation in the brain resulting in the formation of $A\beta$ plaques in the cortex and hippocampus, thus recapitulating important aspects of AD pathogenesis in human brains (Holcomb *et al* 1998). The density of plaques is directly related to the age of the mouse: the first plaques appear between the second and the third month, the plaque density then grows continuously at least until the eighteenth month of

the mouse life (Gordon *et al* 2002). In this work, we demonstrate the feasibility of detecting $A\beta$ plaque-pathology by impedance measurements in a first series of *ex vivo* experiments using brains from 18-month-old $A\beta$ depositing APPPS1 transgenic mice, as well as from control, age-matched non-transgenic mice and 1-month-old pre-depositing APPPS1 mice. We show that impedance measurement constitutes a valuable technique to monitor the presence of $A\beta$ plaques in the hippocampus and more particularly in the dentate gyrus.

2. Materials and methods

2.1. Probe design and microfabrication

The probe used in this work is presented in figures 1(b)–(c). Eight 50 μm diameter platinum electrodes were patterned and organized in a vertical array with inter-electrode distance of 400 μm . Both electrode size and inter-electrode distances were specifically chosen considering the requirements of tissue impedance spectroscopy, as detailed previously (Bédier *et al* 2014). Indeed, the volume probed when measuring impedance is determined by the electrode size. In general, larger measurement volumes sample more tissue and thus lead to better signal-to-noise ratio, but the measurement volume also needs to be small enough to distinguish structures of a size of hundreds of micrometres. With a micro-electrode diameter of 50 μm , the volume probed can be estimated to be a half sphere measuring a few times the microelectrode diameter (between 100 μm and 200 μm). The inter-electrode distance is chosen in such a way that the eight-electrode array cover a large range of depths within the mouse brain (2.8 mm).

The flexible multi electrode array was fabricated using standard microfabrication techniques, presented in detail elsewhere (Metz *et al* 2004, Cheung *et al* 2007). Briefly, an adhesion layer of a titanium tungsten alloy and a sacrificial layer of aluminium are sputter deposited on a silicon wafer. A 10 μm polyimide (PI2611, HD Microsystems) is then spin coated. A sandwich layer of Ti/Pt/Ti (50 nm/200 nm/50 nm) is sputter deposited and patterned through a photoresist layer in order to define the electrodes and electronic tracks. This layer is covered by a second 10 μm thick polyimide layer. A final etching step enables to open the electrode contacts and to define the device outlines. The devices are detached by anodic dissolution of the aluminium layer (Metz *et al* 2005). Connectors are glued using conductive silver paste (EPO-TEK H20E, Epoxy Technology, USA). A biocompatible epoxy is used for encapsulation of the connector-device junction. The total thickness of the flexible probe tip 20 μm , enabling good conformity with penetrated tissues.

2.2. Electrical impedance spectroscopy measurements

Impedance spectroscopy measurements were performed using an impedance analyser (Agilent 4294A, Agilent technologies, USA). A sinusoidal voltage of 50 mV was applied and the

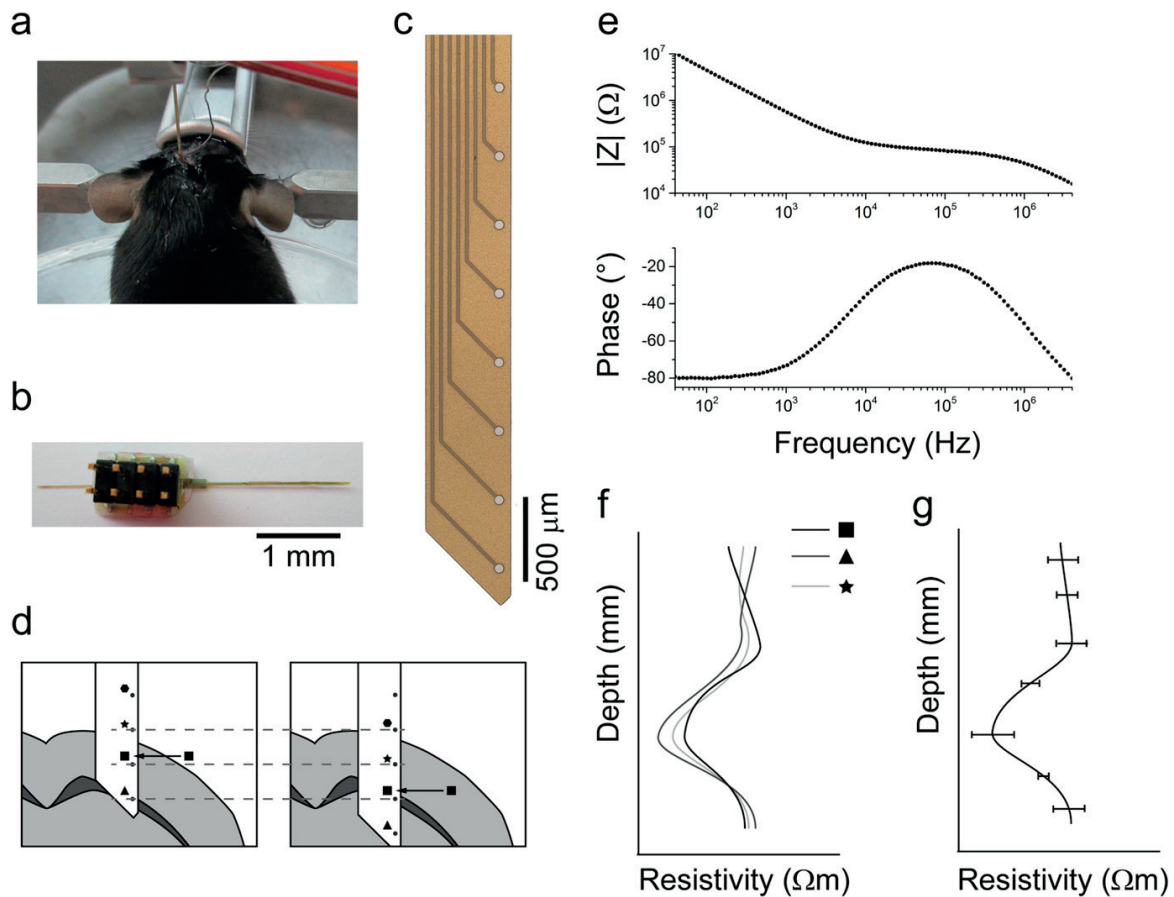


Figure 1. Impedance measurement device and configuration. (a) Photograph image of a *post mortem* stereotaxically implanted mouse. (b) Photograph image of the probe with glued connector and capillary facilitating probe manipulation. (c) Microscope image of the polyimide probe used for measurements consisting of an array of eight $50\ \mu\text{m}$ diameter platinum electrodes. (d) Schematic representation of the probe insertion into the brain tissues. Each geometrical shape (triangle, square, star and disc) represents one of the eight electrodes of the array. Electrodes are gradually inserted into the brain and impedance spectra are recorded at every $100\ \mu\text{m}$ step. (e) Typical impedance characteristics measured in the mouse brain (example of a wild-type mouse). (f) Schematic representation of resistivity profiles resulting from the recorded impedance spectra analysis. Each profile is obtained from one electrode of the array. (g) Schematic representation of the final mean profile and associated standard deviations.

frequency was swept between 40 Hz and 4 MHz. The obtained spectrum reflects the different capacitive and resistive elements of the measured electrical system: electrode-tissue interfacial double layer, resistivity of the tissue surrounding the electrode and parasitic capacitance between platinum tracks and tissue through the polyimide. The other elements of the system—the resistance of the platinum tracks, the bulk tissue resistance and the counter electrode double layer capacitance—have a negligible impact on the impedance spectrum in the measured frequency range. We used the peak resistance frequency (PRF) method in order to isolate the resistance of the tissue surrounding the electrode from the other elements (Kasi *et al* 2011): the tissue resistance is approximated by the value of the impedance modulus at the frequency at which the phase is closest to zero. The resistivity is then calculated by dividing the resistance by a constant factor (called cell constant), depending of the microelectrode

diameter (Newman 1966) and determined by measuring the impedance spectrum of the microelectrode placed in a saline solution of known resistivity.

The probe was mounted on a stereotaxic frame and inserted vertically into the mouse brain at determined stereotaxic coordinates, as illustrated on figure 1(a). Figure 1(d) presents the method used for resistivity recordings. Brain resistivity profiles were obtained by inserting the probe within the brain and by lowering it by steps of $100\ \mu\text{m}$. At each step, the impedance spectrum was recorded and the surrounding tissue resistivity was extracted for each electrode by PRF. Thanks to the array configuration, the resistance at a given point was recorded several times (by each electrode passing it). This method allowed to obtain a resistivity profile for each electrode, as presented in figure 1(e). By considering the profiles obtained for the different electrodes together, we

obtained a resistivity profile with standard deviation for each point probed, as presented in figure 1(f).

2.3. Mice

Male and female wild-type (WT) and APPPS1 transgenic mice (kindly provided by Professor M Jucker, HIH, Tübingen, Germany) were used. APPPS1 animals co-express the KM670/671NL Swedish mutation of human amyloid precursor protein and the L166P mutation of human presenilin 1 under the control of the Thy-1 promoter and show age-dependent accumulation of parenchymal A β plaques (Radde *et al* 2006). Both WT and APPPS1 mice were generated on a C57BL/6J background. All animal experiments were conducted in accordance with local and federal directives for the care and use of laboratory animals. Experiments were performed on both male and female mice aged of 18-months (old mice) or 1-month (young mice).

2.4. Surgery and setup

All mice were euthanized by carbon dioxide inhalation, then placed on a stereotaxic frame. Measurements were carried within two hours of the death of the animal. Holes were drilled in the skull using a dummy cannula (25 G) and bilateral measurements were performed at the following stereotaxic coordinates: -2.1, 1.5 (in mm, anterior, lateral to bregma). The counter electrode consisting in a platinum wire was placed inside the brain approximately 3 mm anterior to bregma. Care was taken to avoid drying of the cortical surface and the skull was covered with phosphate buffered saline (Sigma Aldrich, Saint Louis, MO). The probe was placed in the taxic clamp of the stereotaxic frame and gradually inserted vertically into the skull and brain.

2.5. Histology and staining

Immediately after impedance profiling, mice brains were removed and fixed overnight using 4% paraformaldehyde (PFA) in PBS, pH 7.4, followed by 48 h incubation in 30% sucrose. Brains were frozen in optimal cutting temperature compound and subsequently sectioned on a freezing-sliding microtome to collect 30 μ m coronal sections. Sections corresponding to spatial coordinates used for impedance measurements were selected and stained. To visualize A β deposits sections were immunostained using the A β monoclonal antibody 6E10 and DAB for revelation. After washing the cryoprotectant with PBS, sections were incubated for 10 min in 3% H₂O₂ in PBS to inhibit endogenous peroxidase. No further pretreatment was required. Sections were blocked in 1% BSA in PBS for 20 min. Mouse α -amyloid (clone 6E10, Covance) diluted 1:750 in 1% BSA was incubated overnight at 4 °C under agitation. After PBS washes, the secondary antibody mouse Immpress (ready to use, Vector Laboratories) was applied for 30 min at room temperature. Revelation was performed with DAB (3,3'-Diaminobenzidine, Sigma-Aldrich). Sections were mounted on slides and counterstained with Mayer's hematoxylin. Brain sections were also stained

with Cresyl violet and hematoxylin-eosin according to standard protocols.

2.6. Imaging and quantitative analysis

Large area images were obtained using a Leica DM5500 microscope in bright field with an 20 \times objective and a motorized stage. In order to quantify the load of A β plaques in the probed brain areas, and the probed area was graphically selected and binarized using image analysis software (ImageJ). Since the DAB stained plaques appear dark brown in the original image, they give rise to black pixels after binarization, while the rest of the image remains white. The percentage of black pixels per surface unit was reported for each depth. Likewise, local cell density was quantified by counting stained cell nuclei per surface unit. We used identical squares of 100 μ m side length for the quantification of both the plaques and the cell density, and evaluated five such squares for each experimental condition (APPPS1 versus WT, young versus old mice, at each measurement depth).

2.7. Statistics

Statistical analysis was based on at least five series of experiments. Standard deviations are indicated on the graphs. By using a paired *t*-test, data were considered to be statistically significant when the two-tailed *p*-values were $p < 0.001$ (***), $p < 0.01$ (**) or $p < 0.05$ (*). No multiple testing corrections were performed.

3. Results and discussion

For performing impedance spectroscopy measurements, a flexible probe equipped with a microelectrode array comprising eight 50 μ m diameter disc electrodes vertically separated by a distance of 400 μ m was fabricated and implanted *post mortem* into the mice brains (figure 1(a)). Figure 1(b) presents a photograph of the complete probe before implantation. On figure 1(c), a microscope image of the probe tip is presented. The eight microelectrodes are visible on the right side. The probe was inserted gradually inside the brain and impedance measurements were performed at steps of 100 μ m with each electrode of the array against a distant reference electrode. Each point of interest along the profile is therefore measured by each electrode passing it, as schematized in figure 1(d). We therefore obtain 8 resistivity values measured at the same brain coordinate allowing us to extract the mean resistivity profiles along with the standard deviation as schematized in figures 1(f)–(g). To extract the tissue resistivity from the impedance measurements, we used the PRF method (Mercanzini *et al* 2007, Bédurier *et al* 2014). Figure 1(e) shows typical spectroscopic data from which we extract the value for obtaining resistivity values.

In order to check the correct insertion of the probe inside the tissues, we first compared the resistivity measured by the different electrodes of the array for a given coordinate and depth. Comparable values were obtained for a given region

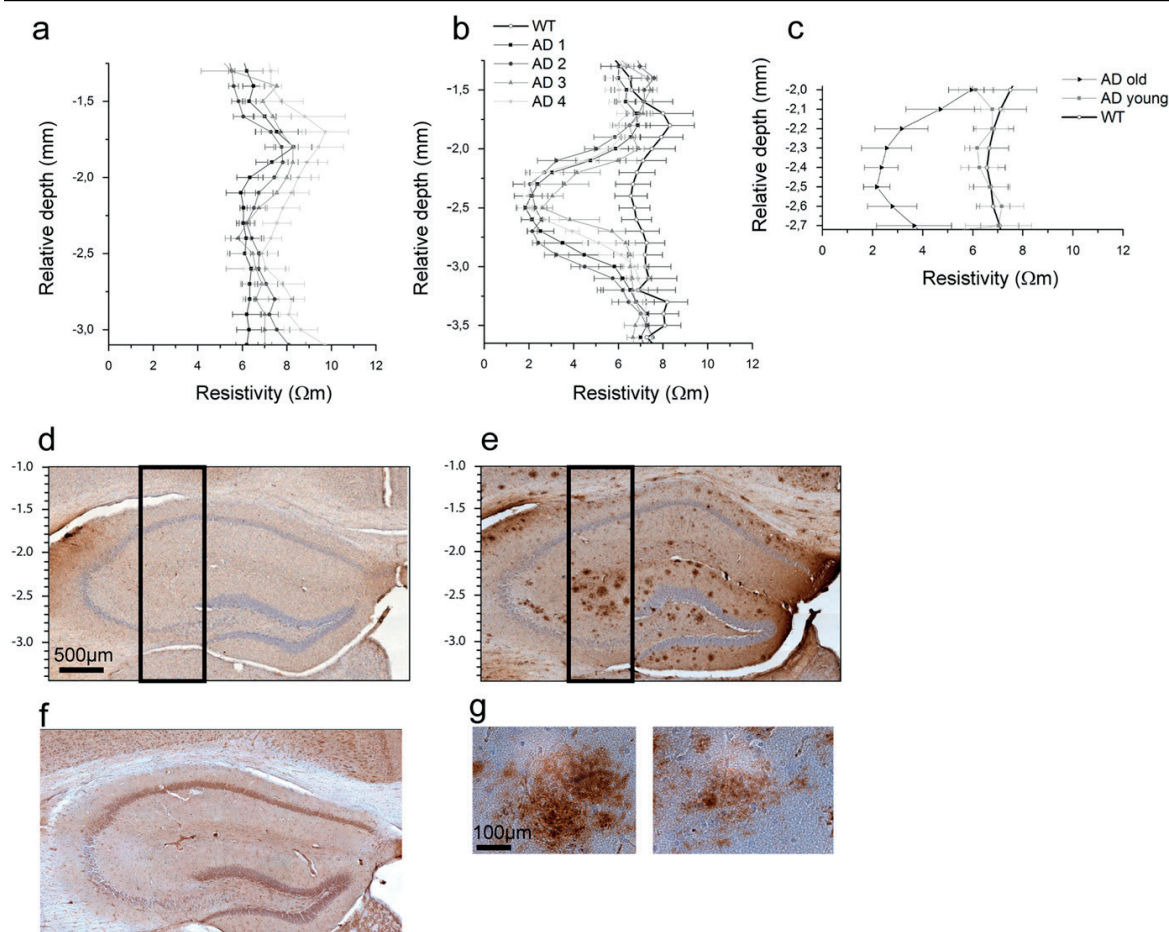


Figure 2. (a)–(c) Resistivity profiles obtained in the hippocampus of mice (2.1 mm anterior to Bregma; 1.5 mm medio-lateral in mm). (a) Resistivity profiles obtained for 18-months-old WT mice. (b) Resistivity profiles obtained for 18-months-old AD mice compared to the mean profile obtained for the WT mice. (c) Control profile obtained for a 1-month-old AD mouse in comparison to 18-months-old AD mice and 18-months-old WT mice. (d)–(f) Microscope image of histological sections of mice brains in the measurement region. Cell nuclei appear in blue and A β plaques are revealed with DAB, in brown. Black rectangles indicate the measurement area. (d) Brain of an 18-months-old WT mouse. (e) Brain of a 18-months-old APPPS1 mouse. (f) Brain of a 1-month-old APPPS1 mouse. (g) Zoomed area on A β plaques observed in the hippocampus of an 18-months-old APPPS1 mouse.

for successive measurements performed with successive microelectrodes showing that the resistivity measurement is essentially electrode-independent and demonstrating that the penetration of the developed neural probe inside the brain tissues creates minimal tissue damage.

Figures 2(a)–(c) presents the resistivity profiles obtained in the hippocampus area for post-mortem WT mice and for APPPS1 mice. For each mouse, measurements were performed in both brain hemispheres. Figure 2(a) shows the results obtained for two 18-months-old WT mice. We observe that all the resistivity profiles are similar. For each profile, we note nearly constant resistivity values except in one area corresponding to depths comprised between -1.7 mm and -1.9 mm where resistivity values increase. In order to correlate these observations with anatomical features, brain histology and consecutive Haematoxylin-Eosin as well as Cresyl

violet and anti-A β plaques stainings were performed in the measurement area. Results are shown in figure 2(d). We observed that the tissue resistivity increase corresponds to fibre tracts located below the cortex. This result is in accordance with impedance measurements performed previously at other stereotaxic coordinates (anterior to Bregma; medio-lateral in mm: $-0.7;1$ and $-0.7;1.5$) (Bédier *et al* 2014). Figure 2(b) presents the resistivity profiles obtained for APPPS1 transgenic mice and gives a comparison with the mean profile obtained for WT mice. All profiles were acquired at the same stereotaxic coordinates. We first observe that all resistivity profiles measured in AD mice brains exhibit the same shape, namely stable resistivity values around $7 \Omega\text{m}$ for depth smaller than -1.75 mm followed by a distinct resistivity decrease for depths comprised between -1.75 mm and -3.00 mm (minimal resistivity values are about

1.75 Ωm). In the last 500 micrometres (from -3.00 mm to -3.5 mm), we observe a resistivity increase, back to values $7\ \Omega\text{m}$. As we can see from the mean profile obtained for WT mice brains, the distinct resistivity decrease observed in AD mice hippocampus was not observed in the WT mice brains, where resistivity values consistently remained high, namely between $6.8\ \Omega\text{m}$ and $7.8\ \Omega\text{m}$, along the whole measurement depth. We thus observed a significant difference between resistivity profiles from 18-month-old, $A\beta$ depositing APPPS1 transgenic mice and from age-matched non-transgenic mice. In order to check that the differences of resistivity values observed are not linked to non-specific structural alterations induced by the APPPS1 genetic modification, we measured resistivity profiles in young, predepositing APPPS1 mice. Figure 2(c) gives a comparison between profiles obtained from old and young AD mice and from old WT mice. There was no resistivity drop for the young APPPS1 mice, and also no significant difference between resistivity profiles of old WT mice and young APPPS1 mice. This indicates that prior to the onset of the deposition of the plaques, there is no structural difference between the APPPS1 and WT brains detectable via impedance profiling. Thus, we can conclude that the observed resistivity shift is specific to aged APPPS1 mice.

In order to correlate the alteration of the resistivity profile to pathological features in the APPPS1 mice, we obtained histological sections of the measured brain areas and stained for $A\beta$ plaques, known to be the hallmark of aged APPPS1 mice. Figures 2(d) and (e) show microscope images of the measured area in both WT (d) and AD (e) mice brains. As expected from the genetic modification present in APPPS1 mice, histopathological assessment shows an accumulation of $A\beta$ plaques in the APPPS1 mice; also as expected, young APPPS1 mice show no detectable $A\beta$ aggregates (figure 2(f)).

We further observe that the density of plaques is particularly high in the middle layer of the hippocampus (lacunosum moleculare). This layer corresponds to the observed resistivity decrease, suggesting that the drop in resistivity is correlated with the presence of $A\beta$ plaques. To further check this assertion, we quantified from the histological sections the local $A\beta$ plaque load, that we compared to measured local resistivity values for the three APPPS1 mice as well as the age-matched WT controls examined in this study.

Figure 3 shows the results of this quantification. Figures 3(a) and (c) illustrate the typical visual aspect of the areas where the $A\beta$ plaque load quantifications was performed, for WT and AD mice respectively. Figures 3(b), (d)–(f) depict the quantification results, for a WT mouse brain and for three different APPPS1 brains, respectively. The plaque load profile on figure 3(b), obtained on a WT mouse brain, serves as a negative control for the $A\beta$ plaque load quantification protocol, and indicates that in the absence of clearly visible plaques, only a small background plaque load signal is observed. On the plaque load profiles obtained for all three AD brains, the area of high plaque density in the hippocampus is clearly identifiable. Also, by comparison with the corresponding resistivity values, an inverted correlation between $A\beta$ plaque load and resistivity values can be detected

for all three AD brains. Indeed, relative depths corresponding to low impedance values consistently exhibited high $A\beta$ plaque load. These results confirmed that resistivity profiles are linked to the presence of $A\beta$ plaques, and further demonstrate that this dependency is quantitative. In the cortex located just above the fibre tract, we can see some $A\beta$ plaques, albeit at a much lower density than in the hippocampus. However, their presence does not appear to be correlated to particularly low resistivity values. This observation raises the question of the sensitivity of the resistivity measurement. It appears that a minimal density of $A\beta$ plaques is needed to be detected through resistivity measurement. We estimate the $A\beta$ plaques detection threshold to correspond to a score of about 17% positive pixels, as it can be observed in the profiles presented in figure 3(d). This threshold depends on the tissue volume probed with the microelectrodes, depending itself on the microelectrode diameter. In order to reduce this threshold and to be able to detect small $A\beta$ plaques, it should be possible to reduce the probed tissue volume by reducing the microelectrode diameter.

We recently demonstrated that resistivity in the mouse brain cortex is linearly correlated with cell density (Bédier *et al* 2014). To further explain the resistivity drop observed in AD mice hippocampus, we therefore quantified cell density in this particular area. We detected a decrease of 12% in the total number of cells in this area for the AD mice relative to WT mice. This is consistent with the known phenotype of APPPS1 mice (Radde *et al* 2006), in which minor neuronal loss has been demonstrated in close proximity to the plaques. We also assessed the influence of the plaques on the local cell density by quantifying both the cell density and the plaque loads in squares of $100\ \mu\text{m}$ side length, in histological sections of the hippocampal area of both AD and WT mice.

Figures 4(a) and (b) present the distribution of squares in function of the number of cells they comprise for both WT and AD mice. For WT mice, scores of squares comprising 0–5 cells, 5–10 cells and 10–15 cells are in the same range, showing a certain degree of homogeneity in the cell distribution. This is not the case in AD brains, where most of the squares either show a very low (0–5) or a large number of cells (more than 10), while very few squares comprise an intermediate number (5–10), indicating a strong heterogeneity in the cell density. We also quantified the percentage of $A\beta$ plaque load in the same picture squares. The results are shown in the graph of figure 4(c). We clearly see that when the number of cells is low, $A\beta$ plaque load is high: for squares comprising 0–5 cells, the mean $A\beta$ plaque load is $62 \pm 7\%$. Conversely, when the cell number is high, $A\beta$ plaque load is reduced, even null. Indeed, when cell density was comprised between 20 cells/square and 25 cells/square, $A\beta$ plaque load raises by only $2 \pm 1\%$. Taking into account the results presented in figures 4(a)–(c), we deduce that the presence of $A\beta$ plaques results in a reduction of the cell density in the vicinity of the plaques coupled with a general heterogeneity of the cell density. These results confirm the hypothesis that $A\beta$ plaques tend to push the cells away, creating alternating regions of low and high cell densities according to their presence or absence (Spires-Jones and Hyman 2014).

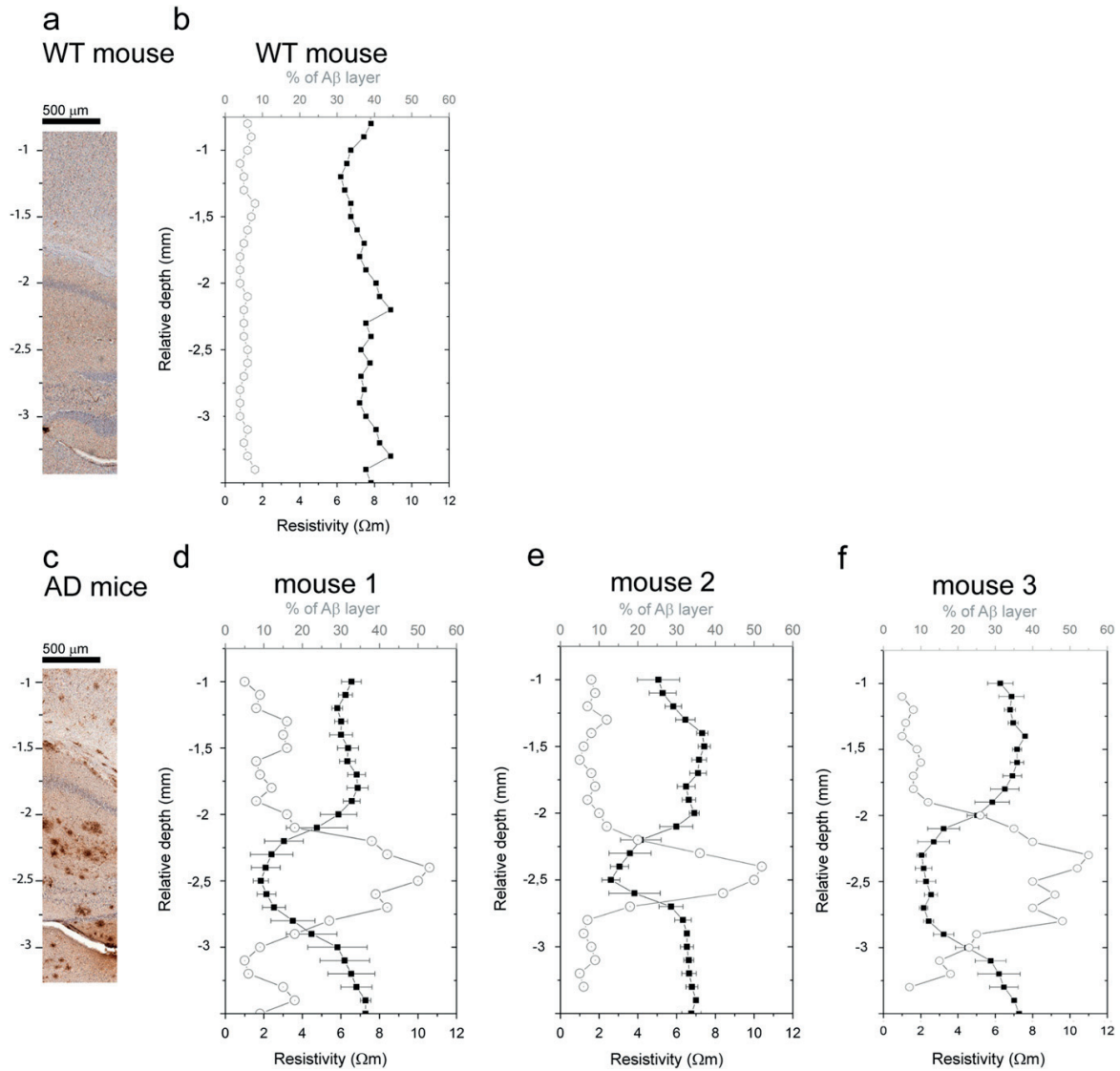


Figure 3. (a), (c) Microscope image examples of measurement areas analysed to get the percentage of Aβ-plaques. (b), (d)–(f) Corresponding resistivity profiles plotted with percentage of area occupied by Aβ-plaques. (a), (b) 18-months-old WT mice. (c)–(f) 18-months-old AD mice.

Figure 4(d) is a schematic representation that sums up the observed phenomena and gives an interpretation to explain the resistivity drop in the hippocampus of aged AD mice. The previously described results are taken into account, namely: (i) the hippocampal region where the resistivity drop was observed contains a high density of Aβ plaques, (ii) tissue resistivity is correlated with the cell density, (iii) AD hippocampus shows a reduced number of cells around plaques and an increased heterogeneity in the cell distribution and (iv) areas with high Aβ plaques load exhibit very low cell density. These results converge to unravel that tissue loaded with Aβ plaques *in vivo* (post mortem, inside brain tissues) exhibit a lower resistivity than healthy tissue. Indeed, areas occupied by the Aβ plaques have a low cell density and as a

consequence a low resistivity. Amit *et al* (2012) investigated Aβ peptide conductivity and showed that Aβ peptide sequence and assembly conditions can lead to different conductivities. This underlines that synthetic Aβ aggregates cannot be directly compared with *in vivo* plaques. Moreover, in the *in vivo* configuration, the plaques are embedded in the extracellular matrix and in a diffusive medium which, beside the proteins, also contains a large amount of cerebrospinal fluid exhibiting a lower resistivity than tissue regions populated by cells (Bédier *et al* 2014). As a consequence, the plaques and the surrounding tissue regions where cells are missing have a lower resistivity than the healthy tissue. These regions of low resistivity are distributed over the hippocampus and form a ‘percolating system’, as schematized by

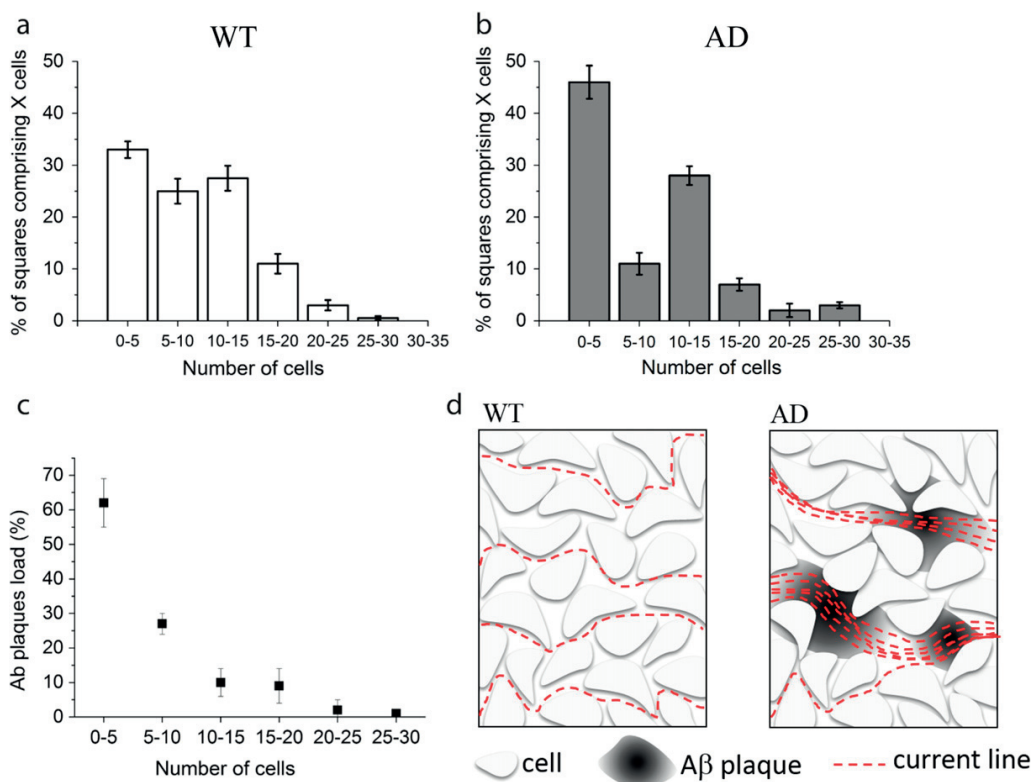


Figure 4. Analysis of cells and $A\beta$ plaque-distribution in the hippocampus of aged WT and AD mice. For each condition, quantitative data result from the analysis of three independent areas. Pictures of the hippocampus area were divided into squares of $100 \times 100 \mu\text{m}$ in which the number of cells was counted. (a) Distribution of cells in the hippocampus of aged WT mice. (b) Distribution of cells in the hippocampus of aged AD mice. (c) $A\beta$ plaque load related to the number of cells. (d) Schematic representation of the passive electrical behaviour of the hippocampus of WT (left) and AD (right) mice.

the current lines of figure 4(d), such as shown by Seoane *et al* (2005). This ‘percolating network’ results in a low resistivity for the complete tissue region affected by $A\beta$ plaques. In contrast, in the case of wild-type and young APPPS1 transgenic mice, the cell density is homogeneous over the whole tissue due to the absence of $A\beta$ plaques. This results in the absence of a percolating system of low resistivity regions. As a consequence, the measured resistivity values are significantly higher in both WT mice as well as young APPPS1 transgenic mice.

4. Conclusion

Altogether, the data presented in this study demonstrate that *in situ* resistivity measurement with implanted microelectrode array is a good method to detect the presence of cerebral $A\beta$ load *ex vivo* and monitor the effects of aging in the AD APPPS1 mice model. This method does not require prior $A\beta$ staining, precluding the risk of variations in tissue uptake of dyes or tracers, and consequently ensuring reproducible data collection. Furthermore, the flexible minimally invasive probe allows to measure $A\beta$ load in deep brain structures such as the

hippocampus that is not possible using other label free techniques. To the best of our knowledge, such measurements have never been reported elsewhere. We anticipate that the use of this technique will help to improve the diagnosis and monitoring of $A\beta$ loads *in vivo* after having first evaluated the long-term integration of the probe inside the brain tissues. This technique will further enable the continuously monitoring of $A\beta$ plaque progression avoiding thus the use of extensive numbers of animals for time point studies and also giving new information about unravelled dynamic phenomena in the disease progression. As such, it can be used to evaluate the efficiency of $A\beta$ -targeting therapeutic strategies.

Acknowledgments

Stoicescu Foundation and Brazilian Swiss Joint Research Programme No. BJRJP 0112-09 are gratefully acknowledged for their partial financial contribution to this work. We would like to thank Dr Thomas Braschler for his helpful discussions and the EPFL histology, bioimaging and optics core facilities for their excellent technical assistance.

References

- Amit M, Cheng G, Hamley I W and Ashkenasy N 2012 Conductance of amyloid beta based peptide filaments: structure-function relations *Soft Matter* **8** 8690–6
- Ball M J 1977 Neuronal loss, neurofibrillary tangles and granulovacuolar degeneration in the hippocampus with ageing and dementia. a quantitative study *Acta Neuropathol. (Berl.)* **37** 111–8
- Ball M J, Fisman M, Hachinski V, Blume W, Fox A, Kral V A, Kirshen A J, Fox H and Merskey H 1985 A new definition of Alzheimer's disease: a hippocampal dementia *Lancet* **1** 14–6
- Bloudek L M, Spackman D E, Blankenburg M and Sullivan S D 2011 Review and meta-analysis of biomarkers and diagnostic imaging in Alzheimer's disease *J. Alzheimers Dis.* **26** 627–45
- Bolmont T, Bouwens A, Pache C, Dimitrov M, Berclaz C, Villiger M, Wegenast-Braun B M, Lasser T and Fraering P C 2012 Label-free imaging of cerebral β -amyloidosis with extended-focus optical coherence microscopy *J. Neurosci.* **32** 14548–56
- Bédier A, Joris P, Mosser S, Delattre V, Fraering P C and Renaud P 2014 Accurate resistivity mouse brain mapping using microelectrode arrays *Biosens. Bioelectron.* **60** 143–53
- Cheung K C, Renaud P, Tanila H and Djupsund K 2007 Flexible polyimide microelectrode array for *in vivo* recordings and current source density analysis *Biosens. Bioelectron.* **22** 1783–90
- Gordon M N, Holcomb L A, Jantzen P T, DiCarlo G, Wilcock D, Boyett K W, Connor K, Melachrinou J, O'Callaghan J P and Morgan D 2002 Time course of the development of alzheimer-like pathology in the doubly transgenic PS1+APP mouse *Exp. Neurol.* **173** 183–95
- Hardy J A and Higgins G A 1992 Alzheimer's disease: the amyloid cascade hypothesis *Science* **256** 184–5
- Holcomb L, Gordon M N, McGowan E, Yu X, Benkovic S, Jantzen P, Wright K, Saad I, Mueller R, Morgan D *et al* 1998 Accelerated alzheimer-type phenotype in transgenic mice carrying both mutant amyloid precursor protein and presenilin 1 transgenes *Nat. Med.* **4** 97–100
- Hyman B T, Van Hoesen G W and Damasio A R 1990 Memory-related neural systems in Alzheimer's disease: an anatomic study *Neurology* **40** 1721–30
- Kasi H, Meissner R, Babalian A, Lintel H van, Bertsch A and Renaud P 2011 Direct localised measurement of electrical resistivity profile in rat and embryonic chick retinas using a microprobe *J. Electr. Bioimpedance* **1** 84–92
- Killiany R J, Hyman B T, Gomez-Isla T, Moss M B, Kikinis R, Jolesz F, Tanzi R, Jones K and Albert M S 2002 MRI measures of entorhinal cortex versus hippocampus in preclinical AD *Neurology* **58** 1188–96
- Mercanzini A, Reddy S, Velluto D, Colin P, Maillard A, Bensadoun J-C, Bertsch A, Hubbell J A and Renaud P 2007 Controlled release drug coatings on flexible neural probes *29th Annual Int. Conf. of the IEEE Engineering in Medicine and Biology Society (Lyon, France)* pp 6612–5
- Metz S, Bertsch A, Bertrand D and Renaud P 2004 Flexible polyimide probes with microelectrodes and embedded microfluidic channels for simultaneous drug delivery and multi-channel monitoring of bioelectric activity *Biosens. Bioelectron.* **19** 1309–18
- Metz S, Bertsch A and Renaud P 2005 Partial release and detachment of microfabricated metal and polymer structures by anodic metal dissolution *J. Microelectromech. Syst.* **14** 383–91
- Mosconi L, Berti V, Glodzik L, Pupi A, De Santi S and de Leon M J 2010 Pre-clinical detection of Alzheimer's disease using FDG-PET, with or without amyloid imaging *J. Alzheimers Dis.* **20** 843–54
- Nestor P J, Scheltens P and Hodges J R 2004 Advances in the early detection of Alzheimer's disease *Nat. Med.* **10** S34–41
- Newman J 1966 Resistance for flow of current to a disk *J. Electrochem. Soc.* **113** 501–2
- Portelius E, Westman-Brinkmalm A, Zetterberg H and Blennow K 2006 Determination of β -amyloid peptide signatures in cerebrospinal fluid using immunoprecipitation-mass spectrometry *J. Proteome Res.* **5** 1010–6
- Radde R, Bolmont T, Kaeser S A, Coomaraswamy J, Lindau D, Stoltze L, Calhoun M E, Jäggi F, Wolburg H, Gengler S *et al* 2006 Abeta42-driven cerebral amyloidosis in transgenic mice reveals early and robust pathology *EMBO Rep.* **7** 940–6
- Seoane F, Lindercrantz K, Olsson T, Kjellmer I, Flisberf A and Bagenholm R 2005 Spectroscopy study of the dynamics of the transecephalic electrical impedance in the perinatal brain during hypoxia *Physiol. Meas.* **26** 849–63
- Spires-Jones T L and Hyman B T 2014 The intersection of amyloid beta and tau at synapses in Alzheimer's disease *Neuron* **82** 756–71
- Yan P, Bero A W, Cirrito J R, Xiao Q, Hu X, Wang Y, Gonzales E, Holtzman D M and Lee J-M 2009 Characterizing the appearance and growth of amyloid plaques in APP/PS1 mice *J. Neurosci.* **29** 10706–14

A Compressible Scaffold for Minimally Invasive Delivery of Large Intact Neuronal Networks

Amélie Bédurier,* Thomas Braschler, Oliver Peric, Georg E. Fantner, Sébastien Mosser, Patrick C. Fraering, Sidi Benchérif, David J. Mooney, and Philippe Renaud

Millimeter to centimeter-sized injectable neural scaffolds based on macroporous cryogels are presented. The polymer-scaffolds are made from alginate and carboxymethyl-cellulose by a novel simple one-pot cryosynthesis. They allow surgical sterility by means of autoclaving, and present native laminin as an attachment motive for neural adhesion and neurite development. They are designed to protect an extended, living neuronal network during compression to a small fraction of the original volume in order to enable minimally invasive delivery. The scaffolds behave as a mechanical meta-material: they are soft at the macroscopic scale, enabling injection through narrow-bore tubing and potentially good cellular scaffold integration in soft target tissues such as the brain. At the same time, the scaffold material has a high local Young modulus, allowing protection of the neuronal network during injection. Based on macroscopic and nanomechanical characterization, the generic geometrical and mechanical design rules are presented, enabling macroporous cellular scaffold injectability.

1. Introduction

It is a clinical observation that the adult human brain typically fails to repair large-scale tissue damage.^[1] This contrasts with the observation that neurons are continuously generated in the subventricular zone and dentate gyrus,^[2,3] and it is indeed the hope and aim of cell-based therapies to extend the brain's regeneration capacity to large-scale lesions. A major limitation on the path to successful neural tissue engineering and deep brain transplantation is the development of minimally invasive surgical techniques and scaffolds. Indeed, the surgical

procedures involved in implanting complex and large solid grafts into the brain are very invasive and can easily lead to further tissue damage rather than the desired reconstruction outcome.^[4] A number of minimally invasive delivery methods have been proposed, allowing to apply in situ gelling formulations, micro-particulate scaffold suspensions, partially dissociated tissue, or neural stem cell suspensions through narrow-bore needles.^[5–15] Unfortunately, without the guidance of a large-scale organized scaffold, the cells typically build chaotic structures rather than repairing the native tissue architecture as desired.^[14] As a result, the associated functional recovery is never complete and data from successful human clinical studies are extremely scarce.^[15] We propose here to address this current major bottleneck of neural tissue engineering by the use of a smart cellular scaffold system, which is highly and reversibly compressible, allowing for minimally invasive implantation of large, potentially preorganized constructs. To achieve this goal, several requirements must be met: The scaffold material must be highly compressible, such that mL-scale volumes can be delivered through narrow-bore tubing or needles, yet it should recover its original shape, volume and organization after the injection process. It should protect differentiated neurons with their extended neurites during the compression associated with the delivery process, but nevertheless behave as a globally soft material to minimize glial scarring reactions in the brain.^[16] For the long-term culture necessary to develop differentiated neuronal networks, and in light of potential clinical translation, the scaffolds need to be reliably sterilized, preferentially by autoclaving. Last but not least, it is desirable to be able to provide native extracellular matrix (ECM) proteins to guide cell adhesion and differentiation. Macroporous scaffolds with shape memory amenable to injection through narrow-bore tubing can be fabricated by different techniques, such as emulsion polymerization, lyophilization, and cryogelation.^[17–19] We base our scaffolds on the process of cryogelation, involving polymerization of a hydrogel precursor at subzero temperature, since this has been observed to produce particularly robust gels, and since the possibility of neuronal tissue engineering with cryogels has been reported.^[19–21] We provide a novel cryogel fabrication paradigm, consisting of a

Dr. A. Bédurier, Dr. T. Braschler, Prof. P. Renaud
STI-IMT-LMIS4, Station 17, EPFL
1015, Lausanne, Switzerland
E-mail: amelie.beduer@epfl.ch

Dr. T. Braschler, Dr. S. Benchérif, Prof. D. J. Mooney
School of Engineering and Applied Sciences
Harvard University,
02138, Cambridge, MA, USA

O. Peric, Prof. G. E. Fantner
STI-IBI-LBNI, Station 17, EPFL
1015, Lausanne, Switzerland

S. Mosser, Prof. P. C. Fraering
SV-BMI-CMSN, Station 15, EPFL
1015, Lausanne, Switzerland

DOI: 10.1002/adhm.201400250



simple one-pot carbodiimide-based cryosynthesis, and a coating method for native cell-adhesive proteins applicable after autoclave sterilization of the scaffolds. The newly developed protocol is the first to simultaneously address the requirement for autoclave sterilization, native ECM protein presentation, and scaffold injectability; at the same time, it avoids tedious precursor synthesis. It provides mL-scale scaffolds that can be injected through 1 mm needles while indeed protecting a live-extended neural network at cell densities approaching the one of native cortical gray matter. We also investigate the precise mechanical and geometrical properties providing for injectability and cell protection, by means of a novel atomic force microscopy (AFM) sample preparation technique and mechanical testing of the scaffolds. The shape-memory properties, finally, will allow adapting exactly the scaffold shape and volume, as well as cell density and neural growth to the tissue to be reconstructed, before in vivo injection. The system is therefore an ideal candidate for personalized tissue engineering.

2. Results

To prepare macroporous scaffolds suitable for 3D cell culture, we used a cryogelation process, which consists in hydrogel polymerization at subzero temperatures, using ice crystal

formation to define the pore space. Hydrogels presented in this work consisted in sodium alginate and carboxymethyl-cellulose (CMC), selected for their known biocompatibility and potentially favorable effects on neurons in culture.^[22–25] We initiate the polymerization via carbodiimide activation of the carboxylic acid residues on the carbohydrate moieties of the gel prepolymers, followed by amide bond formation with adipic dihydrazide, which results in the covalent crosslinking of the gels (details about the process are available in Supporting Information 1). Carrying out this process at subzero temperature allows creating macroporous hydrogels, referred to as cryogels, characterized by large interconnected pores, as schematized in Figure 1A. These scaffolds are sterilized by autoclave, coated with appropriate cell-adhesive molecules (poly-L-ornithine, PLO, and laminin), and finally seeded with neuronal cells. The cell-laden cryogels can be partially dehydrated, reducing the scaffold size, and allowing for injection of the cellular scaffold through a syringe needle, as shown in Figure 1A. After injection, cellular scaffolds retrieve their initial size and shape, by uptake of liquid injected along with the cryogel. Cell integrity and morphology are preserved throughout the injection process. Figure 1B presents scanning electron microscope (SEM) images showing the microscopic architecture of the cryogel scaffolds, made either from alginate or CMC. The cryogelation process resulted in highly porous structures for both polymers. The pore

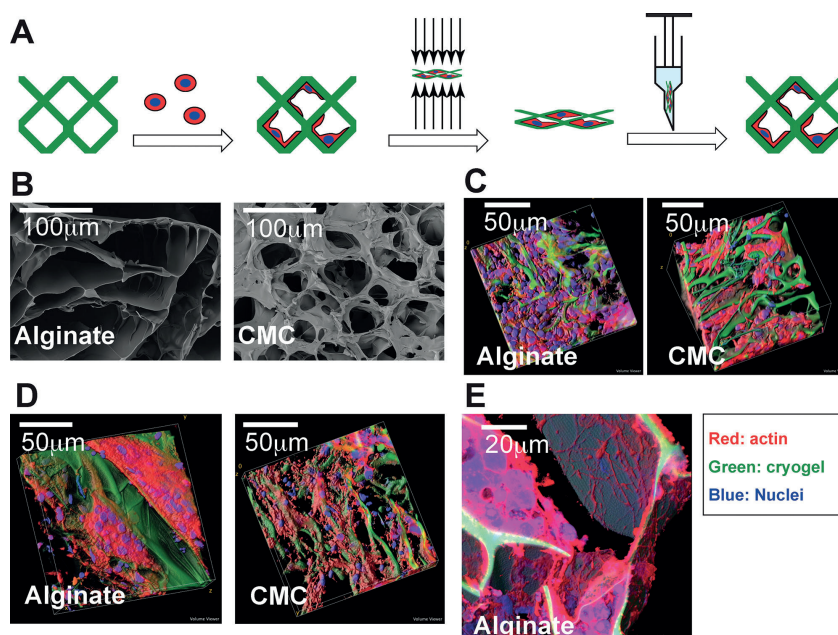


Figure 1. Structure, neuronal cell adhesion, and injection principle for macroporous alginate and carboxymethyl-cellulose (CMC) cryogels. A) Scaffold-protected injection of adherent cells: The cells are seeded on a macroporous cryogel scaffold coated with suitable adhesion motifs (poly-L-ornithine and laminin), and allowed to adhere and spread. The scaffold is then partially dehydrated, losing up to 90% of its volume without cell damage, and can be passed through an injection device such as a syringe before swelling back to its original volume. Cell integrity is protected throughout the process due to the particular mechanical and structural properties of the cryogels. B) Structure of alginate (3%) and CMC (1%) cryogels by scanning electron microscopy. C,D) Confocal micrographs of the human neuronal cell line SHSY-5Y (Figure 1C) and primary mouse cortical neurons (Figure 1D) on alginate and CMC cryogels. E) Closer view of a mouse primary neuron culture on a cryogel, showing the extensive neurite network visible on areas not covered by the cell bodies. For Figure 1C–E, the nuclei are blue (DAPI), the gel is labeled green (aminofluorescein, incorporated covalently), and the actin cytoskeleton is labeled red (rhodamine-phalloidin); all gels were coated with PLO/laminin.

dimensions are comprised between 20 and 500 μm and depend on the exact cryogelation process parameters (details about pore volumes are given below). Cryogel formation using alginate as a starting material allowed obtaining 3D scaffolds with relatively thin walls (ca. 1–5 μm). They were somewhat thicker in the case of CMC-scaffolds (Figure 1B). After coating with PLO and laminin, the 3D scaffolds were seeded with neuronal cells (human neuroblastoma neuronal cell line SH-SY5Y or primary cortical mouse neurons). Seeding was carried out by first partially dehydrating cryogels (by pressing them against a sterile gauze) and rehydrating them with the cellular suspension. At the initial time of 3D plating, the dissociated neural cells had a spherical morphology, without visible neurites. Over time in culture, there was considerable process outgrowth resulting in the formation of 3D, interconnected neural networks. After 7 d of culture, cellular scaffolds were fixed and observed by confocal microscopy. Figure 1C,D present 3D confocal images of the resulting cellular scaffolds for the human neural cell line SH-SY5Y (1C) and primary cortical mouse neurons (1D). The analysis demonstrates a complex and dense cellular 3D architecture for both the human cell line and the mouse primary cortical neurons, for both alginate and CMC-based cryogels, with an approximately homogeneous cell density throughout the 1 mm thick scaffolds. In addition, the mouse primary neurons also presented a widespread and dense neural network, as exemplified in the zoomed view given in Figure 1E. Thus, the 3D cryogels developed here allow to obtain high cell density 3D cellular scaffolds on the millimeter size scale when coated with appropriate cell-adhesive motives. The process is versatile with respect to the choice of hydrogel and cell types.

In order to further characterize the interaction between cells and cryogel scaffolds, in particular regarding cell adherence, spreading and development, we further investigated the role of scaffold coating, mean pore volume, and polymer concentration. To do so, we quantified cell densities obtained on the scaffolds after 7 d of culture of the human neuronal cell line SH-SY5Y on different cryogel and control substrates, distinguishing “round cells” exhibiting rounded cell bodies without visible neurites, from “spread cells” exhibiting at least one sprouting neurite.

Figure 2A shows how different combinations PLO, a synthetic positively charged polyelectrolyte, and laminin, an ECM protein known to favor neurite development, affect the cell density and morphology on the cryogel scaffolds. Applying either PLO or laminin alone provides a statistically significant increase in overall cell adhesion (the total cell densities were $4.5 \pm 0.9 \times 10^6 \text{ cells mL}^{-1}$ for PLO coating, $3.7 \pm 0.4 \times 10^6 \text{ cells mL}^{-1}$ for laminin coating versus $1.5 \pm 0.3 \times 10^6 \text{ cells mL}^{-1}$ for the control condition consisting in pristine alginate cryogels, $P < 0.001$ vs control in both cases), but the majority of the cells remained rounded. Only the combination of PLO followed by laminin allowed to obtain a high density of spread cells $43 \pm 6 \times 10^6 \text{ cells mL}^{-1}$ ($P < 0.001$ vs control) while keeping the round cell density low ($4.6 \pm 6 \times 10^6 \text{ cells mL}^{-1}$, which is comparable to the round densities found for other coating conditions). Hence in the remainder of this report, the specific coating combination consisting in PLO, followed by laminin, was used for all cell culture experiments. Next, we investigated the role of scaffold mean pore volume on cell density and morphology. For this, we employed scaffolds with a mean pore volume ranging

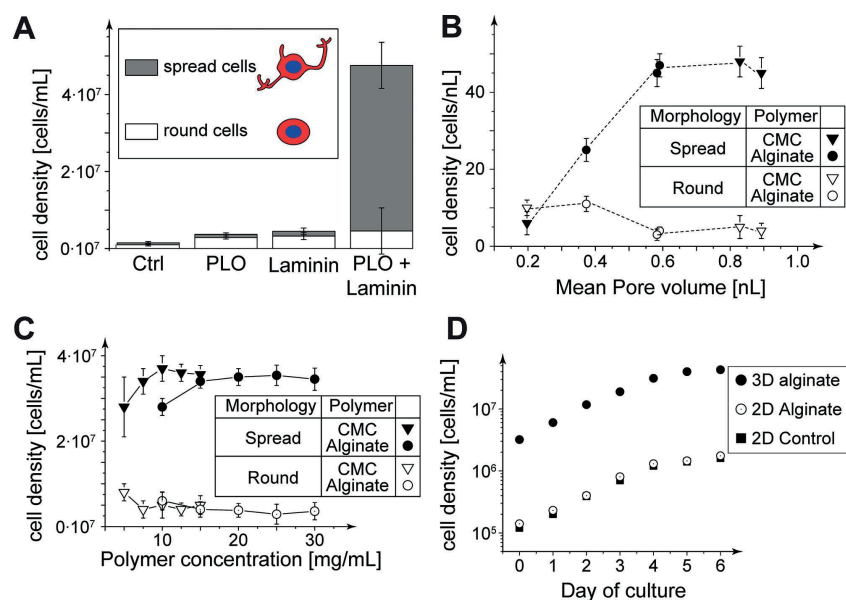


Figure 2. Parameters influencing cell adhesion and growth for the human neuronal cell line SH-SY5Y on the cryogels and 2D controls. A) The combination of PLO and laminin coating efficiently promotes cell attachment and spreading. B) Relation between pore volume and cell adhesion; the different pore volumes were obtained by varying the cryogelation substrate. C) Cell adhesion and spreading as a function of the original alginate or CMC concentration prior to cryogelation. D) Growth kinetics. With the exception of the specific conditions in Figure 2A, all cryogels as well as the 2D control substrates (Figure 2D) were coated with PLO/Laminin.

from 0.2 to 0.9 nL, obtained by modifying cryogel gelatin speed and polymer types. Figure 2B shows that the total cell density decreases significantly for pore volumes lower than 0.6 nL, with a concomitant relative increase in the ratio of round to spread cells. This indicates that the cryogel synthesis conditions should be chosen to achieve a mean pore volume of 0.6 nL or above. Figure 2C shows the effect of the polymer concentration in the initial reaction mixture on the cell density and morphology. We observe a slight decrease in cell density for the lowest polymer concentrations, most likely related to the difficulty encountered in manipulating the resulting very soft gels.

Next, we studied the effects of the cryogel scaffolds on cell duplication of the human neuronal cell line SH-SY5Y. Since both the scaffold material and the specific 3D configuration could potentially affect cell growth, we compared the growth curves obtained for 3D alginate cryogel scaffolds both to a control consisting of a plain coverslip, and a 2D alginate hydrogel (all PLO/Laminin coated). The results are summarized in Figure 2D. The sustainable cell density is higher on 3D scaffolds than on the 2D surfaces. The effect can clearly be ascribed to the 3D structure, since the mere presence of a 2D alginate substrate does not influence the sustainable cell density compared to the plain glass control. The growth rates on the other hand are comparable for all three configurations. This indicates that although the 3D cryogel configuration permits to achieve higher final cell densities, it has no influence on the replication rate per se. We obtained similar results for 2D and 3D CMC gels (data not shown).

The purpose of the cryogel scaffolds developed here is specifically to enable injection of preformed neural engineered tissue through narrow-bore tubing such as syringe needles. It is therefore of primary interest to analyze survival once cellular constructs have been injected through a syringe needle. For

doing this, we quantified cell survival using the trypan blue test at 7 d post-seeding, for both the human neuronal cell line SH-SY5Y and mouse primary cortical neurons. We then performed syringe injections through a 16G needle (1 mm inner diameter), and quantified the cell viability again at 24 h and 48 h post-injection (the tests are performed on different samples to avoid artifacts due to trypan blue toxicity). Survival results obtained for human neural cell line and for primary mouse neurons are, respectively, presented in Figure 3A,B. Control conditions consisted in 2D surfaces made of alginate and CMC and also in plain glass coverslips. Viabilities for control conditions were quantified at the same time points with respect to the beginning of the culture as for the cryogel conditions but without the injection step.

Figure 3A indicates that cell survival scores did not decrease significantly following the cellular scaffold injection step for the SH-SY5Y cell line ($P = 0.86$ for alginate scaffolds 48 h after injection, $P = 0.92$ for CMC scaffolds 48 h after injection). Likewise, Figure 3B indicates that the injection step does not affect the viability of the mouse primary neurons on the 3D scaffolds, neither for the alginate nor for the CMC cryogels ($P = 0.90$ for alginate scaffolds 48 h after injection, $P = 0.86$ for CMC scaffolds 48 h after injection). This means that the cryogel scaffolds are able to protect not only the human cell line SH-SY5Y during the injection step, but also the more delicate primary neurons with their extended neurites. Figure 3A also indicates that the SH-SY5Y cells show very high and comparable survival rates regardless of the substrate (Alginate and CMC 3D scaffolds, 2D polymer substrates and glass coverslip control). In contrast, for the mouse primary cortical neurons, survival is significantly better on the 3D scaffolds than on the 2D controls (for example, cell survival on the 3D alginate scaffolds was $82 \pm 8\%$ compared to only $57 \pm 7\%$ on 2D alginate surfaces, $P < 0.001$). Indeed,

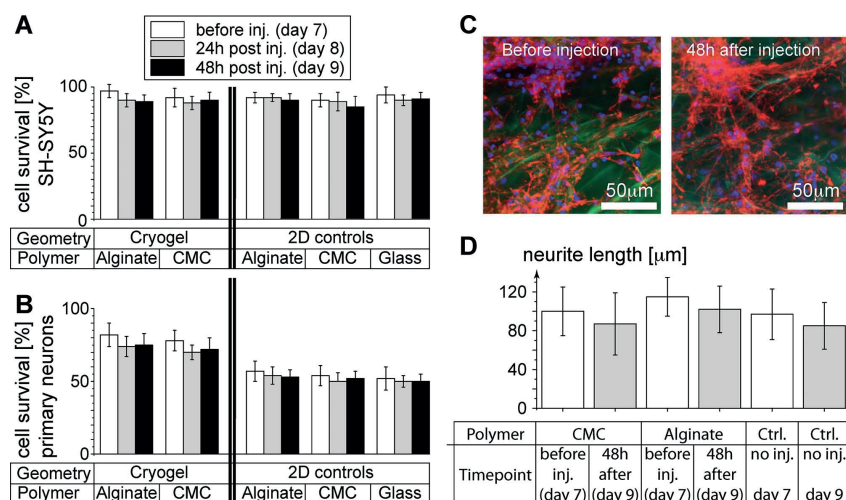


Figure 3. Cell survival and integrity during scaffold injection. A) Quantification of cell viability for the neuronal cell line SH-SY5Y before, 24 and 48 h after injection through a syringe. B) Quantification of cell viability for mouse primary neurons before, 24 and 48 h after injection through a syringe. The viabilities for the 2D controls in Figure 3A,B are taken at the same time points, but without the injection procedure. C) Representative images of mouse primary neurons on a cryogel before and 48 h after injection. Actin is labeled by means of rhodamine-phalloidin. D) Average neurite length extracted from images before and 48 h after injection. The cryogels used are synthesized in glass molds; both the cryogels and the 2D controls were PLO/Laminin coated.

the cell density obtained on 2D surfaces correspond to a high degree of confluence, which is apparently not very favorable for the survival of these primary cells under our culture conditions. In the 3D configuration, the resulting volumetric density is reduced, potentially explaining the better survival scores.

To assess the long-term outcome of CMC and alginate 3D scaffolds seeded with primary neural cells (40×10^6 cells mL⁻¹) were also maintained in culture during 21 d, with half-media change twice weekly from 7 d on. The survival scores on the cryogels remained comparable to the ones obtained for the 7-d culture: $87 \pm 4\%$ for alginate cryogels and $84 \pm 6\%$ for CMC cryogels.

Beyond cell survival, we also require the scaffolds to protect cell morphology during the scaffold injection step. Indeed, primary neurons develop dense neurite networks on the scaffolds, typically connecting clusters of neurons together; breakage of these networks must be avoided. Figure 3C presents z-projections of confocal images (observation thickness: 50 μ m), before and 48 h post-injection, indicating qualitatively that no major damage to the neural network occurs. To quantitatively assess the neurite network before and 48 h after scaffold injection through a 1-mm syringe needle, we measured neurite mean lengths before and after the injection step for both type of cellular scaffolds (primary neurons grown on alginate and CMC cryogels) (Figure 3D). We observe that the injection step has no significant influence on neurite length ($P = 0.94$ for alginate scaffolds, $P = 0.95$ for CMC scaffolds). Furthermore, neurite lengths on 3D cryogels are comparable to those measured for neurons cultured on glass coverslips (control condition). Likewise, we measured the neurite length at 24 h and 7 d post-injection, and also found no significant difference to the respective controls. The successful protection of both cell viability and differentiated morphology despite the extensive volumetric compression of the scaffolds during syringe injection is a key result of the present study, underpinning the great potential of the 3D cellular injectable cryogels for neural tissue engineering and transplantation strategies.

In order to explain the observed neural protection during the compression associated with syringe injection, we characterized the mechanical properties of the cryogels both experimentally and theoretically. The characteristic highly porous structure of the cryogels (Figure 1B) suggests that they should behave as mechanical meta-materials,^[26,27] with potentially very large differences between a locally stiff, cell-protective environment, and a low apparent macroscopic bulk stiffness, enabling extensive scaffold compression and ultimately syringe injection. Indeed, adapting a model from foam mechanics,^[26,28] we obtain a simple relation between the apparent macroscopic stiffness, described by the bulk modulus B_{bulk} and the local stiffness of the cryogel wall material, described by the Young modulus E_{wall} . The development is given in Supporting Information 4, and yields (Equation S21, Supporting Information):

$$E_{\text{bulk}} = 2 * E_{\text{wall}} * \Phi^3 * F_{\text{struct}} \quad (1)$$

where Φ is the volume fraction occupied by the scaffold walls, and F_{struct} is a dimension-less structural factor, on the order of unity, and depending on the polymer-type. Equation 1 outlines the crucial importance of the wall volume fraction: with a wall

volume fraction Φ in the range of 1%–10%, one may expect the cryogels to be 3 to 6 orders of magnitude softer globally than locally.

Atomic force microscopy has recently been identified as a useful tool to evaluate the local stiffness of cryogels.^[27] Using this technique in conjunction with a specifically developed sample preparation method, we evaluated the wall Young modulus E_{wall} in an aqueous environment on covalently immobilized cryogel fragments on a glass coverslide (experimental details are given in Supporting Information 2). Figure 4A shows the topography of the immobilized cryogel fragments, whereas Figure 4B,C show close-up views of a fiber-shaped fragment along with the local Young modulus. The cryogel fragments appear as elevated areas on the topography image (Figure 4A,B), and as soft areas on the comparatively hard glass substrate in the Young modulus image (Figure 4C). Figure 4D shows the average Young modulus of the cryogel fragments as a function of the polymer type (alginate or CMC) and initial concentration used to synthesize the cryogels. While we find the alginate cryogels to be locally stiffer than the CMC cryogels ($E_{\text{wall}} = 117$ vs 4.2 MPa, Table 1), we also find the local stiffness to be independent of the initial polymer concentration ($P = 0.52$ for the alginate gels, $P = 0.39$ for the CMC gels).

Next, we determined the wall volume fraction Φ by weighing the cryogels in the fully hydrated state, and after forceful dehydration. The result is shown in Figure 4E. To a first approximation, we can consider the wall volume fraction to be proportional to the initial polymer concentration. This confirms that during the cryosynthesis, an approximately constant final polymer concentration is reached within the cryogel wall,^[32] explaining the approximately constant Young modulus for each cryogel type (alginate and CMC, Figure 4D). Further, from the slope of the regression lines in Figure 4E, we can estimate the final polymer concentration in the scaffold walls for each of the two cryogel types. The results are given in Table 1. They indicate that while very high local polymer concentrations are reached indeed, the walls should still be considered to be hydrogels, since they contain more than 70% water by weight.

Finally, we examined apparent bulk modulus of the cryogels by means of compression of macroscopic samples (disks of 4 mm diameter and 1 mm height) with a mechanical testing device (details are given in Supporting Information 3). The resultant macroscopic Young moduli E_{bulk} were found to be in the kPa range (Figure 4F) rather than the MPa range observed for the local Young moduli. Furthermore, Equation 1 quantitatively links the bulk moduli to the local Young moduli (linear fit in Figure 4F), and also allows to determine the structural strength factor F_{struct} for each of the two polymers (Table 1). It is noteworthy that the CMC cryogels, despite a lower local Young modulus, are macroscopically stiffer at a given polymer concentration than the corresponding alginate cryogels. This is in part due to a higher volume fraction, but mostly due to a higher structural constant F_{struct} . Finally, Equation 1 also quantitatively explains mechanical data on cryogels presented by others, previously explained only qualitatively (detailed discussion in Supporting Information 4).^[27]

Given the strikingly different local and bulk elastic properties of the cryogel scaffolds, we next investigated how the presence of relatively hard cryogel walls can protect the soft cells during

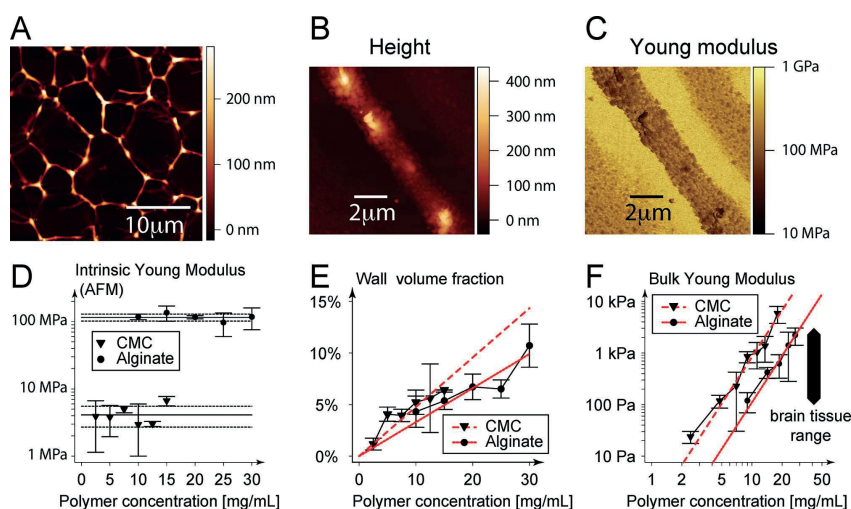


Figure 4. Microscopic and macroscopic mechanical properties of cryogels. A) Height image of CMC cryogel fibers immobilized on a glass substrate (1% initial CMC concentration) by atomic force microscopy (AFM). B) AFM Height image of a single alginate cryogel fiber (from a 1.5% initial alginate cryogel). C) AFM Young modulus map corresponding to Figure 4B, as determined by the quantitative nanomechanical mapping in PeakForce Mode (PeakForce QNM). D) Intrinsic Young moduli of cryogel fibers from alginate and CMC cryogels with different initial polymer concentration, measured by AFM. E) Fraction of the volume occupied by the cryogel walls as a function of the initial polymer concentration. F) Apparent bulk Young moduli as a function of initial alginate, respectively, CMC concentration, determined by mechanical testing of macroscopic cryogel samples, along with best fit theoretical lines relating intrinsic modulus, wall fraction and apparent bulk modulus. The range of Young moduli for brain tissue is taken from literature.^[29–31]

Table 1 Estimated intrinsic local and apparent bulk mechanical parameters of the alginate and CMC cryogels. The errors for the intrinsic Young modulus are the standard deviations of the means; the errors for the polymer concentration within the cryogel fibers are obtained from the linear regression (Figure 4E); the error on the structural factor results from the associated linear regression (Figure 4F) and propagated errors from the intrinsic Young modulus measurement as well as the estimation of the polymer concentration within the cryogel fibers.

Polymer	Intrinsic Young modulus [MPa] (Figure 4D)	Polymer concentration within the cryogel fibers [% w/w] (Figure 4E)	Structural factor F_{struct} (Figure 4F)
Alginate	117 ± 14	27.2 ± 1.9	0.013 ± 0.004
CMC	4.2 ± 1.4	19.4 ± 1.5	0.92 ± 0.52

the compression process. For this, we used finite element modeling (FEM, carried out in the COMSOL software suite) of a simplified cryogel structure, comprising a simplified pair of adherent neurons with neurites (Figure 5A). As a control, we also simulate the same cell geometry, but embedded in a homogeneous gel without pores (Figure 5D). We chose the Young moduli of the different elements to reflect approximately the situation in a 1% CMC cryogel. According to Table 1, the local Young modulus should be 4.2 MPa; the wall volume fraction is about 4.3% (Figure 4E), so together with a structural factor of 0.92 (Table 1), one would expect an apparent global Young modulus on the order of 0.6 kPa for the cryogel (Equation 1). Hence, we used $E = 0.6$ kPa for the homogeneous control gel. The cells, including the neurites, are modeled with a Young modulus of 0.2 kPa, taken from literature.^[33]

For the cryogel structure and the homogeneous control, we attempted to simulate the deformation and corresponding

mechanical stresses using COMSOL for a uniaxial compression of 25% and 75%. We report the resulting von Mises stress, since this measure has been shown to be a good indicator of the probability of material failure under various load conditions. The cryogel structure easily admits 75% compression and beyond, the resulting von Mises stress distribution is shown in Figure 5B,C, respectively. On the contrary, the simulations for the homogeneous gel do not converge beyond 30% compression, enabling us to estimate the von Mises stress only for the 25% compression case (Figure 5E). The non-convergence for larger compression agrees with what would be observed if these experiments were carried out physically: while a cryogel would survive a 75% compression and beyond while maintaining mechanical integrity, a bulk gel would burst if compressed beyond some 20–30%.^[19]

The distribution of the von Mises stress shows that in the case of the cryogel, the hydrogel absorbs almost all the elastic energy (Figure 5B,C), whereas in the bulk gel, the elastic energy transmitted to the gel respectively the cells is similar (Figure 5E). As a result, the cells are exposed to higher stresses in the bulk gel at similar compression (Table 2).

Taken together, these results indicate that accumulation of elastic energy by the cryogel structure, rather than transmission to the cells, offers the mechanical protection enabling high compression fractions while preserving neurons and extended neurites during the injection procedure. The high pore fraction, the small wall thickness, and the locally high Young modulus all contribute to this phenomenon (see Supporting Information 5 and discussion part for details).

In order to facilitate the use of the injectable cryogels scaffolds in different settings, we further investigated how different

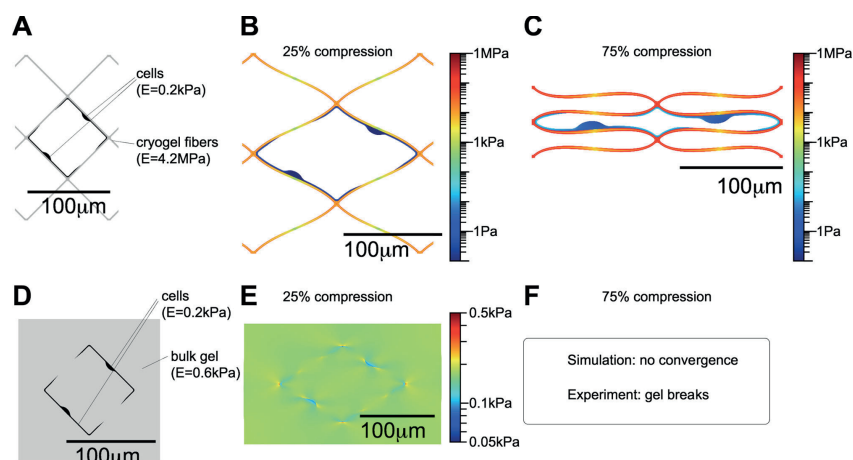


Figure 5. Finite element simulation. A) simplified structural model of the cryogel with a pair of adherent cells. B) Finite element simulation of a 25% compression of the cryogel. The deformation is imposed and corresponds to 25% of the height of the cryogel structure; the colors code for the von Mises stress, a known overall measure for material loading. C) Finite element simulation of a 75% compression of the cryogel structure. D) simplified structural model of a corresponding bulk gel with identical cell geometry and a bulk Young modulus corresponding to the apparent bulk modulus of the cryogel. E) Finite element simulation of a 25% compression of the bulk gel with cells, with imposed deformation. The colors again code for the von Mises stress, although it should be noted that the scales are different for Figure 5E as compared to Figure 5B,C. F) For 75% compression, the FEM simulation for the homogeneous control gel does not converge.

Table 2. Maximum von Mises stress sustained by the cells.

	25% Compression	75% Compression
Cryogel	15 Pa	46 Pa
Bulk gel	222 Pa	Not applicable (gel breaks)

synthesis parameters affect the final cryogel scaffold structure and performance. Results are presented in Figure 6. First, we compared three freezing strategies involving different substrates (Figure 6A): A first strategy consisted in pipetting the prepolymer solution onto a precooled Teflon plate (row “Teflon” in Figure 6A); a second strategy consisted in sandwiching the prepolymer solution between two glass cover slides by means of 1 mm high plastic spacers, and then placing the assembly on a precooled aluminum plate (row “Glass” in Figure 6A); the third strategy consisted in pipetting the prepolymer solution directly onto the precooled aluminum plate (row “aluminum” in Figure 6A). In each case, we assessed the linear pore dimensions and calculated the mean pore volume. We also calculated an anisotropy index, corresponding to the largest pore diameter divided by the smallest one on 2D sections. The smallest and most isotropic pores are observed for the “aluminum” scenario. This is expected, since aluminum has by far the highest thermal conductivity of the three substrates used,^[34,35] and since it is well known that cryogels with smaller pores are generally obtained for the highest freezing rates due to the increased ice crystal nucleation rate.^[36] Figure 6B summarizes the maximum volumes that we succeeded to inject through a 16G syringe needle without breakage, for gels of different composition (alginate or CMC, with and without PLO/Laminin coating) and pore volume. The maximum cryogel scaffold volume successfully

injected was 3 mL, obtained with a coated CMC-cryogel, exhibiting the smallest pore size. Larger volumes have not been investigated. Contrary to Figure 6B where we injected cryogel scaffolds a single time, for Figure 6C, we injected a standard spherical cryogel scaffold of 100 μ L through a 16G syringe needle (1 mm inner diameter), and quantified the number of times we could repeat the process before the cryogel would break into pieces. Since in practice, one would inject a cryogel only a single time, this gives a safety margin in terms of gel integrity. We find a relatively narrow optimum of prepolymer concentration for each polymer: 0.75% prepolymer concentration for the CMC cryogels and 2% prepolymer concentration for the alginate cryogels. In addition, we show that the PLO/Laminin coating reinforces the gel and makes it more robust against breakage. Figure 6D finally shows pore interconnectivity as assessed by the wicking test;^[19] for CMC cryogels, we observe a drop in pore interconnectivity beyond 1% prepolymer concentration, while the alginate cryogels show high interconnectivity throughout the entire concentration range.

3. Discussion

In neural tissue engineering, the use of scaffolds serving as organized cell carriers is considered necessary due to the low cell survival and engraftment efficiency observed for cells transplanted in suspension.^[37,38] The surgical procedures needed to place scaffolds of clinically relevant size are however associated with a high risk of further tissue damage.^[6] To the best of our knowledge, there is still no solution able to simultaneously address large-size tissue reconstruction, potentially deep inside the brain, and to provide preorganized neural tissue constructs. Here, we present a novel type of highly compressible cryogel

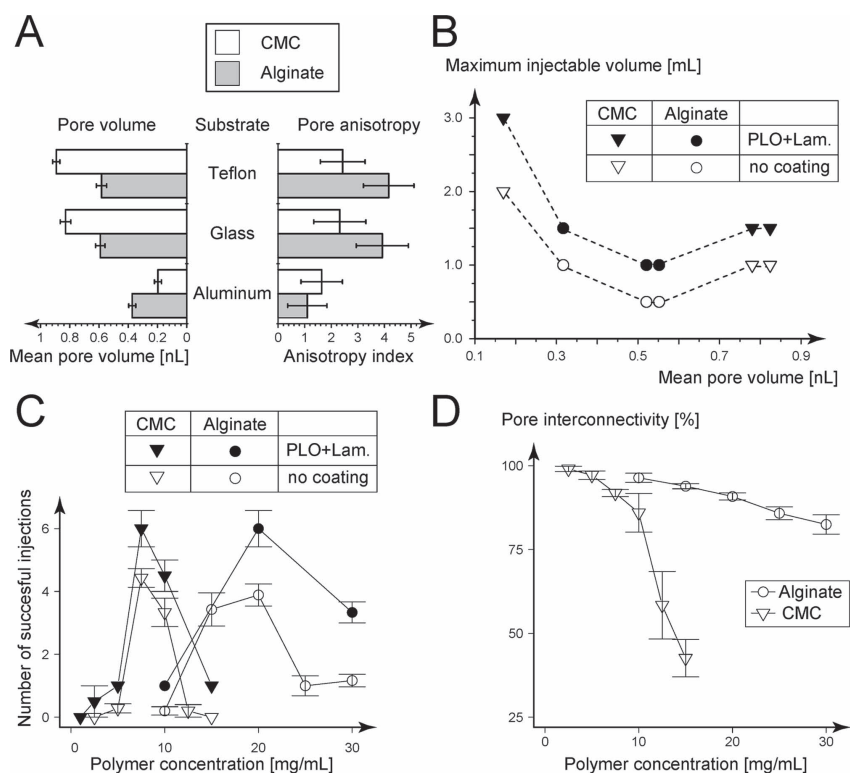


Figure 6. Control and optimization of the structural parameters and injectability of the cryogels. A) Cryogelation on different substrates affects pore size and pore anisotropy. B) Maximum injectable volumes (spherical gel geometry, injection through a 16G needle). C) Injectability as a function of the initial polymer concentration and the coating. Cryogelation performed on glass substrates. D) Pore interconnectivity as a function of the initial polymer concentration. Cryogelation performed on glass substrates. The errorbars indicate standard deviations of the mean.

scaffold, specifically adapted to minimally invasive delivery of differentiated neuronal networks by transient compression to about 10% of the initial volume. Based on a novel one-pot carbodiimide cryogel synthesis, the scaffolds advantageously combine desirable properties: They allow attachment, spreading and neurite formation by primary neurons due to the presentation of native laminin.^[21] Their highly porous nature allows injection through narrow-bore tubing.^[18,19] The scaffolds also present the advantage of reliable sterilization, of prime importance in light of potential clinical translation: By performing the deposition of the cell-adhesive coating only after cryogel synthesis, we are able to avoid microbiologically unsafe washing with ethanol solutions, which had to be employed with cryogel scaffolds having laminin or RGD peptides incorporated already during the synthesis step.^[19,21,39] Further, the scaffolds extend the domain of volumes injectable through a 16-Gauge (1 mm) needle into the mL-range. Taken together, these properties enable the development of an extended neuronal network made from primary cells that can subsequently be highly compressed for minimally invasive delivery into the central nervous system. It is, to the best of our knowledge, the first demonstration of a compressible living neural network.

We find the success of cell seeding, attachment, and spreading on the cryogel scaffolds to be critically dependent on the prior

coating of the cryogels with suitable cell adhesive motives (here, the combination of PLO and laminin, Figure 2A), confirming findings for neuronal culture on other substrates.^[40] We also find a minimal pore volume of 0.6 nL to be required for optimal adhesion and spreading (Figure 2B), corresponding to a mean pore diameter of about 100 μm , in line with results reported for neural tissue engineering.^[21] Additional important architectural parameters are the total pore fraction (Figure 4E: $1 - \phi = 89\%$ for the 3% alginate cryogels, and $>90\%$ for all other compositions, in accordance with literature recommendations^[41] and also the fraction of the pore space interconnected^[42] to the outside world ($>80\%$ for all scaffolds except the CMC 1.25% and 1.5%, Figure 6D) since only the accessible pores will be colonized. Provided suitable cell-adhesive coating, pore size, and interconnectivity, the cryogels support live cell densities up to 50×10^6 cells mL^{-1} , for both the human neuronal cell line SH-SY5Y (Figure 2) and mouse primary neurons (data not shown), for culture periods beyond 1 week. These cell densities approach the ones found in the mouse cortex (92×10^6 cells mL^{-1}), and exceed the live densities achievable with homogeneous gels by about one order of magnitude.^[43,44] The 3D structure, with its high available surface area and high pore space for nutrient diffusion, rather than the specific material, is responsible for sustaining high viability at these high cell densities (Figure 3B).

Beyond attachment, the cryogel coating also provides cues for cell spreading (Figure 1E), and neurite extension by the mouse primary neurons (Figure 1E, Figure 3C,D). At the same time, neural cells also need to communicate with their peers.^[45–47] In the cryogel scaffolds, we find that the neurites largely follow the gel walls, but are also able to bridge small gaps (Figure 1E). In addition, the somata of individual cells are found to adhere to the cryogel walls; but with higher cell density, organized multi-layered structures are also formed (Figure 1E). This suggests an equilibrium between strong cell–matrix interaction and cell–cell interaction, which is considered suitable for tissue formation. Indeed, if the cell–matrix interaction is too strong, the cells will line the scaffold surface with minimal 3D organization and potentially loss of cell functionality;^[46] if the cell–matrix interaction is too weak, the cells tend to adopt rounded morphology, and oftentimes undergo cell death due to lack of adhesion.^[48]

In order to identify criteria to enable injection of the cellular scaffolds, we carried out bulk and nanomechanical characterization. By aligning the results obtained on the alginate and CMC cryogels, we are able to establish the following design rules for scaffold injectability (Supporting Information 5): minimal bulk Young modulus ($E_{\text{bulk}} \geq 0.1$ kPa) and minimal microscopic Young modulus ($E_{\text{wall}} \geq 100$ kPa) for appropriate manual handling, maximal wall volume fraction ($\Phi < 10\%$) for limiting local strain (Equation S29, Supporting Information), and high pore interconnectivity for enabling fluid evacuation. The protection of the cells during the injection process is due to the concentration of the elastic energy within the cryogel material (Figure 5). The nanomechanical analysis confirms the high local Young moduli necessary for this (Figure 4D, Table 1: $E_{\text{wall}} = 117$ MPa for alginate-based cryogels, respectively, 4.2 MPa for CMC-based cryogels). The high local Young modulus may also be advantageous in terms of neurite formation, since stiffer substrates have been linked to the formation of both more numerous and more highly branched neurites.^[49]

The macroscopic compression analysis on the other hand confirms the low bulk stiffness (Figure 4F, 0.85 kPa for the 1% CMC vs 2.2 kPa for the 3% alginate cryogels used in the cell culture and live injection experiments), facilitating compression prior to injection with minimal force. In addition, the brain is a relatively soft organ, with elastic moduli reported in the 0.1–3 kPa range, depending on the region and measurement technique employed.^[29–31] Since it has been reported that mismatch between the local stiffness and implanted devices may be linked to a strong adverse glial reaction,^[16] it may be necessary to match the bulk stiffness of the scaffold to the local brain tissue Young modulus for in vivo experiments. Given the strong dependence of the bulk modulus on the initial polymer concentration (Figure 4F), it is straightforward to match to any desired Young modulus in the range reported for the brain; the necessary initial polymer concentration can indeed be calculated by Equation 1.

Finally, we demonstrate that cryogels with neurons exhibiting already substantial neurite extension can be compressed and syringe-injected, without damaging the cells (Figure 3). To the best of our knowledge, these scaffolds are the first to combine macroscopic size and injectability through a narrow-bore conduit for neuronal tissue engineering applications. The results demonstrate that suitably designed macroporous scaffolds

allow to protect morphologically differentiated primary cells, going a fundamental step beyond the demonstration of injectability of cell suspensions or robust cell lines along with shape-memory scaffolds.^[18,19] Given that cell density, neurite development and scaffold organization are preserved throughout the injection process, the scaffolds will allow to transfer in vivo not only the cells, but also their precise spatial organization.

4. Conclusions

We present a novel neural engineering scaffold that can be injected through a syringe needle, while conserving cell viability, morphology, and organization as well as scaffold integrity, even in the presence of differentiated neurites. The system is an answer to a major dilemma encountered in neural tissue engineering for the central nervous system: scaffolds should be preorganized and potentially large, but at the same time they should be delivered in a minimally invasive fashion to avoid further tissue damage. The scaffolds developed here are both: organized at a large size scale, and nevertheless injectable thanks to their compressibility. They open up an avenue of experiments and approaches hitherto thought impossible: spatial localization of adhesion motives and cells could be used to organize the scaffold into physiologically relevant regions, while chemical gradients could be used to guide long range connections before implantation. The features obtained could be quality-checked before implantation, and then minimally invasively delivered while maintaining shape, volume, viability, and neural network organization.

5. Experimental Section

Chemicals: The following chemicals were obtained from Sigma–Aldrich: Sodium alginate (catalog number A0682-100 G, molecular weight $M_n = 110$ kDa, $M_w = 242$ kDa, polydispersity 2.2 by gel permeation chromatography), sodium CMC (419338-100 G, 700 kDa according to the manufacturer's datasheet), *N*-(3-dimethylaminopropyl)-*N'*-ethylcarbodiimide hydrochloride EDC (E7750-25G), Morpholinoethanesulfonic acid MES hydrate (M2933-100G), adipic acid dihydrazide (AAD) (A0638-25G), aminofluorescein (07980 Fluka-1G), NaOH (S8045–500G), ethylene-diamine-tetraacetic acid EDTA (EDS), phosphate buffered saline (PBS) (P4417-50TAB), laminin (L-2020), paraformaldehyde, (158127-500 g) Triton X-100 (X100–100 mL), papain. Fetal bovine serum was obtained from PAA Laboratories, DMEM cell culture medium, penicillin streptomycin from GIBCO, neurobasal medium, and B27 from Invitrogen, and Glutamax from Life Technologies.

Cryogel Synthesis: Cryogels were synthesized based on established carbodiimide chemistry.^[50] Details are given in Supporting Information 1. Briefly, either alginate or CMC is dissolved in deionized water (DI) to the desired concentration, and crosslinking initiated by means of addition of AAD and a small excess of the carbodiimide EDC. The reaction mixture is rapidly placed at -20 °C in a mold, resulting in ice crystal formation prior to completion of gel crosslinking; if not specified otherwise, cryogels were formed on molds made from glass coverslides and suitable spacers (Supporting Information 1). After 24 h, the cryogels are thawed, washed in DI, EDTA 10×10^{-3} M and PBS, and autoclaved in PBS; the space occupied by the ice crystals during the cryo-incubation now becomes pore space. If not specified otherwise, alginate cryogels were synthesized using the 3% composition as listed in Table S2 (Supporting Information 1), whereas CMC cryogels

were synthesized according to the 1% composition listed in Table S3 (Supporting Information 1). For visualization purposes, we also synthesized fluorescent cryogels by addition of aminofluorescein during the crosslinking reaction, since aminofluorescein will react with EDC-activated carboxylic acid groups under the same conditions as AAD (for details, see Supporting Information 1).^[51]

SEM: Cryogel samples were lyophilized, gold coated and imaged using a Zeuss's Merlin SEM operated at 5 keV and secondary electron detection.

Pore Fraction and Interconnectivity: The pore fraction and interconnectivity can be estimated from the weight loss under different dehydration conditions. The interconnected pore space is assessed by the wicking test, that is by the relative amount of water that can be withdrawn from a fully hydrated cryogel by means of a paper towel.^[19] Similarly, the total pore space can be assessed by force-full compression (estimated mechanical pressure on the order of 1 MPa). The wall volume fraction, finally, is calculated as 1 minus the fraction occupied by the pore space.

Bulk Young Modulus: Bulk Young moduli were obtained by mechanical compression of cryogels with a defined disk geometry (typically, 4 mm diameter, 1 mm height). The measurements were performed on a TextureAnalyzer TA.XT plus (Stable Microsystems). Sample force-distance curves and the fitting procedure to obtain the Young moduli are given in Supporting Information 2.

Local Young Modulus by Atomic Force Microscopy: The local Young modulus of the cryogel fibers was determined by AFM imaging using the PeakForce Quantitative Nanomechanical Mapping (QNM) mode (Bruker, FastScan). To enable AFM imaging and Young modulus quantification, cryogel fibers with a height ranging from 50 nm to 1 μ m were immobilized on an otherwise flat substrate. Supporting Information 3 provides the experimental details on the immobilization and imaging procedures; a comparison to Force-Volume imaging and COMSOL simulation of the hydrogel indentation process to evaluate the influence of the underlying substrate and the tip geometry are also provided.

Syringe Injection: For systematic injection tests, roughly spherical cryogels of 100 μ L (ca. 6 mm in diameter) were prepared for various concentrations of alginate and CMC according to the protocol given above and detailed in Supporting Information 1. The finished cryogels were dehydrated by mechanical compression against a gauze, inserted into a syringe, and pushed through a syringe needle measuring 1 mm in inner diameter (16 Gauge). To investigate maximal injectable cryogel volumes, spherical cryogels of different volumes were fabricated and injected once through the same syringe needle. Injection was considered successful when the cryogels remained visually intact after the injection process.

Pore Volume and Anisotropy: Cryogels were cut into thin slices along two perpendicular directions while still frozen. After thawing, images were taken using a bright-field microscope ($\times 10$ objective), binarized, and the dimensions of at least 200 pores for each fabrication condition and cryogel composition were recorded using ImageJ software. The pore volume was estimated as the product of biggest, smallest, and mean pore diameter, whereas the pore anisotropy was calculated as the ratio between the biggest and the smallest pore dimension.

Cryogel Coating: Unless specified otherwise, autoclave-sterilized cryogels were coated prior to cell culture to allow the cells to adhere to the cryogel scaffolds. To do so, cryogel samples were first partially dehydrated by compressing them mechanically against a sterile gauze. A PLO (1 mg mL⁻¹ diluted in sterile deionized water) droplet of 10 times the cryogel volume was then deposited on top of each cryogel and left for 1 h at 37 °C. The PLO droplet was then removed, and the cryogel samples rinsed with DI water. Finally, the cryogels were again partially dehydrated under sterile conditions, and laminin (1 μ g mL⁻¹ in sterile DI water) was added onto the cryogel samples (1 \times cryogel sample volume) and left for 4 h at 37 °C. Prior to initiation of cell culture, samples were rinsed with sterile DI water and compressed again immediately before cell seeding.

2D Control Substrates: 2D control samples for alginate and CMC substrates were fabricated on coverslips. To ensure permanent adhesion

of the hydrogels to the glass slides, the coverslips are first coated with a molecular adhesion layer of alginate or CMC. The procedure coincides with the coverslide activation step used in the AFM sample preparation, given in Supporting Information 3. Once these molecular adhesion layers established, we deposited the bulk gel layers. To do so, we used the 1% recipe for the CMC and the 3% recipe for the alginate also used for the cryogel fabrication (Supporting Information 1), but rather than placing the reaction mixture at -20 °C, we dried a drop of the reaction mixture on the coverslips prior to completion of polymerization by using a stream of pressurized air. To ensure complete polymerization, we expose the dried slides to 170 °C dry heat for 20 min; to remove unreacted products, we sequentially washed them in NaOH 100 $\times 10^{-3}$ M, EDTA 10 $\times 10^{-3}$ M, and PBS, prior to 70% ethanol sterilization.

Neuronal Cell Line: The human neuroblastoma-derived cell line (SH-SY5Y) was grown in DMEM medium supplemented with 10% fetal bovine serum and 1% penicillin streptomycin in Petri dishes. Cells were subculture twice a week, and maintained at 37 °C and 5% CO₂. All reported experiments were performed using cells with less than 20 passages from purchase.

Primary Cortical Cells: All experimental procedures were carried out according to the Swiss federation rules for animal experiments. Mouse primary cortical neurons were prepared from embryonic day 17 Of1 fetal mouse brains. Cortices were digested in medium containing papain (20 U mL⁻¹) and dissociated by mechanical trituration. Cells were plated in neurobasal medium supplemented with 2% B27 and 2 $\times 10^{-3}$ M Glutamax. Unless otherwise specified, all substrates (cryogels, but also planar control substrates) were coated with PLO/Laminin as described above. All cells were kept in a humidified 5% CO₂ atmosphere at 37 °C.

Cryogel Seeding and Culture: SH-SY5Y cells or mouse primary cortical neurons were seeded onto cryogel and control substrates at a typical density of 4000 cells mm⁻³. A droplet (volume equal to the cryogel volume) containing the cells is placed onto the partially dehydrated cryogel sample and incubated for 45–60 min. Cell culture medium (500 μ L) was then added and cells were maintained at 37 °C, 5% CO₂. At experimental endpoints, the cellular scaffolds or control substrates were fixed with 4% paraformaldehyde for characterization. Cell distribution was homogeneous throughout the 1 mm thick scaffold. For culture periods beyond 7 d, half-media were changed twice weekly.

Analysis of Cell Morphology: To observe cells and quantify their morphology, cells were fixed with 4% buffered formaldehyde during 20 min. After PBS washes, actin cytoskeleton and cell nuclei were stained (permeabilization with Triton X-100 (0.3% in PBS), followed by phalloidin-Atto565 (Sigma-Aldrich) at a dilution of 1:200 and 4'-6-diamidino-2-phenyl indole (DAPI) used at 300 $\times 10^{-9}$ M). Fluorescence images were acquired using a confocal fluorescent microscope Zeiss LSM 700 with a -20 \times air objective or with a 40 \times oil objective. Images of at least 200 cells on four randomly chosen observation fields were captured and analyzed for each experimental condition and for each experiment. Experiments were repeated at least three times. Cell density was quantified as the number of cell nuclei in a given volume. SH-SY5Y cells were designated as "spread" when they developed at least one sprouting neurite from the soma measuring at least 15 μ m in length, otherwise, they are considered "round." Based on confocal images, neurite length was measured using the plugin NeuronJ of ImageJ. For cell survival analysis, samples were rinsed with HEPES-buffered salt solution (HBS), and incubated in a trypan blue solution (0.4% in HBS) for 2 min at room temperature. The samples were then washed with HBS, and the cells of five independent observation fields were observed and counted on the whole sample thickness using a bright-field microscope with $\times 20$ objective (Leica DM5500). Cell viability (in%) resulted from the ratio between the number of non-stained cells and the total cell number.

Finite Element Simulation: Finite element modeling (FEM) was performed in COMSOL version 4.3b. The gel and the cells were modeled as nearly incompressible linear elastic materials, while the pore space was considered void. The boundary conditions were set to free movement for all boundaries except for the top and bottom boundary, which were used to impose the compression in z direction. The simulations were run in 2D, using the SolidMechanics physics, with

an in-plane stress 2D approximation. The materials were all supposed to be linearly elastic with appropriate local Young moduli, and a Poisson ratio of 0.48.

Statistical Analysis: Unpaired, two-sided *t*-tests were used for direct comparison of pairs of outcome variables. To test whether the injection procedure had a significant effect on cell viability or neurite length, the difference between the outcome measures before and at a given time point after injection was compared to the difference at identical time points under control conditions by means of an adapted *t*-test with a compound estimation of the standard deviation and a corresponding adjustment of the number of degrees of freedom. To assess the relation between the initial polymer concentration and the local Young modulus, *F*-tests were applied to the analysis of variance associated with the linear regression. No multiple testing corrections were used. Error bars indicate standard deviations, except where otherwise noted.

Supporting Information

Supporting Information is available from the Wiley Online Library or from the author.

Acknowledgements

A.B. and T.B. contributed equally to this work. The authors thank the EPFL biomaging and optics core facilities, as well as the EPFL Molecular and Hybrid Materials Characterization Center, for their excellent technical assistance, and Blake Erickson for his help with the AFM imaging. This work was funded by the Swiss National Science Foundation, Grant PBELP3-133350, IZKOZ2_154342 and 205321_134786, by the Brazilian Swiss Joint Research Programme No.BJRP 0112-09 and by the European Research Council under the European Union's Seventh Framework Programme (FP7/2007-2013)/ERC grant agreement n°307338.

Received: May 13, 2014

Revised: July 31, 2014

Published online: September 1, 2014

- [1] T. Back, *Cell Mol. Neurobiol.* **1998**, *18*, 621.
- [2] B. A. Reynolds, S. Weiss, *Science* **1992**, *255*, 1707.
- [3] F. H. Gage, *Science* **2000**, *287*, 1433.
- [4] K. van Kuyck, M. Welkenhuysen, L. Arckens, R. Sciot, B. Nuttin, *Neuromodulation* **2007**, *10*, 244.
- [5] E. Bible, D. Y. S. Chau, M. R. Alexander, J. Price, K. M. Shakesheff, M. Modo, *Biomaterials* **2009**, *30*, 2985.
- [6] D. Fon, A. Al-Abboodi, P. P. Chan, K. Zhou, P. Crack, D. I. Finkelstein, J. S. Forsythe, *Adv. Healthcare Mater.* **2014**, *3*, 761.
- [7] C. R. Freed, P. E. Greene, R. E. Breeze, W. Y. Tsai, W. DuMouchel, R. Kao, S. Dillon, H. Winfield, S. Culver, J. Q. Trojanowski, D. Eidelberg, S. Fahh, *N. Engl. J. Med.* **2001**, *344*, 710.
- [8] A. J. Mothe, T. Zahir, C. Santaguida, D. Cook, C. H. Tator, *PLoS One* **2011**, *6*, e27079.
- [9] O. Lindvall, P. Brundin, H. Widner, S. Rehncrona, B. Gustavii, R. Frackowiak, K. L. Leenders, G. Sawle, J. C. Rothwell, C. D. Marsden, A. Björklund, *Science* **1990**, *247*, 574.
- [10] M. Abematsu, K. Tsujimura, M. Yamano, M. Saito, K. Kohno, J. Kohyama, M. Namihira, S. Komiya, K. Nakashima, *J. Clin. Invest.* **2010**, *120*, 3255.
- [11] S. Kriks, J. W. Shim, J. Piao, Y. M. Ganat, D. R. Wakeman, Z. Xie, L. Carrillo-Reid, G. Auyeung, C. Antonacci, A. Buch, L. Yang, M. F. Beal, D. J. Surmeier, J. H. Kordower, V. Tabar, L. Studer, *Nature* **2011**, *480*, 547.
- [12] T. Yuan, W. Liao, N. H. Feng, Y. L. Lou, X. Niu, A. J. Zhang, Y. Wang, Z. F. Deng, *Stem Cell Res. Ther.* **2013**, *4*, 73.
- [13] R. M. Richardson, A. Singh, D. Sun, H. L. Fillmore, D. W. Dietrich, M. R. Bullock, *J. Neurosurg.* **2010**, *112*, 1125.
- [14] A. Farin, C. Y. Liu, I. A. Langmoen, M. L. J. Apuzzo, *Neurosurgery* **2009**, *65*, 831.
- [15] T. C. Burns, G. K. Steinberg, *Expert Opin. Biol. Ther.* **2011**, *11*, 447.
- [16] P. Moshayedi, G. Ng, J. C. Kwok, G. S. Yeo, C. E. Bryant, J. W. Fawcett, K. Franze, J. Guck, *Biomaterials* **2014**, *35*, 3919.
- [17] S. Zhou, A. Bismarck, J. H. G. Steinke, *J. Mater. Chem. B* **2013**, *1*, 4736.
- [18] A. J. Thornton, E. Alsborg, M. Albertelli, D. J. Mooney, *Transplantation* **2004**, *77*, 1798.
- [19] S. A. Bencherif, R. W. Sands, D. Bhatta, P. Arany, C. S. Verbeke, D. A. Edwards, D. J. Mooney, *Proc. Natl. Acad. Sci. U.S.A.* **2012**, *109*, 19590.
- [20] V. I. Lozinsky, I. Y. Galaev, F. M. Plieva, I. N. Savina, H. Jungvid, B. Mattiasson, *Trends Biotechnol.* **2003**, *21*, 445.
- [21] M. Jurga, M. B. Dainiak, A. Sarnowska, A. Jablonska, A. Tripathi, F. M. Plieva, I. N. Savina, L. Strojek, H. Jungvid, A. Kumar, B. Lukomska, K. Domanska-Janik, N. Forraz, C. P. McGuckin, *Biomaterials* **2011**, *32*, 3423.
- [22] H. Yang, W. O'Hali, H. Kearns, J. R. Wright Jr, *Transplantation* **1997**, *64*, 28.
- [23] T. Miyamoto, S. Takahashi, H. Ito, H. Inagaki, Y. Noishiki, *J. Biomed. Mater. Res.* **1989**, *23*, 125.
- [24] M. Matyash, F. Despang, R. Mandal, D. Fiore, M. Gelinsky, C. Ikonomidou, *Tissue Eng. Part A* **2012**, *18*, 55.
- [25] T. Koike, S. E. Pfeiffer, *Dev. Neurosci.* **1979**, *2*, 177.
- [26] J. H. Lee, J. P. Singer, E. L. Thomas, *Adv. Mater.* **2012**, *24*, 4782.
- [27] P. B. Welzel, J. Friedrichs, M. Grimmer, S. Vogler, U. Freudenberg, C. Werner, *Adv. Healthcare Mater.* **2014**, DOI:10.1002/adhm.201400102.
- [28] L. J. Gibson, M. F. Ashby, *Cellular Solids: Structure and Properties*, Cambridge University Press, Cambridge, UK **1997**.
- [29] H. Metz, J. McElhane, A. K. Ommaya, *J. Biomech.* **1970**, *3*, 453.
- [30] Z. Taylor, K. Miller, *J. Biomech.* **2004**, *37*, 1263.
- [31] G. T. Fallenstein, V. D. Hulce, J. W. Melvin, *J. Biomech.* **1969**, *2*, 217.
- [32] H. Kirsebom, G. Rata, D. Topgaard, B. Mattiasson, I. Y. Galaev, *Macromolecules* **2009**, *42*, 5208.
- [33] E. Spedden, J. D. White, E. N. Naumova, D. L. Kaplan, C. Staii, *Biophys. J.* **2012**, *103*, 868.
- [34] R. C. Weast, M. J. Astle, W. H. Beyer, *Handbook of Chemistry and Physics*, 64th ed., CRC Press, Inc., Boca Raton, FL, USA **1984**.
- [35] H. Czichos, *Hütte: Die Grundlagen der Ingenieurwissenschaften*, Springer Verlag, Berlin **2000**.
- [36] B. M. A. Carvalho, S. L. Da Silva, L. H. M. Da Silva, V. P. R. Minim, M. C. H. Da Silva, M. L. Carvalho, L. A. Minim, *Separation Purification Rev.* **2014**, *43*, 241.
- [37] E. Garbayo, G. Delcroix, P. C. Schiller, C. N. Montero-Menei, in *Tissue Engineering of Tissue and Organ Regeneration*, (Ed: D. Eberli), Intech, Rijeka, Croatia **2011**.
- [38] P. Brundin, G. Barbin, O. Isacson, M. Mallat, B. Chamak, A. Prochiantz, F. H. Gage, A. Björklund, *Neurosci. Lett.* **1985**, *61*, 79.
- [39] R. N. Nye, T. B. Mallory, *Boston Med. Surg. J.* **1923**, *189*, 561.
- [40] Y. Sun, Z. Huang, W. Liu, K. Yang, K. Sun, S. Xing, D. Wang, W. Zhang, X. Jiang, *Biointerphases* **2012**, *7*, 29.
- [41] R. Lanza, R. Langer, J. Vacanti, *Principles of Tissue Engineering*, Academic Press, London **2013**.

- [42] A. Tripathi, N. Kathuria, A. Kumar, *J. Biomed. Mater. Res. A* **2009**, *90*, 680.
- [43] A. Schuz, G. Palm, *J. Comp. Neurol.* **1989**, *286*, 442.
- [44] M. C. Laplaca, V. N. Vernekar, J. T. Shoemaker, D. K. Cullen, in *Methods in Bioengineering: 3D Tissue Engineering*, (Eds: F. Berthiaume, J. Morgan), Artech House Publishers, London **2010**.
- [45] B. Nadarajah, P. Alifragis, R. O. Wong, J. G. Parnavelas, *Nat. Neurosci.* **2002**, *5*, 218.
- [46] H. Kaji, G. Camci-Unal, R. Langer, A. Khademhosseini, *Biochim. Biophys. Acta* **2011**, *1810*, 239.
- [47] A. Beduer, I. Gonzales-Calvo, C. Vieu, I. Loubinoux, L. Vaysse, *Macromol. Biosci.* **2013**, *13*, 1546.
- [48] S. M. Frisch, E. Ruoslahti, *Curr. Opin. Cell Biol.* **1997**, *9*, 701.
- [49] M. L. Previtera, C. G. Langhammer, B. L. Firestein, *J. Biosci. Bioeng.* **2011**, *110*, 459.
- [50] X. Zhao, N. Huebsch, D. J. Mooney, Z. Suo, *J. Appl. Phys.* **2010**, *107*, 63509.
- [51] T. Braschler, A. Valero, L. Colella, K. Pataky, J. Brugger, P. Renaud, *Lab Chip* **2010**, *10*, 2771.

**ADVANCED
HEALTHCARE
MATERIALS**

Supporting Information

for *Adv. Healthcare Mater.*, DOI: 10.1002/adhm.201400250

A Compressible Scaffold for Minimally Invasive Delivery Of
Large Intact Neuronal Networks

*Amélie Béduer, * Thomas Braschler, Oliver Peric, Georg
E. Fantner, Sébastien Mosser, Patrick C. Fraering, Sidi
Benchérif, David J. Mooney, and Philippe Renaud*

Supporting Information 1: Cryogel Synthesis

General remarks on the crosslinking and labeling chemistry

The cryogels are synthesized by carbodiimide activation of the carboxylic acid residues and the carbohydrate moieties (alginate and carboxymethyl-cellulose), followed by amide bond formation with adipic dihydrazide, which results in the covalent crosslinking of the gels.

Although stabilizers of activated esters such as N-hydroxysuccinimide (NHS) or hydroxybenzotriazole (HOBT) are sometimes used for this type of amino- to carboxyl coupling, we found it easier to directly take advantage of the particularly low pKa of the adipic dihydrazide to obviate the need for these stabilizers. It is indeed possible to carry out the crosslinking reaction with high yields at a pH ranging from 5 to 6 without the need for either NHS or HOBT. In this case, sufficient buffering capacity must however be provided by the addition of a suitable buffer such as a morpholino-ethane-sulfonate (MES).

Likewise, for the fluorescent labeling, we use aminofluorescein. Indeed, aminofluorescein has an aromatic amino group that will react like the acid hydrazine groups at pH 5-6, without the need for NHS or HOBT. It can therefore be included in the reaction mixture without further precaution and will get bound to the carboxyl-groups with very high yield, making the fluorescent labeling very practical. As a drawback, it should be noted that fluorescein derivatives photobleach quite quickly, at least when compared to more advanced dyes such as the Alexa or Atto series.

Due to its sensitivity to hydrolysis, we need to add the carbodiimide last. We use N-(3-dimethylaminopropyl)-N'-ethylcarbodiimide hydrochloride (EDC) by dissolving it in an equal amount of water (e.g., 10 μ L of deionized water to dissolve 10mg EDC), and then

transferring the resulting solution to the reaction mixture. This initiates gel formation, such that mixing needs to be carried out quickly, with immediate transfer to a mold at -20°C if cryogel formation is desired.

The following tables give the detailed recipes and procedures used throughout this study. DI is deionized water; AAD is adipic acid dihydrazide; CMC is carboxymethyl-cellulose; EDC is water-soluble carbodiimide; MES is morpholino-ethane-sulfonic acid; PBS is phosphate buffered saline; EDTA is ethylene-diamine-tetraacetic acid (adjusted to pH 8 with NaOH, e.g., approximately Na₃H-EDTA).

MES buffer pH 5.5 0.5M

MES-hydrate (solid)	NaOH (solid)	Adjust to final volume with DI
97.6g	3.66g	1L

Table S1: Preparation of MES buffer.

Alternatively, the NaOH can be provided as a liquid solution, for instance as 91.5mL of NaOH 1M.

Alginate cryogels

Nominal percentage	Sodium alginate, 30mg/mL in DI	DI	MES buffer, pH 5.5, 0.5M	AAD 50mg/mL	EDC
3%	1mL	-	0.1mL	26 μL	12mg dissolved in 12 μL DI
2.5%	1mL	0.2mL	0.1mL	26 μL	12mg dissolved in 12 μL DI
2%	1mL	0.5mL	0.1mL	26 μL	12mg dissolved in 12 μL DI
1.5%	0.5mL	0.5mL	50μL	13μL	6mg dissolved in 6μL DI
1%	0.5mL	1mL	50μL	13μL	6mg dissolved in 6μL DI

Table S2: Recipe for the alginate cryogels.




Carboxymethyl-Cellulose cryogels

Nominal percentage	CMC 15mg/mL in DI	CMC 10mg/mL in DI	DI	MES buffer, pH 5.5, 0.5M	AAD 50mg/mL	EDC
1.5%	1mL	-	-	0.1mL	10.5 μ L	8mg dissolved in 8 μ L DI
1.25%	0.5mL	0.5mL	-	0.1mL	9 μ L	6mg dissolved in 6 μ L DI
1%	-	1mL	-	0.1mL	7 μ L	4mg dissolved in 4 μ L DI
0.75%	-	1mL	0.333mL	0.1mL	7 μ L	4mg dissolved in 4 μ L DI
0.5%	-	1mL	1mL	0.1mL	7 μ L	4mg dissolved in 4 μ L DI
0.25%	-	1mL	3mL	0.1mL	7 μ L	4mg dissolved in 4 μ L DI

Table S3: Recipes for the CMC cryogels

Detailed protocol

The detailed protocol for production of sterile cryogels is outlined in Table S4:

Illustration	Description
	1. Polymer premix Alginate or CMC + AAD + MES buffer; amounts see table above
	2. Pre-cool to 4°C This step is required for the CMC cryogels only
	3. Add activator The EDC is dissolved in an equal amount of water (e.g. 10 μ L for 10mg); it is typically possible to make a stock solution for several gels, provided the

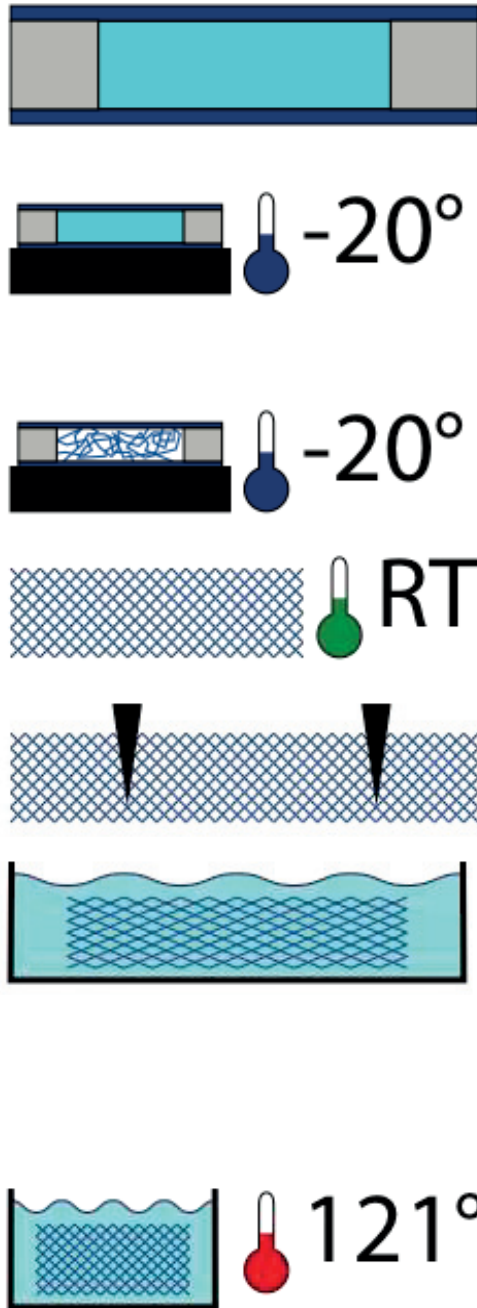


Table S4: Cryogel synthesis protocol

stock is used within an hour

4. Transfer to mold

Mix rapidly, transfer to mold. A convenient way to make a mold is to use plastic spacers (on the order of 1mm height) and two coverslides

5. Transfer to -20°C

For large molds, the molds need to be pre-cooled; for the coverslide molds described above, it is enough to place the assembled mold on a pre-cooled metal block in the freezer

6. Incubate at -20°C

Freezing causes structuration

Polymerization time at least 24h

7. Thaw, unmold

Remove from mold; from this step on, the gels should never be allowed to dry completely.

8. Stamp

If desired, punch out disks of the desired size (typically, 4mm diameter disks)

9. Wash out unreacted products

We use the following washing steps: 1) DI, 2) 100mM NaOH, 3) 10mM EDTA pH 8, 4) DI, 5) PBS, 6) PBS. The washing steps can be done in Falcon tubes, with 5 min incubation for each step.

10. Autoclave

To minimize hydrolysis, the gels are autoclaved in PBS.

Fluorescently labeled gels

In order to be able to use the fluorescent gels along with traditional cell labeling techniques such as visualization of actin filaments by rhodamine-phalloidin, the gels need to have a suitable brightness. If they are too bright, the spectral spillover makes observation of the neighboring channels (e.g., rhodamine) impossible; if they are too dim, too high laser intensities lead to exaggerated photobleaching. Empirically, we find the following cryogel compositions appropriate for confocal microscopy along with rhodamine-phalloidin labeling of the actin cytoskeleton:

CMC 1%: Addition of 12 microliters of aminofluorescein 1mM to the reaction mixture outlined in Table S3, prior to the addition of EDC

Alginate 3%: Addition of 24 microliters of aminofluorescein 1mM to the reaction mixture outlined in Table S2, prior to the addition of EDC

We prepare an aminofluorescein stock solution as follows: First, we prepare a 100mM stock solution by mixing 35mg aminofluorescein + 300 microliters NaOH 1M + 700 microliters DI; we then dilute this solution 1:100 with DI to obtain the 1mM solution used for the labeling.

The washing steps outlined in Table S4, including the autoclave step, suffice to remove unreacted aminofluorescein.

Supporting Information 2: Bulk Young Modulus Estimation

Mechanical testing of cryogels

Bulk testing of cryogels can be performed in a setup for linear compression of a sample of known disk geometry (we use a TextureAnalyzer Plus apparatus from Stable Microsystems). In this setting, the deformation is imposed, and the resulting stress is recorded as the reaction force acting on the chuck. The deformation strain is given by:

$$\varepsilon = \Delta L/L_0 \quad (S5)$$

where L_0 is the undeformed disk height, and ΔL the distance of compression. The stress is given by:

$$\sigma = F/A \quad (S6)$$

where F is the force exerted by the chuck and $A=\pi r^2$ is the disk diameter. The Young modulus relates the strain to the stress:

$$\sigma = E*\varepsilon \quad (S7)$$

Given an experimental stress-strain relation, the Young modulus can be determined by the slope of a regression line fitted to a linear portion of the stress-strain relation. For the cryogels, we use the portion from 0 to 0.5 strain (e.g., 50% compression) for the fitting of the Young modulus.

Sample Stress-Strain curve and extraction of the Young modulus

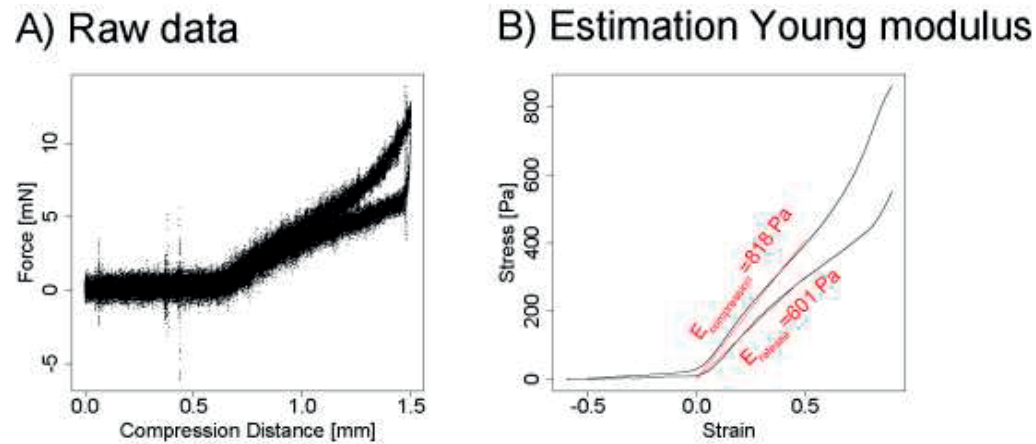


Figure S8: Raw force-distance curve for a 1% CMC cryogel (A) along with the stress-strain relation (B) extracted by low-pass filtering and application of equation S5 and S6. The linear fits in Figure S8-B are obtained by means of equation S7.

Figure S8 shows the force distance curve as raw data obtained from the TextureAnalyzer Plus (Stable Microsystems) used for the mechanical testing (A) along with the stress-strain relation extracted and used for the determination of the Young modulus (B). The strain is extracted from the compression-distance curve by means of equation S5 and the known initial gel thickness whereas the stress is obtained by relating the force to the cross-section area by means of equation S6. Since the cryogels show some hysteresis, two separate Young modulus values are obtained by fitting straight lines according to S7, one in the compression phase, one in the release phase. The hysteresis is due to viscous, rather than plastic effects, since repeated measurements yield essentially identical stress-strain relations. Since one expects viscous effects to increase the stress in the compression phase, and to decrease it in the release phase of the mechanical test, we take the average of the two moduli to be representative of the true bulk elastic modulus. In the example shown, the mean Young modulus would have a value of 709Pa.

Supporting Information 3: Imaging and local Young modulus quantification of cryogels by Atomic Force Microscopy AFM

Sample preparation

It is difficult to obtain local Young moduli of the cryogel wall material on intact macroscopic cryogels because of the presence of comparatively very large pores between the cryogel material to be analyzed. One way to address this problem consists in the selective probing of cryogel fibers localized by means of microscopic imaging simultaneously performed with the atomic force microscopy AFM measurements^[1]. Even so, obtaining contiguous images remains a challenge.

Hence, in order to obtain samples amenable to contiguous imaging, and to avoid the need for simultaneous optical microscopy and AFM instrumentation, we immobilize shallow pieces of cryogel walls on a solid, flat substrate. To do so, we carry out the cryogelation process on specially prepared slides, which provide for covalent attachment sites during the gel formation process, and then manually brush off most of the cryogel by using a water jet. In this way, it is possible to obtain cryogel material to be imaged with a topographical height between 100nm and 1 μ m, suitable for AFM.

The detailed process of sample preparation is outlined in Figure S9. We start out with Novellus “Assistant” round coverslips made from borosilicate glass, onto which we deposit a drop of alginate solution (3%) or CMC solution (1%) depending on whether we ultimately need to image alginate or CMC cryogels.

For the CMC slides, we dry the coverslips at 80°C in a well-ventilated oven for 30 minutes. We then wash off the bulk dry material, leaving behind an invisible, but strongly hydrophilic layer. We then hardbake this layer in dry heat at 190°C for another 30 minutes.

For the alginate slides, we directly expose the slides to dry heat at 170°C for 30 minutes, and then wash off the dried, and slightly caramelized bulk material, and again obtain a strongly attached, highly hydrophilic, but invisible layer of attached polysaccharide.

For both of types, we then proceed with the cryogel synthesis as outlined in the main text and Supporting Information 1. Once the cryopolymerization is complete, we find the cryogel to adhere firmly to the substrate; we remove most of the bulk cryogel by manually directing a weak water jet at the bulk material, leading to the formation of a cleavage plane some 100nm to 1µm above the glass surface. The adhesion of cryogel fragments to the glass slide can be confirmed by checking the slides under an optical microscope by the appearance of a network of fine lines corresponding to the cryogel wall fragments.

As a side note, we sometimes find similar traces after removal of cryogels from untreated glass slides as well, but the process is made reproducible by the pre-treatment protocol outlined here. Likewise, it is fully possible to simply use tweezers to remove the bulk cryogel after the synthesis, but the water jet method is more reproducible in our hands. For reasons unclear to us, we need to perform a two-step procedure (80°C, wash, 190°C) for the CMC, whereas a one step heat procedure (170°C) is sufficient for the alginate attachment.

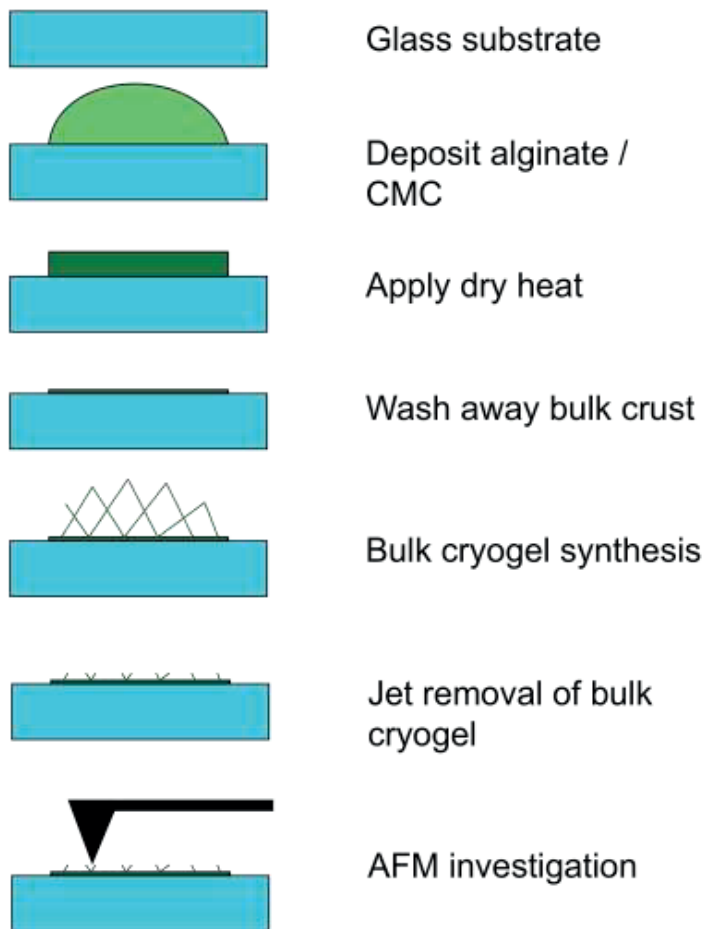


Figure S9. Sample preparation method for cryogel imaging.

AFM measurement method

The AFM measurements themselves are carried out in an aqueous environment, using Bruker’s peak force mode for Quantitative Nanomechanical Mapping (QNM) imaging. We use the TAP150A tip (Bruker, designated as MPP-12120-10) for the alginate samples, and the ScanAsyst-Fluid tip (Bruker) for the carboxymethyl-cellulose samples. We use the absolute calibration method for the following elements:

- Calibration of the “deflection error” on a sapphire sample
- Calibration of the spring constant via the “thermal tune” method
- Checking of the tip integrity on a Tipcheck sample.

As outlined below (section “tip geometry”), constraints arising from lateral resolution and Young modulus quantification on very thin samples require us to work with an indentation too large for the DMT model^[2], but too small for the Sneddon model^[3], such that we use reference samples of known elastic modulus to calibrate the Young modulus measurement; the necessary correction factor is then applied to the Young modulus measurements for the unknown samples measured during the same AFM session. For our experimental settings, we find the correction factor to vary somewhat within the range of 0.5 to 2.0.

Further, for an alginate and a CMC sample, we also have performed a direct comparison between a Force-Volume measurement and the QNM image. Indeed, historically, the Force-Volume technique is older and therefore more generally accepted in the AFM field than the peak-force controlled QNM mode. It is also much slower, and suffers from a series of additional drawbacks and problems as compared to the more recent peak-force controlled QNM imaging mode, so once the equivalence of the two methods for our types of samples established, we consistently used the QNM imaging.

Comparison with force-volume

We performed a comparison between the Force-Volume (FV) mode and the peak-force controlled QNM imaging on a randomly chosen region on a 3% alginate sample, which we imaged with both techniques, and similarly, a randomly chosen region on a 1.25% CMC sample.

The Figures S10 and S11 below show the comparison between the measurements:

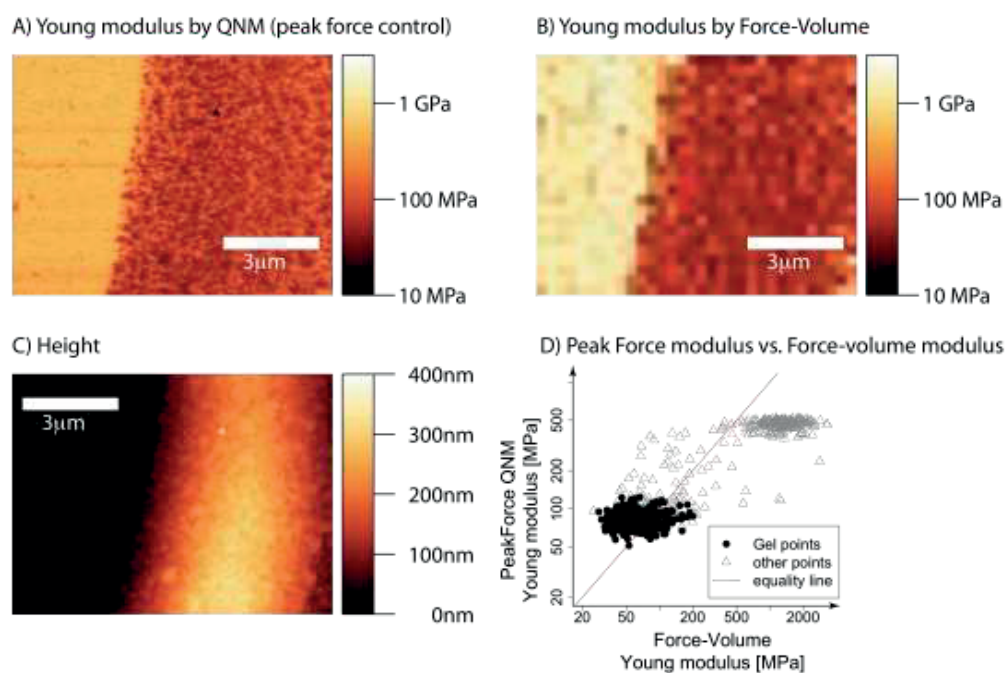


Figure S10: Force-Volume vs. PeakForce for Alginate. Comparison of QNM Peak Force (A) to Force-Volume imaging (B) for a 3% alginate cryogel sample. For D) gel points are defined as points with a height of more than 120nm on the topographical image (C), all others are considered as “other points”.

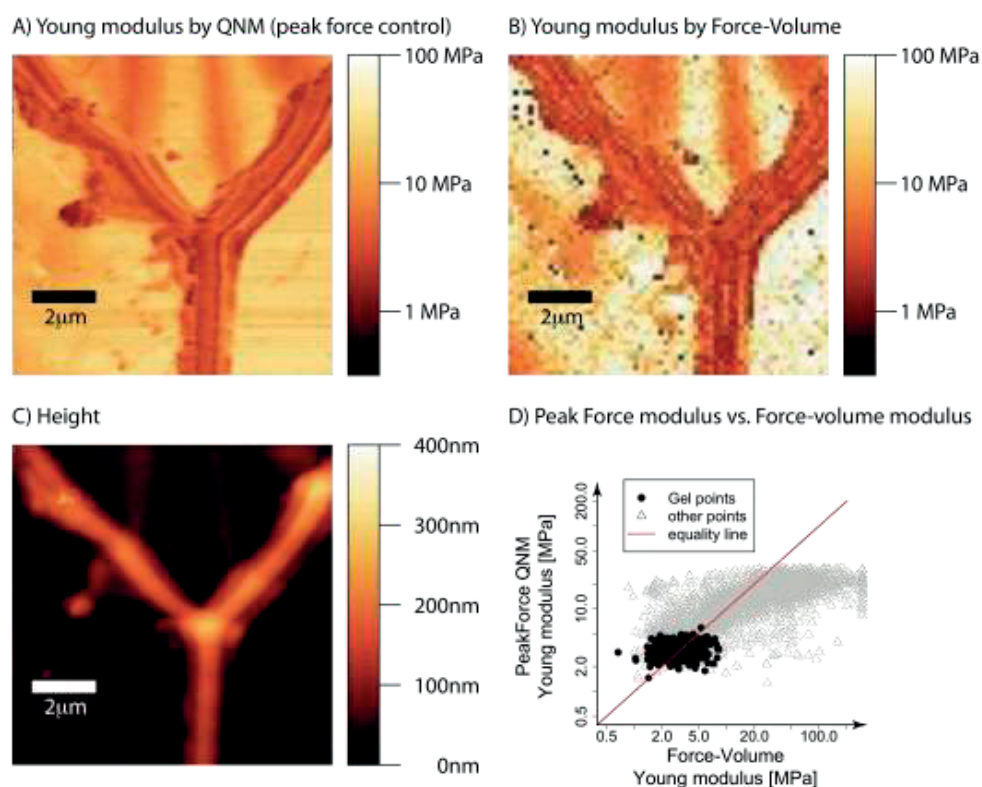


Figure S11: Force-Volume vs. PeakForce for CMC. Comparison of QNM PeakForce (A) and force-volume imaging (B) for a 1.25% CMC cryogel sample. For D) gel points are defined as points with a height of more than 120nm on the topographical image (C), all others are considered as “other points”.

The moduli determined with the two techniques are on the same order of magnitude (Alginate sample: PeakForce QNM 82 +/- 12 MPa vs. Force volume 68 +/- 28 MPa; CMC: PeakForce QNM 3.2MPa +/- 0.7 MPa vs. 3.2MPa +/- 1.3MPa for the force-volume modulus; comparison on the gel points defined by having more than 120nm height on the height map), confirming that PeakForce QNM effectively gives quantitative results that are comparable to Force-Volume imaging.

Given that the PeakForce imaging mode is much faster than the force-volume mode, we did not perform any supplementary experiments in force-volume mode.

In terms of the gel physics involved, the absence of an important difference between PeakForce and Force-Volume imaging also suggests that there is no important stress relaxation phenomenon taking place on the time scale between 1s (pixel acquisition time in FV) and 1ms (pixel acquisition time in PeakForce QNM) on the size scale of the tip radius (10-20nm).

Discussion of systematic errors

A series of potential systematic errors may affect the estimation of the local Young modulus via AFM imaging, the most important being limited sample thickness and a mismatch between the mathematical models used to extract the Young modulus and the actual tip geometry due to indentation beyond the spherical region of the tip. A minor source of systematic error is the unknown Poisson coefficient of the samples.

Sample thickness

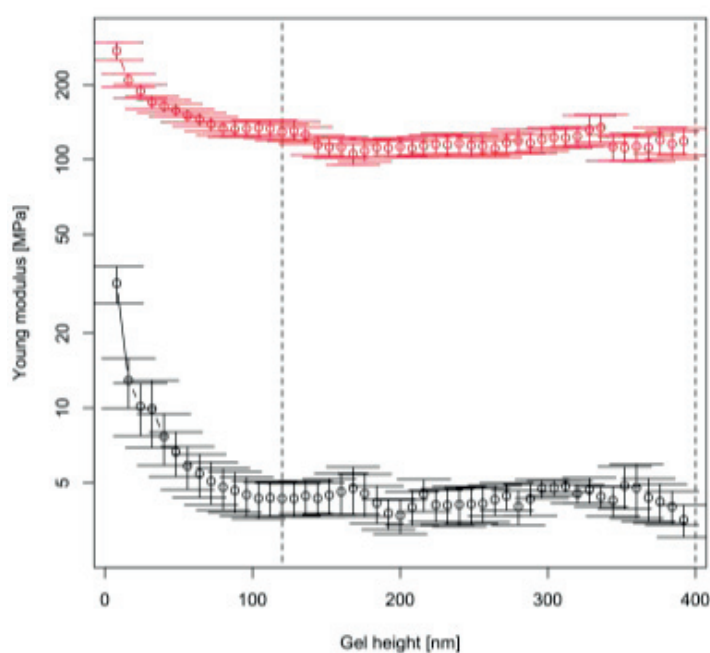


Figure S12: Young moduli estimations as a function of sample thickness. The upper dots (red) are for the alginate samples, the lower dots (black) for the CMC samples. We have visually chosen 120nm as the minimal height required for the Young modulus estimation (left dashed

line); in order to avoid damage to the tip, we have also limited the measurements to regions with topographical features 400nm or less (right dashed line). Error bars indicate standard deviations of the mean.

It is well-known that determination of the hardness of a material by indentation is in part influenced by the underlying material^[4]. The practical question is how thick the soft cryogel fragments need to be such that the influence of the underlying hard glass substrate can be neglected. To answer this question, we have combined the data from all the samples underpinning Figure 4 in the main text, and plotted the estimated Young modulus as a function of the local topographical height. The result is shown in Figure S12. Based on this view of the data, we have chosen to consider only points with a minimal topographical height of 120nm to limit the influence of the underlying glass substrate, since beyond the Young modulus estimation for points with a gel thickness of more than 120nm remains essentially constant.

Tip geometry

Young moduli are defined for homogeneous deformation, and a model is needed to extract the Young modulus from the force distance curves obtained in AFM imaging. For shallow indentations, the tip can be considered spherical, and the appropriate model is the DMT model^[2]. For deep indentations, the tip can be considered conical, and the appropriate model is known as the Sneddon model^[3].

Ideally, the tips are chosen such that either the DMT model or the Sneddon model can be applied fully; with the specific sample at hand, we however face a series of limitations making this impossible in practice:

1. The signal to noise ratio is generally improved by large forces, and therefore large indentations.
2. We are however limited by the low sample thickness, and too high indentation forces would lead to an exaggerated influence of the underlying glass substrate.
3. In theory, large forces with shallow indentations can also be achieved with tips with large radii, by sacrificing resolution; given the submicrometric feature size in our samples, this is not a feasible option.

Overall, the need for sufficiently high resolution forces us to use tips with small radii (typically, 10-20nm); the need for a sufficient signal to noise ratio requires us to apply forces that produce indentations which are too large for the DMT model; and the shallow thickness precludes the use of forces sufficiently large to entirely warrant application of the Sneddon model. The scope of the present hydrogel study does not warrant the development and implementation of our own, intermediate model, and we systematically use the DMT model, but apply a correction by means of a reference sample. Indeed, Figure S13 shows that depending on the exact gel geometry, the blind use of a given model may lead to a systematic error of 50% in the force estimation for forces on the order of 20nN, employed in practice; this would typically result in a similar systematic error on the order of a factor of 2 or 3 for the Young modulus estimation. Assuming that the indentation process is similar for materials of similar Young modulus, this can be corrected for by the application of a correction factor obtained on a known reference sample (reference sample for the alginate cryogels: the 100MPa regions on the PS-LDPE-12M reference sample from Bruker; reference sample for the CMC cryogels: PDMS-SOFT-2-12M from Bruker, 3.5MPa).

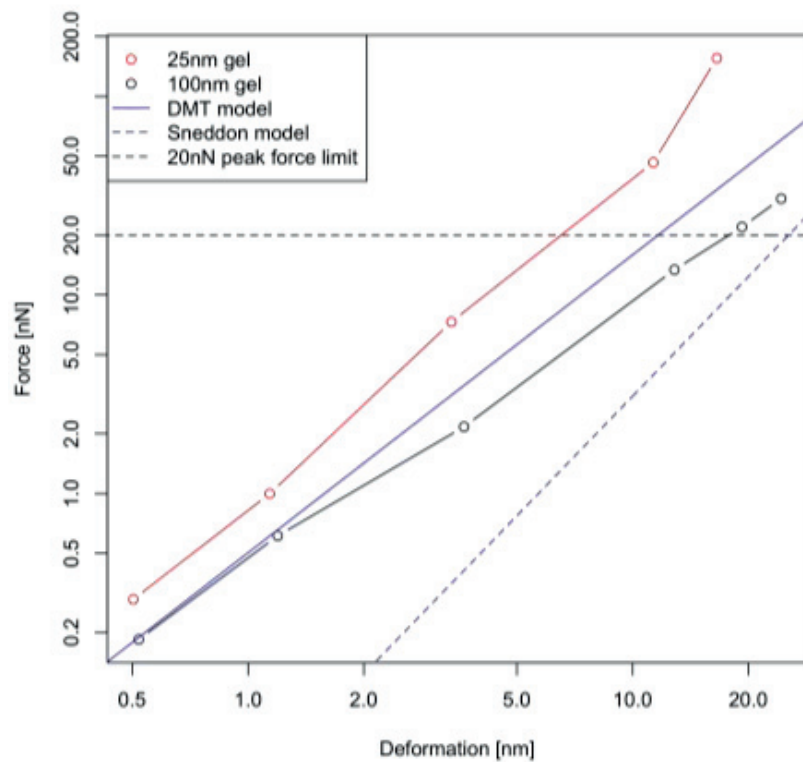


Figure S13: Simulation of the indentation force, and comparison to the DMT and Sneddon model.

Poisson ratio

The estimation of the Young modulus requires knowledge of the Poisson ratio. For hydrogels, many researchers assume a Poisson ratio of 0.5 on the basis the high water content makes the gel essentially incompressible^[5]. In any case, the relative influence of the Poisson ratio on the determination of the Young modulus is limited to 25% in the DMT model in the range of a Poisson ratio of 0-0.5, making the potential error associated with this assumption small in comparison with the other systematic errors.

Supporting Information 4: Relation between local and apparent bulk mechanical properties

Local and bulk Young modulus

The hydrogel sponges used in this study consist of generally less than 10% wall material and more than 90% pore space (Figure 4E in the main text). Thus, they behave as mechanical meta-material with bulk (apparent) properties that can be very different from the local properties. A large body of theory is available for the mechanical description of such porous, regular mechanical materials, traditionally referred to as cellular solids^[6], or more precisely, foams^[6], for the 3D structures considered here. The “cells”, in this context, refer to the physical unit structure of the foam, which consists of a pore space and its associated walls.

Foams in general are classified into open and closed structures. In fully closed foams, the pore spaces are separated by sheet-like polymer walls termed “faces”, whereas in fully open foams, the wall-material is wire-like, and the pore cells all communicate directly with their immediate neighbors^[6]. The cryogels presented here are intermediate: although much of the pore space is interconnected, a continuous sheet of wall material often separates two neighboring pores, with fluidic connections through additional pore cells. Since the closed faces can bear mechanical loads, we deem it more appropriate to use the formalism of closed foams, despite the fluidic interconnectivity.

For closed foams, the apparent bulk modulus of the structure E_{bulk} is known to be related to the third power of the volume fraction Φ occupied by the solid phase (i.e. the cryogel walls), and the local Young modulus of the wall material E_{wall} ^[7]:

$$E_{\text{bulk}} = C * \Phi^3 * E_{\text{wall}} \tag{S14}$$

Where C is a proportionality constant, which depends on the exact geometry of the structures, but most importantly not on the absolute pore size^[6, 7].

To further evaluate C , we shall consider a simple beam mechanical model of the cryogels. Given the overall irregularity of the cryogels, we replace the different elements by a single representative cantilever, of dimensions:

$$h = \Phi * D / 2 \quad (S15)$$

$$l = D / 2 \quad (S16)$$

$$w = D / 2 \quad (S17)$$

where h, l and represent respectively the height, length and width of the cantilever, while D is the mean pore diameter. Assuming a homogeneous rectangular cross section, the spring constant of such a cantilever is given by^[8]:

$$k = E_{\text{wall}} / 4 * w * (h/l)^3 = E_{\text{wall}} * D * \Phi^3 \quad (S18)$$

where E_{wall} is the intrinsic Young modulus of the wall material.

In a hypothetical homogeneous bulk material of Young modulus E_{bulk} , the force necessary to uniaxially compress an element of $D/2 \times D/2 \times D/2$ would be given by:

$$F = E_{\text{bulk}} * A * \Delta L / L = k * \Delta L \Rightarrow k = E_{\text{bulk}} * A / L = E_{\text{bulk}} * D / 2 \quad (S19)$$

By requiring the spring constant to be identical for the hypothetical bulk and the cryogel sample, we obtain:

$$E_{\text{bulk}} * D/2 = E_{\text{wall}} * D * \Phi^3 \Rightarrow$$

$$E_{\text{bulk}} = 2 * E_{\text{wall}} * \Phi^3 \tag{S20}$$

By comparing equation S20 and equation S14, we therefore obtain $C=2$.

We do however not expect equation S20 to hold exactly for cryogels, since there are very strong underlying structural assumptions, which are probably not met strictly by the variety of structures produced from different polymers and varying conditions during cryosynthesis. To account for the potentially variable mechanical stability of different cryogel structures, we generalize equation S20 as follows:

$$E_{\text{bulk}} = 2 * E_{\text{wall}} * \Phi^3 * F_{\text{struct}} \tag{S21}$$

where F_{struct} is a structural factor equal to 1 for an exact match with the simple beam mechanical model. Equation S21 implies that cryogels with low wall volume fraction (i.e., on the order of 1%) can exhibit a bulk elastic modulus 6 orders of magnitude weaker than the local Young modulus, underscoring the importance of the concept of a mechanical metamaterial.

In the main text, we confirm equation S21 by comparison of AFM and bulk Young moduli. It is however noteworthy that we find equation S21 also to be quantitatively applicable to experimental data presented by others^[1]. Indeed, in reference^[1], local and bulk moduli are

given for starPEG:heparin cryogels, along with the corresponding porosity data for two different precursor concentrations (reported in Table S22). By comparing the reported wall fractions for the two precursor concentrations, we find that Φ differs by a factor of 3.76, whereas the bulk Young modulus differs by a factor of 75, which is consistent with a power law near Φ^3 , as predicted by equation S21.

Precursor concentration	Local Young modulus	Bulk Young modulus	Wall fraction (1-Porosity)
4.3%	1500kPa	4kPa	0.025
11.8%	1500kPa	300kPa	0.094

Table S22: Literature data for starPEG:heparin cryogels^[1].

Local and bulk strain

An order-of-magnitude estimate of the maximum strain encountered by the cryogel wall material can also be obtained from the beam model presented above. At a given macroscopic strain $\epsilon_{\text{macroscopic}}$ the tip deflection of the equivalent cantilever is given by:

$$\omega(x=L) = D/2/\sqrt{2} * \epsilon_{\text{macroscopic}} \quad (\text{S23})$$

where $\omega(x)$ is the deflection from the neutral position along the beam axis x , and $L=D/2$ the length of the beam as defined above. In beam mechanics, the local deformation of a singly supported beam is given by:

$$\omega(x) = \rho * L^3 / (6 * E_{\text{wall}} * I) * (3 * (x/L)^2 - (x/L)^3) \quad (\text{S24})$$

where ρ is the load applied to the cantilever tip, and I its cross-sectional moment of inertia.

Applying equation S23 and S24, we obtain:

$$D/2/\sqrt{2} * \epsilon_{\text{macroscopic}} = \rho * L^3 / (3 * E_{\text{wall}} * I) \quad (\text{S25})$$

The local deflection can also be used to get the local radius of curvature:

$$R = 1 / \omega''(x) = 1 / (\rho * L / (E_{\text{wall}} * I) * (1 - x/L)) \quad (\text{S26})$$

The radius of curvature is minimal for $x=0$, such that with equation S25, we obtain:

$$R_{\min} = \frac{2\sqrt{2}}{3} \frac{L^2}{D} \frac{1}{\epsilon_{\text{macroscopic}}} \approx \frac{L^2}{D} \frac{1}{\epsilon_{\text{macroscopic}}} \quad (\text{S27})$$

The maximum strain occurs at the beam surface, at $z=h/2$ from the equilibrium line, and has the magnitude:

$$\epsilon_{\max} = \frac{h}{2R_{\min}} = \frac{Dh}{2L^2} \epsilon_{\text{macroscopic}} \quad (\text{S28})$$

By using the definitions given by equation S15 and S16, this evaluates to:

$$\epsilon_{\max} = \Phi \epsilon_{\text{macroscopic}} \quad (\text{S29})$$

During the compression for injection, $\epsilon_{\text{macroscopic}} \approx 1$, since nearly all the pore space is lost. This indicates that during injection, the maximum strain encountered by the scaffold is simply given by the wall volume fraction:

$$\epsilon_{\max, \text{injection}} = \Phi \quad (\text{S30})$$

Homogeneous hydrogels typically break at a uniaxial compressive strain of about 20%.^[9] The critical component is likely the lateral extension due to the isovolumetric nature of rapid hydrogel compression, which is half the compressive strain at a Poisson ratio of 0.5, such that we expect an upper bound for the volume fraction:

$$\Phi \leq 0.1 \quad (\text{S31})$$

Hence, for wall volume fractions less than 10%, we expect the cryogels to be compressible up to the obliteration of the pore space without loss of mechanical integrity, whereas we expect mechanical failure before pore obliteration otherwise. Equation S31 therefore places an upper bound on the wall volume fraction for injectable macroporous scaffolds.

Supporting Information 5: Design rules for injectable macroporous scaffolds

Based on the comparison of the mechanical, geometrical and injectability properties of the cryogel scaffolds presented here, it is possible to extract elementary design rules for providing injectability for macroporous scaffolds. Firstly, at least for manual syringe loading, the scaffolds need to have a minimal stiffness. We find the lower threshold for successful manual handling to be roughly given by the 0.5% CMC and 1% alginate scaffolds, both of which have a bulk Young modulus of about 0.12kPa, such that we can consider a bulk Young modulus of 0.1kPa to be the lower threshold for successful manual handling, namely for manual compression prior to syringe loading.

A second criterion arises through the requirement for reversible compression up to near complete obliteration of the pores without mechanical failure of the wall material. We show in Supporting Information 4 that a low wall volume fraction allows for lower local strains at a given bulk deformation (Equation S29), and that for typical hydrogel materials, the volume fraction of the wall material should be less than 10% to avoid wall material failure upon essentially complete compression (Equation S30, S31). In addition, the pore volume should obviously be interconnected to allow rapid evacuation of the pore fluid during the compression. Finally, equation 1 in the main text implies that a minimal bulk stiffness of 0.1kPa at a volume fraction of 10% requires a wall material with a Young modulus at least 3 orders of magnitudes higher, that is on the order of 100kPa or higher.

Bibliography

- [1] P. B. Welzel, J. Friedrichs, M. Grimmer, S. Vogler, U. Freudenberg, C. Werner, *Adv Healthc Mater* **2014**.
- [2] B. V. Derjaguin, V. M. Muller, Y. P. Toporov, *Journal of Colloid and Interface Science* **1975**, *53*, 314.
- [3] I. N. Sneddon, *International Journal of Engineering Science* **1965**, *3*, 47.
- [4] H. C. Andersen, in *Tales, Told for Children. First Collection. First Booklet: The Princess and the Pea*, (Ed: C. A. Reitzel), Copenhagen, Denmark **1835**.
- [5] R. Sunyer, A. J. Jin, R. Nossal, D. L. Sackett, *PLoS One* **2012**, *7*, e46107.
- [6] L. J. Gibson, M. F. Ashby, *Cellular Solids: Structure and properties*, Cambridge University Press, Cambridge, UK **1997**.
- [7] J. H. Lee, J. P. Singer, E. L. Thomas, *Adv Mater* **2012**, *24*, 4782.
- [8] T. Akihiro, S. Minoru, H. Kazuhiro, O. Shigeru, *Measurement Science and Technology* **1996**, *7*, 179.
- [9] S. A. Bencherif, R. W. Sands, D. Bhatta, P. Arany, C. S. Verbeke, D. A. Edwards, D. J. Mooney, *Proc. Natl. Acad. Sci. U. S. A.* **2012**, *109*, 19590.

Copyright WILEY-VCH Verlag GmbH & Co. KGaA, 69469 Weinheim, Germany, 2013.

Chapter IV

General discussion and perspectives

IV.1) Discussion

The A β peptides, believed to be the causative agents of AD, are generated by the subsequent cleavage of APP by β - and γ -secretases. Alternative processing of APP by α -, followed by γ -secretase, generates the shorter p3 peptides, and precludes the generation of A β (see Fig. 4, Chapter I). Thus, α - and β -secretases directly regulate A β production¹¹¹. Although modulating the activity of β -secretase emerged as a promising therapeutic targets to cure AD, clinical research was hampered by the lack of specificity and poor bioavailability of chemical compounds^{144,148,149}. The next target on the list became γ -secretase whose inhibition abolishes the generation of A β . Unfortunately, γ -secretase processes a growing list of substrates including the Notch receptor¹²⁵. Thus, its *in vivo* inhibition altered numerous physiological processes and revealed strong adverse effects including the worsening of cognitive functions¹³⁰⁻¹³³. Importantly, the cleavage of sAPP β by the γ -secretase complex generates A β of various length: the forty amino-acid long A β 40 is the main and non-pathogenic peptide whereas the long A β 42 and A β 43 are the most aggregating and toxic species⁶⁸⁻⁷⁰. Indeed, the A β 42/A β 40 ratio is a marker for AD: it remains low in healthy brains (0.1-0.2) and may increase up to two in the brain of AD patients^{42,71}.

The idea emerged that safe AD treatments should specifically block the processing of APP to reduce the production of A β as well as the A β 42/A β 40 ratio, without affecting the cleavage of other substrates. This goal can be achieved by the delivery of chemical compounds (γ -secretase modulators²²² and β -secretase inhibitors²²³) or by the identification of endogenous modulators of γ -secretase and APP processing.

γ -Secretase endogenous modulators

A growing list of proteins modulating A β production were identified. They control various molecular mechanisms such as the regulation of APP maturation (Fe65¹⁸³), processing by secretases (TMP21¹⁷⁸, X11¹⁸², Reticulon family proteins²²⁴) or interfering with APP trafficking and/or lysosomal degradation (AP2¹⁸⁶, APMAP⁷², Tspan6⁷², Nogo⁷², Sorla¹⁸¹, Beclin1¹⁸⁵, PICALM^{186,225}). In accordance with our study in which we show that PS phosphorylation does not affect γ -secretase activity (see manuscript page 60), no kinase or phosphatase has yet been shown to regulate γ -secretase activity. Most proteins interacting physically with the secretases or APP are well studied for their implication in protein trafficking or protein autophagic/lysosomal degradation. However these proteins may fulfill yet unknown physiological functions. This is particularly true for APMAP, whose only known function is related to *in vitro* adipogenesis^{226,227}, its physiological function is currently under investigation in our lab. In our study page 31, we shed the light on the role of APMAP in AD brain as a suppressor of A β production. Yet, APMAP depletion increased

A β levels whereas its overexpression didn't affect A β production *in vitro*. Thus, APMAP does not appear to have a therapeutic potential, but *in vivo* experiments have to be performed to clearly address this question.

Biological functions of APMAP

APMAP expression is necessary for *in vitro* adipogenesis and is stimulated by the peroxisome proliferator-activated receptor γ (PPAR γ)^{226,227}. Adipocyte play an active role in the regulation of two well-known modulators of A β production: cholesterol which stimulates the processing of APP by secretases^{123,170,228,229}, and Leptin, which decreases the levels of A β peptides^{230,231}. Indeed, PPAR γ activation promote adipogenesis, and has been shown to inhibit the production of A β and increase its clearance^{232–237}. The A β -lowering effects of PPAR γ may be mediated by Leptin, cholesterol, APMAP (see manuscript page 31), or by other unknown molecular pathways. Yet, inhibition of the cleavage of Notch by γ -secretase induced PPAR γ expression^{238,239}, and points out a potential regulatory feedback loop. Interestingly, PPAR γ is expressed in the human/mouse brain^{240,241} and displays neuroprotective effects (reviewed in ^{242,243}). Indeed, its activation led to a decrease in A β burden together with decreased microglial activation in AD mouse models^{244–246}.

Additionally, it should be noticed that adipose tissues are subdivided into two classes: the white adipose tissue which is highly present in obese individuals and stores excess energy as triglycerides, and the brown adipose tissue which metabolizes fat to produce heat²⁴⁷. In addition to its A β -lowering effect, PPAR γ expression favors the generation of brown adipose tissue, thus increasing energy expend and decreasing body weight^{238,248}. In agreement with these molecular mechanisms, obesity and metabolic syndromes are risk factors for sporadic AD^{249–251}. Thus, we expect constitutive APMAP knock-out mice to display decreased brown adipose tissue, associated to increased body weight and A β levels.

APMAP, APP processing and CTF production

Due to its importance in AD pathogenesis and A β generation, APP has been widely studied. No clear physiological function has been assessed so far, but the APP gene family (including APP, APLP1 and APLP2) has been shown to be implicated in early stages development^{84,85} and lipid metabolism^{90,116}. Furthermore, its processing appears to mediate an equilibrium between neurotrophic and neurotoxic effects mediated by α - and β -secretase cleavages, respectively^{99–106}. Yet, the highly regulated processing of APP involves a high number of enzymes, including the well-studied α -, β -, and γ -secretases as well as several caspases, but also η - and θ -secretases (Fig. 9). Surprisingly and in agreement with the modified profile of APP-CTFs following APMAP depletion in HeLa cells (See Fig. 3 page 35), we observed in untreated HeLa cells high amounts of the 80

amino-acid long APP-CTF resulting from θ cleavage, in comparison to C83 and C99⁷². This either suggest a processing of C83 or C99 at by θ secretase²⁵², or efficient APP processing by this enzyme. Furthermore, we observed N-terminal degradation of APP-CTF and identified 6 new cleavage sites located between the θ site and APP transmembrane domain⁷² (see Fig. 9, red arrowheads). The mechanism responsible for the generation of these shorter APP-CTFs may involve yet unknown secretases, or may be linked to APP degradation, possibly by cathepsins²⁵³. Further studies are required to draw a complete list of the enzymes implicated in the processing/degradation of APP, and investigate the physiological relevance of the generated APP fragments.

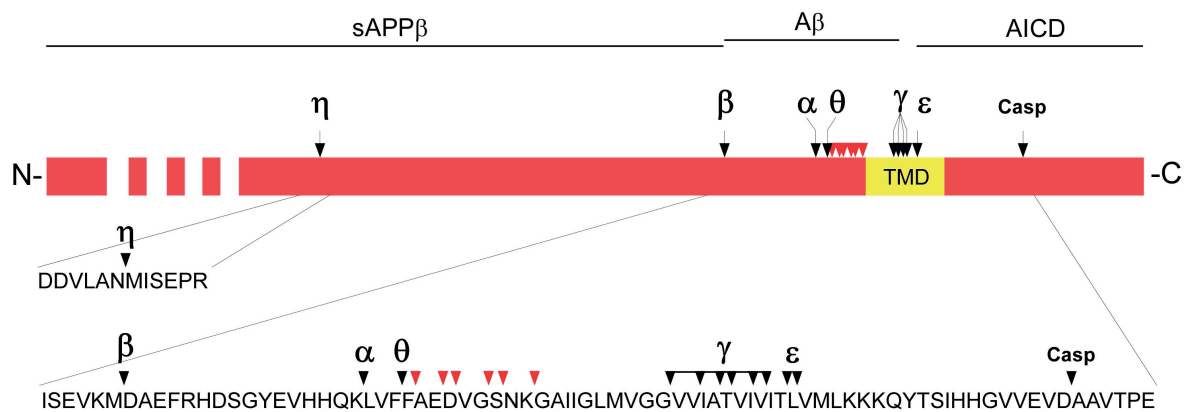


Figure 9: APP cleavage sites. Human APP is cleaved at numerous sites by specific enzymes: η (*MT5-MMP*⁶²), β (*BACE1*¹⁴²), α (*ADAM10*¹⁴⁷ and *TACE*²⁵⁴), θ (*Bace2*^{255,256}), γ (γ secretase²²²), ϵ (ϵ secretase²²²), Casp (*Caspases 6, 8 and 9*^{119–121}). The 6 new APP cleavage sites reported in the manuscript page 31 are indicated by red arrowheads. The transmembrane domain (TMD) is highlighted in yellow. The sequences of sAPP β , A β and AICD are indicated above.

Surprisingly, pharmacological inhibition of the γ -secretase complex increased the levels of the longest C80, in comparison to shorter APP-CTFs (Fig. S11 page 54). Because γ -secretase is an intramembrane cleaving protease, we exclude that short APP-CTFs (from C79 to C71) are generated by the proteolytic activity of this enzyme. Yet, we do not know if all APP-CTFs share the same affinity for being processed by γ -secretase. If not, we think that C80 may display the highest affinity. Also, one may hypothesize that shorter APP-CTFs are generated in the lysosome; the blockage of γ -secretase would leads to non-physiological accumulation of C80 which might impair C80 trafficking/degradation into the lysosome, thus altering the generation of short APP-CTFs. Moreover, PS is known to regulate endosomal and lysosomal function by acting on calcium homeostasis¹³⁸. One cannot exclude that γ -secretase inhibitors may affect PS function, alter lysosomal trafficking/function and block the degradation of C80 into shorter APP-CTFs.

Phosphorylation and γ -secretase activity

γ -Secretase subunits carry various PTMs including glycosylation, palmitoylation and phosphorylation which appear to modulate the intracellular trafficking of the γ -secretase complex (see section II.1.b). We showed in the manuscript page 60 that PS1 phosphorylation does not affect the enzymatic activity of γ -secretase in our cell-free assays. In sharp contrast, previous studies showed that PS phosphorylation at residues S319-T320 and T354 increased A β production^{196,257}, whereas addition of a phosphate at residues S353 and S357 decreased substrate processing and alters insulin signaling^{195,258}. All previous studies are *in vivo* or cell-based experiments, thus we think that PS phosphorylation may influence stability/degradation or subcellular trafficking of the γ -secretase complex rather than its enzymatic activity. Indeed, phosphorylation at S346 has been shown to decrease PS processing by caspases and inhibit apoptosis¹⁹⁷. As γ -secretase trafficking may be influenced by PS phosphorylation, it would be of great interest to perform subcellular fractionation and phosphorylation analyses to identify subcellular compartment-specific phosphorylation patterns.

γ -Secretase and cytoskeleton dynamics

In the last two decades, γ -secretase has fostered attention due to its role in A β production⁴³. Nevertheless the physiological importance of γ -secretase also requires a special attention, as the lack of cleavage of its numerous substrates is embryonically lethal^{125,141}. Cell differentiation¹²⁶, synaptic plasticity^{127,128}, cytoskeleton dynamics^{129,259}, APP transcription regulation are some of the functions regulated by the proteolytic activity of γ -secretase. We recently showed that γ -secretase activity affects the phosphorylation state of the actin binding protein Cofilin, and regulates cytoskeleton dynamics²⁵⁹. In contrast, no developmental defects have been observed on individuals carrying PS-FAD mutation, all inducing a loss of enzymatic activity^{260,261}. Therefore, other mechanisms may affect the phosphorylation state of Cofilin, and compensate the loss of γ -secretase activity in PS-FAD patients. We found that the phosphorylation/activation of Cofilin is mediated by the processing of APP by γ -secretase. Although fibrillary A β have been shown to modulate Cofilin phosphorylation²⁶², the effect of FAD remains unclear: it could solely promote the aggregation of A β peptides or act via the activation of alternative signaling pathways.

Also, several studies highlighted the implication of Cofilin in the aggressiveness and metastasis of various cancer types^{204,263–265}, and suggest a critical role for γ -secretase via the Cofilin and the well-studied Notch pathways in cancer pathologies (reviewed in ^{266,267}).

Electrical impedance and brain structures

In addition to the investigation of the molecular mechanisms leading to neurodegeneration and brain shrinkage, we considered new and low-cost methods for monitoring brain structural changes. We optimized the detection of brain structures by electrical impedance measurements, which makes possible the discriminate between cortical layers, white matter and subcortical nuclei²⁶⁸. This method could for example assist the implantation of deep brain stimulation electrodes in the substantia nigra of Parkinson's disease patients²⁶⁹, or allow monitoring of brain structural changes in AD or any neurodegenerative disorder. We indeed observed *ex-vivo* electrical impedance variations in AD mice hippocampus, induced by structural alterations caused by A β plaques²⁷⁰. Therefore *in vivo* experiments in living mice shall be performed to provide a proof of concept for our method, while accuracy in the measurements still remains to be improved for the detection of small nuclei such as the substantia nigra.

Neuronal scaffold and brain repair

In the context of stem cell therapies, electric impedance measurements may also be interesting for the accurate cell injection in damaged brain areas. To this extent, we developed a new injectable extracellular matrix-like scaffold to improve neuronal cell engraftment and integration in damaged tissues²⁷¹. We optimized the *in vitro* neuronal culture on our cryogel with mouse primary cortical neurons. In the future, our cryogel could be injected alone in the brain of patients suffering from severe brain damages and serve as a bandage promoting brain tissue repair. Alternatively, neuronal stem cells may first be cultured *in vitro* in our cryogel and then be injected into the brain of patients, and potentiate the replacement of dead cells. For this last approach, it should be noticed that the origins of cells and their differentiation is critical for safe and potent stem cell therapies^{214,215}. In parallel, previous studies reported the utilization of chemical-free stem cell differentiation procedures, based on the shape of cell culture substrates²⁷²⁻²⁷⁶. Further *in vivo* investigations are required to determine the cell-differentiation potential of our cryogel, improve this characteristic, and prove the efficiency of our cryogel scaffold in promoting the regeneration of brain tissues.

IV.2) Perspectives

Generation and characterization of an APMAP-KO mice

We identified APMAP as an endogenous activator of A β production in AD. While APMAP is known to be necessary for *in vitro* adipogenesis, no *in vivo* experiments have been performed so far. We showed that depletion of APMAP yields strong A β phenotype, thus we want to investigate the

physiological functions of APMAP by generating a mouse lacking this gene (APMAP-KO). Mice stem cells heterozygous for the APMAP-KO allele are available at the KOMP repository²⁷⁷, thus accelerating the generation of homozygous APMAP-KO mice. We will first observe if such mice are viable, fertile or display any major phenotype. Secondly and in accordance with the adipogenesis-related function of APMAP, we will initiate metabolic characterization to assess fat storage, glucose/general metabolism and energy expenditure. Then and linked to the effect of APMAP on A β production, we will perform behavioral tests to determine learning capacity, memory and anxiety, as well as biochemical analyses to monitor the processing of APP in our mice. APMAP-KO mice can later be bred with the AD mouse model APPPS1²⁰⁸ to study the effect of APMAP suppression on A β plaques dynamics.

The fact that *in vitro* APMAP depletion increases toxic A β while its overexpression shows no effects suggest that APMAP may not be used as a therapeutic target to decrease the production of A β . To further confirm these *in vitro* observations, a mouse overexpressing APMAP should be generated and characterized in order not to miss a potent therapeutic function for our protein.

Biochemical analyses to decipher APMAP functions

In parallel to the *in vivo* studies, we may take advantage of our highly purified APMAP to perform crystallization studies and X-ray diffraction and decipher APMAP three dimensional structure. Then, structure-function homology would allow the discovery of protein domains or enzymatic functions. Indeed, APMAP shares thirty percent homology with paraoxonases, both proteins display arylesterase enzymatic activity, which participate in the detoxification of organic compounds^{278–280}. We aim at confirming the arylesterase activity of purified APMAP in cell-free activity assays. Also, the APMAP/paraoxonases sequence homology suggest similar biological roles such as anti-inflammatory and anti-oxidant functions. This purified APMAP could also be used to identify binding partners and highlight APMAP-related signaling pathway. This approach, together with protein expression (Stable Isotope Labeling with Amino acids in Cell culture, SILAC) and gene expression (Illumina sequencing®) analysis of APMAP-KO mice would reveal signaling pathway affected by APMAP and suggest physiological function and biological mechanisms for our candidate.

Investigate the degradation of APP-CTFs

APP-CTF analysis (see Fig. S11 page 54) revealed 1) that C80 is the major APP-CTF fragment in these cells, 2) the existence of N-terminal processing of APP-CTFs and 3) the influence of APMAP and γ -secretase activity on APP-CTFs cleavage sites. We ignore if short APP-CTFs are generated by a regulated proteolytic cleavage or by a degradation by the autophagic/lysosomal pathway. We plan

to perform *in vitro* experiments to find in which cellular compartment these cleavages occur, and identify the enzymes/molecular mechanisms implicated. We also plan to conduct researches on the N-terminal cleavage of APP-CTFs in other cell types including primary cortical neurons, as well as in the mouse and human brain. Finally, we aim at observing the effect of PS-FAD and APP-FAD mutations on the generation of shorter APP-CTFs.

Because APMAP modulates the production of short APP-CTFs, we will study the trafficking of recombinant APP fused with GFP inside primary cortical neurons from either WT mice or APMAP-KO mice. Protein extract of both mice brains will also be performed to monitor the effect of APMAP on APP-CTFs processing *in vivo*.

In conclusion, our data show that the adipocyte differentiation protein APMAP is an endogenous suppressor of A β production in the brain, by interfering with the degradation of APP-CTF by the lysosomal/autophagic pathway. Further work is ongoing to understand the biological functions and mechanisms of APMAP, and possibly identify new therapeutic targets to safely cure AD.

Bibliography

1. Levy, M. L., Cummings, J. L. & Kahn-Rose, R. Neuropsychiatric symptoms and cholinergic therapy for Alzheimer's disease. *Gerontology* **45 Suppl 1**, 15–22 (1999).
2. Reisberg, B. *et al.* Behavioral symptoms in Alzheimer's disease: phenomenology and treatment. *J. Clin. Psychiatry* **48 Suppl**, 9–15 (1987).
3. Kukull, W. A. *et al.* Causes of death associated with Alzheimer disease: variation by level of cognitive impairment before death. *J. Am. Geriatr. Soc.* **42**, 723–726 (1994).
4. Glenner, G. G. & Wong, C. W. Alzheimer's disease: initial report of the purification and characterization of a novel cerebrovascular amyloid protein. *Biochem. Biophys. Res. Commun.* **120**, 885–890 (1984).
5. Kosik, K. S., Joachim, C. L. & Selkoe, D. J. Microtubule-associated protein tau (tau) is a major antigenic component of paired helical filaments in Alzheimer disease. *Proc. Natl. Acad. Sci. U. S. A.* **83**, 4044–4048 (1986).
6. Jellinger, K. A. & Bancher, C. Neuropathology of Alzheimer's disease: a critical update. *J. Neural Transm. Suppl.* **54**, 77–95 (1998).
7. Braak, H. & Braak, E. Staging of alzheimer's disease-related neurofibrillary changes. *Neurobiol. Aging* **16**, 271–278 (1995).
8. Meyer-Luehmann, M. *et al.* Exogenous Induction of Cerebral β -Amyloidogenesis Is Governed by Agent and Host. *Science* **313**, 1781–1784 (2006).
9. Clavaguera, F. *et al.* Transmission and spreading of tauopathy in transgenic mouse brain. *Nat. Cell Biol.* **11**, 909–913 (2009).
10. Frost, B., Jacks, R. L. & Diamond, M. I. Propagation of tau misfolding from the outside to the inside of a cell. *J. Biol. Chem.* **284**, 12845–12852 (2009).
11. Thal, D. R., Del Tredici, K. & Braak, H. Neurodegeneration in normal brain aging and disease. *Sci. Aging Knowl. Environ. SAGE KE* **2004**, pe26 (2004).

12. Bateman, R. J. *et al.* Clinical and Biomarker Changes in Dominantly Inherited Alzheimer's Disease. *N. Engl. J. Med.* **367**, 795–804 (2012).
13. Alzheimer Europe - Research - European Collaboration on Dementia - Cost of dementia - Prognosis to 2030. at <<http://www.alzheimer-europe.org/Research/European-Collaboration-on-Dementia/Cost-of-dementia/Prognosis-to-2030>>
14. Viña, J. & Lloret, A. Why women have more Alzheimer's disease than men: gender and mitochondrial toxicity of amyloid-beta peptide. *J. Alzheimers Dis. JAD* **20 Suppl 2**, S527–533 (2010).
15. Wimo, A. *et al.* The economic impact of dementia in Europe in 2008-cost estimates from the Eurocode project. *Int. J. Geriatr. Psychiatry* **26**, 825–832 (2011).
16. Corbett, A. *et al.* Drug repositioning for Alzheimer's disease. *Nat. Rev. Drug Discov.* **11**, 833–846 (2012).
17. Davies, P. & Maloney, A. J. Selective loss of central cholinergic neurons in Alzheimer's disease. *Lancet Lond. Engl.* **2**, 1403 (1976).
18. Perry, E. K. *et al.* Correlation of cholinergic abnormalities with senile plaques and mental test scores in senile dementia. *Br. Med. J.* **2**, 1457–1459 (1978).
19. Wilcock, G. K., Esiri, M. M., Bowen, D. M. & Smith, C. C. Alzheimer's disease. Correlation of cortical choline acetyltransferase activity with the severity of dementia and histological abnormalities. *J. Neurol. Sci.* **57**, 407–417 (1982).
20. Dajas-Bailador, F. A., Heimala, K. & Wonnacott, S. The allosteric potentiation of nicotinic acetylcholine receptors by galantamine is transduced into cellular responses in neurons: Ca²⁺ signals and neurotransmitter release. *Mol. Pharmacol.* **64**, 1217–1226 (2003).
21. Moriguchi, S., Zhao, X., Marszalec, W., Yeh, J. Z. & Narahashi, T. Modulation of N-methyl-D-aspartate receptors by donepezil in rat cortical neurons. *J. Pharmacol. Exp. Ther.* **315**, 125–135 (2005).
22. Greenamyre, J. T. The role of glutamate in neurotransmission and in neurologic disease.

- Arch. Neurol.* **43**, 1058–1063 (1986).
23. Albin, R. L. & Greenamyre, J. T. Alternative excitotoxic hypotheses. *Neurology* **42**, 733–738 (1992).
24. Francis, P. T., Sims, N. R., Procter, A. W. & Bowen, D. M. Cortical pyramidal neurone loss may cause glutamatergic hypoactivity and cognitive impairment in Alzheimer's disease: investigative and therapeutic perspectives. *J. Neurochem.* **60**, 1589–1604 (1993).
25. Aging, N. I. on. Alzheimer's Disease Medications Fact Sheet. *National Institute on Aging* (2011). at <<https://www.nia.nih.gov/alzheimers/publication/alzheimers-disease-medications-fact-sheet>>
26. Albert, M. S. *et al.* The diagnosis of mild cognitive impairment due to Alzheimer's disease: Recommendations from the National Institute on Aging-Alzheimer's Association workgroups on diagnostic guidelines for Alzheimer's disease. *Alzheimers Dement.* **7**, 270–279 (2011).
27. Ewers, M., Sperling, R. A., Klunk, W. E., Weiner, M. W. & Hampel, H. Neuroimaging markers for the prediction and early diagnosis of Alzheimer's disease dementia. *Trends Neurosci.* **34**, 430–442 (2011).
28. Mathis, C. A. *et al.* Synthesis and evaluation of ¹¹C-labeled 6-substituted 2-arylbenzothiazoles as amyloid imaging agents. *J. Med. Chem.* **46**, 2740–2754 (2003).
29. Klunk, W. E. *et al.* Imaging brain amyloid in Alzheimer's disease with Pittsburgh Compound-B. *Ann. Neurol.* **55**, 306–319 (2004).
30. Aizenstein, H. J. *et al.* Frequent amyloid deposition without significant cognitive impairment among the elderly. *Arch. Neurol.* **65**, 1509–1517 (2008).
31. Choi, S. R. *et al.* Preclinical properties of ¹⁸F-AV-45: a PET agent for Abeta plaques in the brain. *J. Nucl. Med. Off. Publ. Soc. Nucl. Med.* **50**, 1887–1894 (2009).
32. Silverman, D. H. S. Brain ¹⁸F-FDG PET in the diagnosis of neurodegenerative dementias: comparison with perfusion SPECT and with clinical evaluations lacking nuclear imaging. *J. Nucl. Med. Off. Publ. Soc. Nucl. Med.* **45**, 594–607 (2004).

33. Greicius, M. D., Srivastava, G., Reiss, A. L. & Menon, V. Default-mode network activity distinguishes Alzheimer's disease from healthy aging: evidence from functional MRI. *Proc. Natl. Acad. Sci. U. S. A.* **101**, 4637–4642 (2004).
34. Buckner, R. L., Andrews-Hanna, J. R. & Schacter, D. L. The brain's default network: anatomy, function, and relevance to disease. *Ann. N. Y. Acad. Sci.* **1124**, 1–38 (2008).
35. Heo, J.-H. *et al.* White matter hyperintensities and cognitive dysfunction in Alzheimer disease. *J. Geriatr. Psychiatry Neurol.* **22**, 207–212 (2009).
36. Fjell, A. M., Amlie, I. K., Westlye, L. T. & Walhovd, K. B. Mini-mental state examination is sensitive to brain atrophy in Alzheimer's disease. *Dement. Geriatr. Cogn. Disord.* **28**, 252–258 (2009).
37. Sperling, R. A. *et al.* Toward defining the preclinical stages of Alzheimer's disease: Recommendations from the National Institute on Aging-Alzheimer's Association workgroups on diagnostic guidelines for Alzheimer's disease. *Alzheimers Dement.* **7**, 280–292 (2011).
38. Über eine eigenartige Erkrankung der Hirnrinde | ALZFORUM. at <http://www.alzforum.org/papers/uber-eine-eigenartige-erkrankung-der-hirnrinde>
39. facts_figures_2015.pdf. at https://www.alz.org/facts/downloads/facts_figures_2015.pdf
40. Hardy, J. & Selkoe, D. J. The amyloid hypothesis of Alzheimer's disease: progress and problems on the road to therapeutics. *Science* **297**, 353–356 (2002).
41. Haass, C. *et al.* Normal Cellular Processing of the β -Amyloid Precursor Protein Results in the Secretion of the Amyloid β Peptide and Related Molecules. *Ann. N. Y. Acad. Sci.* **695**, 109–116 (1993).
42. Hardy, J., Duff, K., Hardy, K. G., Perez-Tur, J. & Hutton, M. Genetic dissection of Alzheimer's disease and related dementias: amyloid and its relationship to tau. *Nat. Neurosci.* **1**, 355–358 (1998).
43. Hardy, J. & Allsop, D. Amyloid deposition as the central event in the aetiology of Alzheimer's disease. *Trends Pharmacol. Sci.* **12**, 383–388 (1991).

44. Doens, D. & Fernández, P. L. Microglia receptors and their implications in the response to amyloid β for Alzheimer's disease pathogenesis. *J. Neuroinflammation* **11**, 48 (2014).
45. Hayes, A., Thaker, U., Iwatsubo, T., Pickering-Brown, S. M. & Mann, D. M. A. Pathological relationships between microglial cell activity and tau and amyloid beta protein in patients with Alzheimer's disease. *Neurosci. Lett.* **331**, 171–174 (2002).
46. Rapoport, M., Dawson, H. N., Binder, L. I., Vitek, M. P. & Ferreira, A. Tau is essential to beta -amyloid-induced neurotoxicity. *Proc. Natl. Acad. Sci. U. S. A.* **99**, 6364–6369 (2002).
47. Ittner, L. M. *et al.* Dendritic function of tau mediates amyloid-beta toxicity in Alzheimer's disease mouse models. *Cell* **142**, 387–397 (2010).
48. Citron, M. Strategies for disease modification in Alzheimer's disease. *Nat. Rev. Neurosci.* **5**, 677–685 (2004).
49. Wisniewski, T., Ghiso, J. & Frangione, B. Peptides homologous to the amyloid protein of Alzheimer's disease containing a glutamine for glutamic acid substitution have accelerated amyloid fibril formation. *Biochem. Biophys. Res. Commun.* **179**, 1247–1254 (1991).
50. Scheuner, D. *et al.* Secreted amyloid beta-protein similar to that in the senile plaques of Alzheimer's disease is increased in vivo by the presenilin 1 and 2 and APP mutations linked to familial Alzheimer's disease. *Nat. Med.* **2**, 864–870 (1996).
51. Lemere, C. A. *et al.* Sequence of Deposition of Heterogeneous Amyloid β -Peptides and APO E in Down Syndrome: Implications for Initial Events in Amyloid Plaque Formation. *Neurobiol. Dis.* **3**, 16–32 (1996).
52. Rumble, B. *et al.* Amyloid A4 protein and its precursor in Down's syndrome and Alzheimer's disease. *N. Engl. J. Med.* **320**, 1446–1452 (1989).
53. Jonsson, T. *et al.* A mutation in APP protects against Alzheimer's disease and age-related cognitive decline. *Nature* **488**, 96–99 (2012).
54. Dyrks, T. *et al.* Identification, transmembrane orientation and biogenesis of the amyloid A4 precursor of Alzheimer's disease. *EMBO J.* **7**, 949–957 (1988).

55. Kang, J. *et al.* The precursor of Alzheimer's disease amyloid A4 protein resembles a cell-surface receptor. *Nature* **325**, 733–736 (1987).
56. Tanaka, S. *et al.* Tissue-specific expression of three types of beta-protein precursor mRNA: enhancement of protease inhibitor-harboring types in Alzheimer's disease brain. *Biochem. Biophys. Res. Commun.* **165**, 1406–1414 (1989).
57. Li, Q. X., Fuller, S. J., Beyreuther, K. & Masters, C. L. The amyloid precursor protein of Alzheimer disease in human brain and blood. *J. Leukoc. Biol.* **66**, 567–574 (1999).
58. Gandy, S. The role of cerebral amyloid beta accumulation in common forms of Alzheimer disease. *J. Clin. Invest.* **115**, 1121–1129 (2005).
59. Checler, F. Two-steps control of cellular prion physiology by the extracellular regulated kinase-1 (ERK1). *Prion* **6**, 23–25 (2012).
60. Esch, F. *et al.* Cleavage of Amyloid-Beta Peptide During Constitutive Processing of Its Precursor. *Science* **248**, 1122–1124 (1990).
61. Haass, C., Hung, A. Y., Schlossmacher, M. G., Teplow, D. B. & Selkoe, D. J. beta-Amyloid peptide and a 3-kDa fragment are derived by distinct cellular mechanisms. *J. Biol. Chem.* **268**, 3021–3024 (1993).
62. Willem, M. *et al.* η -Secretase processing of APP inhibits neuronal activity in the hippocampus. *Nature* (2015). doi:10.1038/nature14864
63. Nixon, R. A. & Yang, D.-S. Autophagy failure in Alzheimer's disease--locating the primary defect. *Neurobiol. Dis.* **43**, 38–45 (2011).
64. Busciglio, J., Gabuzda, D. H., Matsudaira, P. & Yankner, B. A. Generation of beta-amyloid in the secretory pathway in neuronal and nonneuronal cells. *Proc. Natl. Acad. Sci. U. S. A.* **90**, 2092–2096 (1993).
65. Seubert, P. *et al.* Isolation and quantification of soluble Alzheimer's beta-peptide from biological fluids. *Nature* **359**, 325–327 (1992).
66. Haass, C. *et al.* Amyloid beta-peptide is produced by cultured cells during normal

- metabolism. *Nature* **359**, 322–325 (1992).
67. Shoji, M. *et al.* Production of the Alzheimer amyloid beta protein by normal proteolytic processing. *Science* **258**, 126–129 (1992).
68. Sastre, M. *et al.* Presenilin-dependent γ -secretase processing of β -amyloid precursor protein at a site corresponding to the S3 cleavage of Notch. *EMBO Rep.* **2**, 835–841 (2001).
69. Weidemann, A. *et al.* A novel epsilon-cleavage within the transmembrane domain of the Alzheimer amyloid precursor protein demonstrates homology with Notch processing. *Biochemistry (Mosc.)* **41**, 2825–2835 (2002).
70. Takami, M. *et al.* γ -Secretase: Successive Tripeptide and Tetrapeptide Release from the Transmembrane Domain of β -Carboxyl Terminal Fragment. *J. Neurosci.* **29**, 13042–13052 (2009).
71. Kuperstein, I. *et al.* Neurotoxicity of Alzheimer's disease A β peptides is induced by small changes in the A β 42 to A β 40 ratio. *EMBO J.* **29**, 3408–3420 (2010).
72. Mosser, S. *et al.* The adipocyte differentiation protein APMAP is an endogenous suppressor of A β production in the brain. *Hum. Mol. Genet.* **24**, 371–382 (2015).
73. Haass, C., Kaether, C., Thinakaran, G. & Sisodia, S. Trafficking and proteolytic processing of APP. *Cold Spring Harb. Perspect. Med.* **2**, a006270 (2012).
74. Nixon, R. A. Autophagy, amyloidogenesis and Alzheimer disease. *J. Cell Sci.* **120**, 4081–4091 (2007).
75. Schettini, G., Govoni, S., Racchi, M. & Rodriguez, G. Phosphorylation of APP-CTF-AICD domains and interaction with adaptor proteins: signal transduction and/or transcriptional role - relevance for Alzheimer pathology. *J. Neurochem.* **115**, 1299–1308 (2010).
76. Tomita, S., Kirino, Y. & Suzuki, T. Cleavage of Alzheimer's amyloid precursor protein (APP) by secretases occurs after O-glycosylation of APP in the protein secretory pathway. Identification of intracellular compartments in which APP cleavage occurs without using toxic agents that interfere with protein metabolism. *J. Biol. Chem.* **273**, 6277–6284 (1998).

77. Yazaki, M. *et al.* Mutation of potential N-linked glycosylation sites in the Alzheimer's disease amyloid precursor protein (APP). *Neurosci. Lett.* **221**, 57–60 (1996).
78. Bhattacharyya, R., Barren, C. & Kovacs, D. M. Palmitoylation of Amyloid Precursor Protein Regulates Amyloidogenic Processing in Lipid Rafts. *J. Neurosci.* **33**, 11169–11183 (2013).
79. Vassar, R. *et al.* β -Secretase Cleavage of Alzheimer's Amyloid Precursor Protein by the Transmembrane Aspartic Protease BACE. *Science* **286**, 735–741 (1999).
80. Prasad, H. & Rao, R. The Na⁺/H⁺ exchanger NHE6 modulates endosomal pH to control processing of amyloid precursor protein in a cell culture model of Alzheimer disease. *J. Biol. Chem.* **290**, 5311–5327 (2015).
81. Mueller, T. *et al.* Modulation of gene expression and cytoskeletal dynamics by the amyloid precursor protein intracellular domain (AICD). *Mol. Biol. Cell* **18**, 201–210 (2007).
82. Wang, H. *et al.* Cathepsin L Mediates the Degradation of Novel APP C-Terminal Fragments. *Biochemistry (Mosc.)* **54**, 2806–2816 (2015).
83. Tharp, W. G. & Sarkar, I. N. Origins of amyloid-beta. *Bmc Genomics* **14**, 290 (2013).
84. Guo, Q., Wang, Z., Li, H., Wiese, M. & Zheng, H. APP physiological and pathophysiological functions: insights from animal models. *Cell Res.* **22**, 78–89 (2012).
85. Müller, U. C. & Zheng, H. Physiological functions of APP family proteins. *Cold Spring Harb. Perspect. Med.* **2**, a006288 (2012).
86. Dawson, G. R. *et al.* Age-related cognitive deficits, impaired long-term potentiation and reduction in synaptic marker density in mice lacking the beta-amyloid precursor protein. *Neuroscience* **90**, 1–13 (1999).
87. Phinney, A. L. *et al.* No hippocampal neuron or synaptic bouton loss in learning-impaired aged beta-amyloid precursor protein-null mice. *Neuroscience* **90**, 1207–1216 (1999).
88. Seabrook, G. R. *et al.* Mechanisms contributing to the deficits in hippocampal synaptic plasticity in mice lacking amyloid precursor protein. *Neuropharmacology* **38**, 349–359 (1999).
89. Cousins, S. L., Dai, W. & Stephenson, F. A. APLP1 and APLP2, members of the APP family

- of proteins, behave similarly to APP in that they associate with NMDA receptors and enhance NMDA receptor surface expression. *J. Neurochem.* **133**, 879–885 (2015).
90. Grimm, M. O. W. *et al.* Regulation of cholesterol and sphingomyelin metabolism by amyloid-beta and presenilin. *Nat. Cell Biol.* **7**, 1118–1123 (2005).
 91. Heber, S. *et al.* Mice with combined gene knock-outs reveal essential and partially redundant functions of amyloid precursor protein family members. *J. Neurosci. Off. J. Soc. Neurosci.* **20**, 7951–7963 (2000).
 92. von Koch, C. S. *et al.* Generation of APLP2 KO mice and early postnatal lethality in APLP2/APP double KO mice. *Neurobiol. Aging* **18**, 661–669 (1997).
 93. Herms, J. *et al.* Cortical dysplasia resembling human type 2 lissencephaly in mice lacking all three APP family members. *EMBO J.* **23**, 4106–4115 (2004).
 94. Kibbey, M. C. *et al.* beta-Amyloid precursor protein binds to the neurite-promoting IKVAV site of laminin. *Proc. Natl. Acad. Sci. U. S. A.* **90**, 10150–10153 (1993).
 95. Clarris, H. J. *et al.* Identification of heparin-binding domains in the amyloid precursor protein of Alzheimer's disease by deletion mutagenesis and peptide mapping. *J. Neurochem.* **68**, 1164–1172 (1997).
 96. Mok, S. S. *et al.* Expression and analysis of heparin-binding regions of the amyloid precursor protein of Alzheimer's disease. *FEBS Lett.* **415**, 303–307 (1997).
 97. Behr, D., Hesse, L., Masters, C. L. & Multhaup, G. Regulation of amyloid protein precursor (APP) binding to collagen and mapping of the binding sites on APP and collagen type I. *J. Biol. Chem.* **271**, 1613–1620 (1996).
 98. Soba, P. *et al.* Homo- and heterodimerization of APP family members promotes intercellular adhesion. *EMBO J.* **24**, 3624–3634 (2005).
 99. Ring, S. *et al.* The secreted beta-amyloid precursor protein ectodomain APPs alpha is sufficient to rescue the anatomical, behavioral, and electrophysiological abnormalities of APP-deficient mice. *J. Neurosci. Off. J. Soc. Neurosci.* **27**, 7817–7826 (2007).

100. Turner, P. R., O'Connor, K., Tate, W. P. & Abraham, W. C. Roles of amyloid precursor protein and its fragments in regulating neural activity, plasticity and memory. *Prog. Neurobiol.* **70**, 1–32 (2003).
101. Taylor, C. J. *et al.* Endogenous secreted amyloid precursor protein- α regulates hippocampal NMDA receptor function, long-term potentiation and spatial memory. *Neurobiol. Dis.* **31**, 250–260 (2008).
102. Lannfelt, L. *et al.* Amyloid beta-peptide in cerebrospinal fluid in individuals with the Swedish Alzheimer amyloid precursor protein mutation. *Neurosci. Lett.* **199**, 203–206 (1995).
103. Sennvik, K. *et al.* Levels of alpha- and beta-secretase cleaved amyloid precursor protein in the cerebrospinal fluid of Alzheimer's disease patients. *Neurosci. Lett.* **278**, 169–172 (2000).
104. Colciaghi, F. *et al.* [alpha]-Secretase ADAM10 as well as [alpha]APPs is reduced in platelets and CSF of Alzheimer disease patients. *Mol. Med. Camb. Mass* **8**, 67–74 (2002).
105. Han, P. *et al.* Suppression of cyclin-dependent kinase 5 activation by amyloid precursor protein: a novel excitoprotective mechanism involving modulation of tau phosphorylation. *J. Neurosci. Off. J. Soc. Neurosci.* **25**, 11542–11552 (2005).
106. Nikolaev, A., McLaughlin, T., O'Leary, D. D. M. & Tessier-Lavigne, M. APP binds DR6 to trigger axon pruning and neuron death via distinct caspases. *Nature* **457**, 981–989 (2009).
107. Carrillo-Mora, P. *et al.* Amyloid Beta: Multiple Mechanisms of Toxicity and Only Some Protective Effects?, Amyloid Beta: Multiple Mechanisms of Toxicity and Only Some Protective Effects? *Oxidative Med. Cell. Longev. Oxidative Med. Cell. Longev.* **2014**, **2014**, e795375 (2014).
108. Lalowski, M. *et al.* The nonamyloidogenic" p3 fragment (amyloid beta 17-42) is a major constituent of Down's syndrome cerebellar preamyloid. *J. Biol. Chem.* **271**, 33623–33631 (1996).
109. Wei, W. L., Norton, D. D., Wang, X. T. & Kusiak, J. W. A beta 17-42 in Alzheimer's disease activates JNK and caspase-8 leading to neuronal apoptosis. *Brain* **125**, 2036–2043 (2002).
110. Yankner, B. *et al.* Neurotoxicity of a Fragment of the Amyloid Precursor Associated with

- Alzheimers-Disease. *Science* **245**, 417–420 (1989).
111. The Gamma-Secretase-Mediated Proteolytic Processing of APP C-Terminal Fragments as a Therapeutic Target for Alzheimer's Disease. at <<http://infoscience.epfl.ch/record/166943>>
 112. Rotz, R. C. von *et al.* The APP intracellular domain forms nuclear multiprotein complexes and regulates the transcription of its own precursor. *J. Cell Sci.* **117**, 4435–4448 (2004).
 113. Pardossi-Piquard, R. *et al.* Presenilin-Dependent Transcriptional Control of the A β -Degrading Enzyme Neprilysin by Intracellular Domains of β APP and APLP. *Neuron* **46**, 541–554 (2005).
 114. Kim, H. S. *et al.* C-terminal fragments of amyloid precursor protein exert neurotoxicity by inducing glycogen synthase kinase-3 beta expression. *Faseb J.* **17**, 1951–+ (2003).
 115. Ryan, K. A. & Pimplikar, S. W. Activation of GSK-3 and phosphorylation of CRMP2 in transgenic mice expressing APP intracellular domain. *J. Cell Biol.* **171**, 327–335 (2005).
 116. Liu, Q. *et al.* Amyloid precursor protein regulates brain apolipoprotein e and cholesterol metabolism through lipoprotein receptor LRP1. *Neuron* **56**, 66–78 (2007).
 117. Leissring, M. A. *et al.* A physiologic signaling role for the gamma-secretase-derived intracellular fragment of APP. *Proc. Natl. Acad. Sci. U. S. A.* **99**, 4697–4702 (2002).
 118. Checler, F. *et al.* The gamma/epsilon-secretase-derived APP intracellular domain fragments regulate p53. *Curr. Alzheimer Res.* **4**, 423–426 (2007).
 119. Lu, D. C., Soriano, S., Bredesen, D. E. & Koo, E. H. Caspase cleavage of the amyloid precursor protein modulates amyloid beta-protein toxicity. *J. Neurochem.* **87**, 733–741 (2003).
 120. Weidemann, A. *et al.* Proteolytic processing of the Alzheimer's disease amyloid precursor protein within its cytoplasmic domain by caspase-like proteases. *J. Biol. Chem.* **274**, 5823–5829 (1999).
 121. Pellegrini, L., Passer, B. J., Tabaton, M., Ganjei, J. K. & D'Adamio, L. Alternative, non-secretase processing of Alzheimer's beta-amyloid precursor protein during apoptosis by caspase-6 and -8. *J. Biol. Chem.* **274**, 21011–21016 (1999).

122. Kimberly, W. T. *et al.* Complex N-linked Glycosylated Nicastrin Associates with Active γ -Secretase and Undergoes Tight Cellular Regulation. *J. Biol. Chem.* **277**, 35113–35117 (2002).
123. Runz, H. *et al.* Inhibition of intracellular cholesterol transport alters presenilin localization and amyloid precursor protein processing in neuronal cells. *J. Neurosci. Off. J. Soc. Neurosci.* **22**, 1679–1689 (2002).
124. Pasternak, S. H. *et al.* Presenilin-1, nicastrin, amyloid precursor protein, and gamma-secretase activity are co-localized in the lysosomal membrane. *J. Biol. Chem.* **278**, 26687–26694 (2003).
125. Haapasalo, A. & Kovacs, D. M. The Many Substrates of Presenilin/ γ -Secretase. *J. Alzheimers Dis.* **25**, 3–28 (2011).
126. De Strooper, B. *et al.* A presenilin-1-dependent gamma-secretase-like protease mediates release of Notch intracellular domain. *Nature* **398**, 518–522 (1999).
127. Bot, N., Schweizer, C., Ben Halima, S. & Fraering, P. C. Processing of the synaptic cell adhesion molecule neurexin-3beta by Alzheimer disease alpha- and gamma-secretases. *J. Biol. Chem.* **286**, 2762–2773 (2011).
128. Tomita, T., Tanaka, S., Morohashi, Y. & Iwatsubo, T. Presenilin-dependent intramembrane cleavage of ephrin-B1. *Mol. Neurodegener.* **1**, 2 (2006).
129. Uemura, K. *et al.* Characterization of sequential N-cadherin cleavage by ADAM10 and PS1. *Neurosci. Lett.* **402**, 278–283 (2006).
130. Searfoss, G. H. *et al.* Adipsin, a biomarker of gastrointestinal toxicity mediated by a functional gamma-secretase inhibitor. *J. Biol. Chem.* **278**, 46107–46116 (2003).
131. Milano, J. *et al.* Modulation of notch processing by gamma-secretase inhibitors causes intestinal goblet cell metaplasia and induction of genes known to specify gut secretory lineage differentiation. *Toxicol. Sci. Off. J. Soc. Toxicol.* **82**, 341–358 (2004).
132. Wong, G. T. *et al.* Chronic treatment with the gamma-secretase inhibitor LY-411,575 inhibits beta-amyloid peptide production and alters lymphopoiesis and intestinal cell differentiation. *J.*

- Biol. Chem.* **279**, 12876–12882 (2004).
133. Cummings, J. What can be inferred from the interruption of the semagacestat trial for treatment of Alzheimer's disease? *Biol. Psychiatry* **68**, 876–878 (2010).
134. Fraering, P. C. Structural and Functional Determinants of gamma-Secretase, an Intramembrane Protease Implicated in Alzheimer's Disease. *Curr. Genomics* **8**, 531–549 (2007).
135. Lee, S.-F. *et al.* A conserved GXXXG motif in APH-1 is critical for assembly and activity of the gamma-secretase complex. *J. Biol. Chem.* **279**, 4144–4152 (2004).
136. Marinangeli, C. *et al.* Presenilin transmembrane domain 8 conserved AXXXAXXXG motifs are required for the activity of the γ -secretase complex. *J. Biol. Chem.* **290**, 7169–7184 (2015).
137. Shah, S. *et al.* Nicastrin functions as a gamma-secretase-substrate receptor. *Cell* **122**, 435–447 (2005).
138. Coen, K. *et al.* Lysosomal calcium homeostasis defects, not proton pump defects, cause endo-lysosomal dysfunction in PSEN-deficient cells. *J. Cell Biol.* **198**, 23–35 (2012).
139. Bai, X.-C. *et al.* An atomic structure of human γ -secretase. *Nature* (2015). doi:10.1038/nature14892
140. Mangialasche, F., Solomon, A., Winblad, B., Mecocci, P. & Kivipelto, M. Alzheimer's disease: clinical trials and drug development. *Lancet Neurol.* **9**, 702–716 (2010).
141. Shen, J. *et al.* Skeletal and CNS defects in Presenilin-1-deficient mice. *Cell* **89**, 629–639 (1997).
142. Luo, Y. *et al.* Mice deficient in BACE1, the Alzheimer's beta-secretase, have normal phenotype and abolished beta-amyloid generation. *Nat. Neurosci.* **4**, 231–232 (2001).
143. CoMentis and Astellas to Present Alzheimer's Disease Research at International Conference on Alzheimer's Disease (ICAD). *Marketwire* at <<http://www.marketwired.com/press-release/comentis-astellas-present-alzheimers-disease-research-international-conference-on-alzheimers-883083.htm>>
144. Butini, S. *et al.* The structural evolution of β -secretase inhibitors: a focus on the

- development of small-molecule inhibitors. *Curr. Top. Med. Chem.* **13**, 1787–1807 (2013).
145. Augelli-Szafran, C. E. *et al.* Discovery of notch-sparing gamma-secretase inhibitors. *Curr. Alzheimer Res.* **7**, 207–209 (2010).
146. Crump, C. J., Johnson, D. S. & Li, Y.-M. Development and mechanism of γ -secretase modulators for Alzheimer's disease. *Biochemistry (Mosc.)* **52**, 3197–3216 (2013).
147. Lammich, S. *et al.* Constitutive and regulated alpha-secretase cleavage of Alzheimer's amyloid precursor protein by a disintegrin metalloprotease. *Proc. Natl. Acad. Sci. U. S. A.* **96**, 3922–3927 (1999).
148. Hock, C. *et al.* Treatment with the selective muscarinic agonist talsaclidine decreases cerebrospinal fluid levels of total amyloid beta-peptide in patients with Alzheimer's disease. *Ann. N. Y. Acad. Sci.* **920**, 285–291 (2000).
149. Hock, C. *et al.* Treatment with the selective muscarinic m1 agonist talsaclidine decreases cerebrospinal fluid levels of A beta 42 in patients with Alzheimer's disease. *Amyloid Int. J. Exp. Clin. Investig. Off. J. Int. Soc. Amyloidosis* **10**, 1–6 (2003).
150. Relkin, N. R. *et al.* 18-Month study of intravenous immunoglobulin for treatment of mild Alzheimer disease. *Neurobiol. Aging* **30**, 1728–1736 (2009).
151. Reitz, C. Alzheimer's disease and the amyloid cascade hypothesis: a critical review. *Int. J. Alzheimers Dis.* **2012**, 369808 (2012).
152. Mandel, S. A. *et al.* Cell signaling pathways and iron chelation in the neurorestorative activity of green tea polyphenols: special reference to epigallocatechin gallate (EGCG). *J. Alzheimers Dis. JAD* **15**, 211–222 (2008).
153. Rezai-Zadeh, K. *et al.* Green tea epigallocatechin-3-gallate (EGCG) modulates amyloid precursor protein cleavage and reduces cerebral amyloidosis in Alzheimer transgenic mice. *J. Neurosci. Off. J. Soc. Neurosci.* **25**, 8807–8814 (2005).
154. Nalivaeva, N. N., Beckett, C., Belyaev, N. D. & Turner, A. J. Are amyloid-degrading enzymes viable therapeutic targets in Alzheimer's disease? *J. Neurochem.* **120 Suppl 1**, 167–185

- (2012).
155. Cabrol, C. *et al.* Small-molecule activators of insulin-degrading enzyme discovered through high-throughput compound screening. *PLoS One* **4**, e5274 (2009).
 156. Saito, T. *et al.* Somatostatin regulates brain amyloid beta peptide Abeta42 through modulation of proteolytic degradation. *Nat. Med.* **11**, 434–439 (2005).
 157. Nelson, M. P. & Shacka, J. J. Autophagy Modulation in Disease Therapy: Where Do We Stand? *Curr. Pathobiol. Rep.* **1**, 239–245 (2013).
 158. Chiba, T. in *Neurodegenerative Diseases* (ed. Kishore, U.) (InTech, 2013). at <http://www.intechopen.com/books/neurodegenerative-diseases/emerging-therapeutic-strategies-in-alzheimer-s-disease>
 159. Lloret, A., Fuchsberger, T., Giraldo, E. & Viña, J. Molecular mechanisms linking amyloid β toxicity and Tau hyperphosphorylation in Alzheimer's disease. *Free Radic. Biol. Med.* **83**, 186–191 (2015).
 160. Hu, J.-P. *et al.* Valproate reduces tau phosphorylation via cyclin-dependent kinase 5 and glycogen synthase kinase 3 signaling pathways. *Brain Res. Bull.* **85**, 194–200 (2011).
 161. Hampel, H. *et al.* Lithium trial in Alzheimer's disease: a randomized, single-blind, placebo-controlled, multicenter 10-week study. *J. Clin. Psychiatry* **70**, 922–931 (2009).
 162. Schirmer, R. H., Adler, H., Pickhardt, M. & Mandelkow, E. Lest we forget you--methylene blue... *Neurobiol. Aging* **32**, 2325.e7–16 (2011).
 163. Renolleau, S. *et al.* Specific caspase inhibitor Q-VD-OPh prevents neonatal stroke in P7 rat: a role for gender. *J. Neurochem.* **100**, 1062–1071 (2007).
 164. Yang, L. *et al.* A novel systemically active caspase inhibitor attenuates the toxicities of MPTP, malonate, and 3NP in vivo. *Neurobiol. Dis.* **17**, 250–259 (2004).
 165. Choi, Y. *et al.* Minocycline attenuates neuronal cell death and improves cognitive impairment in Alzheimer's disease models. *Neuropsychopharmacol. Off. Publ. Am. Coll. Neuropsychopharmacol.* **32**, 2393–2404 (2007).

166. Seabrook, T. J., Jiang, L., Maier, M. & Lemere, C. A. Minocycline affects microglia activation, Abeta deposition, and behavior in APP-tg mice. *Glia* **53**, 776–782 (2006).
167. Chiba, T., Yamada, M. & Aiso, S. Targeting the JAK2/STAT3 axis in Alzheimer’s disease. *Expert Opin. Ther. Targets* **13**, 1155–1167 (2009).
168. Kauwe, J. S. K. *et al.* Genome-wide association study of CSF levels of 59 Alzheimer’s disease candidate proteins: significant associations with proteins involved in amyloid processing and inflammation. *PLoS Genet.* **10**, e1004758 (2014).
169. Lambert, J.-C. *et al.* Genome-wide association study identifies variants at CLU and CR1 associated with Alzheimer’s disease. *Nat. Genet.* **41**, 1094–1099 (2009).
170. Proitsi, P. *et al.* Genetic predisposition to increased blood cholesterol and triglyceride lipid levels and risk of Alzheimer disease: a Mendelian randomization analysis. *PLoS Med.* **11**, e1001713 (2014).
171. Saunders, A. M. *et al.* Association of apolipoprotein E allele epsilon 4 with late-onset familial and sporadic Alzheimer’s disease. *Neurology* **43**, 1467–1472 (1993).
172. Fenoglio, C. *et al.* Absence of TREM2 polymorphisms in patients with Alzheimer’s disease and Frontotemporal Lobar Degeneration. *Neurosci. Lett.* **411**, 133–137 (2007).
173. McGeer, P. L. & McGeer, E. G. NSAIDs and Alzheimer disease: epidemiological, animal model and clinical studies. *Neurobiol. Aging* **28**, 639–647 (2007).
174. Harrington, C. *et al.* Rosiglitazone Does Not Improve Cognition or Global Function when Used as Adjunctive Therapy to AChE Inhibitors in Mild-to-Moderate Alzheimer’s Disease: Two Phase 3 Studies. *Curr. Alzheimer Res.* **8**, 592–606 (2011).
175. Sánchez-Ferro, A., Benito-León, J., Mitchell, A. J. & Bermejo-Pareja, F. A review of the potential therapeutic role of statins in the treatment of Alzheimer’s disease: current research and opinion. *Neuropsychiatr. Dis. Treat.* **9**, 55–63 (2013).
176. Choi, S. S., Lee, S.-R., Kim, S. U. & Lee, H. J. Alzheimer’s disease and stem cell therapy. *Exp. Neurobiol.* **23**, 45–52 (2014).

177. Introduction to revised criteria for the diagnosis of Alzheimer's disease: National Institute on Aging and the Alzheimer Association Workgroups «CNS Chronicle. at <<http://www.cnschronicle.com/2012/10/introduction-to-revised-criteria-for-the-diagnosis-of-alzheimers-disease-national-institute-on-aging-and-the-alzheimer-association-workgroups/#>>
178. Chen, F. *et al.* TMP21 is a presenilin complex component that modulates gamma-secretase but not epsilon-secretase activity. *Nature* **440**, 1208–1212 (2006).
179. He, G. *et al.* Gamma-secretase activating protein is a therapeutic target for Alzheimer's disease. *Nature* **467**, 95–98 (2010).
180. Hussain, I. *et al.* The role of γ -secretase activating protein (GSAP) and imatinib in the regulation of γ -secretase activity and amyloid- β generation. *J. Biol. Chem.* **288**, 2521–2531 (2013).
181. Andersen, O. M. *et al.* Neuronal sorting protein-related receptor sorLA/LR11 regulates processing of the amyloid precursor protein. *Proc. Natl. Acad. Sci. U. S. A.* **102**, 13461–13466 (2005).
182. Borg, J. P., Yang, Y., De Taddéo-Borg, M., Margolis, B. & Turner, R. S. The X11alpha protein slows cellular amyloid precursor protein processing and reduces Abeta40 and Abeta42 secretion. *J. Biol. Chem.* **273**, 14761–14766 (1998).
183. Sabo, S. L. *et al.* Regulation of beta-amyloid secretion by FE65, an amyloid protein precursor-binding protein. *J. Biol. Chem.* **274**, 7952–7957 (1999).
184. Kimberly, W. T., Zheng, J. B., Guénette, S. Y. & Selkoe, D. J. The intracellular domain of the beta-amyloid precursor protein is stabilized by Fe65 and translocates to the nucleus in a notch-like manner. *J. Biol. Chem.* **276**, 40288–40292 (2001).
185. Pickford, F. *et al.* The autophagy-related protein beclin 1 shows reduced expression in early Alzheimer disease and regulates amyloid beta accumulation in mice. *J. Clin. Invest.* **118**, 2190–2199 (2008).
186. Tian, Y., Chang, J. C., Fan, E. Y., Flajolet, M. & Greengard, P. Adaptor complex

- AP2/PICALM, through interaction with LC3, targets Alzheimer's APP-CTF for terminal degradation via autophagy. *Proc. Natl. Acad. Sci. U. S. A.* **110**, 17071–17076 (2013).
187. Van den Steen, P. E., Opdenakker, G., Wormald, M. R., Dwek, R. A. & Rudd, P. M. Matrix remodelling enzymes, the protease cascade and glycosylation. *Biochim. Biophys. Acta* **1528**, 61–73 (2001).
188. Risso, G., Blaustein, M., Pozzi, B., Mammi, P. & Srebrow, A. Akt/PKB: one kinase, many modifications. *Biochem. J.* **468**, 203–214 (2015).
189. Arawaka, S. *et al.* The levels of mature glycosylated nicastrin are regulated and correlate with gamma-secretase processing of amyloid beta-precursor protein. *J. Neurochem.* **83**, 1065–1071 (2002).
190. López, A. R. *et al.* Production of active glycosylation-deficient γ -secretase complex for crystallization studies. *Biotechnol. Bioeng.* (2015). doi:10.1002/bit.25675
191. Herreman, A. *et al.* gamma-Secretase activity requires the presenilin-dependent trafficking of nicastrin through the Golgi apparatus but not its complex glycosylation. *J. Cell Sci.* **116**, 1127–1136 (2003).
192. Mo, J.-S. *et al.* Phosphorylation of Nicastrin by SGK1 Leads to Its Degradation through Lysosomal and Proteasomal Pathways. *Plos One* **7**, e37111 (2012).
193. Jo, E.-H. *et al.* Akt1 phosphorylates Nicastrin to regulate its protein stability and activity. *J. Neurochem.* **134**, 799–810 (2015).
194. Cheng, H. *et al.* S-palmitoylation of gamma-secretase subunits nicastrin and APH-1. *J. Biol. Chem.* **284**, 1373–1384 (2009).
195. Maesako, M. *et al.* Gain of function by phosphorylation in Presenilin 1-mediated regulation of insulin signaling. *J. Neurochem.* **121**, 964–973 (2012).
196. Ryu, Y. S. *et al.* Dyrk1A-mediated phosphorylation of Presenilin 1: a functional link between Down syndrome and Alzheimer's disease. *J. Neurochem.* **115**, 574–584 (2010).
197. Fluhner, R., Friedlein, A., Haass, C. & Walter, J. Phosphorylation of presenilin 1 at the

- caspase recognition site regulates its proteolytic processing and the progression of apoptosis. *J. Biol. Chem.* **279**, 1585–1593 (2004).
198. Kirschenbaum, F., Hsu, S. C., Cordell, B. & McCarthy, J. V. Substitution of a glycogen synthase kinase-3 beta phosphorylation site in presenilin 1 separates presenilin function from beta-catenin signaling. *J. Biol. Chem.* **276**, 7366–7375 (2001).
199. Lau, K. F. *et al.* Cyclin-dependent kinase-5/p35 phosphorylates Presenilin 1 to regulate carboxy-terminal fragment stability. *Mol. Cell. Neurosci.* **20**, 13–20 (2002).
200. Lu, Q. *et al.* Alzheimer's disease-linked presenilin mutation (PS1M146L) induces filamin expression and γ -secretase independent redistribution. *J. Alzheimers Dis. JAD* **22**, 235–245 (2010).
201. Wu, J. *et al.* Arc/Arg3.1 regulates an endosomal pathway essential for activity-dependent β -amyloid generation. *Cell* **147**, 615–628 (2011).
202. Fukazawa, Y. *et al.* Hippocampal LTP is accompanied by enhanced F-actin content within the dendritic spine that is essential for late LTP maintenance in vivo. *Neuron* **38**, 447–460 (2003).
203. Rust, M. B. *et al.* Learning, AMPA receptor mobility and synaptic plasticity depend on n-cofilin-mediated actin dynamics. *EMBO J.* **29**, 1889–1902 (2010).
204. Wang, W., Eddy, R. & Condeelis, J. The cofilin pathway in breast cancer invasion and metastasis. *Nat. Rev. Cancer* **7**, 429–440 (2007).
205. Bravo-Cordero, J. J., Magalhaes, M. A. O., Eddy, R. J., Hodgson, L. & Condeelis, J. Functions of cofilin in cell locomotion and invasion. *Nat. Rev. Mol. Cell Biol.* **14**, 405–415 (2013).
206. Minamide, L. S., Striegl, A. M., Boyle, J. A., Meberg, P. J. & Bamburg, J. R. Neurodegenerative stimuli induce persistent ADF/cofilin-actin rods that disrupt distal neurite function. *Nat. Cell Biol.* **2**, 628–636 (2000).
207. Bamburg, J. R. *et al.* ADF/Cofilin-actin rods in neurodegenerative diseases. *Curr. Alzheimer Res.* **7**, 241–250 (2010).

208. Radde, R. *et al.* Abeta42-driven cerebral amyloidosis in transgenic mice reveals early and robust pathology. *EMBO Rep.* **7**, 940–946 (2006).
209. Ashe, K. H. & Zahs, K. R. Probing the biology of Alzheimer’s disease in mice. *Neuron* **66**, 631–645 (2010).
210. Duyckaerts, C., Potier, M.-C. & Delatour, B. Alzheimer disease models and human neuropathology: similarities and differences. *Acta Neuropathol. (Berl.)* **115**, 5–38 (2008).
211. Bolmont, T. *et al.* Label-free imaging of cerebral β -amyloidosis with extended-focus optical coherence microscopy. *J. Neurosci. Off. J. Soc. Neurosci.* **32**, 14548–14556 (2012).
212. Vukovic, J., Blackmore, D. G., Jhaveri, D. & Bartlett, P. F. Activation of neural precursors in the adult neurogenic niches. *Neurochem. Int.* **59**, 341–346 (2011).
213. Inta, D. & Gass, P. Is forebrain neurogenesis a potential repair mechanism after stroke? *J. Cereb. Blood Flow Metab.* **35**, 1220–1221 (2015).
214. Lindvall, O. *et al.* Grafts of fetal dopamine neurons survive and improve motor function in Parkinson’s disease. *Science* **247**, 574–577 (1990).
215. Freed, C. R. *et al.* Transplantation of embryonic dopamine neurons for severe Parkinson’s disease. *N. Engl. J. Med.* **344**, 710–719 (2001).
216. Modo, M., Stroemer, R. P., Tang, E., Patel, S. & Hodges, H. Effects of implantation site of stem cell grafts on behavioral recovery from stroke damage. *Stroke J. Cereb. Circ.* **33**, 2270–2278 (2002).
217. Kriks, S. *et al.* Dopamine neurons derived from human ES cells efficiently engraft in animal models of Parkinson’s disease. *Nature* **480**, 547–551 (2011).
218. Neuser, F., Polack, M., Annaheim, C., Tucker, K. L. & Korte, M. Region-specific integration of embryonic stem cell-derived neuronal precursors into a pre-existing neuronal circuit. *PLoS One* **8**, e66497 (2013).
219. Lavik, E. B., Klassen, H., Warfvinge, K., Langer, R. & Young, M. J. Fabrication of degradable polymer scaffolds to direct the integration and differentiation of retinal progenitors.

- Biomaterials* **26**, 3187–3196 (2005).
220. Fon, D. *et al.* Effects of GDNF-loaded injectable gelatin-based hydrogels on endogenous neural progenitor cell migration. *Adv. Healthc. Mater.* **3**, 761–774 (2014).
221. Bible, E. *et al.* The support of neural stem cells transplanted into stroke-induced brain cavities by PLGA particles. *Biomaterials* **30**, 2985–2994 (2009).
222. Dimitrov, M. *et al.* Alzheimer’s disease mutations in APP but not γ -secretase modulators affect epsilon-cleavage-dependent AICD production. *Nat. Commun.* **4**, 2246 (2013).
223. Vassar, R. BACE1 inhibitor drugs in clinical trials for Alzheimer’s disease. *Alzheimers Res. Ther.* **6**, 89 (2014).
224. Murayama, K. S. *et al.* Reticulons RTN3 and RTN4-B/C interact with BACE1 and inhibit its ability to produce amyloid beta-protein. *Eur. J. Neurosci.* **24**, 1237–1244 (2006).
225. Kanatsu, K. *et al.* Decreased CALM expression reduces A β 42 to total A β ratio through clathrin-mediated endocytosis of γ -secretase. *Nat. Commun.* **5**, 3386 (2014).
226. Albrektsen, T., Richter, H. E., Clausen, J. T. & Fleckner, J. Identification of a novel integral plasma membrane protein induced during adipocyte differentiation. *Biochem. J.* **359**, 393–402 (2001).
227. Bogner-Strauss, J. G. *et al.* Reconstruction of gene association network reveals a transmembrane protein required for adipogenesis and targeted by PPAR γ . *Cell. Mol. Life Sci. CMLS* **67**, 4049–4064 (2010).
228. Simons, M. *et al.* Cholesterol depletion inhibits the generation of beta-amyloid in hippocampal neurons. *Proc. Natl. Acad. Sci. U. S. A.* **95**, 6460–6464 (1998).
229. Howland, D. S. *et al.* Modulation of secreted beta-amyloid precursor protein and amyloid beta-peptide in brain by cholesterol. *J. Biol. Chem.* **273**, 16576–16582 (1998).
230. Tezapsidis, N. *et al.* Leptin: a novel therapeutic strategy for Alzheimer’s disease. *J. Alzheimers Dis. JAD* **16**, 731–740 (2009).
231. Fewlass, D. C. *et al.* Obesity-related leptin regulates Alzheimer’s A β . *FASEB J. Off. Publ.*

- Fed. Am. Soc. Exp. Biol.* **18**, 1870–1878 (2004).
232. De Felice, F. G. *et al.* Protection of synapses against Alzheimer's-linked toxins: insulin signaling prevents the pathogenic binding of Aβ oligomers. *Proc. Natl. Acad. Sci. U. S. A.* **106**, 1971–1976 (2009).
233. Risner, M. E. *et al.* Efficacy of rosiglitazone in a genetically defined population with mild-to-moderate Alzheimer's disease. *Pharmacogenomics J.* **6**, 246–254 (2006).
234. Pedersen, W. A. *et al.* Rosiglitazone attenuates learning and memory deficits in Tg2576 Alzheimer mice. *Exp. Neurol.* **199**, 265–273 (2006).
235. Camacho, I. E. *et al.* Peroxisome-proliferator-activated receptor gamma induces a clearance mechanism for the amyloid-beta peptide. *J. Neurosci. Off. J. Soc. Neurosci.* **24**, 10908–10917 (2004).
236. d'Abramo, C. *et al.* Role of peroxisome proliferator-activated receptor gamma in amyloid precursor protein processing and amyloid beta-mediated cell death. *Biochem. J.* **391**, 693–698 (2005).
237. Sastre, M. *et al.* Nonsteroidal anti-inflammatory drugs repress beta-secretase gene promoter activity by the activation of PPARγ. *Proc. Natl. Acad. Sci. U. S. A.* **103**, 443–448 (2006).
238. Bi, P. *et al.* Inhibition of Notch signaling promotes browning of white adipose tissue and ameliorates obesity. *Nat. Med.* **20**, 911–918 (2014).
239. Huang, Y. *et al.* gamma-secretase inhibitor induces adipogenesis of adipose-derived stem cells by regulation of Notch and PPAR-γ. *Cell Prolif.* **43**, 147–156 (2010).
240. Microarray Data :: Allen Brain Atlas: Human Brain. at <<http://human.brain-map.org/>>
241. ISH Data :: Allen Brain Atlas: Mouse Brain. at <<http://mouse.brain-map.org/>>
242. Quintanilla, R. A., Utreras, E. & Cabezas-Opazo, F. A. Role of PPAR γ in the Differentiation and Function of Neurons. *PPAR Res.* **2014**, 768594 (2014).
243. Kapadia, R., Yi, J.-H. & Vemuganti, R. Mechanisms of anti-inflammatory and neuroprotective actions of PPAR-γ agonists. *Front. Biosci. J. Virtual Libr.* **13**, 1813–1826

- (2008).
244. Mandrekar-Colucci, S., Karlo, J. C. & Landreth, G. E. Mechanisms underlying the rapid peroxisome proliferator-activated receptor- γ -mediated amyloid clearance and reversal of cognitive deficits in a murine model of Alzheimer's disease. *J. Neurosci. Off. J. Soc. Neurosci.* **32**, 10117–10128 (2012).
245. Heneka, M. T. *et al.* Acute treatment with the PPAR γ agonist pioglitazone and ibuprofen reduces glial inflammation and Abeta1-42 levels in APPV717I transgenic mice. *Brain J. Neurol.* **128**, 1442–1453 (2005).
246. Denner, L. A. *et al.* Cognitive enhancement with rosiglitazone links the hippocampal PPAR γ and ERK MAPK signaling pathways. *J. Neurosci. Off. J. Soc. Neurosci.* **32**, 16725–16735a (2012).
247. Saely, C. H., Geiger, K. & Drexel, H. Brown versus white adipose tissue: a mini-review. *Gerontology* **58**, 15–23 (2012).
248. Laplante, M. *et al.* PPAR-gamma activation mediates adipose depot-specific effects on gene expression and lipoprotein lipase activity: mechanisms for modulation of postprandial lipemia and differential adipose accretion. *Diabetes* **52**, 291–299 (2003).
249. Whitmer, R. A., Gunderson, E. P., Barrett-Connor, E., Quesenberry, C. P. & Yaffe, K. Obesity in middle age and future risk of dementia: a 27 year longitudinal population based study. *BMJ* **330**, 1360 (2005).
250. Tezapsidis, N., Smith, M. A. & Ashford, J. W. Central obesity and increased risk of dementia more than three decades later. *Neurology* **72**, 1030–1031; author reply 1031 (2009).
251. Beydoun, M. A., Beydoun, H. A. & Wang, Y. Obesity and central obesity as risk factors for incident dementia and its subtypes: a systematic review and meta-analysis. *Obes. Rev. Off. J. Int. Assoc. Study Obes.* **9**, 204–218 (2008).
252. Abdul-Hay, S. O., Sahara, T., McBride, M., Kang, D. & Leissring, M. A. Identification of BACE2 as an avid β -amyloid-degrading protease. *Mol. Neurodegener.* **7**, 46 (2012).

253. Tagawa, K., Maruyama, K. & Ishiura, S. Amyloid beta/A4 precursor protein (APP) processing in lysosomes. *Ann. N. Y. Acad. Sci.* **674**, 129–137 (1992).
254. Buxbaum, J. D. *et al.* Evidence that tumor necrosis factor alpha converting enzyme is involved in regulated alpha-secretase cleavage of the Alzheimer amyloid protein precursor. *J. Biol. Chem.* **273**, 27765–27767 (1998).
255. Farzan, M., Schnitzler, C. E., Vasilieva, N., Leung, D. & Choe, H. BACE2, a beta -secretase homolog, cleaves at the beta site and within the amyloid-beta region of the amyloid-beta precursor protein. *Proc. Natl. Acad. Sci. U. S. A.* **97**, 9712–9717 (2000).
256. Sun, X., He, G. & Song, W. BACE2, as a novel APP theta-secretase, is not responsible for the pathogenesis of Alzheimer’s disease in Down syndrome. *FASEB J. Off. Publ. Fed. Am. Soc. Exp. Biol.* **20**, 1369–1376 (2006).
257. Kuo, L.-H. *et al.* Tumor necrosis factor-alpha-elicited stimulation of gamma-secretase is mediated by c-Jun N-terminal kinase-dependent phosphorylation of presenilin and nicastrin. *Mol. Biol. Cell* **19**, 4201–4212 (2008).
258. Rezai-Zadeh, K. *et al.* Flavonoid-mediated presenilin-1 phosphorylation reduces Alzheimer’s disease beta-amyloid production. *J. Cell. Mol. Med.* **13**, 574–588 (2009).
259. Barone, E., Mosser, S. & Fraering, P. C. Inactivation of brain Cofilin-1 by age, Alzheimer’s disease and γ -secretase. *Biochim. Biophys. Acta* **1842**, 2500–2509 (2014).
260. Larner, A. J. Presenilin-1 mutations in Alzheimer’s disease: an update on genotype-phenotype relationships. *J. Alzheimers Dis. JAD* **37**, 653–659 (2013).
261. Wines-Samuelson, M. & Shen, J. Presenilins in the developing, adult, and aging cerebral cortex. *Neurosci. Rev. J. Bringing Neurobiol. Neurol. Psychiatry* **11**, 441–451 (2005).
262. Heredia, L. *et al.* Phosphorylation of actin-depolymerizing factor/cofilin by LIM-kinase mediates amyloid beta-induced degeneration: a potential mechanism of neuronal dystrophy in Alzheimer’s disease. *J. Neurosci. Off. J. Soc. Neurosci.* **26**, 6533–6542 (2006).
263. Chen, P., Zeng, M., Zhao, Y. & Fang, X. Upregulation of Limk1 caused by microRNA-138

- loss aggravates the metastasis of ovarian cancer by activation of Limk1/cofilin signaling. *Oncol. Rep.* **32**, 2070–2076 (2014).
264. Lu, L. I., Fu, N. I., Luo, X. U., Li, X.-Y. & Li, X.-P. Overexpression of cofilin 1 in prostate cancer and the corresponding clinical implications. *Oncol. Lett.* **9**, 2757–2761 (2015).
265. Tahtamouni, L. H., Shaw, A. E., Hasan, M. H., Yasin, S. R. & Bamburg, J. R. Non-overlapping activities of ADF and cofilin-1 during the migration of metastatic breast tumor cells. *BMC Cell Biol.* **14**, 45 (2013).
266. Yuan, X. *et al.* Notch signaling: An emerging therapeutic target for cancer treatment. *Cancer Lett.* (2015). doi:10.1016/j.canlet.2015.07.048
267. Chang, C.-Y., Leu, J.-D. & Lee, Y.-J. The actin depolymerizing factor (ADF)/cofilin signaling pathway and DNA damage responses in cancer. *Int. J. Mol. Sci.* **16**, 4095–4120 (2015).
268. Bédurier, A. *et al.* Accurate resistivity mouse brain mapping using microelectrode arrays. *Biosens. Bioelectron.* **60**, 143–153 (2014).
269. Moldovan, A.-S. *et al.* The treatment of Parkinson's disease with deep brain stimulation: current issues. *Neural Regen. Res.* **10**, 1018–1022 (2015).
270. Bédurier, A., Joris, P., Mosser, S., Fraering, P. C. & Renaud, P. Detection of Alzheimer's disease amyloid-beta plaque deposition by deep brain impedance profiling. *J. Neural Eng.* **12**, 024001 (2015).
271. Bédurier, A. *et al.* A compressible scaffold for minimally invasive delivery of large intact neuronal networks. *Adv. Healthc. Mater.* **4**, 301–312 (2015).
272. Maldonado, M. *et al.* The effects of electrospun substrate-mediated cell colony morphology on the self-renewal of human induced pluripotent stem cells. *Biomaterials* **50**, 10–19 (2015).
273. Mahmoudi, M. *et al.* Cell-imprinted substrates direct the fate of stem cells. *ACS Nano* **7**, 8379–8384 (2013).
274. Mashinchian, O. *et al.* Cell-imprinted substrates act as an artificial niche for skin regeneration. *ACS Appl. Mater. Interfaces* **6**, 13280–13292 (2014).

275. Mashinchian, O. *et al.* Regulation of stem cell fate by nanomaterial substrates. *Nanomed.* **10**, 829–847 (2015).
276. Lee, J. S., Lee, J. S., Wagoner-Johnson, A. & Murphy, W. L. Modular peptide growth factors for substrate-mediated stem cell differentiation. *Angew. Chem. Int. Ed Engl.* **48**, 6266–6269 (2009).
277. Knockout Mouse Project (KOMP) Repository. at <<https://www.komp.org/>>
278. Ilhan, A. *et al.* Localization and characterization of the novel protein encoded by C20orf3. *Biochem. J.* **414**, 485–495 (2008).
279. Primo-Parmo, S. L., Sorenson, R. C., Teiber, J. & La Du, B. N. The human serum paraoxonase/arylesterase gene (PON1) is one member of a multigene family. *Genomics* **33**, 498–507 (1996).
280. Sorenson, R. C. *et al.* Reconsideration of the catalytic center and mechanism of mammalian paraoxonase/arylesterase. *Proc. Natl. Acad. Sci. U. S. A.* **92**, 7187–7191 (1995).

Curriculum Vitae

Sébastien MOSSER

Tel. +41 77 434 14 73
E-mail: seb.mosser@gmail.com
Date of birth: 22.08.1988
Nationality: French

Permanent Address :

32 rue Saint-Paul
67115 PLOBSHEIM
FRANCE

RESEARCH INTERESTS

I'm willing to continue my scientific career in the field of neurodegeneration, and investigate the relationship between mental health, metabolism, and protein degradation by the use of biochemical approaches.

EDUCATIONAL BACKGROUND

- 2011- Pres.** **PhD student in neuroscience**, in the team led by Prof. P.C. Fraering at the école polytechnique fédérale de Lausanne (EPFL), Switzerland
- 2009-2011** **Master in Neuroscience**, majored in cellular and integrative neuroscience at the Université de Strasbourg, France
- 2006-2009** **Bachelor in Chemistry**, obtained at the Université de Strasbourg, France. I achieved my 3rd year bachelor at the Freie Universität Berlin, Germany, as Erasmus student
- 2006** **High School diploma majored in Science**

PROFESSIONAL EXPERIENCE

- 2011-Pres.** **PhD thesis:** Ecole Polytechnique Fédérale de Lausanne (EPFL), Lausanne, Switzerland. Brain and Mind institute, Laboratory of Cellular and Molecular Mechanisms of Alzheimer's disease, Chair Merck-Serono in Neuroscience. Reference: Prof. P.C. Fraering: Patrick.fraering@epfl.ch
- 2010-2011** **Master's thesis internship:** Ecole Polytechnique Fédérale de Lausanne (EPFL), Lausanne, Switzerland. Brain and Mind institute, Laboratory of Cellular and Molecular Mechanisms of Alzheimer's disease, Chair Merck-Serono in Neuroscience. Reference: Prof. P.C. Fraering: Patrick.fraering@epfl.ch
- 2009-2010** **Internship:** Institut National de la Santé et de la Recherche Médicale (INSERM), Strasbourg, France. Institute of Neurochemistry, Unit U1121. Reference: Dr. M.H. Metz-Boutigue: metz@neurochem.u-strasbg.fr

TECHNICAL EXPERIENCE

Protein Production, Purification and Analysis: *E.Coli* expression systems; eukaryotic expressions systems, lentivirus production, protein and RNA extraction from cells and tissues, cell-free activity assay, biochemistry

Animal Experimentation: mouse primary cortical neuron culture, mouse handling, colony management, surgery, stereotaxic intracerebral injection, genotyping

Cell Culture and Microscopy: Eukaryotic cells, bacteria, live imaging, confocal microscopy, immunohistochemistry, immunofluorescence, micro-electro array

Nucleic Acids: gene engineering, cloning, PCR, biochemistry of DNA and RNA, siRNA, shRNA, Real Time PCR, Luciferase assays, bioinformatics tools for DNA and RNA analysis

Mass spectrometry: MALDI-TOF Mass spectrometry

LANGUAGES

- **French:** native language

- **English:** fluent

- **German:** fluent

PUBLICATIONS

Mosser, S., Alattia, J.-R., Dimitrov, M., Matz, A., Pascual, J., Schneider, B.L., and Fraering, P.C. (2015). *The adipocyte differentiation protein APMAP is an endogenous suppressor of A β production in the brain.* Hum. Mol. Genet. 24, 371–382.

Barone, E., Mosser, S., and Fraering, P.C. (2014). *Inactivation of brain Cofilin-1 by age, Alzheimer's disease and γ -secretase.* Biochim. Biophys. Acta 1842, 2500–2509.

Matz, A., Halamoda-Kenzaoui, B., Hamelin, R., Mosser, S., Alattia, J.-R., Dimitrov, M., Moniatte, M., and Fraering, P.C. (2015). *Identification of new Presenilin-1 phosphosites: implication for γ -secretase activity and A β production.* J. Neurochem. 133, 409–421.

Bédurier, A., Joris, P., Mosser, S., Delattre, V., Fraering, P.C., and Renaud, P. (2014). *Accurate resistivity mouse brain mapping using microelectrode arrays.* Biosens. Bioelectron. 60, 143–153.

Bédurier, A., Joris, P., Mosser, S., Fraering, P.C., and Renaud, P. (2015). *Detection of Alzheimer's disease amyloid-beta plaque deposition by deep brain impedance profiling.* J. Neural Eng. 12, 024001.

Bédurier, A., Braschler, T., Peric, O., Fantner, G.E., Mosser, S., Fraering, P.C., Benchérif, S., Mooney, D.J., and Renaud, P. (2015). *A compressible scaffold for minimally invasive delivery of large intact neuronal networks.* Adv. Healthc. Mater. 4, 301–312.

Ren, Y., Huang, S.-H., Mosser, S., Heuschkel, M.O., Bertsch, A., Fraering, P.C., Chen, J.-J.J., and Renaud, P. (2015). *A Simple and Reliable PDMS and SU-8 Irreversible Bonding Method and Its Application on a Microfluidic-MEA Device for Neuroscience Research.* Micromachines 6, 1923–1934